2019

HIGH INJECTION PRESSURE DME IGNITION AND COMBUSTION PROCESSES: EXPERIMENT AND SIMULATION

Xiucheng Zhu
Michigan Technological University, xzhu3@mtu.edu

Recommended Citation

Zhu, Xiucheng, "HIGH INJECTION PRESSURE DME IGNITION AND COMBUSTION PROCESSES: EXPERIMENT AND SIMULATION", Open Access Dissertation, Michigan Technological University, 2019.
https://doi.org/10.37099/mtu.dc.etdr/923

HIGH INJECTION PRESSURE DME IGNITION AND COMBUSTION PROCESSES: EXPERIMENT AND SIMULATION

By

Xiucheng Zhu

A DISSERTATION

Submitted in partial fulfillment of the requirements for the degree of

DOCTOR OF PHILOSOPHY

In Mechanical Engineering - Engineering Mechanics

MICHIGAN TECHNOLOGICAL UNIVERSITY

2019

This dissertation has been approved in partial fulfillment of the requirements for the Degree of DOCTOR OF PHILOSOPHY in Mechanical Engineering - Engineering Mechanics.

Department of Mechanical Engineering - Engineering Mechanics

Dissertation Advisor:	*Dr. Seong-Young Lee*
Committee Member:	*Dr. Jeffrey D. Naber*
Committee Member:	*Dr. Youngchul Ra*
Committee Member:	*Dr. David Wanless*
Department Chair:	*Dr. William W. Predebon*

Table of Contents

List of figures ix

List of tables xv

Preface xvi

Acknowledgments xvii

List of abbreviations xviii

Abstract xix

1 Introduction 1

- 1.1 Motivations 4
- 1.2 Objectives 5
- 1.3 Thesis organization 7

2 Diesel spray combustion 9

- 2.1 Compression-ignition combustion 9
- 2.2 Injection and HEUI injector 11
- 2.3 Non-reacting sprays 13
  - 2.3.1 Atomization 13
  - 2.3.2 Global spray parameters: penetrations (liquid, vapor), spray angle . 14
  - 2.3.3 Local spray parameters: air mixing, droplet Size, curvature, etc 16
- 2.4 Reacting sprays 17
  - 2.4.1 Ignition delay 18
  - 2.4.2 Lift-off length (LOL) 19

3 DME spray combustion 21

- 3.1 DME properties 21
- 3.2 DME spray combustion 24
- 3.3 DME chemistry 25

4 CFD simulation overview 28

- 4.1 Spray modeling 29
- 4.2 Combustion modeling 29
- 4.3 Turbulence modeling 30

4.4 Chemical kinetic mechanism....31
4.5 Best practices and typical simulation setup....31

5 Two unconventional combustion concepts....33
5.1 Low temperature combustions....33
5.2 Combustion instability....36

6 Experimental techniques....40
6.1 Fuel delivery system overview....40
6.2 Rate of injection measurement....41
6.3 Optical diagnostics....45
6.3.1 Mie scattering....46
6.3.2 Schlieren and natural luminosity....47
6.3.3 OH* chemiluminescence....48
6.3.4 PLIF for formaldehyde....49

7 Data post-processing....51
7.1 General imaging processing....51
7.2 Image processing: combined schlieren-PLIF imaging....52
7.3 Pressure based data analysis....55
7.4 Intensity-aXial-Time (IXT) plot....58

8 Test conditions....61

9 HEUI injector modeling and ROI experiments for high injection pressure of DME1 64
9.1 Background....64
9.2 HEUI injector mechanism....66
9.3 Bosch-type ROI measurement....68
9.4 Fuel injection systems and capability....69
9.5 Simulink modeling details....71
9.5.1 Spool valve mechanism....73
9.5.2 Intensifier and plunger system....75
9.5.3 Fuel Pump System....76
9.5.4 Needle Valve....76
9.6 Results and discussions....78
9.6.1 Multi-hole injector results....78
9.6.2 Single-hole injector results....84

            9.6.3 Comparison of ROI between diesel and DME 89
        9.7 Concluding remarks 93

10 Experimental investigation on DME combustion: single-hole injector results 95
    10.1 Introduction 95
    10.2 High-speed images and analysis...96
        10.2.1 Non-vaporing spray 97
        10.2.2 Vaporing spray...101
        10.2.3 Combustion of DME...109
    10.3 Apparent heat release rate (AHRR)...110
    10.4 Ignition delay...115
    10.5 Intensity axial time (IXT) plot...121
    10.6 PLIF of CH_2O and overlapped schlieren images 124

11 Experimental and numerical study of diesel vs. DME in a CV: multi-hole results 127
    11.1 Introduction 127
    11.2 Experiment apparatus and conditions...128
    11.3 Numerical Approach 129
    11.4 Results and Discussion..130
    11.5 Conclusions 136

12 Ignition and Formaldehyde Formation in Dimethyl Ether (DME) Reacting Spray under Various EGR Levels: CFD Results 137
    12.1 Introduction 137
    12.2 Experimental and Numerical Setup...138
        12.2.1 Combustion vessel and fuel injection system 138
        12.2.2 Optical diagnostics...139
        12.2.3 CFD simulation setup 141
    12.3 Results and discussion...144
    12.4 Conclusions 154

13 Mechanism of Ignition and Flame Stabilization of High Injection Pressure Dimethyl Ether (DME) Sprays 156
    13.1 Introduction 156
    13.2 Background 157
    13.3 Results and discussions 159
        13.3.1 Non-vaporizing and Vaporizing Spray Characteristics 159

13.3.2 Combustion Characteristics 163
13.4 CFD simulation results 169
13.5 Summary and discussions 173
14 DME Combustion Instability Investigation 174
14.1 Brief overview 174
14.2 Experimental observation: 174
14.2.1 Evidence of occurrence: ringing pressure 174
14.2.2 Data processing methodology 178
14.2.3 Statistic summary of all the ringing cases: qualitatively summarize occurrence conditions 179
14.2.4 Other ringing cases 184
14.2.5 FFT analysis 186
14.3 Results of CFD simulations 187
14.3.1 CFD setup 187
14.3.2 Local pressure 189
14.3.3 FFT from CFD 195
14.3.4 Pressure and heat release coupling 196
14.3.5 Ringing index results 197
14.4 Summary and discussions 199
15 Conclusions and Future Work 201
16 Reference List 206
A Copyright documentation 220

List of figures

Figure 2-1 A typical CI combustion process: rate of injection vs time (top) and heat release rate (HHR) vs time (bottom)........10

Figure 2-2 Schematic of diesel spray structure (A schlieren image at the vaporizing condition)........14

Figure 2-3 Spray penetration and spray angle from DME spray using Mie scattering image........15

Figure 2-4 Quasi-steady diesel spray combustion visualization. Figure reproduced based on the concept in Ref. [Dec 1997,34]........18

Figure 2-5 Flame lift-off length (LOL) from OH* chemiluminescence image for DME reacting spray........20

Figure 5-1 Temperature and equivalence ratio plot for advanced combustion strategies. [Neely et al. 2005, 65]........34

Figure 5-2 Conceptual model for conventional diesel combustion (left) and Low-temperature combustion (right) [Musculus et al. 2013, 66]........35

Figure 6-1 Dual fuel (DME or diesel) delivery system which is compatible for HEUI injector [70]........41

Figure 6-2 Bosch tube type ROI measurement experimental set for HEUI........42

Figure 6-3 A sample output from the Bosch type ROI measurement system, including a measured ROI profile, open/close current signals, and injection pressure........43

Figure 6-4 A typical pressure trace for pre-burn process in CV........45

Figure 6-5 Hybrid of schlieren/Mie scattering and PLIF optical setup........46

Figure 6-6 Mie scattering shows an antenna lobe type pattern........47

Figure 6-7 Laser timing diagram along with the ICCD camera shutter time........50

Figure 7-1 Sample image-set showing image processing procedure starting from a raw schlieren image........52

Figure 7-2 Sample image-set of raw schlieren and PLIF images........53

Figure 7-3 Sample image-set showing image processing procedure of clean vapor boundary detection........54

Figure 7-4 A sample of combined schlieren-PLIF imaging 55

Figure 7-5 Procedure of CV pressure trace post-processing: (a) Raw CV pressure data, (b) Polynomial curve fit, (c) Smoothed pressure, (d) AHRR 56

Figure 7-6 The imaging processing using IXT method 59

Figure 7-7 IXT plot of DME spray combustion with LED light on for liquid Mie scattering 60

Figure 9-1 HEUI injector parts in functional diagram (left) and section view for the injector geometry (right) 67

Figure 9-2 Detailed layout for 1-D MATLAB/Simulink model for HEUI with 5 main functional blocks: control signal, spool valve, intensifier, fuel supply, and needle valve 72

Figure 9-3 Section view of HEUI oil spool, showing the spool valve mechanism [9-15] 73

Figure 9-4 Normalized spool valve inlet and return valve signal. “0” means completely closed, and “1” means fully open 74

Figure 9-5 Section views of schematic for single-hole nozzle (left) and multi-hole nozzle (right) 78

Figure 9-6 Comparison between diesel and DME fuel injection characteristics using injector model: At injection pressure 2000 bar, with oil supply pressure 300 bar, the nozzle is MH 8*155 µm nozzle 80

Figure 9-7 Experimental results of ROI and current waveform for 8x155 µm MH injector, at different injection pressure (750, 1000, 1500, and 2000 bar): diesel (top) and DME (bottom) 82

Figure 9-8 Injector model simulation results of ROI for 8x155 µm MH injector, at different injection pressure (750, 1000, 1500, and 2000 bar): diesel (top) and DME (bottom)...83

Figure 9-9 Effect of injection pressure on the injected fuel volume per stroke, comparing test results and injector model results 84

Figure 9-10 Comparison between diesel and DME fuel injection parameter characteristics using injector model: At injection pressure 1098 bar, with oil supply pressure 140 bar, and nozzle size is 180 µm...85

Figure 9-11 Comparison of ROI for DME at different injection pressures, and nozzle size diameter is 180 µm: experiments (top) and model (bottom) 87

Figure 9-12 Comparison between experimental ROI profile and simulation ROI profile at 1500 bar injection pressure, and nozzle size is 180 µm..89

Figure 9-13 ROI profiles of DME and Diesel at different injection pressures (180 µm nozzle, 2 ms injection duration)..91

Figure 9-14 The total injected mass of DME at different injection pressures 92

Figure 10-1 Mie scattering image comparison between diesel and DME with 1500bar injection pressure at 1.3 ms after start of injection 96

Figure 10-2 Non-vaporizing diesel and DME spray (Inj P= 1500 bar, Ambient= 383K, 14.8kg/m^3, D= 180μm)...99

Figure 10-3 Microscopic imaging for near nozzle spray characteristics 101

Figure 10-4 Diesel and DME sprays under vaporizing condition (Inj P = 1500 bar, Ambient= 900 K, 14.8 kg/m^3, D= 180 μm)...102

Figure 10-5 Liquid and vapor penetration of diesel and DME spray 103

Figure 10-6 Liquid penetration and vapor penetration of DME spray under vaporizing condition (0%O2, 900 K, 14.8kg/m3) 104

Figure 10-7 The effect of ambient temperature, images at ASOI= 2.68 ms (A)Mie scattering, (B)schlieren, (C) luminosity imaging..106

Figure 10-8 Liquid (solid line) and vapor (dash line) penetration profile of diesel and DME...108

Figure 10-9 Combustion of diesel and DME (Inj P= 1500 bar, Ambient= 900 K, 14.8 kg/m3, 15% O_2, D= 180 µm)...110

Figure 10-10 The effect of ambient temperature on the HRR of DME combustion 111

Figure 10-11 The effect of Oxygen level on the HRR of DME combustion..................112

Figure 10-12 The effect of injection pressure on the HRR of DME combustion............113

Figure 10-13 Cumulative heat release of diesel and DME combustion at the condition: ambient density is 14.8 kg/m^3; injection pressure is 1500 bar; nozzle size is 180 µm; injection duration is 2.0 ms, ambient temperature is 900 k, 15% O_2 114

Figure 10-14 Effect of O_2 concentration effect on ignition delay 116

Figure 10-15 Effect of ambient temperature on ignition delay......................................117

Figure 10-16 The effect of injection pressure on ignition delay of DME combustion....118

Figure 10-17 Effect of injection pressure on ignition delay 119

Figure 10-18 IXT plot of DME combustion with different O_2 concentrations (15%, 18%, and 21%) 122

Figure 10-19 IXT plot of DME combustion with varied injection pressure (50/75/100/125/150 MPa)..123

Figure 10-20 Schlieren images (blue) overlap with PLIF images (yellow) under conditions: injection pressure is 1500 bar. Ambient is 900 K, 18% O_2. Injector nozzle size is 180 µm. Injection energizing duration is 2 ms. A, B, and C are corresponding to those in Figure 9-13. The dashed line indicates the front of CH_2O region..125

Figure 10-21 Normalized total Integration of CH_2O under conditions: injection pressure is 1500 bar; Ambient is 900 K, 14.8 kg/m^3, 15%/18%/21% O_2; Injector nozzle size is 180 µm; Injection energizing duration is 2 ms 126

Figure 11-1 Ignition delay comparison between DME and diesel at an injection pressure of 1500 bar. 131

Figure 11-2 Comparison of events in DME (top) and diesel (bottom) ignition and combustion..132

Figure 11-3 Impact of Injection Duration on AHRR (left) and CHR (right) for equivalent DME and diesel energy..134

Figure 11-4 Comparison of Experiment vs. CFD (left); Species, HRR and Temperature evolution (right) 135

Figure 12-1 A schematic of experiments..140

Figure 12-2 Measured and numerical rate of injection..142

Figure 12-3 Ignition delay from experiment and simulation at various O_2 concentrations 145

Figure 12-4 Time-elapsed CH_2O from PLIF images (upper) and simulation (lower) at 18% O_2..146

Figure 12-5 Species evolution from CFD simulation at 18% O_2..147

Figure 12-6 Simulated temperature (top) and HRR (bottom) at each O_2 concentration. 149

Figure 12-7 CH_2O (top) & OH (bottom) formation over simulation time at each O_2 concentration 150

Figure 12-8 Computed ignition delay over O_2 concentration based on temperature, CH_2O, and OH 151

Figure 12-9 Phi-Temperature scatter and contour plots of CH_2O and OH from simulation 153

Figure 13-1 Microscopic imaging of DME spray at the initial stage of injection (non-vaporing condition) 161

Figure 13-2 The spray penetrations of diesel (solid line) and DME (dashed line) (non-vaporing and vaporing conditions) 162

Figure 13-3 AHRR and CHR comparison between diesel and DME, (combusting condition, 15% O_2) 165

Figure 13-4 Schlieren (outer) overlap with PLIF (inner) images (top) and OH* chemiluminescence (bottom), (combusting condition, 18% O_2) 167

Figure 13-5 Normalized total Integration of CH_2O under combusting condition (18% O_2) 169

Figure 13-6 CH_2O profile comparison between experiment and LES 171

Figure 13-7 Key transient DME flame development features. 172

Figure 14-1 Two averaged AHRR results of the combustion at the conditions of injection pressure of 1500 bar (2ms duration), the ambient temperature of 750K, the ambient density of 14.8Kg/m3, and Oxygen level of 18% 175

Figure 14-2 Single AHRR result from a ring case and less ringing case at the conditions of injection pressure of 150 MPa (2ms duration), the ambient temperature of 750K, the ambient density of 14.8Kg/m3, and Oxygen level of 18% 176

Figure 14-3 Natural luminosity from a ring case and less ringing case at the conditions of injection pressure of 1500 bar (2ms duration), the ambient temperature of 750K, the ambient density of 14.8Kg/m3, and Oxygen level of 18% 177

Figure 14-4 Data processing illustration of the oscillation AHRR portion extraction 178

Figure 14-5 AHRR of all the repeated tests (total 11) from the condition of injection pressure of 150 MPa (2ms duration), ambient temperature of 750K, ambient density of 14.8Kg/m3, and Oxygen level of 18% 180

Figure 14-6 P2P of the AHRR extraction vs ringing index 182

Figure 14-7 Ringing index evaluation against peak AHRR 183

Figure 14-8 Ringing index evaluation against the rate of rise of AHRR........................184

Figure 14-9 AHRR at 50 MPa injection pressure but with two different injection durations: 2ms and 3.3ms 185

Figure 14-10 AHRR at 3.3ms injection duration but with two different injection pressures: 50 MPa and 150 MPa...185

Figure 14-11 FFT analysis for three consecutive time domains of the AHRR curve......187

Figure 14-12 Schematic of the CFD simulation setup..188

Figure 14-13 CFD results of CV averaged pressure and local pressure at the sensor location (0,0,0)...191

Figure 14-14 Time elapsed temperature field from the CFD simulation: ambient of 900K and 18% O_2, and nozzle to plate distance is 60 mm 192

Figure 14-15 Time elapsed temperature field from the CFD simulation: ambient of 900K and 18% O2, and nozzle to plate distance is 80 mm 193

Figure 14-16 Local pressure from three different locations 194

Figure 14-17 FFT results of pressure output from CFD...196

Figure 14-18 Pressure, HRR, and the Rayleigh criterion index at the location (2,2,0) of 60 mm case 197

Figure 14-19 RI results of the CFD simulation 198

Figure 14-20 Visualization of RI results of the CFD simulation at plane Z = 4 of case 60 mm 199

List of tables

Table 3-1 Properties of diesel and DME [5] [40] [41]......22

Table 4-1 Typical simulation setup used in this work......32

Table 8-1 Test conditions of multi-hole nozzle injector study......62

Table 8-2 Test conditions of single-hole nozzle injector study......63

Table 9-1 Properties of diesel and DME [9-4] [9-6,7]......66

Table 9-2 Comparison between four common injection technologies in terms of driven mode and characteristics......70

Table 9-3 The configuration details of the injector used in this paper......72

Table 12-1 Summary of test condition......139

Table 14-1 Statistic summary of all the ringing cases......181

Preface

The materials in chapters 9, 11, and 12 are from separate publications. The author's order on the publications along with their status at the time of writing this dissertation is tabulated below. I was the first author for the publication in chapter 9 where I performed experimental work, part of the model development work, and wrote most of the content. For chapter 9, my co-authors at MTU sharing the responsibility of developing Simulink models and describing results. For the publications of chapters 11, 12, I was the third author. I performed all the experiments for chapter 11 and (Rate of injection, Mie, Schlieren, OH* chemiluminescence), experimental data analysis (using MATLAB), and sharing the responsibility of comparing CFD vs experimental data. My co-authors at MTU performed CFD simulation work. For chapter 12, I performed the experiments, helped in data analysis and made plots for PLIF imaging. My advisor has helped in setting up the complicated laser setups and overseeing the experiments (also from a safety point of view) when the testing is initiated.

Chapter	Author order	Publication status	Publication
9	1	Published	Society of Automotive Engineers (Technical Paper)
11	3	Published	National Combustion Meeting
12	3	Published	Proceeding of the Combustion Institute

Acknowledgments

As I start writing this acknowledgment with a feel of the anxiety about completing the dissertation, I cannot say enough how my Ph.D. days have transformed me in so many ways. I had a longing for the field of combustion since my undergraduate and to perform some quality research in this area. I attended Dr. Lee's advanced combustion class together with Le Zhao during my first semester at MTU. We were both invited to join Dr. Lee's research team for the Ph.D. program. I would like to thank Dr. Lee from the bottom of my heart for making this experience an enjoyable one. Dr. Lee leads a student by showing how it's done with all the hard work, determination and wit. There were many times when I wanted to quit, but something just kept me waiting for the next day just curious to see how things would turn up; graduate life has been no less than an eye-opening adventure.

I would like to thank Dr. Jeffrey D. Naber, Dr. Youngchul Ra, and Dr. David Wanless for spending their time and efforts on being my committee members and guiding me in my research with their friendly aura. I want to thank all my colleagues, especially, Dr. Anqi Zhang, Dr. Khanh Cung, Dr. Abdul Moiz, Dr. Le Zhao, Dr. Meng Tang. Their intelligence and diligence have always impressed me and motivated me to become a better researcher. I also want to thank my friends who worked with me in multiple projects which could not completed without your supports: Zhihao Zhao, Tejas Randadive, Kyle Yeakle, Henry Schmidt, William Atkinson. At last, I'd like to thank my family, my parents (Yuzhong Zhu and Guangli Xu), my mother-in-law (Yan Sun). In particular, I want to thank my wife, Mo Li. Your incredible support is part of my success. Thank you for your love and caring for me and our daughter Sophia. As Moiz said, you are the cutest, and I'm the luckiest.

List of abbreviations

IC	internal combustion
AHRR	apparent heat release rate
ASOI	after start of injection
ROI	rate of injection
ASMI	after start of main injection
PLIF	planar laser induced fluorescence
CFD	computational fluid dynamics
CV	combustion vessel
RANS	reynolds averaged numerical simulation
TKE	turbulent kinetic energy
PAH	Poly-aromatic hydrocarbons
IXT	intensity-axial-time
CI	compression ignition
ICCD	intensified charge-couple device
NTC	negative temperature coefficient
PCCI	premixed charge compression ignition
LES	large eddy simulation
NOx	nitric oxides

Abstract

With nearly smokeless combustion, Dimethyl Ether (DME) can be pressurized and used as a liquid fuel for compression-ignition (CI) combustion. However, due to its lower heating value and liquid density compared with diesel fuel, DME has a smaller energy content per unit volume. To obtain an equivalent energy content of diesel, approximately 1.86 times more quantity of DME is required. This can be addressed by a larger nozzle size or higher injection pressure. However, the effect of high injection pressure on DME spray combustion characteristics have not yet been well understood. In order to fill this gap, spray and combustion processes of DME were studied extensively via a series of experiments in a constant-volume and optically accessible combustion vessel. In the current study, a hydraulic electric unit injector (HEUI) with a 180 μm single-hole nozzle was driven by an oil-pressurized fuel injection (FI) system to achieve injection pressure of 1500 bar. The liquid and vapor regions of DME jet were visualized using a hybrid Schlieren/Mie scattering at non-reacting conditions. At reacting conditions, high-speed natural flame luminosity of DME combustion was used to capture the flame intensity, and planar laser-induced fluorescence (PLIF) imaging was used to characterize CH_2O evolution. Spray and combustion characteristics of DME were compared with diesel in terms of rate of injection (ROI), liquid/vapor penetration and, ignition delay. Flame lift-off length (LOL), flame structure, and formaldehyde (CH_2O) formation of DME were also studied through high-speed imaging. The RANS Converge CFD simulation was validated against the experimental and used as a powerful tool to explore the DME spray characteristics under

various conditions. Further insights into DME spray and flame structure were obtained through experimentally validated Large Eddy Simulations (LES) simulations.

1 Introduction

Fossil fuel is playing and will play a leading role in global energy consumption (more than 80%) in a long period of time, due to its high energy density, low cost and large amounts of proven reserves. In the fast-growing transportation sector, petroleum is at the top of the hierarchy (89% in 2014 U.S.) [1]. The large vehicle population is depleting petroleum reserves and producing emissions at an extremely fast pace, which forces US federal law to push the fuel consumption restriction (54 mile-per-gallon for 2025) and emission standard to a more stringent direction [2]. Researchers have raised several solutions to improve fuel economy and reduce exhaust emissions, such as low-temperature combustion (LTC), advanced injection techniques, and high-efficiency low-emission alternative fuels [3]. Lean combustion with EGR is an effective LTC strategy, which can improve efficiency and reduce nitrogen oxide(s) (NOx). It is widely known that the combustion of diesel produces a large amount of particulate matter (PM).

DME as a promising alternative fuel for diesel has been proven to have soot-free combustion, due to its high cetane number (more than 55), low auto-ignition temperature, no carbon-carbon (C-C) bond structure [4, 5]. Without the limitation of soot formation, a higher level of EGR than diesel can be achieved. DME can be produced effectively from various feedstocks, such as natural gas, biogas, and shale gas whose production has grown rapidly in recent years [6]. One viable production method is to convert methane and carbon dioxide to DME, which can capture CO_2 at the same time. As important renewable energy, biofuel has been strongly supported by US policymakers, making up 5.9% of energy consumption in the transportation sector in 2011 [7]. Biofuel's positive influence on environment improvement guarantees its interests to the government, the research community, and the industry. However, there are still some challenges in utilizing DME such as its low energy intensity compared to diesel, low lubricity which may cause corrosion [5]. These properties are limiting the maximum injection pressure of DME which is about 60 MPa in the latest DME engine applications [8]. In addition, DME generates more carbon monoxide (CO) and hydrocarbon (HC) emissions because of much higher volatility, especially when air and fuel are poorly mixed at low ignition temperature. An oxidation catalyst would be necessary to meet the ultra-low emission vehicle (ULEV) CO and HC limits [9].

Attempts of utilizing DME in a CI engine started in the 1990s to characterize its combustion behavior [10]. DME was proved to be an alternative fuel for a small non-turbocharged direct injection diesel engine [11]. It was found possible to manufacture DME from syngas on a large scale using resources like natural gas, coal, and biomass [10]. Later, DME was successfully operated on a CI engine by Kajitani et al. [12]. In the 2000s, researchers were working on applying DME to medium or heavy-duty CI. Gill et al. [13] demonstrated the feasibility of running DME in a heavy-duty CI engine with modifications in the fuel injection system. In 2011, DME with a common rail injection system was applied to medium-duty trucks by Isuzu Central Research Institute. They optimized the compression ratio and the EGR ratio was eventually able to improve exhaust emissions and fuel consumption [8].

In 2004, An et al. [14] studied the effects of injection pressure on the combustion of a heavy-duty diesel engine with common rail DME injection equipment. Various injection pressures from 20-35 MPa were studied. Results showed that higher injection pressure leads to a lower brake specific energy consumption (BSEC) as compared to diesel. In 2008, Kim et al. [15] studied the combustion and emission characteristics of DME at an injection pressure of 50 MPa in a single-cylinder common rail direct injection diesel engine. With the help of a lubrication improver (Lubrizol 539M, Lubrizol), DME showed longer actual injection duration (earlier opening and late closing) than diesel at the same electronically commanded injection duration. Comparing to diesel combustion, the DME combustion showed slightly increased indicated mean effective pressure (IMEP). However, NO_X emissions of DME combustion was higher than those observed in diesel combustion. Recently, Mitsugi et al. [16] obtained visualization of DME spray combustion under high pressure of 6.0 MPa and a high temperature of 920 K in a constant volume combustion vessel (CV). This later was used to develop a spray and combustion model using a reduced chemical kinetic model (27 species, 52 reactions). They reported that, with increased injection pressure, DME has long spray tip penetration with relatively short lift-off length. Soot luminosity from DME combustion was relatively low as compared to Diesel indicating the characteristic of smokeless DME combustion.

Due to the lower heating value and liquid density of DME, additional DME should be injected during one injection event compared to diesel, to deliver comparable energy. Hence higher injection pressure is expected to be adopted. However, the effect of the injection pressure on DME spray combustion characteristics is still not well understood. Thus, it is necessary to explore DME's ignition and combustion processes in engine-like conditions experimentally and computationally for aiding the design of advanced DME combustion in the engine (high-efficiency LTC). Considering the DME's fast vaporizing characteristic and low energy density property, in order to deliver comparable energy per injection with diesel, this study focuses on the high injection pressure (150 MPa) condition.

1.1 Motivations

There is a possibility to design an advanced system that can realize high-efficiency and low-emissions DME combustion in internal combustion engines (ICEs), because of DME's characteristics. The overall motivation of this work is to explore DME ignition and combustion processes at a high injection pressure, via investigating spray dynamics, ignition, flame propagation, and emissions both experimentally and computationally. This will be discussed regarding DME's availability and characteristics as follows,

- DME, which can be derived from renewable fuel, has been proven as a promising surrogate fuel for diesel fuel in a compression-ignition engine. DME has a high cetane number and low CO_2 footprint. Its synthesis progress can provide a possibility for CO_2 capture.
- The rapid increasing shale gas production makes inexpensive DME synthesis viable, which can be competitive with ultra-low sulfur diesel or gasoline on an energy equivalent basis.
- DME with a formula CH_3-O-CH_3 has no C-C bonds. Its mass-based oxygen content is 35% [5]. Thus, DME does not produce soot during combustion and allows a high level of EGR that can decrease NO_x formation. The low NO_x emission can fulfill the ultra-low emission vehicle (ULEV) limits [8]. Without using after-treatment, the engine can improve efficiency due to the lower

pumping losses. However, it produces more carbon monoxide (CO) and hydrocarbon (HC) emissions, implying an oxidation catalyst would be necessary to meet the ULEV limits [9].

- DME has low auto-ignition temperature and very fast vaporization. If operated with an advanced high injection pressure combustion system, it can improve thermal efficiency.
- DME is non-toxic and harmless to human health and environment, except for narcotic effects caused by long-time exposure to high concentration DME mixture [5]. It has a recognizable odor when the mole fraction is larger than 10%, and visible blue flame similar to natural gas [5]. These characteristics can be used to detect leakage and dangerous unexpected burning.
- DME can be produced from various non-petroleum feedstocks, like biomass, natural gas, and syngas. It can reduce the dependency on petroleum and reliance on foreign fuels, then improve national security.

1.2 Objectives

Many feasibility studies were done using DME as an alternative fuel on engines with a low-pressure injection system ranging between 30 and 50 MPa [10,11,12]. None conducted experimental and computational studies of DME spray combustion, under a high injection pressure (150 MPa) in a constant volume combustion vessel and an engine. Additionally, no prior attempts to perform a low-temperature combustion study of DME under engine-like conditions were available. Fundamental understandings of DME ignition and combustion at high injection pressure merits advancement to support advanced combustion strategy design using alternative fuels. This work has the following objectives:

- Conduct experimental investigations of DME spray, ignition, and combustion characteristics under engine-like conditions against diesel. Experiments will be carried out in MTU constant volume combustion vessel and on an engine test bench. A hydraulic electric unit injector will be used to inject DME at pressures ranging from 50 to 150 MPa, with both a single-hole nozzle and a multi-hole nozzle. A variety of experimental diagnostics will be used to probe the spray combustion behavior, including a hybrid Schlieren/Mie scattering setup for the liquid and vapor regions of DME jet, a high-speed natural flame luminosity setup to capture the flame intensity, and a PLIF setup to characterize CH_2O evolution in the DME flame. Comparisons of DME and diesel include the rate of injection (ROI), liquid/vapor penetration, ignition delay, flame lift-off length (LOL), flame structure, and formaldehyde (CH_2O) formation.
- Investigate the DME spray combustion characteristics at low ambient temperature conditions (~750K). Try to explore the pressure oscillation phenomenon found during the tests using the combustion instability hypothesis. Develop a ringing intensity quantification methodology to predict and evaluate the unstable combustion case and maybe its potential damage.

- Use CONVERGE software to perform computational fluid dynamics (CFD) simulations, including model validations against experimental data (both CV and engine data) and investigations of DME combustion by varying the following parameters: ambient temperature, ambient pressure, ambient density, oxygen concentration, and injection pressure. The analysis will cover ignition delay, lift-off length, flame stability, potential chemical pathway, emission formation, and flame to flame interaction. The detailed DME spray and flame structure were investigated through Large Eddy Simulations (LES) simulation.

- Build a one-dimensional (1-D) injector model in Simulink software, which can predict the accurate injection behavior and its reaction to varied fuel properties, injection pressure, ambient conditions, and injector geometries. The injector model will benefit the high-pressure DME injector design by predicting the directional change.

1.3 Thesis organization

The dissertation begins with giving a brief introduction about (conventional diesel sprays along with introducing the state-of-the-art concepts of diesel spray combustion. This is followed by differentiating this conventional diesel spray combustion concept with that of a low-temperature combustion. DME spray combustion is then introduced in terms of fuel properties, DME reaction chemistry, DME spray combustion concepts as a literature review.

Background about CFD simulations and the sub-models used in this study is discussed followed by a chapter introducing the experimental techniques used in the thesis. Data processing methodologies are discussed in the following chapter.

The next 6 chapters come from 6 publications and tentative publications, they followed a through the process as part of this investigation and hence have been laid out in that order. Here is a line-up of publications which will be explained from chapter 9 onwards.

- HEUI injector modeling and ROI experiments for high injection pressure of DME: This chapter is focusing the fuel injection system exploration with a 2D Simulink injector model. The results inspire the injection system performance reacts to the fuel properties changes (from diesel to DME) and the test condition variations.
- Experimental investigation the effect of high injection pressure on DME combustion: single-hole injector results
- Experimental and numerical study of diesel vs. DME in a constant volume combustion vessel: multi-hole results
- ignition and formaldehyde formation in DME reacting spray under various EGR Levels: CFD Results
- Mechanism of ignition and flame stabilization of high injection pressure DME sprays
- DME combustion instability investigation

2 Diesel spray combustion

DME spray combustion serves the role of a promising alternative to diesel spray combustion. Meanwhile, a great amount of work has been done in the diesel compression engine which is well understood compared to DME. In this dissertation study, diesel spray combustion is treated as a reference to DME spray combustion characteristics. This chapter is mainly focusing on the diesel, however, the measures and the techniques mentioned in this chapter can be parallelly applied on DME as well.

2.1 Compression-ignition combustion

Compression-ignition (CI) is one-out-of-two of the most important ignition types in internal combustion engines. The other one is the spark-ignition. A large number of CI engines, especially a diesel engine, are in common use. For its application in automobiles, the four-stroke cycle is widely used: intake, compression, expansion, and exhaust. Driven by high injection pressure, liquid fuel is injected through injector nozzle into the compressed air (high temperature and high pressure) at the end of the compression stroke. The breakup of liquid fuel starts right after exiting nozzle. During the process of penetrating to the deeper chamber, fuel is atomized, vaporized, and mixed with ambient air. Spontaneous ignition happens near top-dead-center (TDC). A typical CI combustion process is described in Figure 2−1.

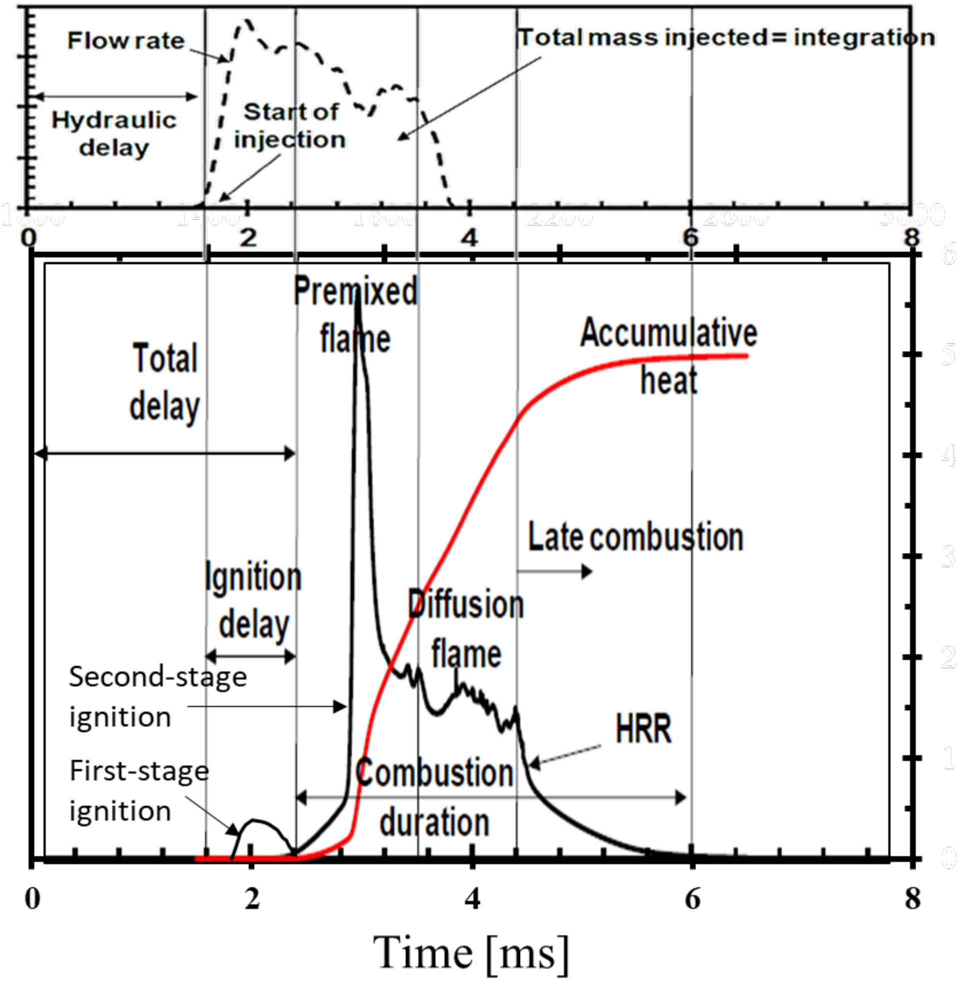

Figure 2-1 A typical CI combustion process: rate of injection vs time (top) and heat release rate (HHR) vs time (bottom)

From the command of injector energizing to the start of injection is the hydraulic delay. The injector driver receives the trigger signal and energizes the injector to inject, the high pressure from the rail takes time to travel through fuel passage inside the injector body to reach the injector needle chamber. The pressure rises to surpass a certain threshold to be able to lift the needle and to deliver pressurized fuel through the nozzle orifice. The delay is mainly caused by the compressibility of the fuel, so it is call hydraulic delay which varies slightly with energizing voltage, back pressure, injection pressure, and fuel temperature.

The liquid fuel gets injected into the hot engine chamber with a fuel rate profile like the one at the top of Figure 2-1. During compression stroke of CI engines, the piston moves towards the engine cylinder head, compresses the air and generates a hot high-density ambient. When the fuel enters this hot environment, liquid fuel undergoes vaporizing, a time delay called 'ignition delay', and auto-ignition. Auto-ignition is the reason why a compression ignition engine also called an auto-ignition engine. The ignition process may have two stages depending on the conditions: the first-stage ignition refers to the low-temperature heat release event (also called cool flame), and the second-stage ignition is the high-temperature ignition. The second-stage ignition is usually followed by a premixed combustion peak which is due to the bulk combustion of the mixed fuel vapor and oxidizer. This premixed peak is affected by the ignition delay. The longer ignition delay allows more time for the liquid fuel to vaporize and mix with the oxidizer, which leads to a higher premixed peak. Following the premixed combustion phase, it is a mixing controlled or injection-rate controlled combustion phase which can be also called a diffusion flame phase. As the injection comes to an end, the heat release quickly drops, the fuel left in the chamber continues to burn, which is called the late combustion phase.

2.2 Injection and HEUI injector

The fuel delivery and injection systems are critical to achieving high-efficiency combustion. There are several types of commercial injection system: distributor pump systems, electronic unit injector system, hydraulically actuated electronic unit injector (HEUI) system, and common rail system. The distributor pump is a mechanical unit, common in older engines but found in much of the developing world that are not subjected to the latest emission regulations. It is a successful system known for its robustness but has limited control (no real-time adjustment of pressure and injection timing). The electronic unit injector is a design that provides control over injection timing over a small window determined by the pumping lobe design.

The HEUI system substitutes the cam by a hydraulically actuated piston, providing for a wider range of injection timing adjustment and injection pressure. The present HEUI system, which provides a pressure amplification, can provide relatively very high pressures. It can also provide for two injection events, such as pilot and main or main and post. However, considering injection stability and durability, the cam-driven mode is not a good choice. The common rail injection technology now is widely used due to its precise injection control and stable high injection pressure. Conversely, the distributor pump system has limited control and hydraulic delays. The electronic unit injector also has the same issue on limited control. In comparing the common rail with the HEUI. The common rail system has a high degree of feasibility to command injection, while the HEUI system can achieve higher injection pressure. So common rail and HEUI systems are both applicable for diesel injection.

One of the significant differences between diesel and DME is fuel viscosity. The low liquid viscosity of DME causes two main challenges in the injection system: leakage and low lubricity. Low lubricity leads to wear of moving surfaces. This situation becomes worse at high injection pressures. In order to resolve these problems, the fuel contacting region must be minimized to reduce the chance of leakage and wear. An HEUI uses engine oil to drive an intensifier to increase the fuel pressure. Fuel is limited to a very small chamber right before the injector nozzle. For DME, taking the low lubricity and compressibility into consideration, the HEUI system provides a promising pathway to retain the high pressure given that the injector high-pressure components are limited to the needle area alone. High pressure does not need to be built at the injector control valve or high-pressure pump. The present study has shown successful operation at pressures above 200 MPa, higher than the 30-50 MPa reported in the literature with DME [10-12].

2.3 Non-reacting sprays

A great amount of research has been done to study spray combustion (most on diesel), which include fundamental spray characteristics studies and experimental works on the engine [17, 18] and the combustion chamber [19-24]. This sub-session is to review the concepts and tools which are used to characterize spray combustion: such as liquid/vapor penetration, ignition, diffusive flame, emissions.

2.3.1 Atomization

There are four breakup regimes: (1) Rayleigh breakup, (2) first wind-induced regime, (3) second wind-induced regime, and (4) atomization [25]. Breakup starts immediately after the fuel exiting nozzle. A typical diesel spray belongs to the atomization regime, at which nozzle diameter is much larger than drop diameter and its atomization is involved with many physical fluid mechanic processes. Atomization is the process of liquid fuel transforming into very small droplets. It can be further divided into four sub-processes including a primary break-up, secondary break-up, coalescence of droplets, and evaporation.

Figure 2−2 shows a schematic of the detailed processes of atomization. During the primary break-up, liquid fuel core exiting near nozzle orifice is segregated into a relatively large structure called ligaments. This is caused by (1) the aerodynamics instabilities between liquid and surrounding gas; (2) turbulence as high velocity flowing through a small orifice with different levels of radial velocities; and (3) cavitation within nozzle orifice [26].

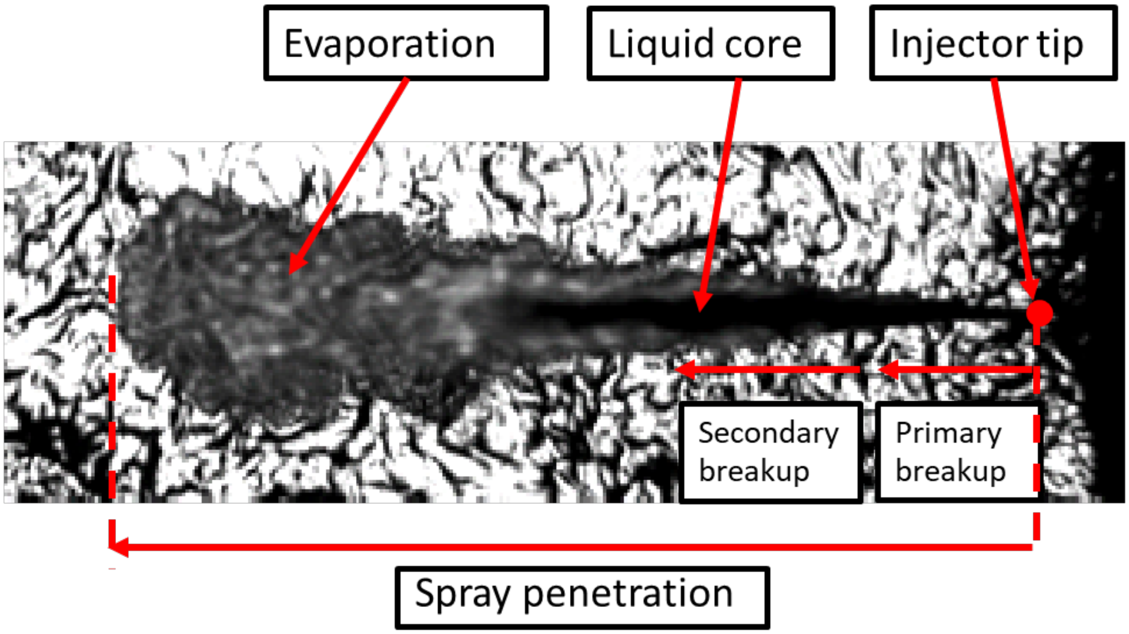

Figure 2-2 Schematic of diesel spray structure (A schlieren image at the vaporizing condition)

2.3.2 Global spray parameters: penetrations (liquid, vapor), spray angle

Global parameters of fuel spray are the parameters used to describe the spray ambient gas interactions on a macroscopic scale. These parameters in this study are liquid/vapor penetration, spray angle, etc. An example of spray penetration and spray angle is shown in Figure 2−3. As the fuel spray penetrates into the ambient environment, the air is entrained to spray core and mixed with fuel droplet, helping fuel droplet to vaporize [27]. When more fuel droplets evaporate to vapor, the penetration rate slows down.

The spray penetration is the longest distance along the spray axis that fuel travels away from the injector tip. It can be either vapor penetration or liquid penetration, depending on the ambient condition. When the ambient temperature is high, liquid fuel evaporates into vapor, but still penetrates into deeper ambient. However, liquid fuel keeps a stable penetration length.

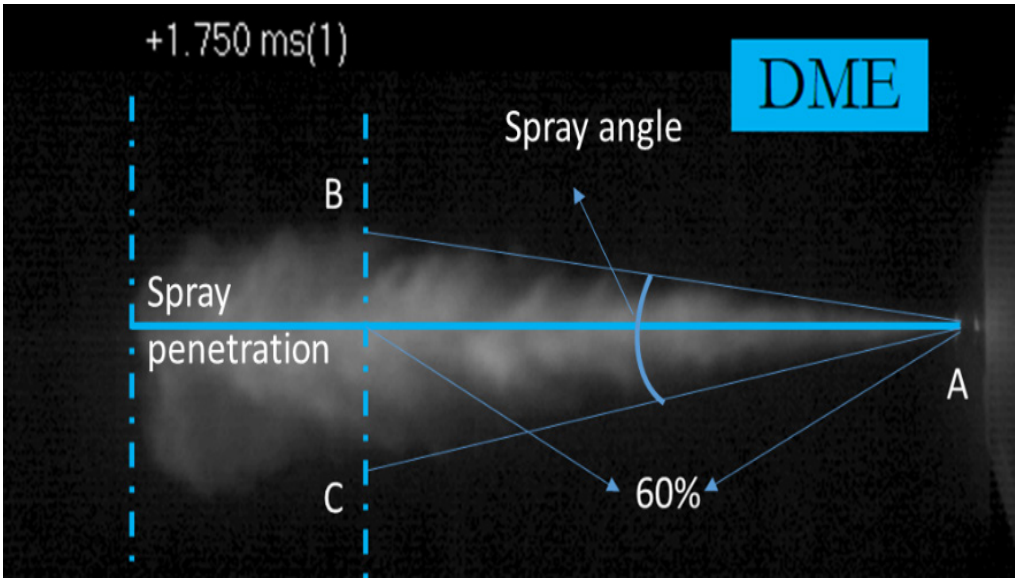

Figure 2-3 Spray penetration and spray angle from DME spray using Mie scattering image

In an IC engine or combustion vessel, spray penetration has the chance to hit the piston head or wall, called wall impingement. Spray penetration is influenced by many factors, such as injection pressure, ambient temperature, and ambient density [28]. Higher injection pressure and low ambient density tend to increase spray penetration. High ambient temperature can decrease the liquid penetration but has no effect on vapor penetration due to momentum conservation. Spray tip penetration has an empirical correlation with ambient temperature and ambient density [29]. Another important parameter of spray is the spray angle which is measured from the experimental images. There are several methods to determine the spray angle. One of them is to select three points on the spray to form a triangle ABC, as shown in Figure 2−3 [30]. Place A is injector tip and places B and C are on the boundary of the spray at a 60% penetration location. Spray angle reaches constant value when the spray becomes stable. It also has a dependence on ambient density. Knowing spray penetration and spray angle, the total spray volume can be estimated [27].

These global spray parameters are very important to study flame initiation and are related to spray combustion characteristics, such as ignition delay and flame lift-off length. Longer penetration and higher spray angle are usually desirable for utilizing mixing that leads to enhancement of combustion since the larger spray area is achieved [27].

2.3.3 Local spray parameters: air mixing, droplet Size, curvature, etc.

A very important local spray parameter is the droplet size. During the process of atomization, droplet size keeps decreasing. Droplet size can be a function of many factors such as time, injection condition, ambient condition. Sauter mean diameter (SMD) is commonly used to describe an average of particle size. The commonly used equation for SMD is given as [31]:

$$D_{SM} = \left(\int D_d^3\, dn\right) / \left(\int D_d^2\, dn\right) \tag{2.1}$$

With “dn” as the number of drops. SMD is an average of all measuring droplets at a given time [32] and the ratio of volume/surface area of droplets. Fuel droplets are injected into the ambient environment, along with air entrainments and heat transfer to ambient air [27]. Heywood has suggested that a ratio of 4 of injector nozzle length/diameter can generate the smallest droplets at low or intermediate injection pressure [31]. High injection pressure will lead to smaller droplet sizes. Other than injection pressure, factors like ambient density and fuel properties also have influences on the droplet size [33].

2.4 Reacting sprays

Figure 2−4 shows the famous conceptual model (Dec model) for diesel reacting spray. This model was developed based on the experimental work in a quasi-steady state [34]. The liquid is injected through the nozzle orifice with a high injection pressure and traveling downstream as vaporization and air mixing happening at the same time. The near nozzle region is called the rich vapor-fuel/air mixture zone where the fuel starts to slowly oxidize with low-temperature reaction chemistry. As the air mixture moves further downstream, it reaches a higher temperature and leaner equivalence ratio. The auto-ignition happens at one or more locations and turns the mixture into an earlier flame kernel. The auto-ignition introduces a sudden volume and temperature raise and initializes the oxidization chain reactions with high-temperature chemistry. A premixed flame is established nearby the ignition location, and soot starts to form. Further downstream, more soot is formed as the flame temperature increase up to ~1600K and oxygen gets used up. It leads to a high soot concentration zone. Therefore, liquid fuel, vaporized fuel, fuel-rich premixed flame, soot formation zone are located along the center of the jet spray in the direction of away from the spray nozzle. The reacting spray is surrounded by a layer of diffusion flame at where the soot experiences the oxidation process and produces thermal NO.

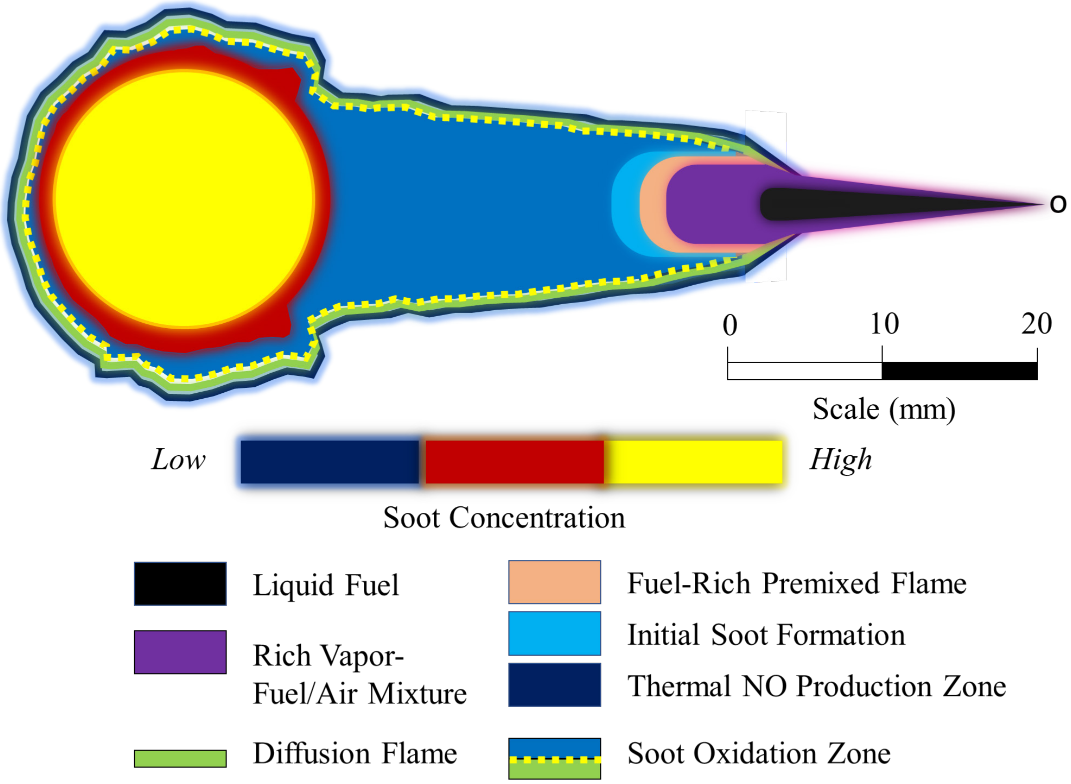

Figure 2-4 Quasi-steady diesel spray combustion visualization. Figure reproduced based on the concept in Ref. [Dec 1997,34]

2.4.1 Ignition delay

Ignition delay in spray combustion experiments is commonly defined as the time between the start of injection (SOI) and ignition. There are several methods to measure ignition delay in practical, using pressure/heat-release-rate raise of auto-ignition or the rising edge of photodiode signal of flame luminosity. The method adopted in this study is using 0.0028 MPa as a threshold on the pressure raise to find the onset of ignition. Ignition delay can be affected by ambient conditions, such as ambient temperature and oxygen levels.

2.4.2 Lift-off length (LOL)

As the ignition happens, a reaction region starts to form. After the initial transient state, the flame becomes sustainable at a relative steady location. The distance between the injector nozzle tip and the steady flame location is defined as LOL. Due to the turbulence flow, the LOL needs to obtain with a set of time-averaging images. In experiments, the camera starts recording after auto-ignition and stops before the end of the injection. LOL has been known as a marker of the initial combustion zone in diesel spray combustion.

Higgins and Siebers [35] measured LOL in their experiments using an intensified CCD camera with a 310 nm band-pass filter (10 nm FWHM) to acquire the specific wavelength light emitted from a burning fuel jet. They mentioned that as much as 20% of air reacts with fuel before LOL [35]. The 310 nm wavelength light contains chemiluminescence from excited-state OH (OH*) and the soot luminosity broadband light emission. However, OH* is short-lived and results from chemical reactions in near-stoichiometric, high-heat-release regions, which means soot has not formed at the LOL location [35]. OH* chemiluminescence is a good indicator of LOL, and the selection of 310 nm optical filter is also confirmed by other papers [36-38]. An example of OH* chemiluminescence is shown in Figure 2-5 with lift-off length indicated in the upstream of the spray.

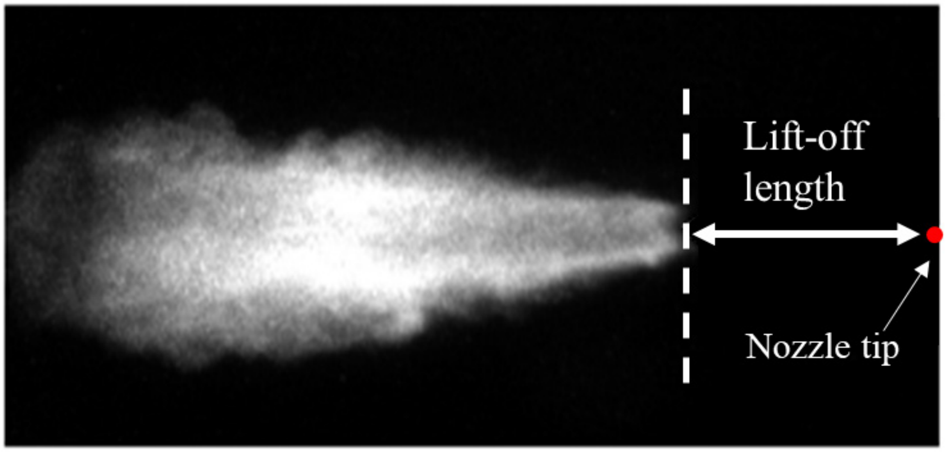

Figure 2-5 Flame lift-off length (LOL) from OH* chemiluminescence image for DME reacting spray

3 DME spray combustion

3.1 DME properties

DME as a promising alternative fuel for diesel has been proven to have soot-free combustion, due to its high cetane number (more than 55), low auto-ignition temperature, no carbon-carbon (C-C) bond structure. DME is the simplest ether and has a low C/H ratio (0.337). It is in the gaseous phase under atmospheric conditions. DME is non-toxic and harmless to human health and environment, except for narcotic effects caused by long-time exposure to high concentration DME mixture [5]. It has a recognizable odor when the mole fraction is larger than 10%, and visible blue flame similar to natural gas [5]. These characteristics can be used to detect leakage and dangerous unexpected burning.

In addition, DME can be produced effectively from various non-petroleum feedstocks, like biomass, natural gas, shale gas, and syngas. Note that shale gas' production has grown rapidly in recent years [6]. DME can be produced inexpensively from abundant shale gas using a number of proven processes, i.e. Topsoe, ENN, Lurgi, etc. [6]. DME and other alcohols (i.e. methanol, ethanol) derived through biochemical processes from biomass is considered as the potential pathway of carbon-neutral fuels [39]. The properties of DME are shown in Table 3-1 along with diesel for comparison.

DME has several advantages compared with diesel including no carbon-carbon (C-C) bond structure provides the smokeless combustion; its quick evaporation and low auto-ignition temperature lead to fast ignition; its high cetane number guarantees the combustion quality and fuel ignitability in CI engine.

However, there are still some challenges in the application of DME in the engine. Its high compressibility requires more compression work from the high-pressure injection pump [40]. The low liquid viscosity (0.12-0.15 $kg^1m^{-1}s^{-1}$) can cause potential damage and wear to the moving and rotating parts including fuel pump, injector plunger, and needle during an injection event. Therefore, additives such as Lubrizol are often used to improve the overall viscosity and lubricity of DME fuel [5]. DME has a lower density and heating value when compared with diesel.

Table 3-1 Properties of diesel and DME [5] [40] [41]

Properties	Diesel	DME
Chemical formula	-	CH_3OCH_3
C/H ratio	0.516	0.337
Molecular weight (g/mol)	170	46.07
Critical temperature (K)	708	400
Critical pressure (Mpa)	3	5.37
Vapor pressure at 293 K (kPa)	<<10	530
Boiling temperature at 1 atm (K)	450-643	248.1
Liquid density at 293 K (kg/m3)	831	667
Modulus of elasticity (N/m2)	1.49E+09	6.37E+08
Liquid viscosity at 298 K (kg/ms)	2–4	0.12–0.15

Surface tension at 298 K (N/m)	0.027	0.012
Lower heating value (MJ/kg)	42.5	28.43
Cetane number	40-50	55-60
Auto-ignition temperature(K)	523	508
Stoichiometric A/F mass ratio	14.6	9
Enthalpy of vaporization (kJ/kg)	300	467.13

The drawback of the DME's low liquid density and heating value of DME can be compensated by increasing the injected fuel mass to reach a similar level of energy content comparable to diesel fuel. The DME engine can meet the US 2010 NOx regulation by increase the EGR level without the help of SCR. The U.S. EPA laboratories have reported that DME fueled engine can achieve high BSFC while generate low emission with a design of relatively high injection pressures (120-150 MPa) and relatively small injector nozzle size (~ 0.16 mm in diameter) [39]. It has also been found that the combination of HCCI engine and DME fuel yields low NOx emission but a relative higher CO and HC emissions due to the high volatility and reactivity [42].

3.2 DME spray combustion

When compared with diesel, it is found that DME has very different spray behavior due to its fuel properties (low liquid viscosity and high compressibility). Park et al. pointed out that, at an injection pressure of 70 MPa, DME has shorter spray penetration compared to diesel, which is believed to be due to DME's fast evaporation. Other studies also investigated the same phenomenon of DME's shorter spray penetration at injection pressure 60 MPa [43,44], by comparing the liquid length at the time of ignition fuel to fuel. They believe that DME's fast evaporation feature leads to a slightly larger spray angle, and its lower density results in the deceleration of the spray momentum.

Kim et al. studied the characteristic of the nozzle flow by computation of the injection rate profile to obtain model input parameters such as discharge coefficient, effective jet velocity, and effective nozzle diameter [45]. The discharge coefficient of DME was shown with a steeper slope compared to diesel. This was due to DME's low viscosity. Because of having a low boiling temperature, DME evaporates rapidly after being injected. This leads to potentially an aggressive fuel-air mixing process that shortens the ignition process, or ignition delay. The ignition delay of DME is experimentally measured and shown to be shorter than typical diesel over a wide range of temperatures 600-950K. The combustion of diesel releases higher energy compared to DME due to its higher LHV. The study of Kim et al. shows the peak pressure of diesel is higher than that of DME for the same injection mass of each fuel [46]. Kim also compared the heat release between diesel and DME and found that about 48% more mass than diesel is needed for DME to have the equivalent heat as diesel produces [45]. They also indicated that lower incomplete combustion products (i.e., HC, CO) are observed in the combustion of DME compared to diesel in a single-cylinder compression ignition engine. NOx level was also shown to be higher in DME combustion than in diesel due to faster ignition characteristics in DME. The heat release rate of DME was lower than diesel due to shorter ignition delay and lower heating value.

To overcome low viscosity and poor lubricity properties of DME, it is often blended with other additives such as Lubrizol or other fuels such as diesel [5, 47]. Ying showed improvement in fuel and energy consumption when running at high engine load using a mixture of diesel/DME with 10-30% by mass of DME [47]. They found that NOx emission was reduced by running diesel/DME blend fuel indicating the potential for clean combustion of a diesel engine. CO_2 level from diesel/DME blend fuel was also less than those that run with neat diesel.

3.3 DME chemistry

Curran [48,49,50] developed the DME mechanism which was in good agreement with experimental results over a wide range of temperature and pressure (650-1300 K and 13-40 bar) [51]. It showed that the unimolecular decomposition into methoxy and methyl radicals is very important in the initial reaction of DME, in which it plays an important role in the pyrolysis and oxidation of DME. DME oxidation mechanism has been reported with the following major oxidation steps: DME is oxidized into methoxymethyl radical which reacts with O_2 to form a methyoxymethylperoxy radical [52]. Two formaldehyde radicals are the major species to produce carbon monoxide, the oxidation of which is the final step to form CO_2. Auto-ignition is due to the accumulation of $CH_3OCH_2OO^*$, CH_2OCH_2OOH, and $O^*OCH_2OCH_2OOH$. Figure 2-6 shows the overall reaction scheme for DME oxidization [50].

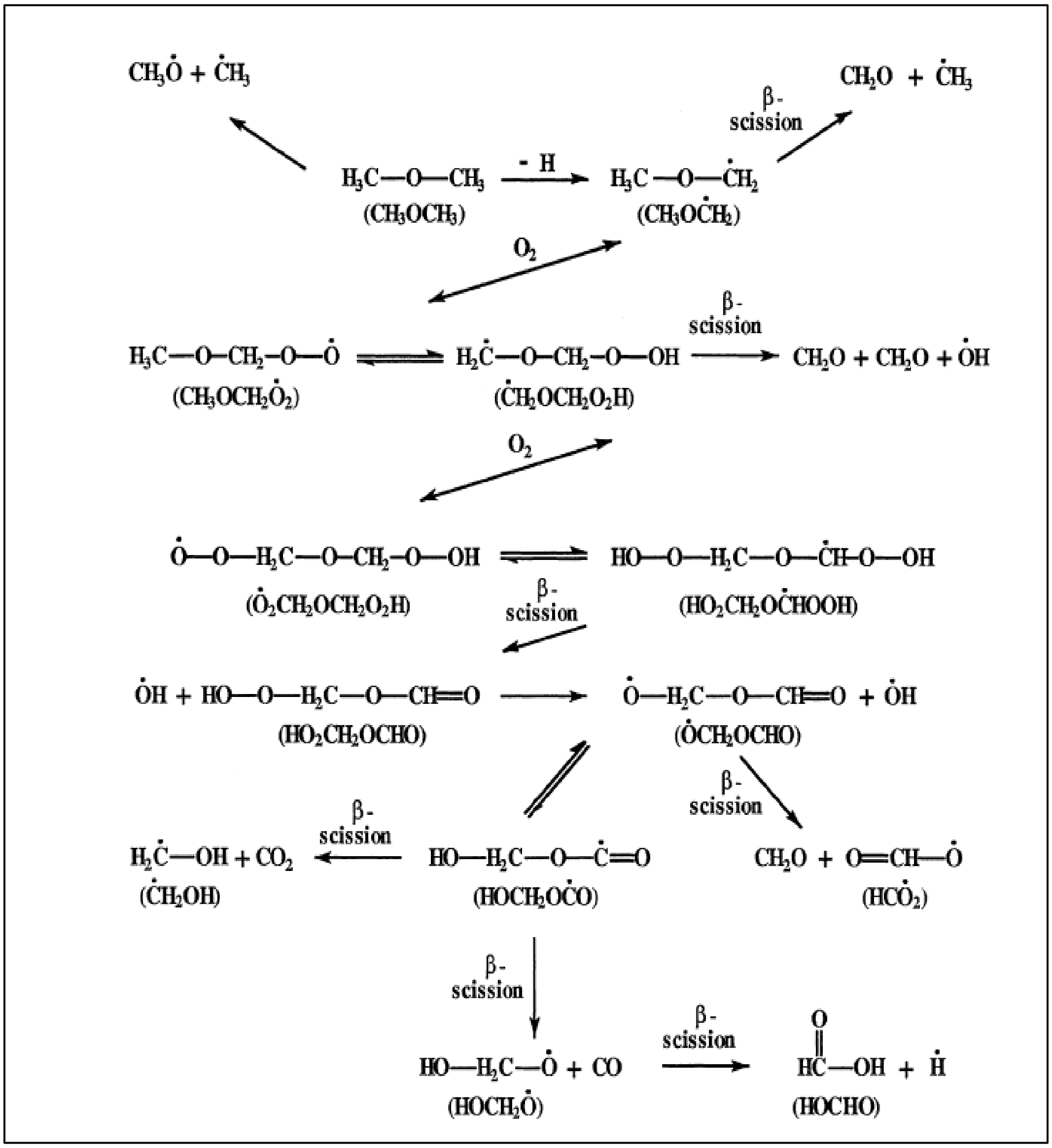

Figure 2-6. Overall reaction scheme for dimethyl ether oxidation [50].

DME has a higher reactivity at low temperatures, which improves ignition properties. DME combustion also shows a two-stage ignition and negative temperature coefficient (NTC), indicating decreased ignition delay for high initial temperature while retarded ignition delay with low-temperature region [53, 54]. The detailed mechanism was tested in shock tube experiments at the stoichiometric conditions and was found that the mechanism predicted well the overall ignition delay and the trend of the cool-flame stage [51]. Good agreement was also found in the experiment and modeling of Jet Stirred Reactor (JSR) [55]. There was still remaining work on the prediction of laminar flame speed, which is an important property of a combustion process, from using Curran's mechanism [56]. However, many studies have indicated that the mechanism of DME developed by Curran is sufficient and accurate enough in the numerical simulations of the fuel [48-50]. Research has been performed to build DME oxidation mechanisms over the lean and rich fuel regime at the different pressure and temperature as listed in Table 2-2. In the present work, we will consolidate all published DME combustion mechanisms based on the experimental results performed herein and select the best mechanisms for our CFD models.

Table 2-2 Past DME chemistry studies

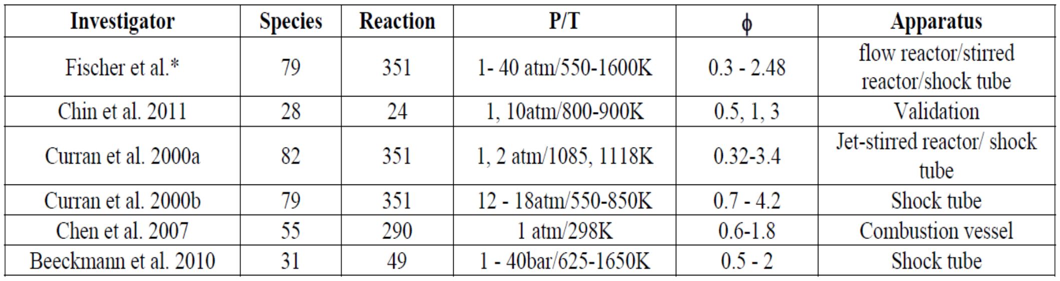

Investigator	Species	Reaction	P/T	ϕ	Apparatus
Fischer et al.*	79	351	1- 40 atm/550-1600K	0.3 - 2.48	flow reactor/stirred reactor/shock tube
Chin et al. 2011	28	24	1, 10atm/800-900K	0.5, 1, 3	Validation
Curran et al. 2000a	82	351	1, 2 atm/1085, 1118K	0.32-3.4	Jet-stirred reactor/ shock tube
Curran et al. 2000b	79	351	12 - 18atm/550-850K	0.7 - 4.2	Shock tube
Chen et al. 2007	55	290	1 atm/298K	0.6-1.8	Combustion vessel
Beeckmann et al. 2010	31	49	1 - 40bar/625-1650K	0.5 - 2	Shock tube

4 CFD simulation overview

J.D. Anderson, Jr said: “Computational fluid dynamics (CFD) is, in part, the art of replacing the governing partial differential equations of fluid flow with numbers, and advancing these numbers in space and/or time to obtain a final numerical description of the complete flow field of interest [57].” The partial differential equations are commonly mass, energy, species, and momentum equations. CFD follows the basic physical rules of mass conservation, energy conservation, and Newton’s second law [57]. It uses a variety of discrete mathematical methods to solve many sorts of practical problems, focusing on numerical experiments, computer simulations, and analysis of various fluid mechanics issues [58]. CFD utilizes computer technologies to obtain detailed results of fluid flow, heat and mass transfer, and combustion.

There are two kinds of CFD codes or software: one is open-source code, such as KIVA and OpenFOAM; another is commercial software, such as CONVERGE, STAR-CD, and AVL FIRE. The currently used software for this study is CONVERGE CFD [59].

As part of this study, the DME spray combustion process is also numerically investigated to gain detailed insights. This chapter shows the overview of CFD models, including spray modeling, turbulence modeling, combustion modeling, chemical mechanism selection, typical simulation setups and best practices which are utilized in running split injection CFD simulations. The major models adopted in the current study are described as follows. Since the CFD simulation is not the main focus of the study, only a brief overview is provided here.

4.1 Spray modeling

Spray model is critical to spray combustion simulations since its setting can influence the spray characteristics output. Spray model is active from the injection to vaporization. ROI profile determines the rate of the drop parcels into a computational domain at the injector tip. A very important sub-model of the spray model is the break-up model. The most widely used break-up model in conventional spray calculation is the Kelvin-Helmholtz-Rayleigh Taylor (KH-RT) break-up length model [59]. Constants in the KH-RT model are tunable to improve the penetration results. The model used in this simulation is KH-RT with no break-up length.

4.2 Combustion modeling

The combustion model plays a vital role in ICE simulations. There are several combustion models, such as SAGE model, Representative Interaction Flamelet (RIF) model, SHELL+(Characteristic Time Combustion) CTC model, and Extended Coherent Flamelet Model 3 Zone (ECFM3Z) model.

SAGE describes the overall chemical reactions through calculation elementary reaction rates, is a detailed chemistry solver. SAGE model allows using detailed chemical kinetics in combustion simulations with a set of CHEMKIN-formatted input files [59]. SAGE calculates the reaction rate of each elementary reaction, while the CFD code solves the transport equations [59]. Along with Adaptive Mesh Refinement (AMR), SAGE has the ability to model different regimes (ignition, premixed, mixing-controlled) [59]. The SAGE solver is used in this study.

RIF model can also deal with detailed chemistry but using a different method. Its chemistry solving process is based on the transformation from mixture fraction space to real 3D space.

SHELL and CTC are individual combustion models. SHELL model solves for the computational cells that in the ignition stage based on eight reactions [60], and CTC solves for those in combustion processes involving seven species (fuel (C_nH_{2m}), O_2, N_2, CO_2, H_2O, CO, and H_2) [61, 62]. These two models can work together to describe the whole spray combustion processes. The 3 Zone ECFM3Z model originates from the Extended Coherent Flame Model (ECFM) [62]. Unlike the ECFM model's application in a premixed environment, ECFM3Z is modified to be used in perfectly or partially mixed mixture which is for diesel-like applications.

4.3 Turbulence modeling

Turbulence can significantly increase the mixing rate of species, energy, and momentum [59]. It is very important in combustion simulation. The basis of solving turbulence problems is the Navier-Stokes (N-S) equation. Due to the scale of turbulence, turbulent numerical simulation methods fall into three categories: direct numerical simulation (DNS), Reynolds averaging approach (RANS) and Large Eddy Simulation (LES).

RANS simulation is the time-averaged simulation of the motion of the fluid flow. RANS turbulence models available in CONVERGE are standard k-ε model and RNG (Renormalization Group) k-ε model. The standard k-ε model assumes that the flow is fully turbulent, and the viscosity of the molecule can be ignored [63]. During the process of averaging the constitutive equations, it is losing fidelity. If the smallest scales of turbulence can be systematically eliminated, the remaining scales of turbulence become more distinguishable. This is the basic theory of RNG k-ε, which is currently used in this work [64].

4.4 Chemical kinetic mechanism

Chemical kinetics is also known as reaction kinetics or reaction mechanism. It is a step by step sequence of elementary reactions, which describes the overall chemical change with the rates of chemical reactions. This information about element reactions and reaction rates are precisely measured and calculated through well controlled experiments. There are two types of chemistry mechanisms used in CFD simulations, one is called full or detailed chemistry mechanism, and the other is reduced chemistry mechanism. The detailed chemical kinetics is rarely used in CFD applications due to its high computational costs. For example, detailed chemical mechanism of a hydrocarbon (such as n-heptane) oxidation reactions may contains more than hundreds of species and thousands of reaction steps. To track all the element reactions, it requires extremely high CPU and memory configurations and long computational time. These limitations prohibit the implementation of full detailed vs reduced chemistry mechanism

As mentioned in the combustion modeling section above, some combustion models such as “SAGE” model requires detailed chemical kinetics.

4.5 Best practices and typical simulation setup

The best practices and typical simulation setup are shown in Table 4-1.

Table 4-1 Typical simulation setup used in this work

	RANS Modeling	LES Modeling
Modeling Tool	CONVERGE v2.1 & 2.3	CONVERGE 2.3
Dimensionality, and type of grid	3D, Adaptive Mesh Resolution	3D, Adaptive Mesh Resolution
Smallest and largest characteristic grid size	Base grid size: 2 mm Finest grid size: 125 µm Gradient base AMR on velocity and temperature fields Fixed embedding in the near nozzle region: 125 µm	Base grid size: 1 mm Finest grid size: 62.5 µm Gradient based AMR on velocity and temperature fields Fixed embedding in the near nozzle region: 62.5 µm
Spray Models	Injection: Blob Atomization & Breakup: KH-RT Collision: No Time Counter Drag-law: Dynamic model Evapporation: Frossling correlation	Injection: Blob Atomization & Breakup: KH-RT Collision: No Time Counter Drag-law: Dynamic model Evaporation: Frossling correlation
Combustion model	Detailed chemistry combustion model with 45 species and 249 reactions	Detailed chemistry combustion model with 45 species and 249 reactions

5 Two unconventional combustion concepts

5.1 Low temperature combustions

As the diesel engine emission standards becoming stricter, the aftertreatment system for NOx and soot particulate matter were introduced and frequently updated to meet the emission standards. The aftertreatment system not only adds extra cost in terms of hardware and maintenance, but also increases the complexity of the system. The common exhaust aftertreatment contains diesel oxidation catalysts (DOC), diesel particulate filters (DPF) and selective catalytic reduction (SCR) catalysts, which usually requires a certain range for the exhaust gas temperature to ensure optimal performance and durability. Some advanced engine combustion strategies could be employed to alleviate the work from the aftertreatment system, including low temperature combustion (LTC), homogeneous charge compression ignition (HCCI), and premixed charge compression ignition (PCCI). The goal of the LTC is to lower combustion temperature to reduce the formation of NOx and/or PM in the chemistry process, but often results in more CO and HC emission instead due to incomplete combustion. Figure 5-1 shows the NOx-soot tradeoff on the equivalence ratio-temperature space and highlights the differences between conventional diesel combustion and the three advanced combustion strategies (PCCI, HCCI, and LTC). Conventional diesel combustion occupies a large region on the map, including operating points located in high soot and NOx formation regions. LTC occupies a similar but smaller region, and also moves toward the lower-left direction (fuel-lean and lower temperature direction). Therefore, LTC can avoid most of the NOx zone and a large portion of the soot zone.

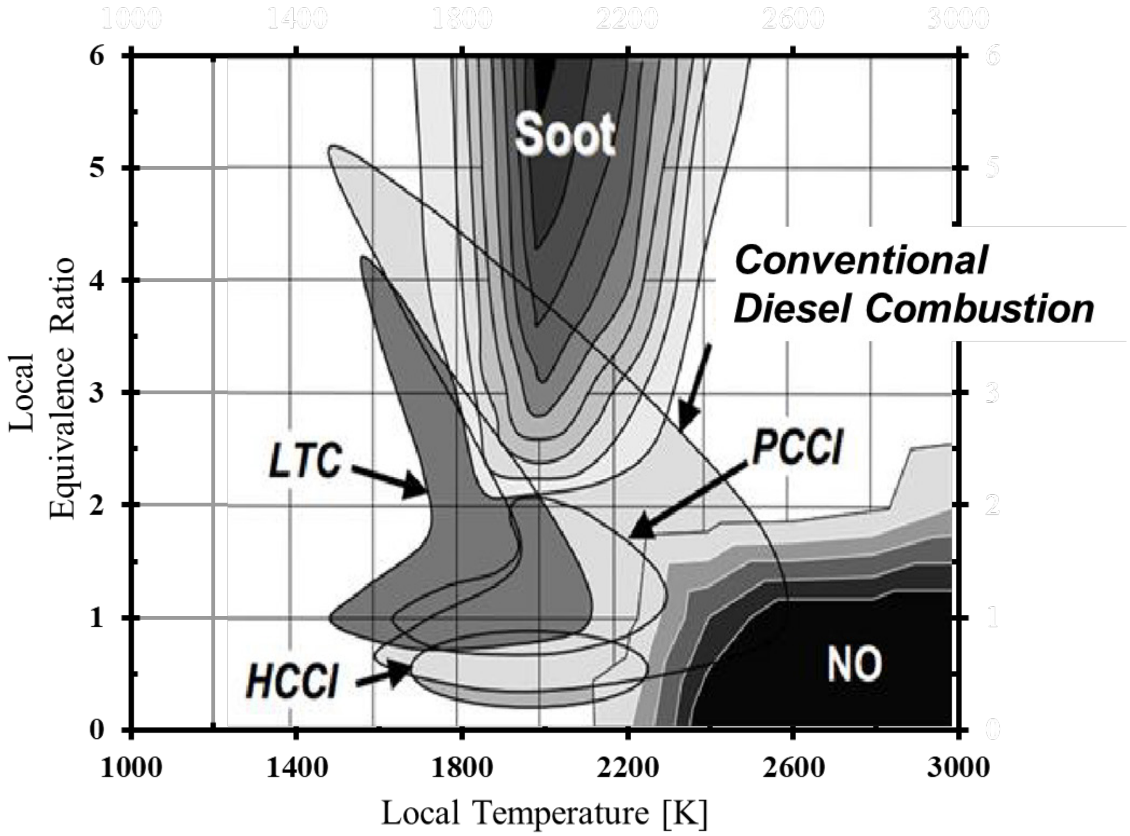

Figure 5-1 Temperature and equivalence ratio plot for advanced combustion strategies. [Neely et al. 2005, 65].

Because the LTC so different from the conventional diesel combustion, a new conceptual model from Musculus et al. 2013 in Figure 5-2 illustrates the differences. For the first few moments after the start of injection, the fuel sprays show very similar patterns under both conventional and LTC conditions. LTC shows a vast different structure from conventional combustion. First, due to the low ambient temperature and pressure, LTC shows much longer liquid length (~10mm longer), thicker diffusion flame, and significant upstream first-stage combustion products remaining which becomes a source of UHC and CO emissions. Comparing to conventional, the first-stage combustion of LTC starts late and occupies the larger flame area, showing a wave-type pattern on air-fuel mixing interface.

The second stage of combustion kicks off later (may be after the impingement on the wall) at the location of the head vortex at where soot forms.

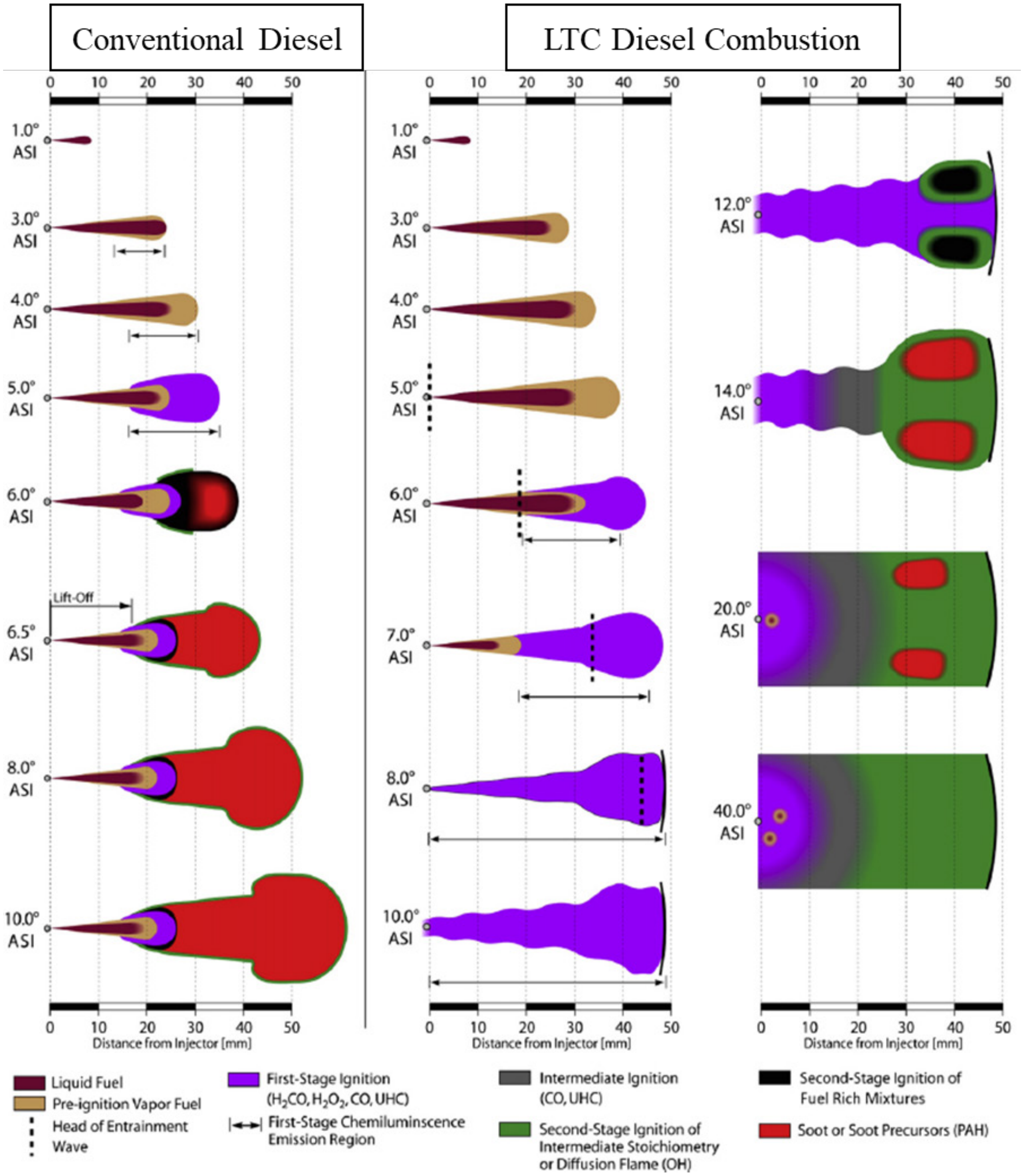

Figure 5-2 Conceptual model for conventional diesel combustion (left) and Low-temperature combustion (right) [Musculus et al. 2013, 66]

So far, the fundamental background knowledge from both experimental and numerical sides are briefly covered. The writing will move to discuss the experimental techniques.

5.2 Combustion instability

Combustion instabilities are physical phenomena exist in a reacting flow, such as in a flame. In the reacting flow, some perturbations are large enough to change the characteristics of the flow in a particular way [67]. Usually, the combustion instability is not desirable to the stable operation of the system. The hazard caused by thermoacoustic instabilities is a major concern in the application of gas turbine and rocket engines.

A well-known type of instability is the thermoacoustic combustion instabilities. In thermoacoustic combustion instability, the perturbation grows and interacts with the flow in an acoustic way. It usually comes with pressure oscillations that have some well-defined frequencies patterns. These pressure oscillations also have high enough amplitudes to trigger serious hazards to the combustor [68]. For example, in rocket engines and gas turbine engines, the instability can cause massive damage to the components and even surroundings during the test. To understand why and how does thermoacoustic instabilities happen, there are several physical processes to check. First see what the feedback of the acoustics in heat-release fluctuations is. Second see the coupling of heat release fluctuations and acoustics in space and time. Third is the check whether the strength of the coupling is stronger than the acoustic losses or not.

There is a sample example showing the thermoacoustic instabilities, which is a horizontal tube (called Rijke tube) with both ends opened. A disc of wire gauze is placed at a distance of one-quarter of the tube length from one end. After heating the wire gauze to glow red hot, the acoustic waves travel up and down the tube producing a sound called Rijke tube sings which is actually a particular pattern of standing waves.

To determine under what conditions the instability will happen, Rayleigh, J. W. S. developed the Rayleigh's criterion [69]: thermoacoustic combustion instabilities will occur if the volume integral of the correlation of pressure and heat-release fluctuations over the whole tube is larger than zero. In a more general form, instabilities will happen when heat release fluctuations are coupled with acoustics pressure fluctuations in space-time, and the strength of coupling is larger than the acoustic losses. By assuming small fluctuations and an inviscid flow, here is the inequality for extended Rayleigh's criterion:

$$\int_0^T \int_V \ \mathrm{p}'\mathrm{q}'\mathrm{dVdt} > \int_0^T \int_S \ \mathrm{p}'\mathbf{u}'.\mathbf{n}\ \mathrm{dSdt} \tag{5-1}$$

Where p' represents pressure fluctuations, q' heat release fluctuations, $\mathbf{u}'$ velocity fluctuations, T is a long enough time interval, V represents volume, S surface, and $\mathbf{n}$ is a normal to the surface boundaries. The left-hand side is the coupling between heat-release fluctuations and acoustic pressure fluctuations, and the right-hand side denotes the loss of acoustic energy at the tube boundaries.

In the applications in internal combustion engines, higher cylinder pressure is required to achieve higher thermal efficiency. Meanwhile, the heat release at high cylinder pressure may trigger the acoustics waves due to the volumetric increase in a short period of time.

The acoustics waves will have the possibilities to coincide with the heat release at some particular regions when a standing wave is formed because of the chamber geometry.

Alvin et.al has performed research on the light-duty single-cylinder diesel engine which allows the optical access to the combustion chamber during engine running. He investigated flame development transience in two combustion regimes: first is called positive ignition dwell regime (ignition starts after the end of injection) realized by short injection duration and long ignition delay), and second is the negative ignition dwell regime (ignition is prior to the end of injection) caused by long injection duration. He found the combustion in the positive regime is dominated by the premixed combustion phase whose efficiency is limited by a dramatically increased chamber pressure. When this problem becomes severe, there will be undesirable pressure ringing which is called diesel knock by the author. Through the high-speed natural hot soot luminosity imaging, the diesel flame was found to oscillate against the normal swirl direction with a certain frequency which matches the pressure ringing frequency. Further experiments showed piolet injection can reduce or eliminate the pressure ringing and flame oscillation.

Zhi et al have studied similar pressure oscillations and chemical kinetics coupling during the gasoline engine knock combustion process. The study was been done with KIVA CFD code using the G-equation combustion model with reduced chemical kinetics and an enhanced wall heat transfer model. The time step (1e-6 s or1e-7 s) was carefully selected with the criteria that sonic wave should take at least one timestep to travel across a computational cell, in order to resolve the local pressure oscillation in the numerical model. FFT analysis was also applied to several locations near to the top in the engine cylinder.

The results show that the pressure is high unevenly distributed during the knocking process. The pressure oscillations and chemical reactions occur at the same time and coupled with each other. The pressure oscillations are in phase with the local HRR through the verification of the "Rayleigh criterion". The Rayleigh index usually becomes positive near the wall and leads to high-frequency pressure oscillation. Finally, compared to non-knocking case, engine knocking significantly enhances wall heat transfer.

6 Experimental techniques

6.1 Fuel delivery system overview

Three phases of experimental work are performed: rate of injection (ROI) measurements, spray combustion tests in combustion vessel (CV), and engine tests. The ROI tests and CV tests share the same dual fuel (diesel or DME) delivery systems, as shown in Figure 6-1. The only difference between them is where the injector connects (combustion vessel or ROI measurement). The fuel delivery system can be divided into two sub-systems: oil and fuel supply. The oil system consists of a 10-gallon oil tank, an oil pump driven by variable speed motor and an injection pressure control valve. The fuel supply side has the compatibility for both diesel and DME. Low-pressure Nitrogen (N_2) is used to maintain the fuel line pressure at a constant value (8 bar for DME, 2 bar for diesel). The low pressure ensures that fuel enters the injector and liquefies DME at normal temperatures. An in-house software, which varies injection pressure and injection duration, was designed to control the fuel delivery system. The software monitors real-time injection pressure, oil rail pressure, and current pulses to injector coils. Data are recorded through a data acquisition system (DAQ) at a rate of 200 kHz.

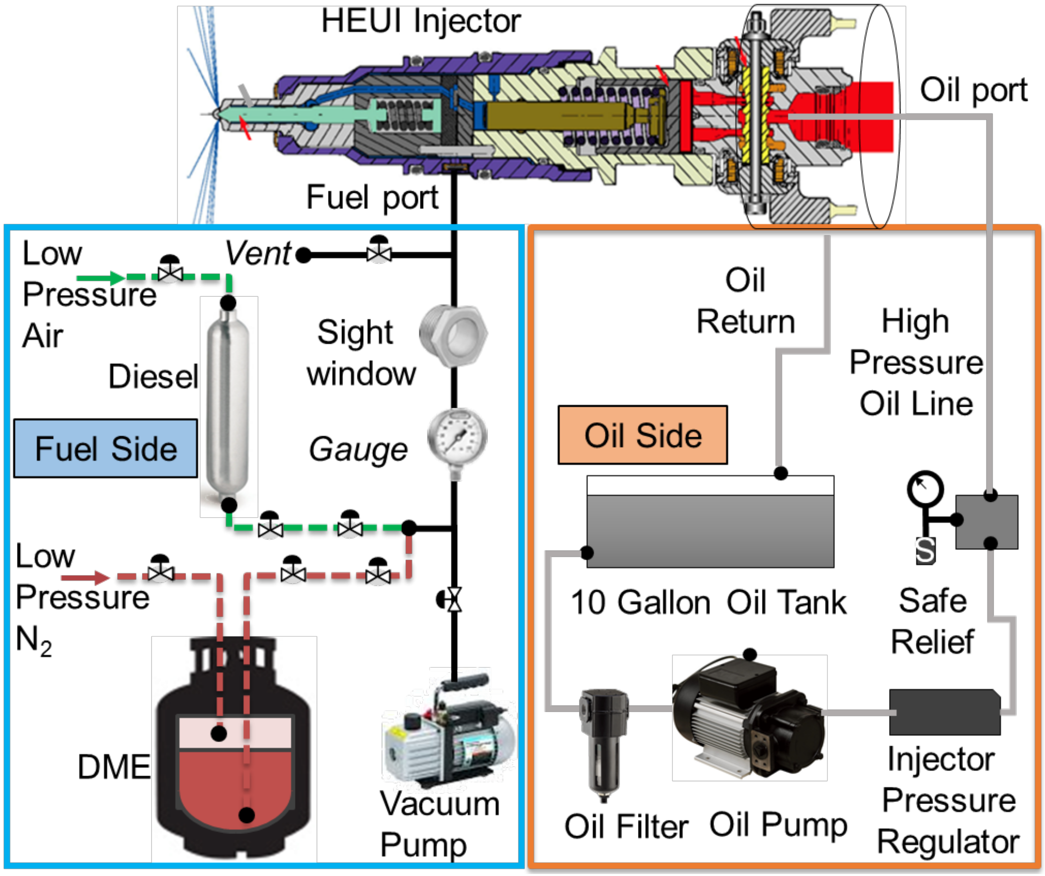

Figure 6-1 Dual fuel (DME or diesel) delivery system which is compatible for HEUI injector [70]

6.2 Rate of injection measurement

A Bosch tube method is used to measure the ROI. The schematic of the ROI measurement setup is shown in Figure 6-2. An attached plate is designed to mount the injector and the ROI cup, sealed by a thin Teflon plate (0.015mm). The ROI cup is connected to a long rolled dynamic tube (Bosch tube). A Kistler pressure transducer is used to collect the pressure wave data within the Bosch tube, and the information is recorded in the DAQ system. The pressure transducer is mounted on the housing of the injector cup.

The injector is mounted on a manifold onto which the ROI system is attached underneath where the injector spray tip is located. Fuel and oil inlets are connected to the fuel delivery system. Two iPOD coil EFS drivers (Model # E8427) power and control the injector's open and close coils. A sample output of the ROI measurement is shown in Figure 6-3, including open/close current signals, injection pressure, and the ROI.

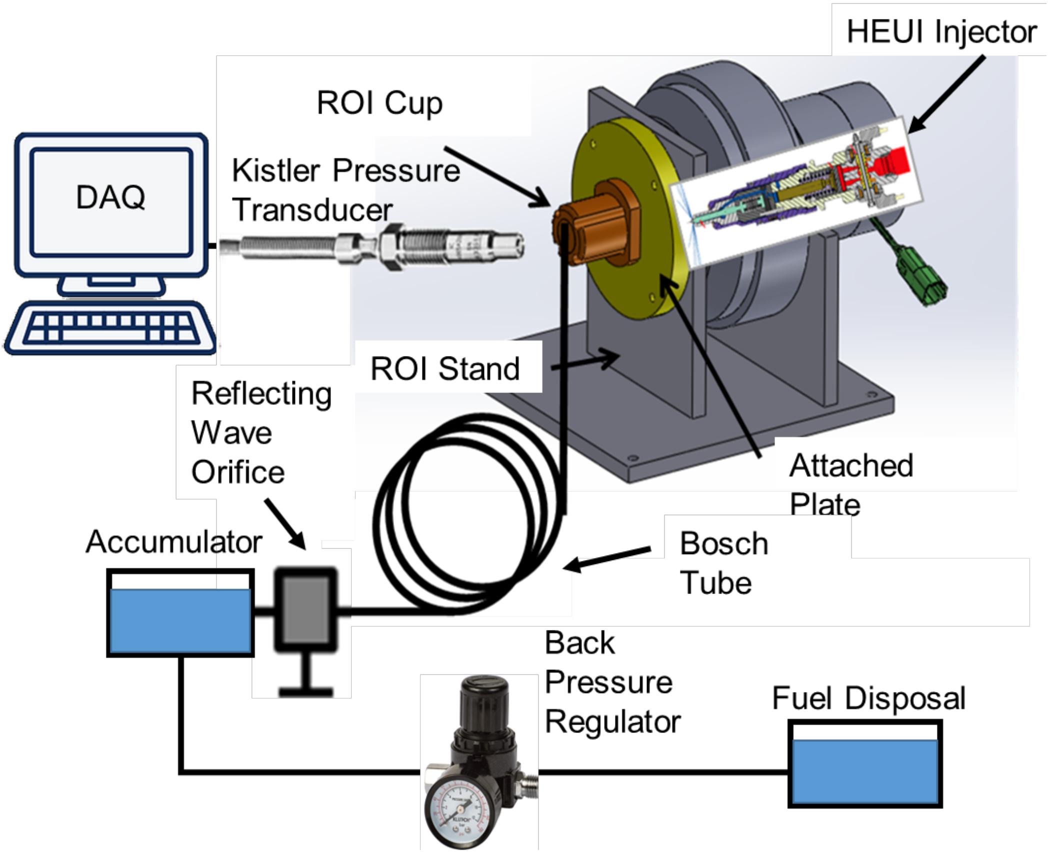

Figure 6-2 Bosch tube type ROI measurement experimental set for HEUI

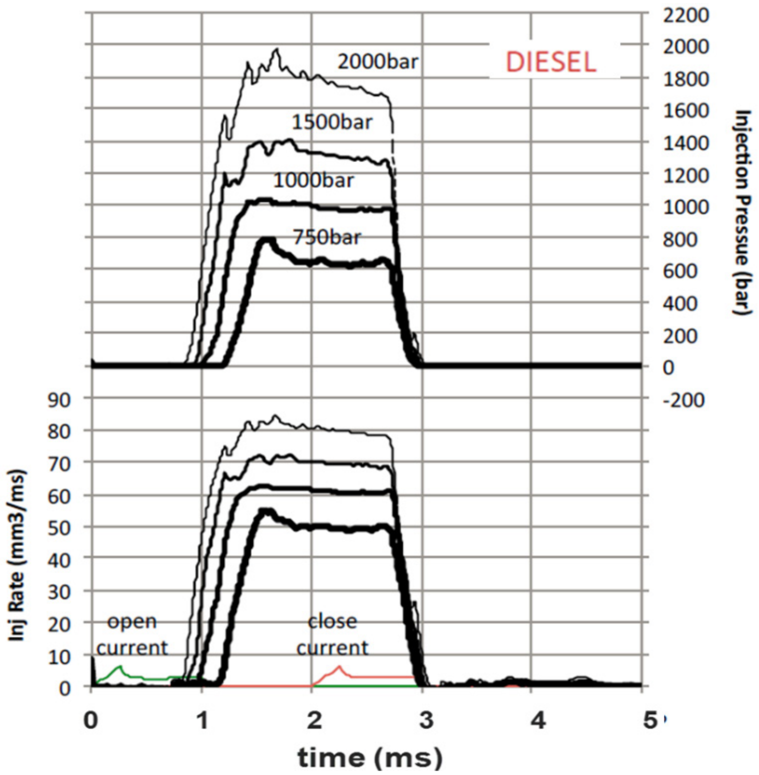

Figure 6-3 A sample output from the Bosch type ROI measurement system, including a measured ROI profile, open/close current signals, and injection pressure

1.1 Combustion vessel apparatus overview

The CV in the Alternative Fuels Combustion Laboratory (AFCL) of Michigan Technological University (MTU) is used to perform the experiments. The vessel has a 1.1-liter constant volume chamber with up to 95% of optical coverage. The chamber has six windows (three types: optical sapphire window, blank metal window, functional window) which can be either used for optical access, or for mounting experimental instruments (the spark plugs, injectors, and fans). There is a total of eight corners on the cubical chamber, which is used to mount an intake valve, an exhaust valve, and a pressure transducer. The pressure measuring system consists of a Kistler 6001 piezo-electric dynamic pressure transducer and a Kistler 5044a charge amplifier [71]. The CV also has temperature control which can maintain the CV body at a stable temperature up to 453 K. The vessel can withstand a maximum temperature of about 2100 K and the pressure up to 345 bar during the combustion event [72].

The chamber generates a desired ambient environment (ambient gas temperature, pressure, and density) though a pre-burn of the premixed combustible gas mixture. Ambient gas temperature ranges from 295K to ~1300 K, and ambient oxygen concentration varies from 0% to 21%. A typical pre-burn process is illustrated with pressure trace, shown in Figure 6-4: (A) The pre-mixed combustion initiated by a spark generates high-temperature and high-pressure conditions in CV; (B) Then the hot environment cools down “slowly” due to the heat transfer with cold vessel in approximately 3 seconds; (C) The fuel is injected when the desired pressure (temperature) is reached [73]. There are usually three kinds of conditions: non-vaporizing, vaporizing, and combustion. The non-vaporizing conditions are generated using N_2 and without pre-burn. With the combustion of a premixed mixture, depending on different levels of O2 in the remaining gas, a vaporizing condition (0% O_2 in the post-combustion gas) or a combusting condition (over 0% O_2 in the post-combustion gas) could be generated.

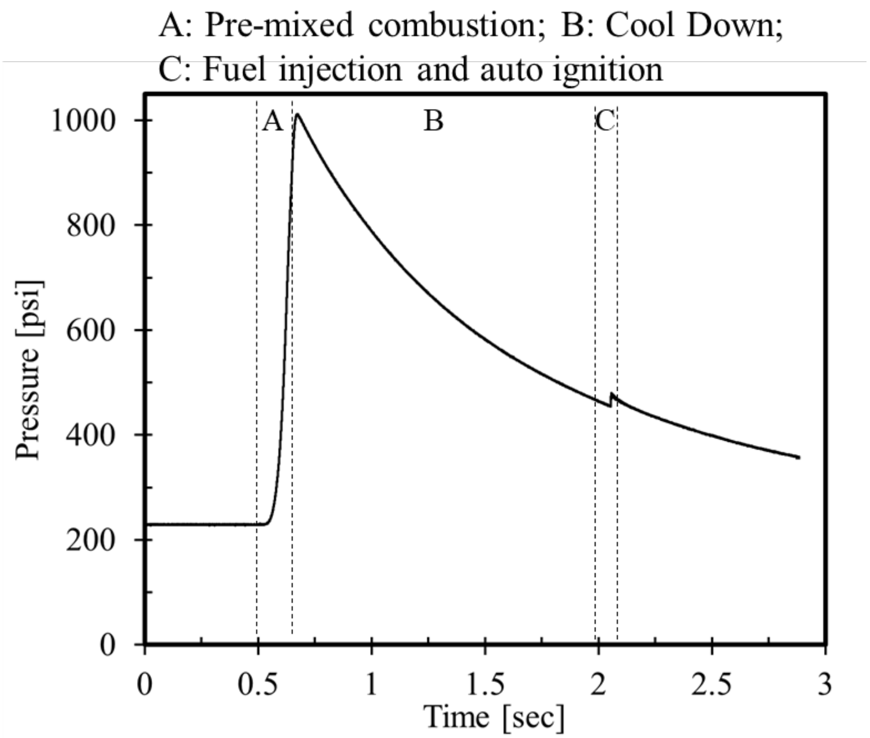

Figure 6-4 A typical pressure trace for pre-burn process in CV

6.3 Optical diagnostics

CV’s sapphire windows provide good optical access, so optical diagnostics are used to characterize spray and combustion. The optical techniques used in the study are Schlieren/shadowgraph, Mie scattering, flame luminosity, OH* chemiluminescence, and planar laser-induced fluorescence (PLIF) of formaldehyde (CH_2O).

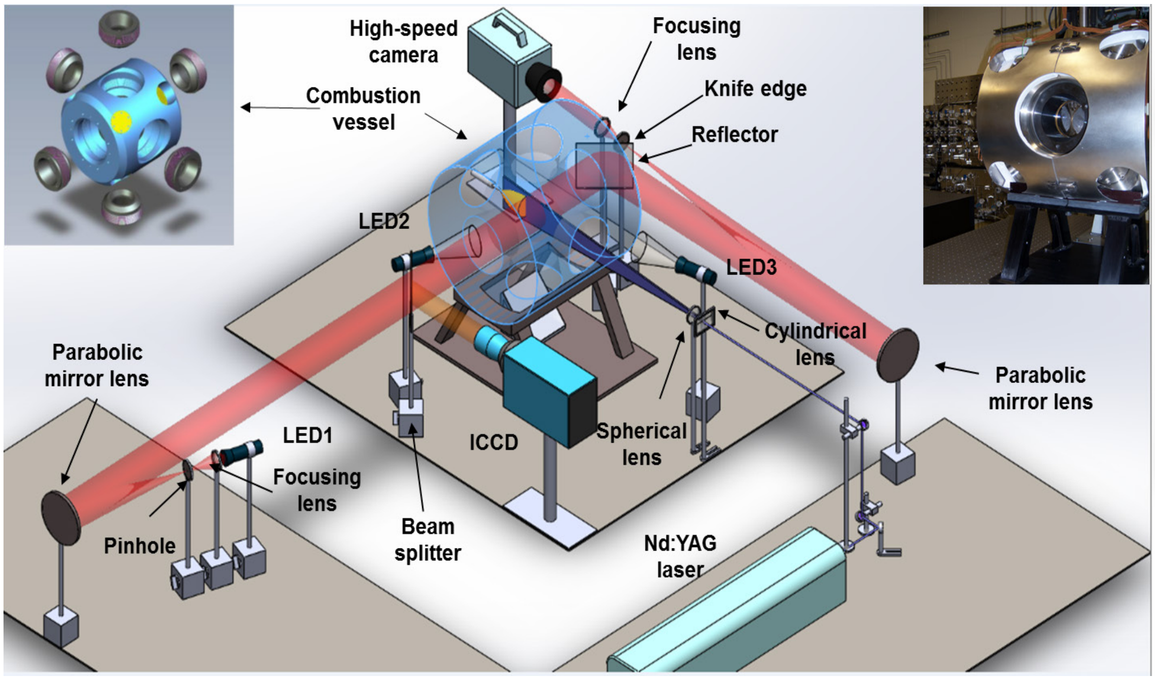

Figure 6-5 Hybrid of schlieren/Mie scattering and PLIF optical setup

6.3.1 Mie scattering

Mie scattering is a phenomenon of elastic scattering of incident light by particles, named after German physicist Gustav Mie [74]. It happens when the size of the particle is larger than or comparable to the wavelength of the incident light and predominates over other types of scattering (e.g. Rayleigh scattering) in these circumstances. As shown in Figure 6-6, the scattered light of Mie scattering shows a pattern like an antenna lobe, with a more concentrated front lobe for larger particles.

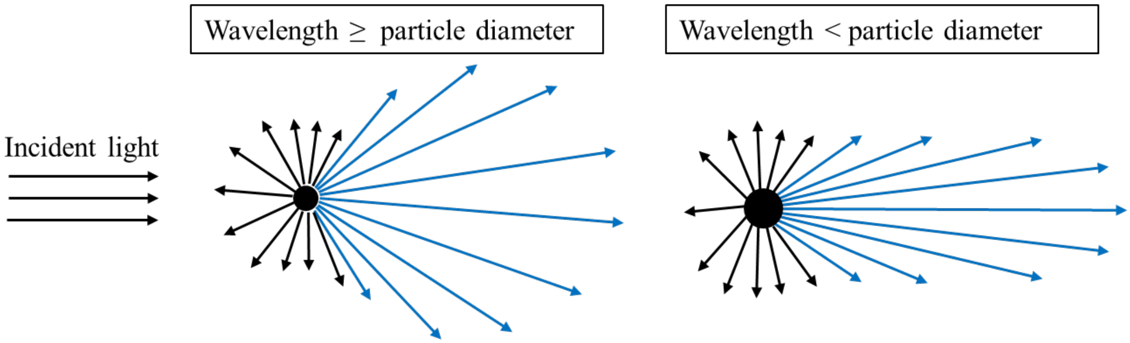

Figure 6-6 Mie scattering shows an antenna lobe type pattern

The Mie scattering technique uses a camera to collect the scattered light from the liquid droplets to visualize the liquid jet. Figure 2-3 shows a typical example of the Mie scattering image. Actually, "Mie scattering" in this study is not pure Mie scattering but is good enough to capture the liquid profile. LED2 in Figure 6-5 is used to obtain uniform light spread throughout the liquid spray region for Mie scattering. A series of images are collected and post-processed in MATLAB to obtain spray characteristics, such as liquid penetration.

6.3.2 Schlieren and natural luminosity

Schlieren technique has the ability to detect the gradients in the refractive index of a transparent medium, caused by density difference [75]. Schlieren technique is adopted to capture the profile of vaporized fuel in a spray jet. The Schlieren technique used here is a modified typical Z-shaped Schlieren setup (one reflector added due to the room restriction). The light source is a light-emitting diode (LED), model Dragon Light HPLS-36AD3500. This model could be operated under a continuous mode, and a pulsed mode, which keeps the LED on up to 25% duty cycle with a higher intensity of emitted light. The light from LED1 goes through a focusing lens and a pinhole is used to generate a point light source.

The pinhole is placed near the focal point of a parabolic mirror (750-mm focal length, 152-mm diameter) to generate a collimated beam of light, which passes the CV through two side sapphire windows. The collimated light is converged by the second parabolic mirror to a high-speed (HS) camera (Photron Fastcam SA1.1). On the focal point of the second parabolic mirror, a pinhole/knife edge is placed to produce the Schlieren effect. An 85-mm f/2.8 Nikon camera lens is used on the camera, together with a bi-concave lens (F.L. 200 mm). The bi-concave lens is used to assist in focusing on the center plane of spray.

Flame luminosity images are captured by the HS camera via the same optical path as the Mie scattering technique. Due to the high intensity of the diesel spray combustion, a neutral density filter (OD3) is applied to avoid saturating the flame luminosity images.

Schlieren and Mie scattering images are both captured using the HS camera. A portion of the test matrix was conducted with hybrid Schlieren and Mie to get liquid and vapor information simultaneously in one spray event. The hybrid setup in this study used the frame rate of 20,000 frames per second (fps), which means 50 μs between adjacent frames. Two LEDs (LED1 and LED2) are set to shine alternatively for each frame.

6.3.3 OH* chemiluminescence

OH* chemiluminescence and PLIF imaging are captured using an intensified CCD camera (DiCam Pro) with a UV lens (105 mm Coastal Optic, UV-MICRO-APO). Unlike the high-speed images from the hybrid Schlieren and Mie scattering technique, there is only one-shot per spray. After ignition, excited OH* radicals are generated in a high heat release rate region (near stoichiometric). Also considering its short lifetime, it can indicate flame initiation [35]. The OH* chemiluminescence is centered at 308 nm wavelength, so a band-pass filter is adopted (310 nm centered, 10nm FWHW). From the schematic in Figure 6-5, a 50/50 (reflection/transmission) beam splitter is mounted in front of the CV side window, without interrupting the hybrid optical arrangement. The shutter time of the ICCD camera varies from 0.5 ms to 1.5 ms, in order to obtain a clear LOL when the flame becomes steady. Figure 2-4 shows a typical example of OH* chemiluminescence image.

6.3.4 PLIF for formaldehyde

The current PLIF setup for formaldehyde diagnostics uses a Continuum Surelite III Nd:YAG laser (355 nm center wavelength) to excite the formaldehyde species. The 355 nm laser pulses, whose average pulse energy is 95 mJ, are generated from the third harmonic of the Nd:YAG laser generator. The laser beam is expanded by a cylindrical lens to a laser sheet (54 mm wide and 0.4 mm thick). This laser sheet points at the injector tip vertically. A short-pass filter (400 ± 20 nm FWHM) is used before the ICCD camera.

Figure 6-7 shows the laser timing diagram and the ICCD camera shutter timing setup. The ICCD camera was in double shutter mode. The first shutter has an exposure time of 1ms but without laser excitation spray. The signal captured by the first shutter is mainly from the OH* chemiluminescence. The second shutter has a 100 ns exposure time and the laser was shot right before the opening of the second shutter. This can avoid the image saturation caused by the direct laser light reflection from the injector wall and allow the fluorescence signal to be captured because there is a delay between laser signal and fluorescence signal. The fluorescent species (formaldehyde) absorb the laser energy and turns into an excited state and then fall back to the ground state with emitted fluorescence, which takes time to happen. Later the PLIF images are processed using a Matlab code and overlapped with Schlieren images for further analysis.

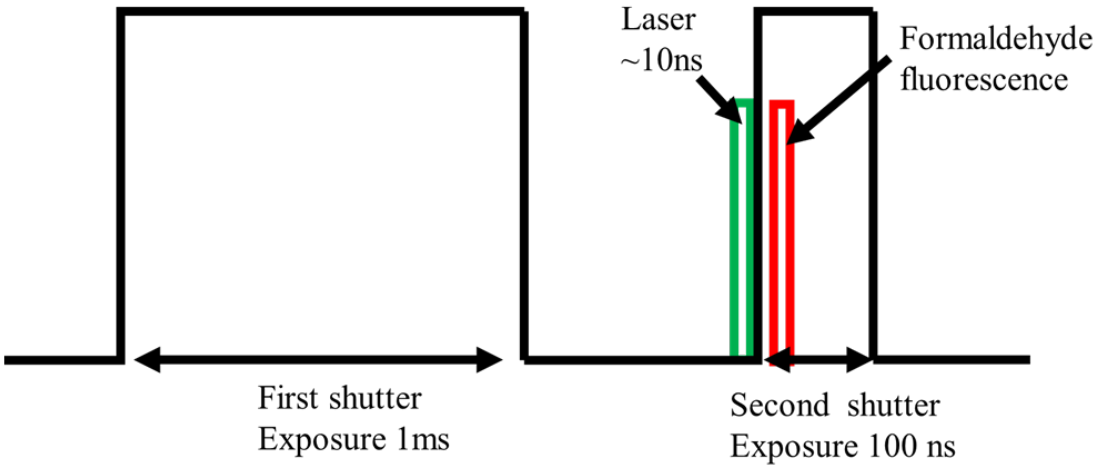

Figure 6-7 Laser timing diagram along with the ICCD camera shutter time

7 Data post-processing

7.1 General imaging processing

The images of spray and flame obtained from the Schlieren and luminosity techniques are valuable information in understanding spray and combustion characteristics. However, the challenge arises during the interpretation of the spray and combustion images due to presence of background noise. The pre-burn process in CV generates a high density, high temperature conditions with a certain level of turbulence within the chamber, combined with buoyancy effect. These results in locally wrinkle as seen from the Schlieren effect that describes the density gradient of the ambient gas. The accurate measurement of spray characteristics (e.g. spray penetration, spray angle) highly relies on identifying accurately spray boundary. Therefore, the background subtraction was performed firstly to remove noise. There are two methods of background subtraction: (1) All the images subtract the same background image which is taken right before the injection ($I_n - I_{background}$), (2) The current image subtracts the previous image in timer series ($I_n - I_{n-1}$). Choose between these two methods based on a trial and error base. Then, the image was converted into a binary image based on a threshold which is a constant value chosen by applying Otsu's method [76] to aid in accurately predicting the boundary. Figure 7-1 shows the procedure of imaging processing.

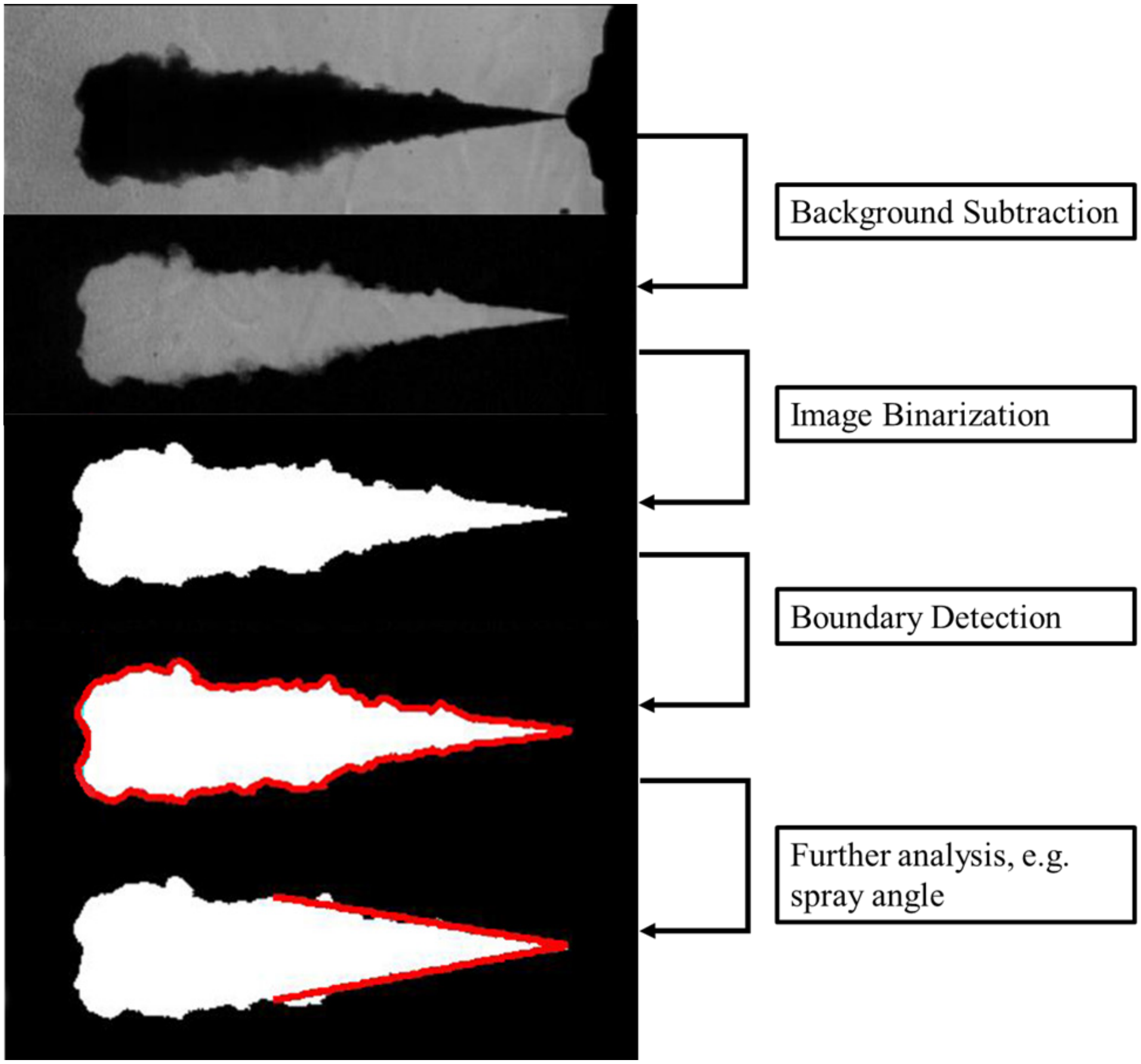

Figure 7-1 Sample image-set showing image processing procedure starting from a raw schlieren image

7.2 Image processing: combined schlieren-PLIF imaging

There is a different image processing procedure for the PLIF images. The raw images needed for this process are Schlieren images and PLIF images. The procedure is to process schlieren and PLIF images separately, then superimpose the PLIF image (50% transparency) on to the schlieren image. A sample image-set of DME spray at the baseline condition is shown in Figure 7-2.

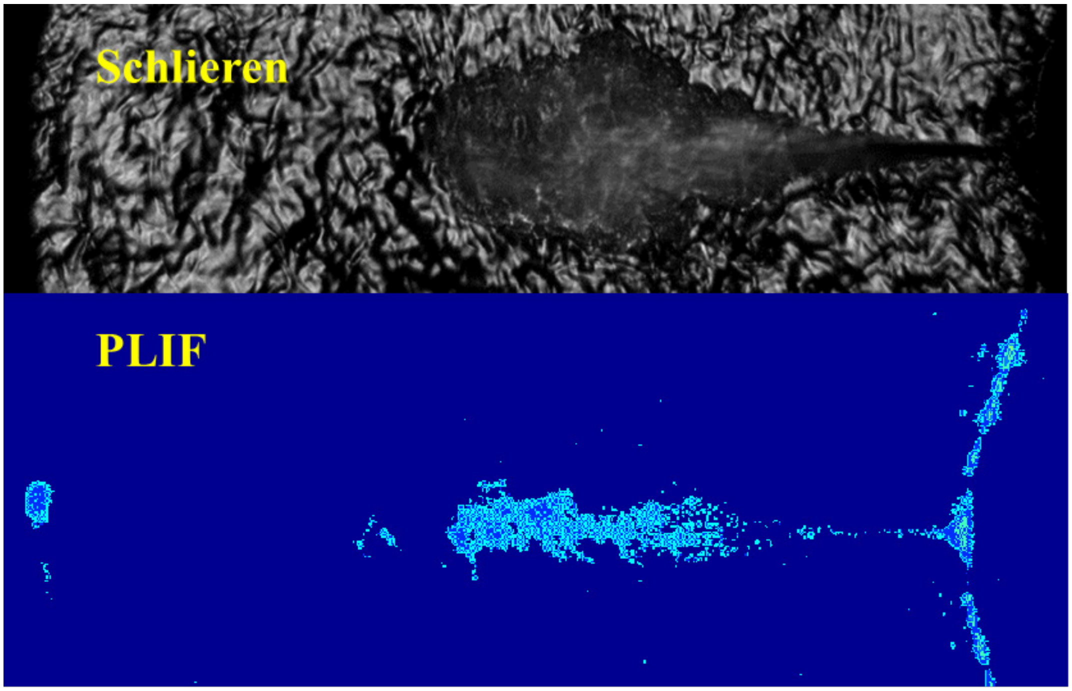

Figure 7-2 Sample image-set of raw schlieren and PLIF images

As shown in Figure 7-3, the raw images are usually with low brightness. The image processing starts with brightness enhancement by adjusting the gamma value. Then the next step is to get a clear vapor boundary detection, including edge detection (canny function), filtering (median filter), background remove (imopen & imclose), and binarization of image. The binarized image is used as a region mask on the raw image to extract the vapor region with a clear boundary.

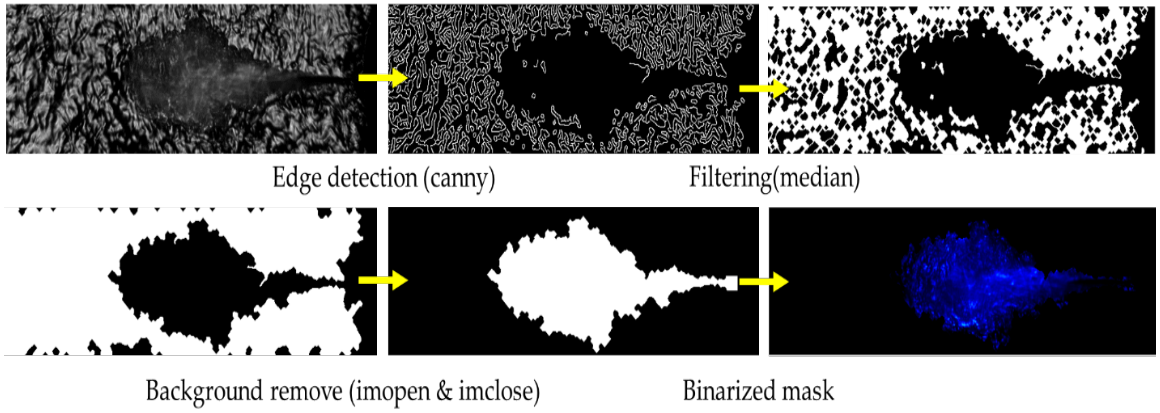

Figure 7-3 Sample image-set showing image processing procedure of clean vapor boundary detection

The colormap is a series of colors that corresponds to the image intensity level for visualization purpose. Two different colormaps are assigned to the schlieren and PLIF images separately. These two maps are modified based on the classic jet colormap. Both start at one end of the jet colormap bar, moving toward each other, and merges in the middle of the jet map. In this way, a strong contrast can be achieved.

The last step is to overlapping two images. However, the sizes of raw schlieren and PLIF images are not the same, which means that a direct overlap is not possible. Based on the resolutions of the PLIF image, resize schlieren image needs to be resized accordingly. The injector tip location is used as a reference during overlapping. Finally, the transparency of the PLIF image is adjusted to avoid blocking too much structure details of the schlieren image. A sample schlieren-PLIF overlapping image is shown in Figure 7-4.

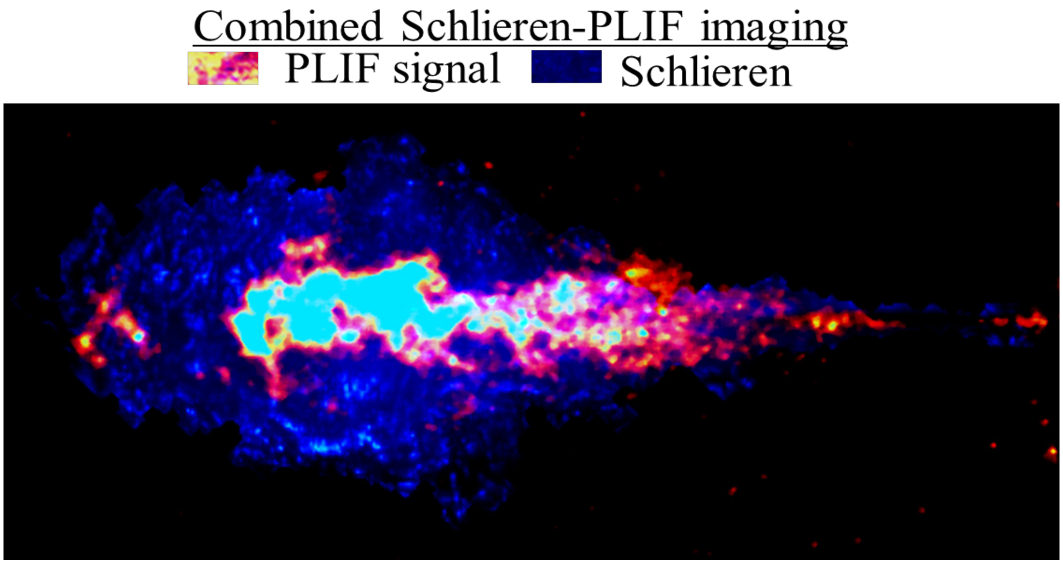

Figure 7-4 A sample of combined schlieren-PLIF imaging

7.3 Pressure based data analysis

As mentioned in the CV apparatus section, the CV pressure was measured through a Kistler 6001 piezo-electric dynamic pressure transducer which is mounted on the bottom-left corner (facing the incoming spray direction) of the CV front wall (opposite to the injector wall). The combustion event happens within several milliseconds, so the data acquisition frequency was set to 150 kHz to capture the pressure trace. The raw pressure signal was then sent into a Kistler 5044a charge amplifier for amplification. Around the compact CV, there are many other electronic devices, for example, the electrical driven injector and cameras. The recorded pressure signal usually contains noise caused by the electro-magnetic interferences between electrical devices. The pressure trace was cleaned before the post-processing.

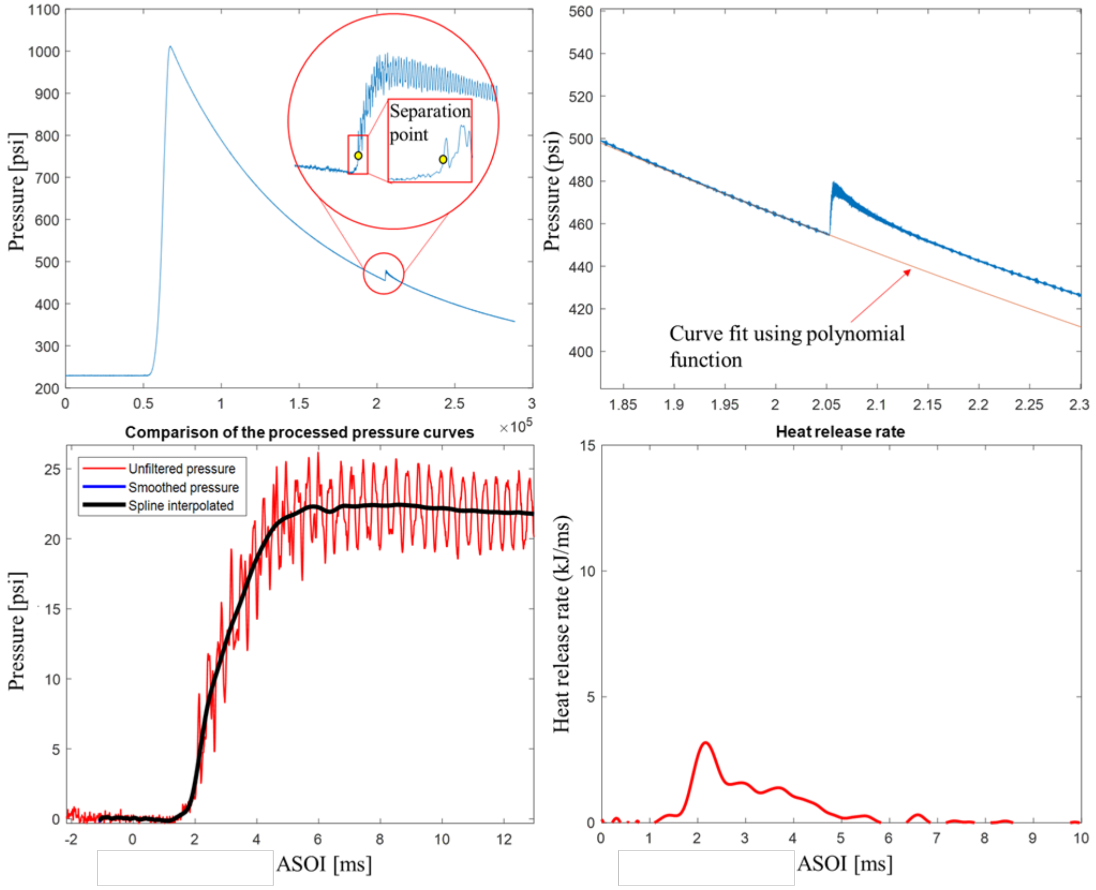

Figure 7-5 Procedure of CV pressure trace post-processing: (a) Raw CV pressure data, (b) Polynomial curve fit, (c) Smoothed pressure, (d) AHRR

Figure 7-5(a) shows a typical raw CV pressure trace and zoomed-in circle view which displays the noisy nature of this signal. A MATLAB code was designed to clean up the pressure trace, extract the transient pressure only related to the the combustion event, and calculate the AHRR. The first step is to perform a polynomial curve fit from 10000 points before the start of injection (SOI) to the SOI timing. Figure 7-5(b) is the comparison between raw pressure with the polynomial curve fit. The polynomial curve fit is the prediction of the pressure trace in the condition without spray injection. The unfiled pressure in Figure 6-5(c) is obtained by subtracting the curve fit from the raw pressure trace. The subtracted pressure is later used in the calculations of AHRR. The subtracted pressure is then cleaned up with a two-portion filter method, and each part has a different level of filter settings. Smoothing was not done with a single filter throughout the pressure, because the pressure trace after the auto-ignition (high rate of pressure raises) has a higher level of oscillations compared to the pressure prior to ignition. A single level filter would either over-smooth or under-smooth one side of the trace. Therefore, the pressure trace is divided into two parts and smoothed separately. The separation point, which is marked out in Figure 6-5(a), is set around the middle point of the first pressure ramp caused by auto-ignition. A 50th order FIR filter with a 5000 Hz cutoff frequency is used for the portion prior to separation point, and a 5th order Butterworth filter with a 1500 Hz cutoff frequency is used for the second part pressure which is after the separation point. Assemble the two smoothed curved together, then perform a spline interpolation alone the entire pressure curve. For the ignition delay measurement, a 0.0028 MPa threshold is selected on the smooth spline pressure curve to find the onset of ignition.

Apparent heat release rate (AHRR) calculation is also based on the smoothed pressure trace. Equation (1) is used to calculate the AHRR:

$$\frac{dQ}{dt} = \frac{\gamma}{(\gamma-1)} P \frac{dV}{dt} + \frac{1}{(\gamma-1)} V \frac{dP}{dt} \tag{7-1}$$

where γ is 1.35 as suggested by Heywood [31] for an appropriate ratio of specific heat prior to combustion, P is vessel pressure, V is the constant CV volume (1.1 L). The dV/dt term is zero in constant volume vessel, so the final equation will be

$$\frac{dQ}{dt} = \frac{1}{(\gamma - 1)} V \frac{dP}{dt} \tag{7-2}$$

7.4 Intensity-aXial-Time (IXT) plot

IXT plot is a plot of temporal and spatial flame luminosity which is the integration of flame luminosity of each frame along with the axial location, defined mathematically as in Figure 7-6. In IXT, “I” is intensity, “X” is axial location, “R” is radial location, “t” is time, and “R” is the radial boundary of a luminosity intensity map. IXT plot was previously used [77] on experimental imagery, it was also be employed on quantitative CFD data in a similar manner by [78]. It was proved to be a very effective tool to investigate and visualize the spray combustion in a manner of summarizing the whole combustion process in a 2D plot with both information of spray axis and time.

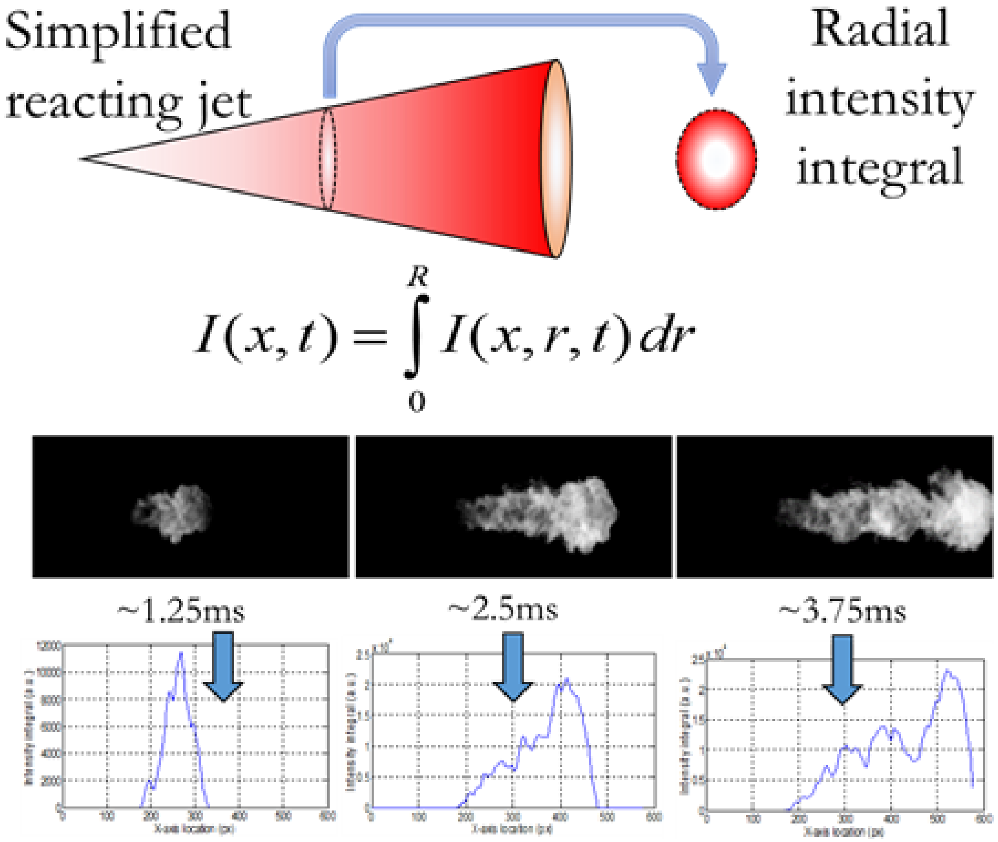

$$I(x,t)=\int_{0}^{R} I(x,r,t)\,dr$$

Figure 7-6 The imaging processing using IXT method

An IXT plot basically transfers a flame luminosity HS video into a 2-D plot, with the capability to provide main spray combustion characteristics including LOL, ignition delay, flame height, liquid length, and luminosity intensity map. Figure 7-7 shows sample results obtained from IXT plot.

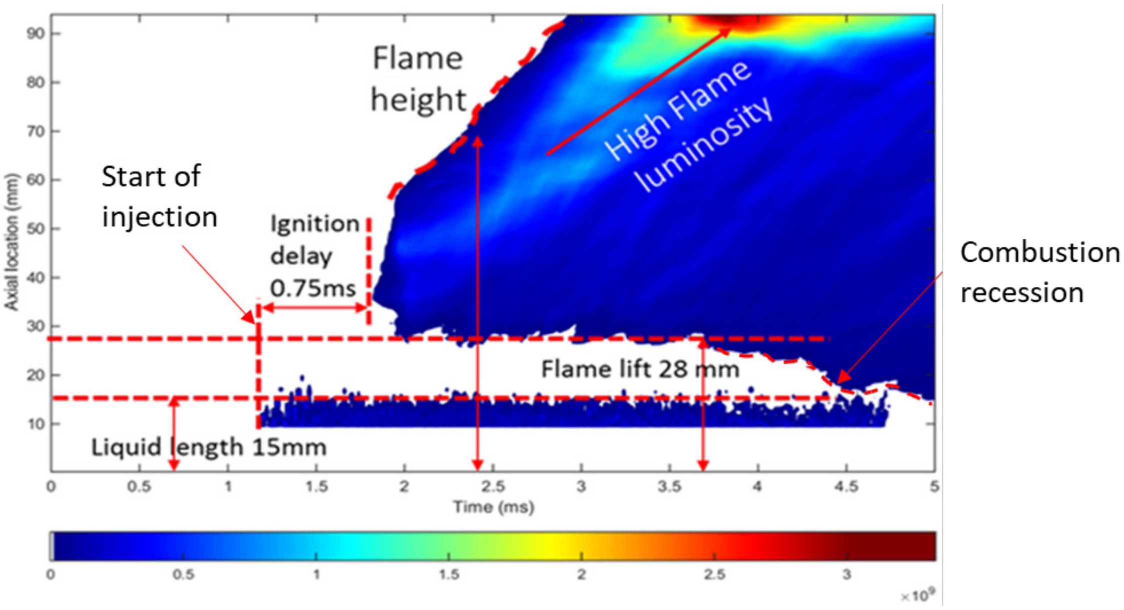

Figure 7-7 IXT plot of DME spray combustion with LED light on for liquid Mie scattering

8 Test conditions

During this study, many tests have been performed. The main focus of these tests is to investigate the spray and combustion characteristics of DME, especially at high-injection pressure conditions. Therefore, non-vaporing, vaporing, and reacting spray tests were considered experimentally and numerically. First, Tables 7-1, 7-2, and 7-3 provide the details of the experimental test matrix which is divided into three parts: multi-hole nozzle injector study, single-hole nozzle injector study, and single-hole low-temperature study. The experimental tests include a variety of optical diagnostics like (1) both Mie scattering and Schlieren techniques were used for vapor and liquid penetration and structure, (2) microscopic imaging for near nozzle spray investigation, (3) natural luminosity, OH* chemiluminescence, and photodiode for diagnosing features like LOL, ID, and soot formation, (4) PLIF techniques were specifically used CH_2O visualization. Some tests were using the the spectroscopic measurement of DME combustion, but the results were not covered in this study. The baseline condition is injection pressure of 150 MPa, injection duration (energizing) of 2.0 ms, the ambient density of 14.8 kg/m3, the ambient temperature of 900 K, ambient composition of 18% O_2. The chamber temperature was kept constant for all the experiments of 90 deg C. The fuel temperature was maintained by a chiller temperature controller between 35-40 deg C. The parametric studies compose a change in ambient temperature, ambient density, oxygen concentration, and injection pressure.

Table 8-1 Test conditions of multi-hole nozzle injector study

Multi-Hole								
Condition	**Measurement**	**Amb O2**	**Amb Dens**	**Inj Press**	**Noz Diam**	**Fuel Type**	**Tamb**	**Inj Dur**
		[%]	**[kg/m3]**	**[Mpa]**	**[µm]**		**[K]**	**[ms]**
Non-Vaporizing	Mie Scattering-Head on	N2	14.8	100, 150	8*155	Diesel, DME	20 deg C (chiller)/110 deg C (CV)	1
			14.8	69		Diesel		0.85
			14.8	200		DME		0.85
	Mie Scattering-Side view		11.8, 14.8, 22.8	100, 150		Diesel, DME		1
			11.8, 14.8, 22.8	69		Diesel		0.85
			11.8, 14.8, 22.8	200		DME		0.85
Vaporizing	Schlieren - Side view	0	14.8	150	8*155	Diesel, DME	750, 900, 1100	1
			22.8			Diesel, DME	900	1
Combusting	Flame Luminosity	15	14.8	150	8*155	Diesel	750, 850, 900, 950, 1000, 1050, 1100	1
				100, 150		Diesel	750, 900, 1100	1
				69		Diesel	750, 900, 1100	0.85
				100		DME	750, 900, 1100	1.74
				150		DME	750, 900, 1100	1.69
				200		DME	750, 900, 1100	0.82

Table 8-2 Test conditions of single-hole nozzle injector study

Single-Hole								
Condition	**Measurement**	**Amb O2**	**Amb Dens**	**Inj Press**	**Noz Diam**	**Fuel Type**	**Tamb**	**Inj Dur**
		[%]	**[kg/m3]**	**[Bar]**	**[µm]**		**[K]**	**[ms]**
Non-voprizing	Schlieren	N2	14.8	1500	180	Diesel	20 deg C (chiller)/110 deg C (CV)	1.5
			14.8	1500	180	DME		1.5, 2, 2.5, 3
			1.0, 14.8, 25	500, 750, 1000, 1250, 1500	180	DME		2
			1.0, 14.8, 25	1500	150	DME		2
			14.8	500, 750, 1000, 1250, 1500	150	DME		2
			14.8	1500	150	DME		1.5, 2, 2.5, 3
	Near nozzle Schlieren		1.0, 14.8, 25	500, 1500	150	DME		2
Vaporizing	Schlieren	0	14.8	1500	180	Diesel	750, 900, 1100	2
Vaporizing	Schlieren	0	14.8, 25, 30	1500	180	Diesel	900	2
Vaporizing	Schlieren	0	14.8, 25, 30	750, 1000, 1500	180	Diesel	900	2
Vaporizing	Schlieren	0	14.8	1500	180	Diesel	900	1.5
Vaporizing	Hybrid	0	14.8	750	180	DME	750, 900, 1100	2
Vaporizing	Hybrid	0	14.8	1000	180	DME	750, 900, 1100	2
Vaporizing	PLIF/Hybrid	0	14.8	1500	180	DME	750, 900, 1100	2
Reacting	PLIF/Schlieren	15	14.8	1000	180	Diesel	900	1
Reacting	PLIF/Schlieren	15	14.8	1500	180	Diesel	900	1
Reacting	Schlieren	15	14.8	1500	180	Diesel	900	2
Reacting	PLIF/Schlieren	15	14.8	1000	180	Diesel	750	1
Reacting	PLIF/Schlieren	15	14.8	1000	180	Diesel	1100	1
Reacting	PLIF/Schlieren	15	14.8	1500	180	Diesel	750	1
Reacting	PLIF/Schlieren	15	14.8	1500	180	Diesel	1100	1
Reacting	PLIF/Hybrid	15	14.8	1500	180	DME	750	2
Reacting	PLIF/Hybrid	15	14.8	1500	180	DME	900	2
Reacting	PLIF/Hybrid	15	14.8	1500	180	DME	1100	2
Reacting	PLIF/Hybrid	21	14.8	1500	180	DME	900	2
Reacting	PLIF/Hybrid	18	14.8	1500	180	DME	750	2
Reacting	PLIF/Hybrid	18	14.8	1500	180	DME	900	2
Reacting	OH*/Hybrid	15	14.8	500,750,1000,1250,1500	180	DME	900	2
Reacting	OH*/Hybrid	15	14.8	1500	180	DME	900	1.5,2,2.5,3
Reacting	OH*/Hybrid	21	14.8	1500	180	DME	900	2
Reacting	OH*/Hybrid	18	14.8	1500	180	DME	750, 800, 850, 900, 950, 1050, 1100	2
Reacting	OH*/Hybrid	18	11.4, 14.8, 18.8, 22.8, 25, 30	1500	180	DME	900	2
Reacting	OH*/Hybrid	18	14.8	1500	180	DME	900	1.5, 2, 2.5, 3, 3.2
Reacting	OH*/Hybrid	18	14.8	500,750,1000,1250,1500	180	DME	900	2

Table 7-3 Test conditions single-hole low-temperature study

Low temperature combustion								
Condition	**Measurement**	**Amb O2**	**Amb Dens**	**Inj Press**	**Noz Diam**	**Fuel Type**	**Tamb**	**Inj Dur**
		[%]	**[kg/m3]**	**[Bar]**	**[µm]**		**[K]**	**[ms]**
Reacting	Flame Luminosity/OH*	15, 18,21	14.8	500	180	DME	750, 775, 800, 900, 1100	3.3
Reacting	Flame Luminosity/OH*	15, 18,21	14.8	500,750,1000,1250,1500	180	DME	750, 900	3.3

9 HEUI injector modeling and ROI experiments for high injection pressure of DME1[1]

9.1 Background

Tier 3 vehicle emission and fuel consumption standards will come into effect starting in 2017 and estimated to reduce 28% nitrogen oxides (NOx) and 10% direct fine particulate matter (PM2.5) of on-road inventory by 2030 [9-1]. Federal law sets the fuel economy target to 54.5 miles per gallon for automobiles in 2025 [9-2]. With the concern of tighter emission standards and depletion of oil reserves, researchers in academia and industry are searching for an advanced alternative fuel, which can result in low emissions as well as high fuel efficiency. Di-Methyl Ether (DME) is a promising clean alternative fuel to diesel [9-3]. DME (CH3OCH3) is the simplest ether. Its high oxygen mass fraction, absence of C-C bond atom structure, and the fast vaporization ability will together achieve efficient and soot-free combustion in diesel engines [9-4]. Integrated into an advanced injection and combustion system, DME also has the potential to meet ultra-low emission vehicle (ULEV) limits in NOx and soot emissions [9-5].

DME, with its high cetane number, can be used in high-efficiency compression-ignition engines. However, DME and diesel still have many different properties. For example, DME is in the gas phase at normal temperatures and pressures, while diesel is a liquid fuel. In order to design advanced fuel delivery, injection and combustion systems for DME, property differences between DME and diesel in table 1 need to be understood. One of the

---

[1] Rearranged from SAE 2016-01-0855. Reference format is shown in 9-X.

important differences between diesel and DME is liquid viscosity. The low liquid viscosity of DME will cause two main challenges in the injection system: leakage and low lubricity. Low lubricity will cause wear of moving surfaces. The situation will become worse at high injection pressures. In order to resolve these problems, the fuel contacting region must be minimized to reduce the chance of leakage and wear. A hydraulically actuated electronic unit injector (HEUI) uses engine oil to drive an intensifier to pressurize the fuel. Fuel limited to a very small chamber right before the injector nozzle. The mechanism of the HEUI will be described in the background section.

From previous experiments, we observed that the DME has a significant injection delay compared to the diesel. Since there are two working fluid systems operating in the fuel injector, the characteristics of fuel injection are considerably influenced by the fuel properties and injector geometry. The present work was done to understand the performance difference between diesel and DME on the HEUI injector, and further to optimize the DME injection system. A one-dimensional HEUI injector model with parameters including injection pressure, nozzle diameter, and injection duration was built. Its output (ROI profile), which can be used as CFD input and injector design reference, plays an important role in affecting spray and combustion characteristics.

Table 9-1 Properties of diesel and DME [9-4] [9-6,7].

Properties	Diesel	DME
Chemical formula	-	CH_3OCH_3
C/H ratio	0.516	0.337
Molecular weight (g/mol)	170	46.07
Critical temperature (K)	708	400
Critical pressure (Mpa)	3	5.37
Vapor pressure at 293 K (kPa)	<<10	530
Boiling temperature at 1 atm (K)	450-643	248.1
Liquid density at 293 K (kg/m3)	831	667
Modulus of elasticity (N/m2)	1.49E+09	6.37E+08
Liquid viscosity at 298 K (kg/ms)	2–4	0.12–0.15
Surface tension at 298 K (N/m)	0.027	0.012
Lower heating value (MJ/kg)	42.5	28.43
Cetane number	40-50	55-60
Auto-ignition temperature(K)	523	508
Stoichiometric A/F mass ratio	14.6	9
Enthalpy of vaporization (kJ/kg)	300	467.13

9.2 HEUI injector mechanism

The HEUI injector consists of a control valve, intensifier piston, plunger, and nozzle. The control valve is a two-position, three-way valve that transmits oil pressure into or out of the intensifier piston. The oil pressure is controlled between 40 and 300 bar and multiplies the fuel pressure via the area ratio between the piston and the plunger. Figure 9-1 shows the cut-view of the HEUI and the corresponding schematic of the injector model.

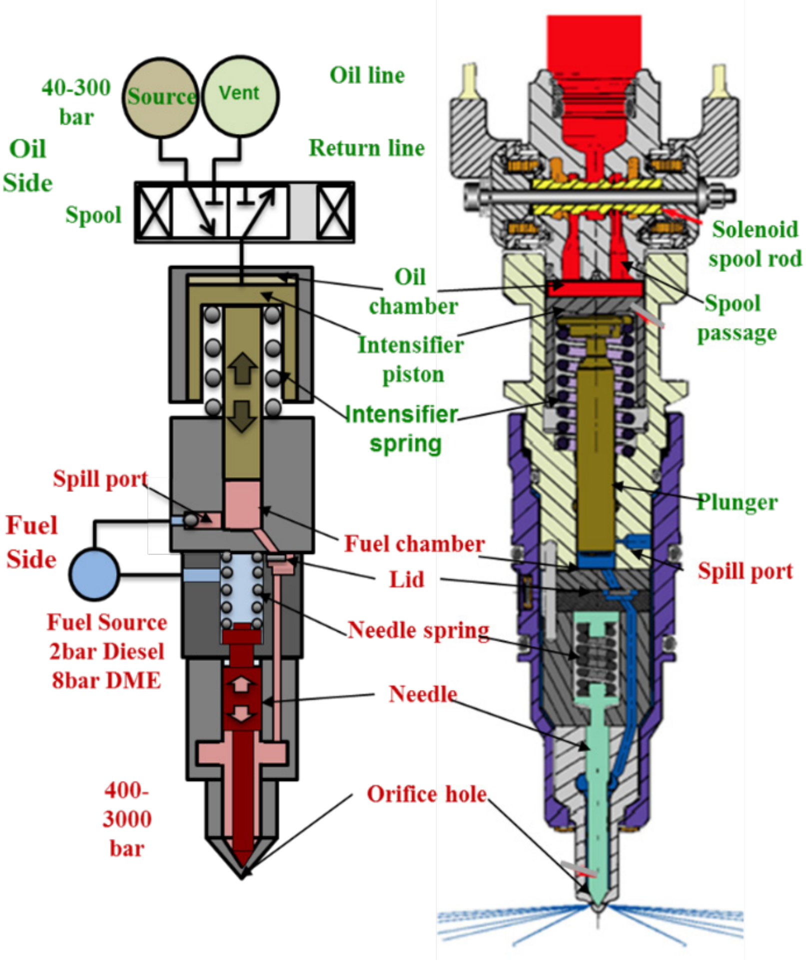

Figure 9-1 HEUI injector parts in functional diagram (left) and section view for the injector geometry (right)

The control valve is driven by two solenoids. The opening occurs by a current pulse from an open coil. The magnetic force moves the spool valve to the opening position. High-pressure oil from the oil rail flows into the oil chamber and reaches the top surface of the intensifier piston as seen in Figure 9-1. Oil pressure pushes the intensifier piston. Once the pre-load spring force of the intensifier is overcome, the piston/plunger moves down and builds up pressure on the fuel side. The fuel pressure keeps fuel inlet closed and the increased fuel pressure acting on the needle to lift it and start the injection flow.

Closing occurs by a current pulse from the close coil. A magnetic force moves the spool valve back to its initial position. The spool valve spills oil from the intensifier piston. The oil pressure and fuel pressure decrease at the same time. A lid check valve located on the passage connecting the intensifier bottom chamber to the needle chamber closes. The lid check valve prevents the pressure in the needle area to drop too fast which may cause some combustion air to enter into the nozzle. The intensifier piston is driven by spring force and returns to the initial position. The injection stops with the return of the piston as it causes fuel pressures to drop and the needle is returned by the action of needle spring.

9.3 Bosch-type ROI measurement

The ROI is the injection profile, defined as the time trace of the instantaneous flow rate [9-8]. It is an important characteristic of injection. There are two popular methods to measure ROI. One is the Bosch type [9-9], and another is the Zuech type [9-10].

The methodology applied in this paper is the Bosch type of ROI measurement. This method measures the pressure wave generated by the injection. It uses the pressure-velocity (Eq. 9-1) equation to calculate the ROI profile based on the measured pressure wave [9-11].

$$P = c \times \rho \times u \qquad (9\text{-}1)$$

$$\frac{dm}{dt} = \rho \times u \times A \qquad (9-2)$$

$$\frac{dm}{dt} = \frac{A}{c} \times P \qquad (9-3)$$

Where P is pressure, c is the speed of sound in fluid, ρ is the density of fluid, u is the flow velocity, m is the mass of fuel, A is the area. Eq. 9-2 is the conservation law of mass. Based on Eq. 9-1 and Eq. 9-2, Eq. 9-3 can be derived. The integration of Eq. 9-3 is the total injected mass.

9.4 Fuel injection systems and capability

There are several types of commercial injection system: distributor pump system, electronic unit injector system, HEUI system, and common rail system. Table 9-2 lists the comparison of these injection systems.

Table 9-2 Comparison between four common injection technologies in terms of driven mode and characteristics

	Distributor Pump	Electronic Unit Injector	HEUI system	Common Rail
Driven Mode	Cam Driven	Cam Driven	Oil Common Rail; Intensifies Fuel at Injector.	High Pressure Fuel
Characteristics	Limited Control; Hydraulic Delays.	Limited Control	Increased Control (but limited); High Fuel Pressures.	High Degree of Feasibility to Command Injections

The distributor pump is a mechanical unit, common in older engines but found in much of the developing world that are not subject to the latest emission regulations. It is a successful system known for its robustness but has limited control (no real-time adjustment of pressure and injection timing). The electronic unit injector is a design that provided control over injection timing over a small window determined by the pumping lobe design. The HEUI system substituted the cam by a hydraulically actuated piston, providing for a wider range of injection timing adjustment and injection pressure. The present HEUI system, which provides a pressure amplification, can provide relatively very high pressures. It can also provide for two injection events, such as pilot and main or main and post. The common rail system has a high degree of feasibility to command injection. For DME, taking the low lubricity and compressibility into consideration, the HEUI system provides a promising pathway to retain the high pressure given that the injector high-pressure components are limited to the needle area alone. High pressure does not need to be built at the injector control vale or high-pressure pump. The present study has shown successful operation at pressures above 2000 bar, higher than the 300-500 bar reported in the literature with DME [9-12~14].

9.5 Simulink modeling details

The injector was modeled using MATLAB/Simulink environment. Figure 9−2 shows the schematic of the model layout. This model contains five main blocks: inlet/relief signal generator, oil spool valve, intensifier, fuel chamber, and needle valve. Each component will be described in detail.

This paper studied an 8-hole injector for application to medium-duty engines (approximately 1.2L cylinder displacement). The multi-hole (MH) injector study would support engine modeling and experimental work using DME fuel. The paper also includes the adaptation of the injector to single hole nozzles. The single hole (SH) injector would be used in dedicated spray and combustion studies supporting DME modeling work of chemical kinetics.

Table 9-3 The configuration details of the injector used in this paper

Injector #	# of holes	Hole sizes (μm)	Hole Angles (degree)	Orifice Configuration
1	8	155	155	Valve Covered Orifice
2	1	180	0	Mini Sac (~ 1mm^3)

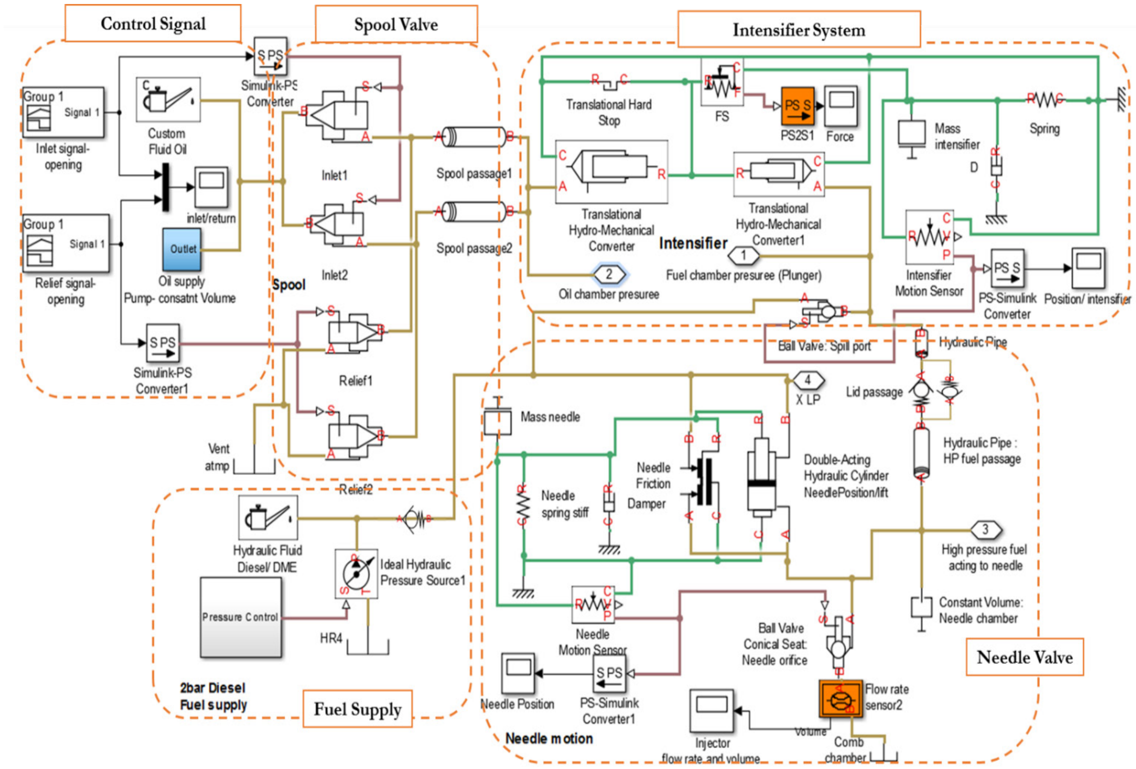

Figure 9-2 Detailed layout for 1-D MATLAB/Simulink model for HEUI with 5 main functional blocks: control signal, spool valve, intensifier, fuel supply, and needle valve

9.5.1 Spool valve mechanism

The opening signal for the spool valve is generated by the signal generator block, as shown in Figure 9-2. The input for the signal generator block is the motion of the injector spool valve attained from experiments.

The spool valve opening area is linearly proportional to the spool valve displacement. Figure 9-3 shows the spool design. As the spool attains the open position, it opens two inlet ports connected to two spool passages. The control signal for the spool valve position is shown in Figure 9-4. Here the inlet signal starts opening at 0.1 ms and fully opens at 0.3 ms. The valve remains open till 2ms and completely closes at 2.18 ms. The inlet and outlet valve openings have a small portion of overlap.

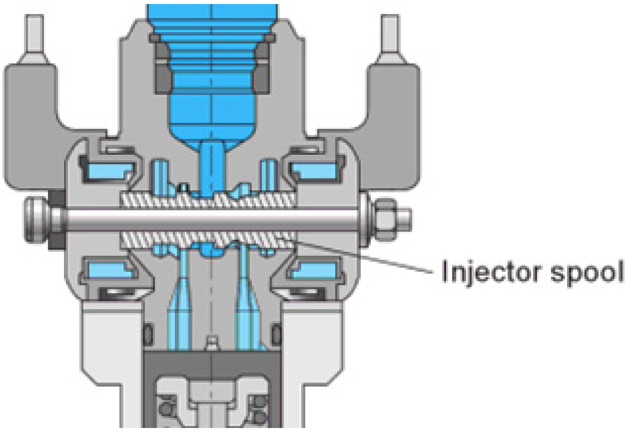

Figure 9-3 Section view of HEUI oil spool, showing the spool valve mechanism [9-15]

In order to simulate the spool valve in Simulink, two similar valves were used for the inlet and outlet respectively. Two hydraulic pipes act as the spool passages. The inlet/outlet line passages are equivalent to cylindrical pipes whose size is 2.56 mm in diameter and 11.8 mm in length. Both passages join into the hydraulic cylinder oil chamber.

The oil supply is modeled as a constant volume chamber with volume 2.89x104 mm3 and high pressure as the initial value. The oil chosen for the injector model is SAE 15W40. The high-pressure forces oil to flow into the spool passages.

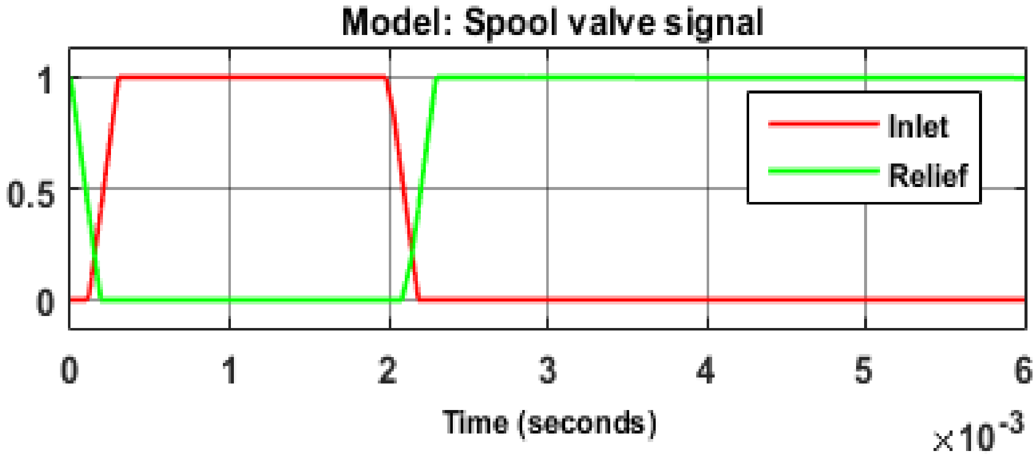

Figure 9-4 Normalized spool valve inlet and return valve signal. “0” means completely closed, and “1” means fully open

The oil spool valve is controlled by the solenoid system. The current pulse energizes the coils which create the magnetic force to move the spool. Once the oil fills the intensifier piston chamber, it starts to push it against the spring. The piston forces the plunger down and starts pressurizing the fuel in the fuel chamber at a rate proportional to the area ratio, the present design being 10x magnification. The high fuel pressure will lift the needle after the needle spring force is overcome and initiate the injection of fuel.

The magnetic force generated in the close coil forces the spool to move to the closed position. The spool valve remains closed when the current pulse e due to the residual magnetism. The oil over the intensified piston is isolated from the high-pressure oil supply. The spool now directs the intensifier piston to vent, and its pressure drops quickly. The intensifier plunger begins returning to the initial position. Fuel pressure decreases until it can no longer lift the needle, whereupon the needle returns and rest on the seat.

9.5.2 Intensifier and plunger system

Intensifier and plunger inside the injector barrel are modeled as a double acting hydraulic cylinder with hard stops. In this subsystem, mass, damper, and spring are all considered for calculating the plunger motion, as well as oil pressure, fuel pressure and spring preload force. The double-acting hydraulic cylinder has the capability to define two different working fluids for two sides of the piston.

The model considers the working fluid compressibility as captured in Eq. 9-4 and 9-5.

Flow rate:

$$q = \frac{d(\frac{\rho}{\rho_l^0} V)}{dt} = \frac{d\left(\frac{\rho}{\rho_l^0}\right)V}{dt} + \left({}^{\rho}/_{\rho_l^o}\right)\varepsilon(v_p)A \tag{9-4}$$

Density:

$$\rho = \frac{\left(\frac{\alpha}{1-\alpha}\right)\rho_g^o + \rho_l^o}{\left(\frac{\alpha}{1-\alpha}\right)\frac{p_O}{p}^{\frac{1}{\gamma}} + e^{\frac{-(p-p_O)}{\beta_l}}} \tag{9-5}$$

Where, α is trapped air, ρ_g^o *and* ρ_l^o are fluid and gas density at atmospheric conditions, γ is specific heat ratio, v_p is the velocity of the intensifier piston, A is the piston area , V is the piston volume, p is the gauge pressure and po is the atmospheric pressure, β_l is bulk modulus, ε (+1 or -1) is orientation constant for piston.

The initial pressure is atmospheric over the intensifier piston and at 8 bar for DME operation (2 bar for diesel) in the fuel chamber. The transitional hard stop restricts the rod motion between the upper bound and the lower bounds. The spring stiffness is 17000 N/m, and the preload deformation is 7.8 x10^{-3} m for the model. The mass of the intensifier plunger system is assumed as 0.06 kg, and the damping of the intensifier system is taken as 5-150 N/ (m/s).

The passage (connecting fuel chamber and needle valve), as shown in Figure 9-2 needle valve section, is considered as a hydraulic pipe 32 mm long and 1.8 mm in diameter. The passage has a one-way check valve (lid valve) opening from the plunger to the needle valve. The lid valve has an orifice (approximately 5% of the valve diameter) allowing for limited two-way flow. The lid valve will prevent the fuel pressure to drop below the feed pressure when the plunger retracts during the closing event. This avoids combustion gases entering the needle sac.

9.5.3 Fuel Pump System

The injector has a fuel supply feed of 0.8 MPa for DME and 0.2 MPa for diesel fuel. In the model the fuel supply line is built as constant supply pressure as shown in Figure 9-2. The fuel supply line is connected to the fuel chamber through a refill check valve. The injector model uses a ball valve with a conical seat for the spill port.

9.5.4 Needle Valve

The needle is supported on a seat by a spring preload force. The injector needle begins to lift when the pressurized fuel force exceeds the preloaded spring force. The needle valve model is built using a ball valve in the conical seat. The needle lift is given by the motion output from a double-acting cylinder with a mass-spring-damper system. Once the needle starts lifting, it opens proportionally to the fuel pressure until it reaches the maximum needle lift. The maximum needle lift is 0.25mm. The area of the needle facing high-pressure fuel is 1.8 mm^2.

The ball valve with a conical seat represents the needle valve. The ROI depends on the fuel pressure and displacement. Eq. 6 is the ball valve seat governing equation. Nozzle flow rate,

$$q = C_D A(h) \sqrt{\frac{2}{\rho}} \frac{p}{(p^2 + p_{cr}^2)^{\frac{1}{4}}} \qquad (9-6)$$

Where, C_D is flow discharge coefficient, $A(h)$ is instantaneous orifice passage area, $h = x_o + x$, x is needle displacement; $p = p_A - p_B$, is pressure difference;

$$p_{cr} = \frac{\rho}{2(Re_{cr} v/(C_D D_H))^2} \qquad (9\text{-}7)$$

The multi-hole injector model is modified from the single-hole injector model. Instead of using one ball valve with a conical seat, eight valves were used in parallel to simulate the MH valve. The schematics for both SH nozzle MH nozzle are shown in Figure 9-5. The SH nozzle is in the vertical direction, but MH nozzles are evenly distributed on the nozzle tip with a cone angle.

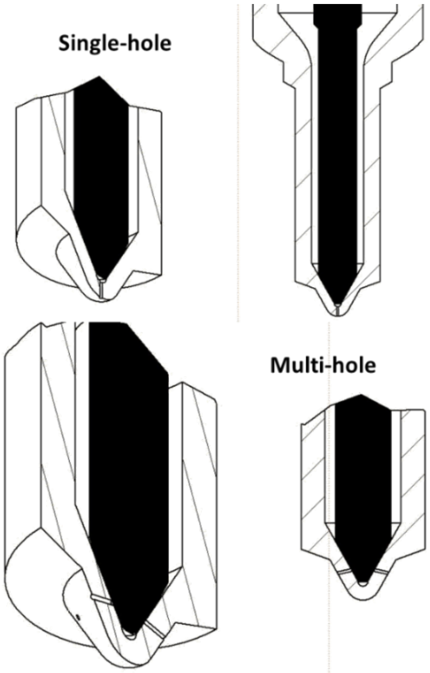

Figure 9-5 Section views of schematic for single-hole nozzle (left) and multi-hole nozzle (right)

9.6 Results and discussions

9.6.1 Multi-hole injector results

Figure 9-6 are results for an 8-hole injector model. It compares diesel and DME in terms of fuel injection parameters at 2000 bar injection pressure. The oil pressure in supply volume initially at 300 bar reduces as the inlet valve opens. The oil pressure drops to 240 bar for DME and 245 bar for diesel. 'P_spool_oil' is the pressure in the oil chamber (over the intensifier piston). Diesel case has higher maximum oil pressure than DME. Nevertheless, the model shows the intensifier piston travels further under DME when compared to diesel case. This is consistent with the maximum fuel pressure achieved, higher for diesel than DME. This is due to DME's higher compressibility. Diesel lifts the needle earlier than DME, due to a faster increase in pressure. Therefore, the fuel injection begins earlier for diesel than DME, which is observed experimentally. The model also shows that the DME fuel has a slower decrease in the fuel chamber pressure, resulting in longer injection duration. The difference in the injection duration between DME and diesel will be reduced at a lower injection pressure. Thus, the total volume of fuel injected is more in DME than diesel.

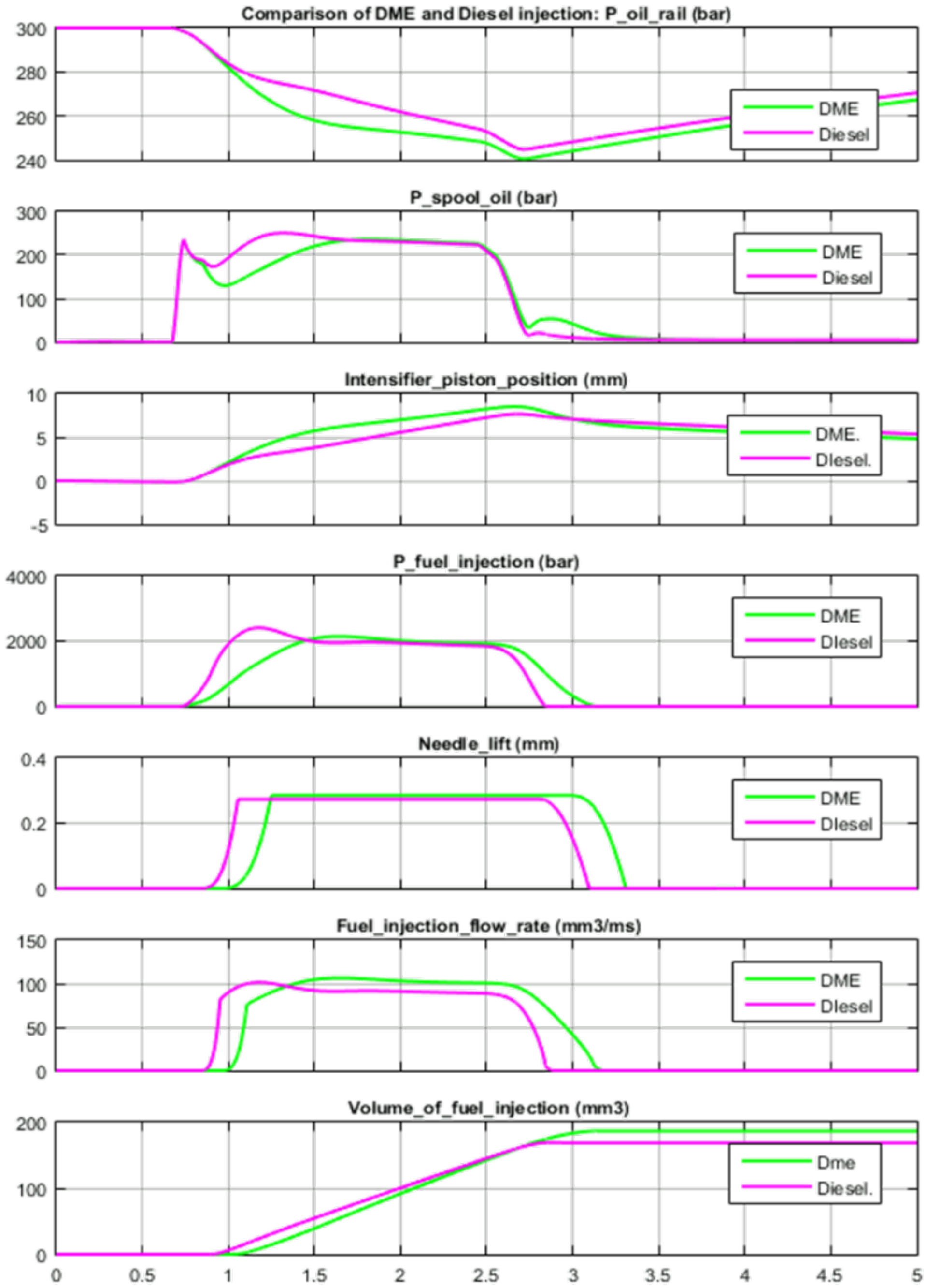

Figure 9-6 Comparison between diesel and DME fuel injection characteristics using injector model: At injection pressure 2000 bar, with oil supply pressure 300 bar, the nozzle is MH 8*155 µm nozzle

The experimental results for ROI of 8-hole injector at different injection pressure (P_{inj} = 750, 1000, 1500, and 2000 bar) are shown in Figure 9-7. The current waveforms of injector coils are also shown on Figure 9-7 indicating an energizing time of 2 ms. At time 0 ms, an open coil signal is sent out. The injections of diesel begin at approximately 1.2, 1.0, 0.9, and 0.8 ms for 750, 1000, 1500, and 2000 bar respectively. However, the injections of DME come out with an additional delay, compared to diesel at the same injection pressure. The delay is reduced as the injection pressure increases. The injections are all ended at around 3 ms, regardless of injection pressure, due to the high flow rate of MH nozzle. But DME's end of injection is 0.2 ms later than diesel, owing to its compressibility. The ROI reaches a steady state under certain injection pressure after the rising rate. Diesel has a relatively large portion of the plateau, indicating a longer duration. Even though the DME has an overall shorter injection duration than diesel, it has a higher flow rate magnitude at the same injection pressure.

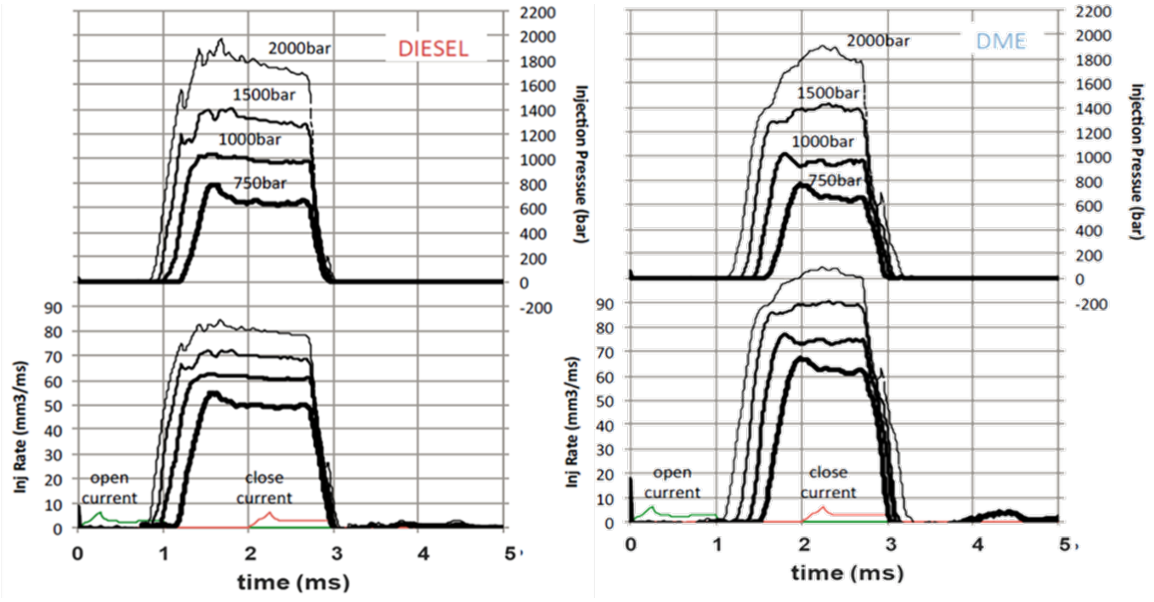

Figure 9-7 Experimental results of ROI and current waveform for 8x155 µm MH injector, at different injection pressure (750, 1000, 1500, and 2000 bar): diesel (top) and DME (bottom)

Figure 9-8 shows the simulation result of the MH injector. The simulation results are fairly matched with experimental data, in terms of injection delay, injection duration, and ROI magnitude. High injection pressure results in short injection delay and high ROI. DME's longer injection delay is well captured by the model. The ROI profiles all show an initial peak and become stable, and then decrease at the same time.

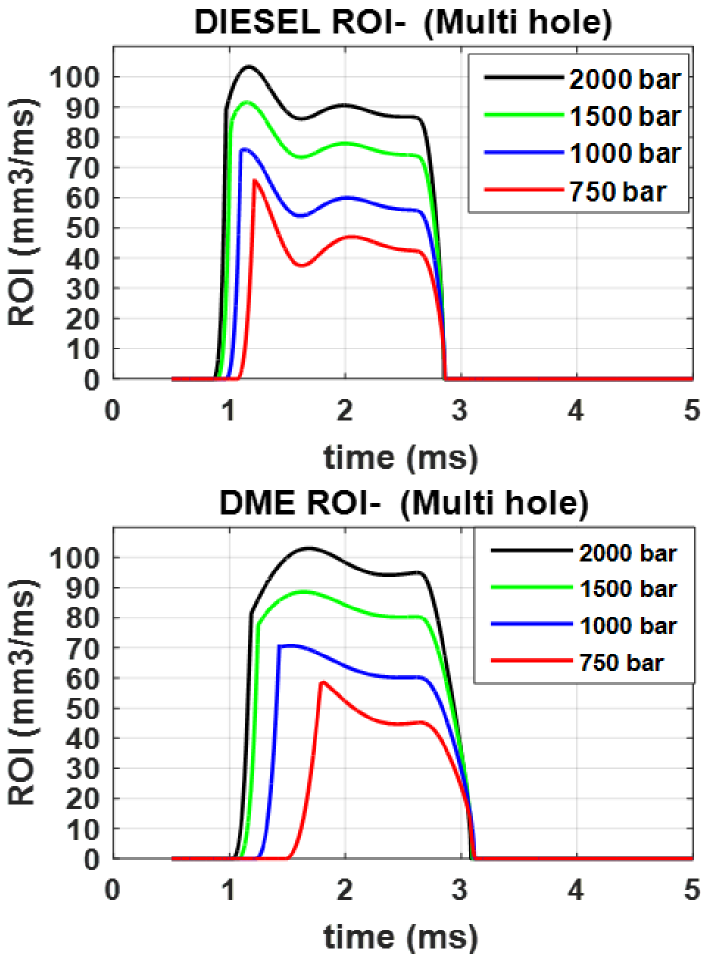

Figure 9-8 Injector model simulation results of ROI for 8x155 µm MH injector, at different injection pressure (750, 1000, 1500, and 2000 bar): diesel (top) and DME (bottom)

The effect of injection pressure on the total injected fuel volume per stroke of plunger is shown in Figure 9-9. DME shows higher injected quantity than diesel at higher injection pressure. The injection pressure tests extended to 2300 bar. At low injection pressure, DME has a lower volumetric flow rate than diesel, due to DME's higher compressibility. But when injection pressure becomes higher than 1000 bar, DME starts showing a higher volumetric flow rate, due to its lower viscosity or flow resistance of DME. This trend too is captured by the model.

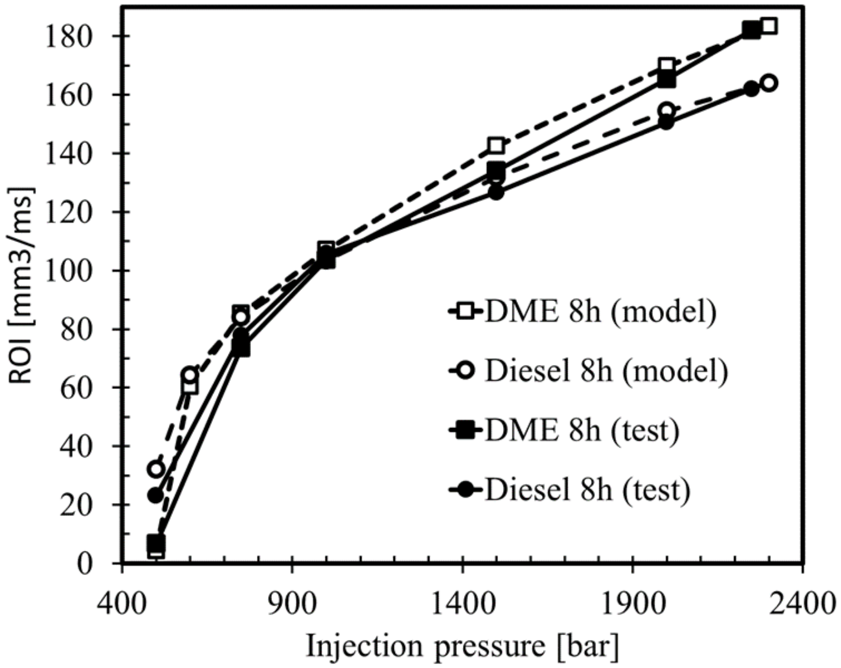

Figure 9-9 Effect of injection pressure on the injected fuel volume per stroke, comparing test results and injector model results

9.6.2 Single-hole injector results

SH injector was made for research studies in the combustion vessel. Spray and combustion tests have been done with SH injectors. The injector model simulation results are obtained at different fuel injection pressures to compare the effect of fuel characteristics (DME vs. Diesel). The simulation is done at the same oil supply pressure and the same injection command.

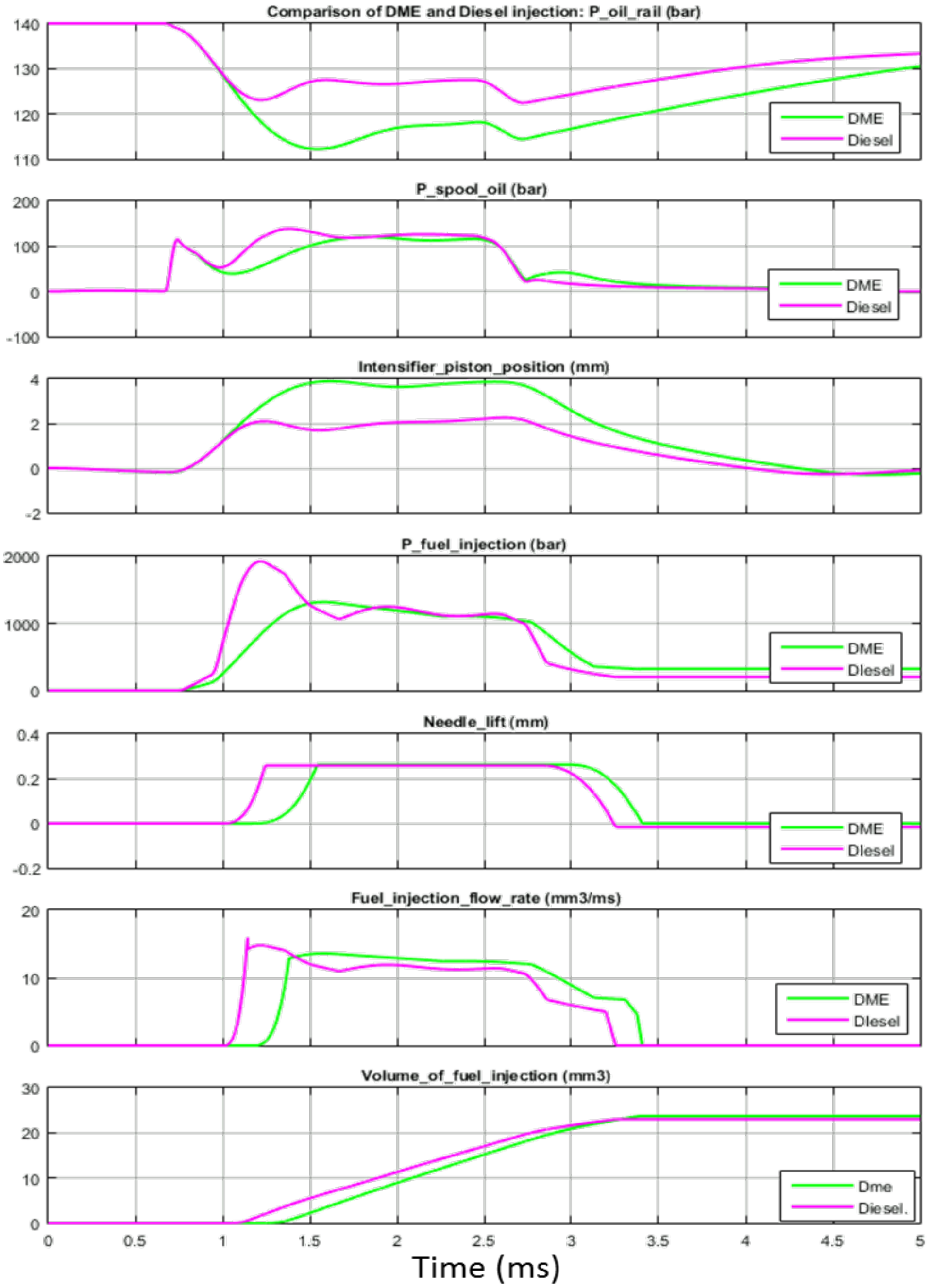

Figure 9-10 Comparison between diesel and DME fuel injection parameter characteristics using injector model: At injection pressure 1098 bar, with oil supply pressure 140 bar, and nozzle size is 180 µm

Figure 9-10 shows an example of the simulation results for a SH 180 μm nozzle injector model at 1098 bar injection pressure. The oil supply pressure from the constant volume in both DME and diesel falls as the control signal opens the inlet valve. The oil pressure drops to 115 bar in DME and 125 bar in diesel case. As in the MH case studies, the SH injector results also show the fuel effect such that DME's higher compressibility results in larger intensifier-plunger motion, taking more time than diesel to compress fuel in the fuel chamber to reach the needle lifting pressure. The needle lifting pressure for DME equals 133. 5 bar, which is large enough to provide the force to overcome needle spring preload. Therefore, in the diesel case, the fuel pressure and needle lift increase earlier and faster than that in DME case.

The diesel fuel chamber is pressurized to higher maximum pressure than DME. The DME fuel shows a slower fall in fuel chamber pressure and plunger position retreats slowly. This results in longer injection duration for DME and more volume injected than diesel fuel.

Figure 9-11 shows the comparison between experimental data and simulation results for the SH injector model at different injection pressures. Different from the MH case, the SH ROI profiles show a two-stages form. The most significant difference between the SH and the MH cases is that the MH nozzle has more total needle passage area, which allows a higher injection flow rate. Assuming the same fuel chamber, the faster the fuel exiting the chamber, the lesser the time needed for chamber pressure to drop to the supply pressure level. After the closing coil acts, the upstream pressure drops, but the high pressure is still kept in the fuel chamber due to the lid check valve. The fuel pressure will continue decreasing before the nozzle closes. The stage between closing coil action and end of injection is called the “second stage”. In this stage, the needle drops gradually and compresses the fuel chamber.

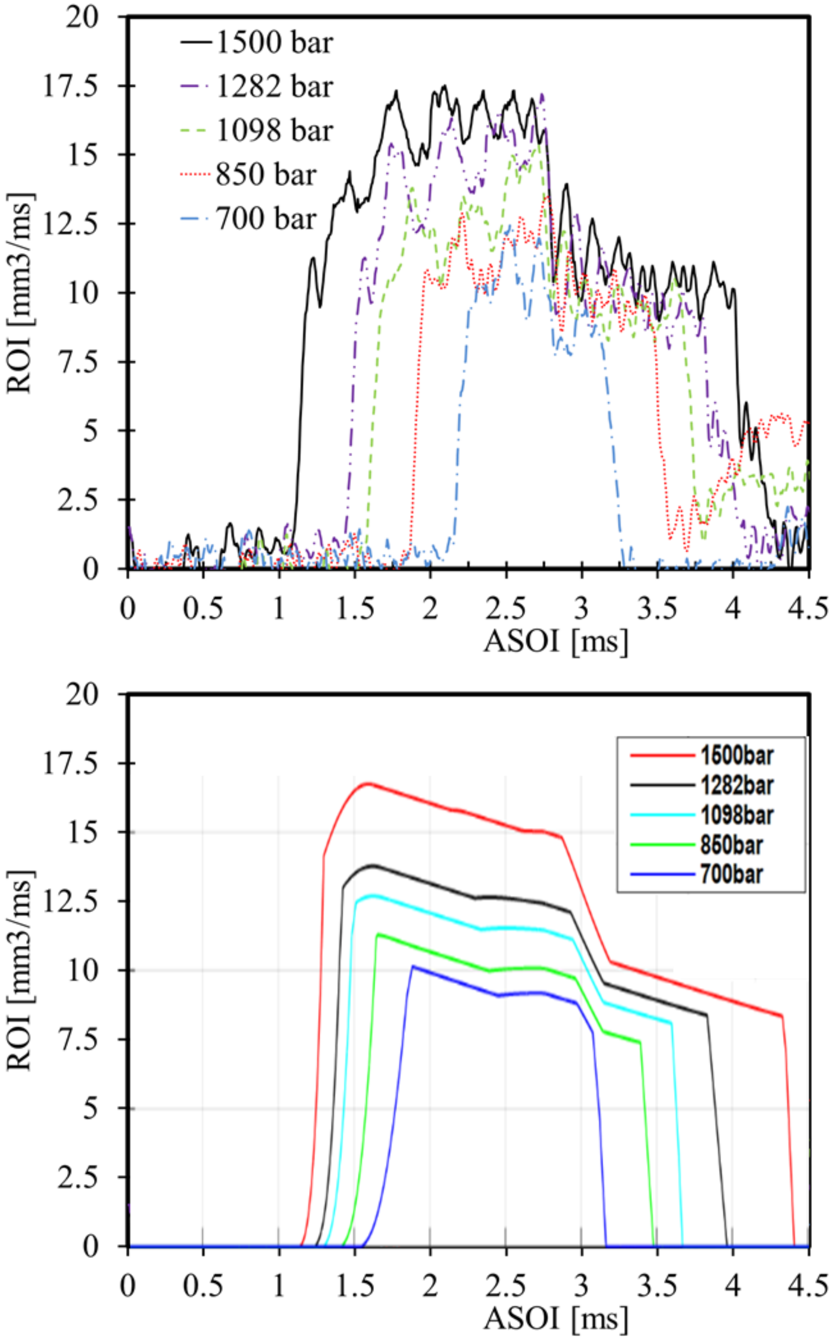

Figure 9-11 Comparison of ROI for DME at different injection pressures, and nozzle size diameter is 180 µm: experiments (top) and model (bottom)

From the experimental data, several observations are found. Higher injection pressure leads to shorter injection delays and longer injection duration. At the first stage, with varied injection pressures, the magnitudes of ROI are changed. Higher pressure always means higher magnitude. The injection pressure difference of about 200 bar generates 1 mm3/ms ROI difference. Stage one ends at the same time (around 2.8 ms). For different injection pressures, the second stage ROI curves have a similar height. The ROI profiles for different pressures have a similar shapes.

The simulation results shown in Figure 9-11 match relatively well with experimental data. Figure 9-12 gives one such comparison. The injection duration of the 1500 bar case is 3.3 ms (starts at 1.1 ms and ends at 4.4 ms). The first stage magnitudes for both simulated data and experimental data are around 16 mm^3/ms. The stage changing happens at 2.8 ms. The second stage magnitude is around 10 mm^3/ms. The simulated result has a sharper closing.

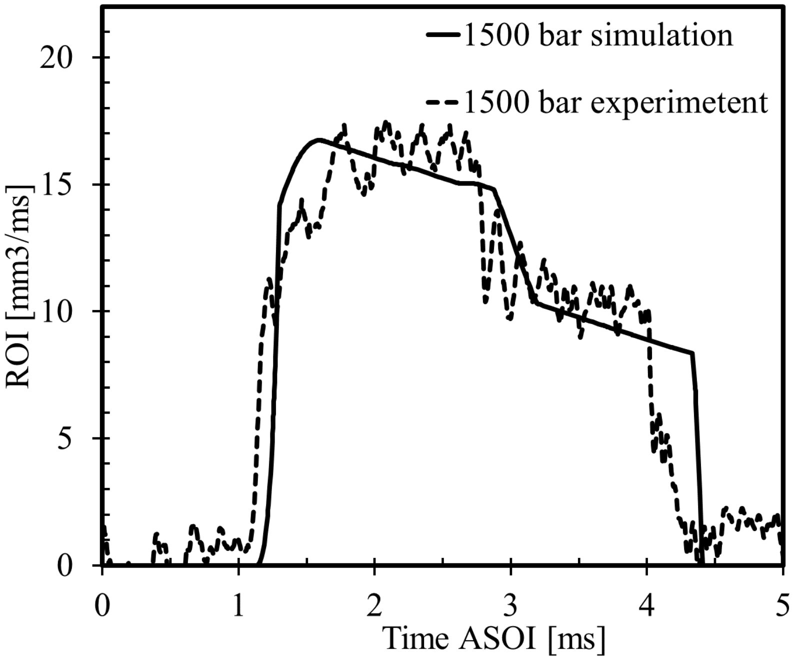

Figure 9-12 Comparison between experimental ROI profile and simulation ROI profile at 1500 bar injection pressure, and nozzle size is 180 µm

9.6.3 Comparison of ROI between diesel and DME

Figure 9-13 shows the ROI profiles of DME and diesel at different injection pressures, respectively. The ROI is presented in volumetric based (mm3/ms). In this test, the energizing time of HEUI is kept 2 ms for all the conditions. For this specific HEUI, there is a hydraulic delay which is the time between the injection command and the actual onset of the injection. This delay is longer than conventional diesel common rail injectors. Regardless of injection pressure, diesel injections have similar hydraulic injection delays, showing around 1.1 ms. However, the hydraulic delays of DME decrease from 2.2 ms to 1.4 ms when injection pressure changes from 700 bar to 1282 bar. The ROI profile shows a two-stage shape. The first stage is relatively higher than the second stage.

For both diesel and DME, there is a drop in ROI around 2.8 ms, which is corresponding to the spool valve closing. The injection still tends to sustain for a short period of time after the spool valve closes. The time between the spool valve closing and the end of injection is defined as the closing period. Higher injection pressures show alonger closing period. However, at the same injection pressure, diesel has a shorter closing period than DME. When the spool valve closes, the pressure in the injector body should be released. However, DME has higher compressibility (e.g. inverse of the modulus of elasticity) than diesel (2x) and thus its pressure release process takes a longer time.

The overall injection duration of DME is more sensitive to the injection pressure change than diesel’s. At low injection pressure, DME has a shorter actual injection duration. Only at high injection pressure (1282 bar in this test), DME has a similar injection duration with diesel. At the same injection pressure, DME has a higher ROI than diesel due to the lower viscosity. However, DME has a lower liquid density. This compensates for the total injected mass. To match the total injected energy content, high injection pressure needs to be applied to deliver more mass when compared to Diesel.

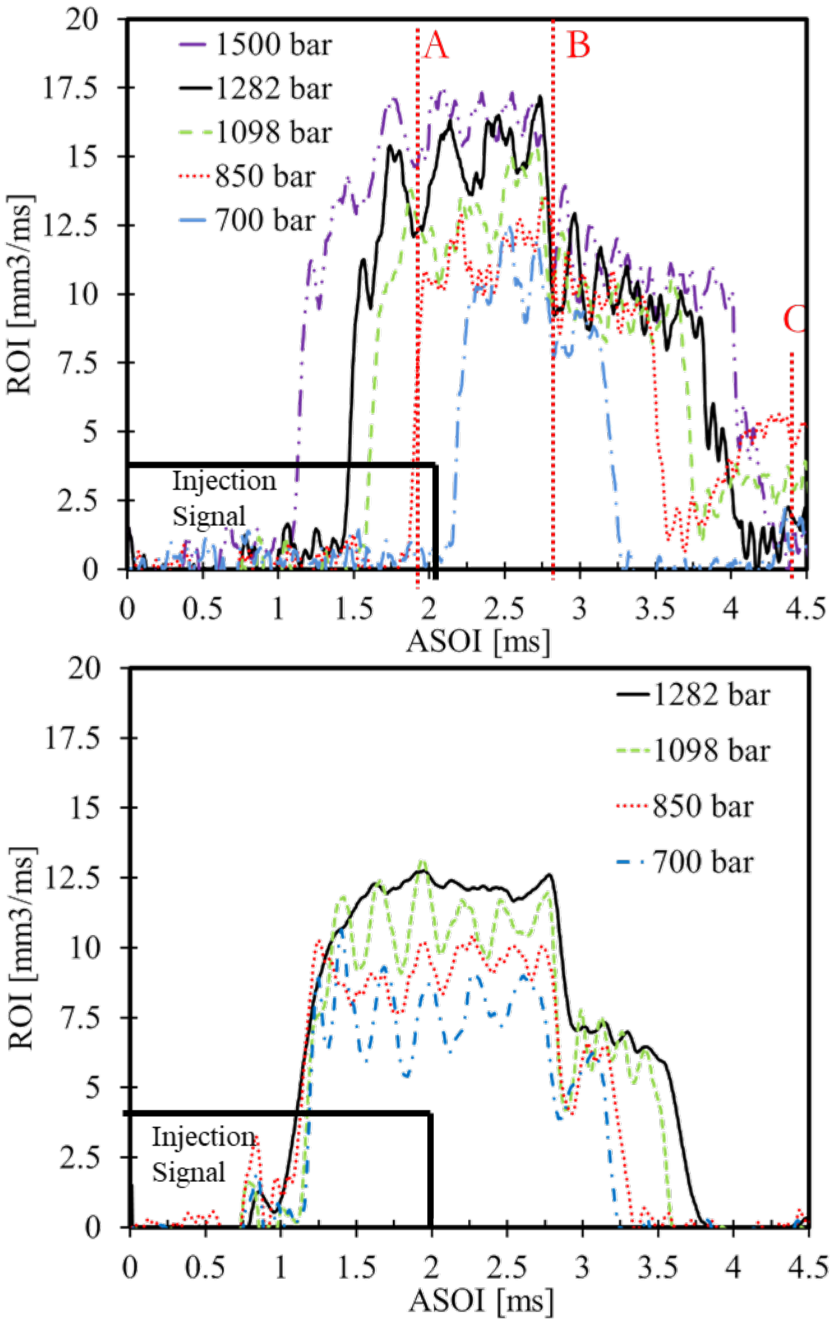

Figure 9-13 ROI profiles of DME and Diesel at different injection pressures (180 µm nozzle, 2 ms injection duration)

Figure 9-14 shows the total injected mass of diesel and DME at different injection pressures. Overall, diesel has a higher total injected mass than DME within the injection pressure range of 700 bar to 1282 bar. Both fuels showed a monotonically increasing trend but with a different increasing rate when injection pressure increases. The total injected mass of DME increased faster with increased injection pressure than that of diesel. This trend implied the high injection can mitigate the differences in energy content (DME compared with diesel) mainly introduced by the low heating value of DME.

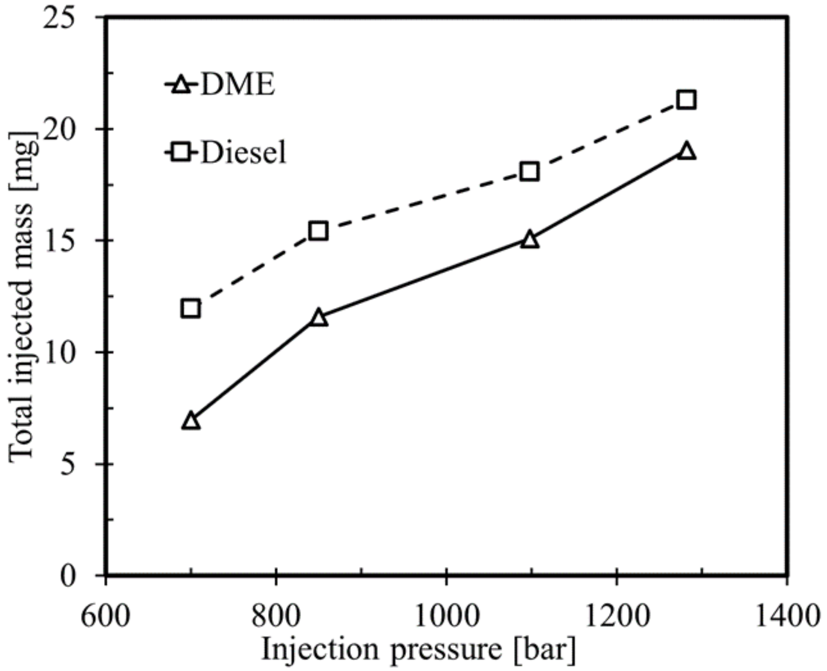

Figure 9-14 The total injected mass of DME at different injection pressures

Mainly due to the compressibility difference at a given injection pressure, DME has longer injection delay than diesel. However, DME's flash boiling and faster evaporation characteristics will improve the atomization process, leading to fast ignition, although this needs to be carefully assessed in the conditions of the combustion chamber as pressures tend to be rather elevated. Another issue of applying DME on the compression-ignition (CI) engine is that the energy density and liquid density of DME are both lower than diesel. Assuming there is an MH 8*155 μm, and its injection pressure is 2000 bar, Multi-hole injector model shows that the total volume per injection is 183.4 mm^3 and 164.1 mm^3 for the DME and the diesel respectively. Diesel of volume 164.1 mm^3 contains 5795.6 J energy (based on lower heating value), which needs 305. 63 mm^3 DME to provide the same amount of energy, regardless of the conversion efficiency. In order to achieve the same amount of energy input comparable to diesel, it needs either more than 4500 bar injection pressure, or upsize the nozzle to 230 μm without changing injection pressure. The extreme high injection pressure is not practical in industrial application, for now, so the application of DME on CI engine needs to focus on how to increase injected volume by enlarging the flow nozzles while maintaining high pressures to enhance the charge air and fuel mixing that is critical for high thermal efficiency.

9.7 Concluding remarks

A 1-D MATLAB/Simulink single-hole/multi-hole injector model has been built and validated against experimental data. Bosch type ROI measurement tests (SH/MH, diesel/DME, varied injection pressures) are performed to provide data for model validation. The validated model is used to predict the ROI profile of SH 180 μm injector at 1500 bar injection pressure. Properties of DME and diesel are compared and investigated in order to provide the basis for future work to optimize a DME injection system in CI engine.

It is found from both experimental and simulation results that higher injection pressure leads to longer injection and shorter injection delay. For SH injector used for dedicated combustion studies and a constant volume chamber, the ROI profiles show a two-stages shape, with the 1st stage ending at the same time. In the 2nd stage, ROIs for different injection pressures all hold the same magnitude. Comparing DME and diesel ROI for the same condition, it is shown that the injection of DME responds slowly and sustains longer than diesel, due to high compressibility.

The MH injector results show that the compressibility effect dominates at low pressure (below 1000 bar injection pressure), but flow resistance has more impact on the high injection pressure side. Therefore, at low injection pressure, diesel has more injected volume than DME, but it is opposite on high injection pressure. The large flow rate in the MH injector shortens the needle closing process dramatically, and the 2nd stage of the SH injector does not occur.

DME results in higher injected total volume (approximately 12 %) at same pressure and duration when tested and simulated with the same nozzle as diesel; however, due to lesser energy content in the DME (approximately 33 %), nozzle size needs to be increased to get injection duration equivalent at the same pressure.

10 Experimental investigation on DME combustion: single-hole injector results

10.1 Introduction

In this chapter, we experimentally explored the injection pressure impact on DME's ignition and combustion processes in a constant volume combustion vessel (CV) under engine-like conditions, using an SH HEUI injector. A wide range of injection pressures from 500 bar to 1500 bar were tested. The effect of varied ambient conditions, such as ambient temperature, pressure, oxygen levels, were also investigated. Down the road, the spray and combustion characteristics of DME were compared with diesel in terms of ROI, penetrations, ID, and AHRR, etc. Due to the fact that only limited tests were performed for diesel combustion, the comparisons of diesel vs DME were made whenever it is possible.

In the current study, the liquid and vapor regions of DME jet were visualized using a hybrid Schlieren/Mie scattering for the non-reacting conditions. DME is also injected into a hot ambient for the combusting conditions. In this case, the high-speed natural flame luminosity was used to capture the flame intensity, and PLIF imaging was used to characterize CH_2O evolution. A high-resolution microscopic imaging technique was also used to investigate near nozzle spray dynamics. Comparison of low and high injection pressures was made in terms of ROI, liquid/vapor penetration, initial jet development, ignition delay, flame LOL, flame structure, and formaldehyde (CH_2O) formation. Liquid penetration was found to be insensitive to injection pressures whereas vapor penetration tends to increase with injection pressures at first and has a decreasing trend. The high-pressure injection has shorter injection and ignition delays, longer injection duration and longer LOL, etc.

10.2 High-speed images and analysis

HS imaging includes Mie scattering, schlieren, and hybrid imaging. By analyzing these images under non-vaporizing and vaporing conditions, we can obtain liquid and vapor penetration. A Matlab program was written to process these images. Figure 10-1 shows the Mie scattering image comparison between diesel and DME with 1500bar injection pressure at 1.3 ms after the start of injection. The DME and diesel testing used the same injection duration (energizing time). Diesel penetrates further than DME at the same time. It could be due to the fact DME vaporizes partially when injected. From the HS images, DME has longer injection delay than diesel and also ends injection earlier, which is due to its larger compressibility.

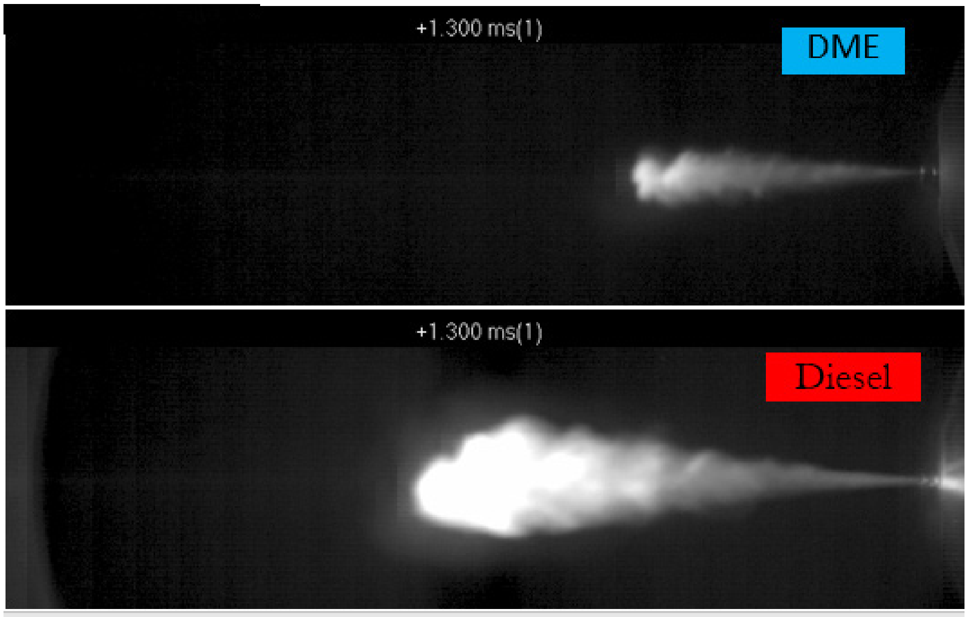

Figure 10-1 Mie scattering image comparison between diesel and DME with 1500bar injection pressure at 1.3 ms after start of injection

10.2.1 Non-vaporing spray

Non-vaporing condition in this paper refers to the 383 K N2 ambient surrounding, 14.8 kg/m3 ambient density with, 234 psi ambient pressure. It is called non-vaporing because diesel usually has no vaporization under this ambient temperature. However, at the temperature of 383 K, the vapor pressure of DME is 3948 kPa (572.6 psi) which is much larger than the test ambient pressure, so DME evaporates easily.

A typical diesel fuel atomization process can be divided into 4 sub-processes including primary break-up, secondary break-up, the coalescence of droplets, and evaporation. The breakup starts immediately after the fuel exiting nozzle, and it is very complex involved with many physical fluid mechanic processes. During the primary break-up, liquid fuel core exiting near nozzle orifice is segregated into a relatively large structure called ligaments and further produces first generation droplets. This is caused by: (1) the aerodynamics instabilities between liquid and surrounding gases; (2) turbulence as high velocity flowing through a small orifice with different levels of radial velocities; and (3) cavitation within nozzle orifice.

High-speed (HS) diesel spray Schlieren images with a frame rate of 40,000 fps are shown in Fig. 6 (top). The images are shown in a time-elapsed manner from 0 ms to 0.8 ms after the start of injection (ASOI) with a time interval of 0.1 ms. One image at ASOI 1.7 ms is also shown, and the spray has already well developed and reaches a steady state. After the start of injection, the spray leaves the nozzle orifice, propagates against the ambient pressure, and expands laterally. More liquid diesel enters the chamber and propagates along the axis direction. The liquid diesel keeps flowing in and pushes the DME which is already in the chamber forward. The spray near the spray orifice can maintain a relative constant spray angle. However, the strong mixing between liquid and surrounding gas destroys the angle in the leading side of the spray and forms a wavy liquid/gas interface. On the interface, some small vortexes are generated and folded backward due to the shear force. The spray core is very dense. Droplets can only be recognized in the mixing region. The last image shows the spray long after the end of the injection, so the droplets are easy to capture now.

Figure 10-2 (bottom) shows the DME spray at the exact same conditions with diesel spray. DME spray shows similar penetration behavior but with a very low penetration velocity. As it is shown in Figure 10-2, DME spray tip penetration is always shorter than diesel case which is at the same ASOI. On the outer edge of the spray, there is some transparent wavy disturbance, which indicates the evaporation of DME. Due to the fact of fast evaporation of DME, evaporation happens within a 20 mm distance from the nozzle orifice. This fast evaporation changed the lateral expansion and led to a slightly larger (about 1 degree) spray angle compared to diesel. The spray angle is only considering within a 60% penetration location. Another difference is the DME spray presents no droplets, which is more obvious in ASOI 4.7 ms images.

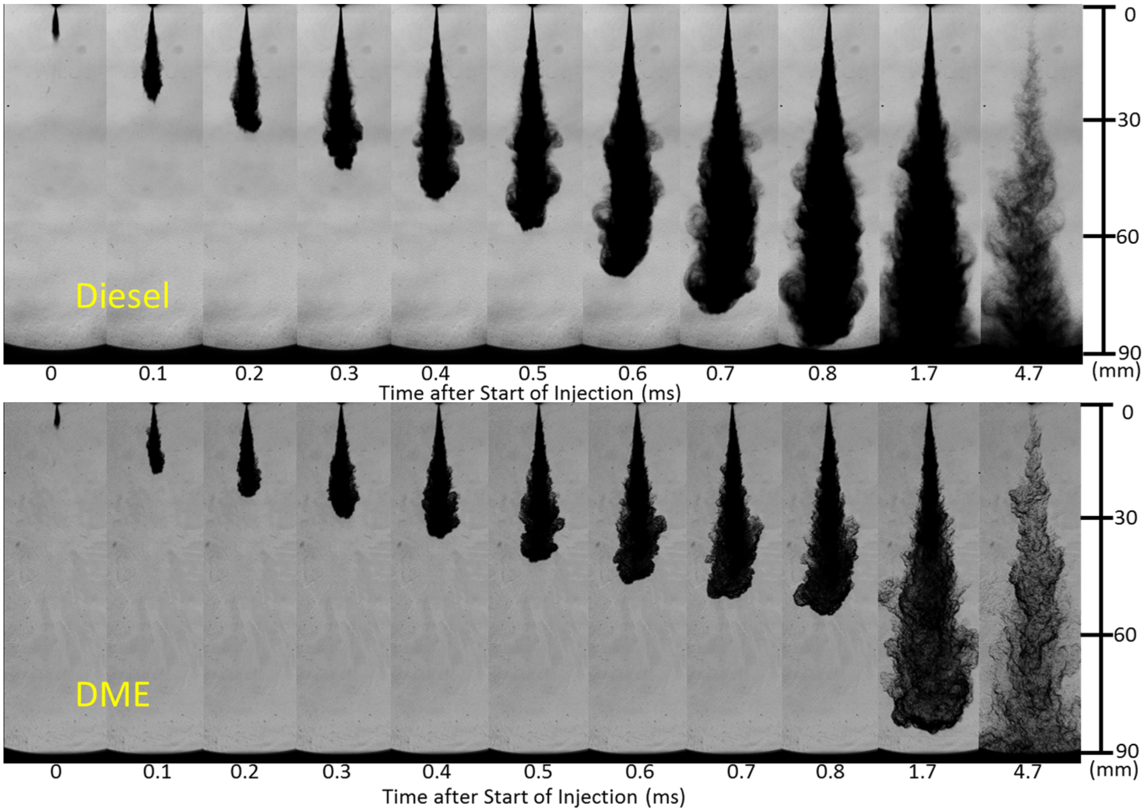

Figure 10-2 Non-vaporizing diesel and DME spray (Inj P= 1500 bar, Ambient= 383K, 14.8kg/m^3, D= 180μm)

The microscopic observation of DME injection was also made at the near nozzle location (0 ~ 6.5 mm from the nozzle) are shown in Figure 10-3. These images are taken with a frame rate of 40, 000 fps. Low and high injection pressures (500 bar and 1500 bar) are compared in three different ambient density conditions (1/14.8/25 kg/m3) at 383 K. The first image of each condition is the start of injection (SOI).

The higher ambient densities delay the injection. From 1 kg/m3 to 14.8 kg/m3 then to 25 kg/m3, the injection delay of 500 bar condition increased 0.1 ms and 0.05 ms respectively, and that of 1500 bar increased 0.025 ms and 0.25 ms. Comparing injection timing, 500 bar case has about 0.7 ms longer injection delay than 1500 bar case. After the SOI, liquid DME enters the chamber and propagates along the axis direction. The liquid DME keeps flowing in and pushes the DME which is already in the chamber forward. The spray penetration has a trend of decreasing with ambient density. However, the 1 kg/m3 cases showed a shorter penetration than 14.8 kg/m3 cases at the same after the start of injection (ASOI), due to the spray plume head folding backward caused by shear. The 1 kg/m3 images indicate a strong mixing happening on the boundary of the spray between DME and air. Vortexes are generated from the shear force.

This is a low-temperature nitrogen ambient condition. However, in the images of 14.8 and 25 kg/m3 and 1500 bar, there are some transparent areas at the interface of fuel and air. The transparent part is DME vapor, due to the flash boiling effect. 1 kg/m3 didn't show the transparent region within 6.5 mm to the nozzle. The edge of the spray showed wavy disturbance but not droplets. DME has very high vapor pressure, low surface tension, and high weber number [10-1]. It is reported the evaporation is too fast, and there is no time for a secondary breakup to happen.

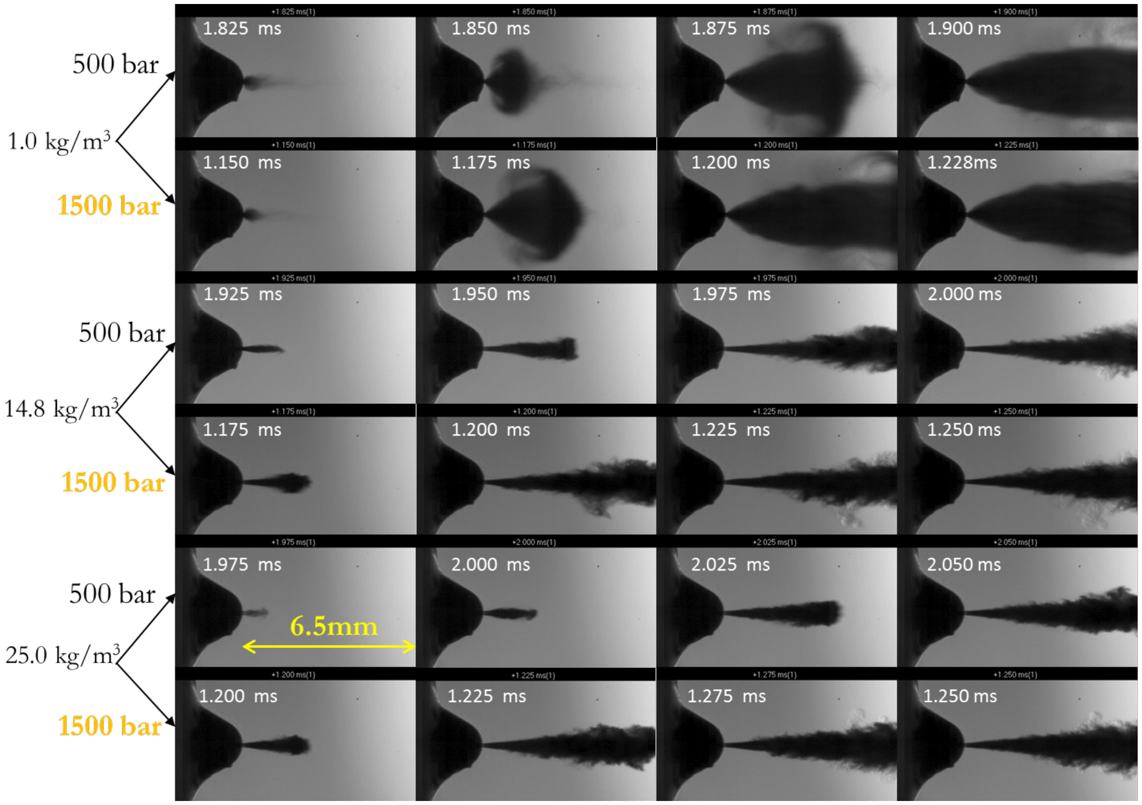

Figure 10-3 Microscopic imaging for near nozzle spray characteristics

10.2.2 Vaporing spray

Figure 10-4 shows the Diesel and DME spray under vaporizing condition which is 900 k ambient temperature. The Schlieren images on the top row show the vapor penetration. The liquid core in Schlieren imaging has very low intensity. The Mie scattering images are shown on the bottom row, indicating liquid penetration. The spray penetration length is the distance that the spray tip traveled away from the nozzle outlet in the axial direction. The liquid penetrations and vapor penetrations of diesel and DME are summarized in Figure 10-5. The overall spray shape of DME and diesel is similar. The vapor penetration increases until it reaches the wall of the vessel. Vapor penetration length increases initially and reaches a constant peak value until the end of the injection. However, diesel spray shows a higher vapor penetration due to high momentum. The momentum difference comes from diesel's higher liquid fuel density. Diesel spray also has a longer liquid length (about 40 mm) than the DME's (about 18 mm). The short liquid length of DME mainly because DME evaporates faster than diesel, is also matching with the 13.29 mm calculated breakup length.

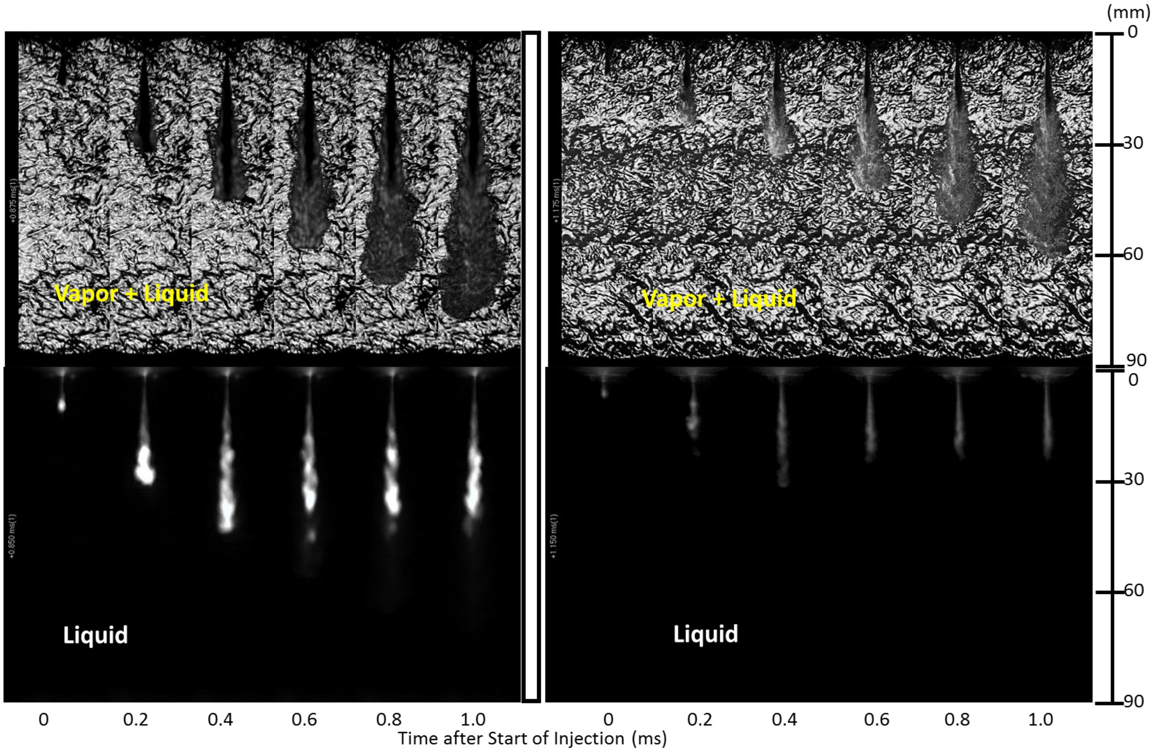

Figure 10-4 Diesel and DME sprays under vaporizing condition (Inj P = 1500 bar, Ambient= 900 K, 14.8 kg/m^3, D= 180 μm)

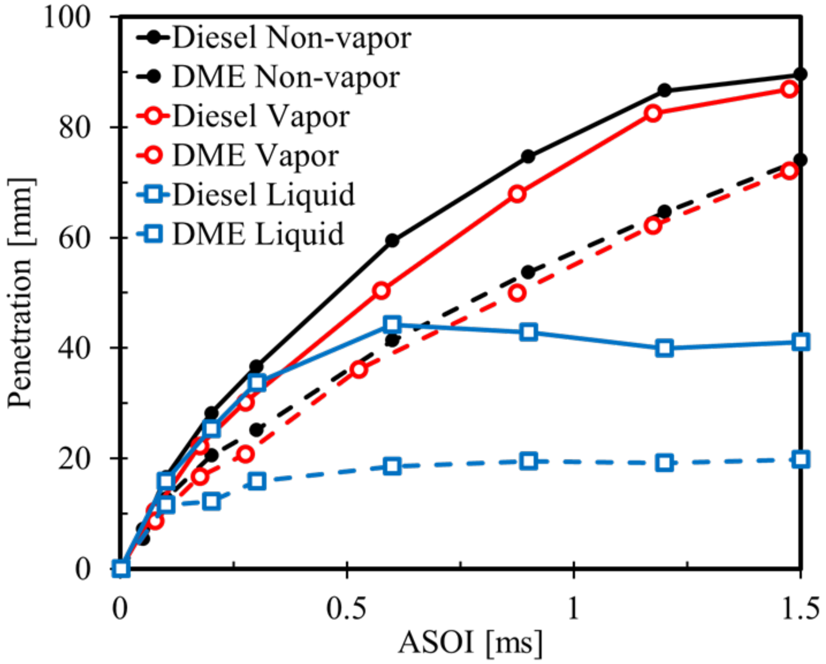

Figure 10-5 Liquid and vapor penetration of diesel and DME spray

Figure 10-6 shows the Liquid penetration and vapor penetration of DME spray under vaporizing conditions. The spray penetration length is the distance that the spray tip traveled away from the nozzle outlet in the axial direction. 1500 bar injection pressure shows a higher vapor penetration due to high momentum, but a shorter liquid length which seems to follow the Levich breakup length [10-2]:

$$L_{brk} = C_l d_{noz} \sqrt{\frac{\rho_l}{\rho_a}} \qquad (10-1)$$

Where ρ_l is liquid density, ρ_a is air density, d_noz is effective diameter of the injector nozzle, and C_l is Levich constant. DME liquid is compressible, so its liquid density is increased with injection pressure. The Levich breakup length should increase while injection pressure increases. The actual breakup length’s decrease may be due to the cavitation in the nozzle and the enhanced air-mixing driven fast-evaporation. Kapus and Ofner [10-3] reported the high-pressure drop between the inlet and the outlet of the nozzle orifice, helps the gas bubbles emerging from cavitation locations (mainly at the inlet edges of the contraction) and mixed with liquid to form a gas-liquid two-phase flow. Ikeda et al. [10-4] defined a cavitation factor (number) which is the pressure drop between inlet pressure and vapor pressure and concluded that the maximum injected mass has a dependence on the cavitation factor. The cavitation actually decreases the effective area of the nozzle. Fast evaporation may happen earlier than the secondary breakup, so the liquid length stays relatively constant for different injection pressures.

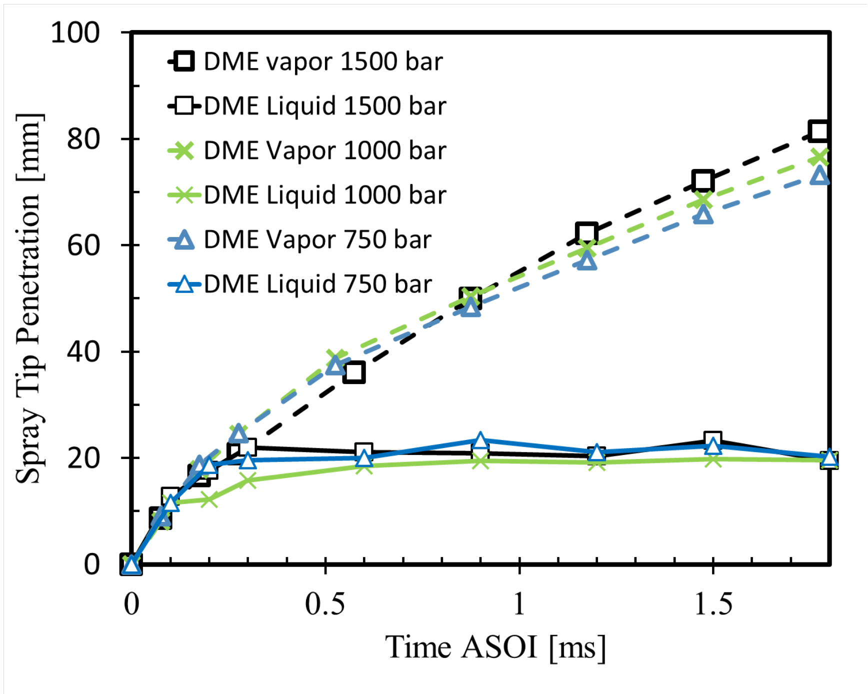

Figure 10-6 Liquid penetration and vapor penetration of DME spray under vaporizing condition (0%O2, 900 K, 14.8kg/m3)

The ambient temperature effect of DME spray and combustion is shown in Figure 10-7. The test condition is as following: ambient density is 14.8 kg/m^3; injection pressure is 1500 bar; nozzle size is 180 μm; injection duration is 2.0 ms. From left to right, there are Mie scattering images (liquid portion), schlieren images (vapor portion), and Luminosity images (flame). From top to bottom, the ambient temperature varies from 750 K to 900 K, then to 1100 K. Mie scattering image and Schlieren under the same ambient temperature come from Hybrid setup, which means Schlieren image always has 25 μs delay than corresponding Mie scattering image. There is an insignificant difference in SOI. Higher ambient temperature (900 K and 1100 K) shortens liquid penetration length but has a negligible effect on vapor penetration. The increase of ambient temperature (900 and 1100 K) results in shorter ignition delay and increases the intensity of the luminosity. At the time shown in Figure 10-7 (ASOI = 2.68 ms), the 750 K case still doesn't have ignition. The decrease in ambient temperature (750 K) increases the possibility of backward flame. Ignition happens near the CV window opposite to injector location and propagates towards the injector tip.

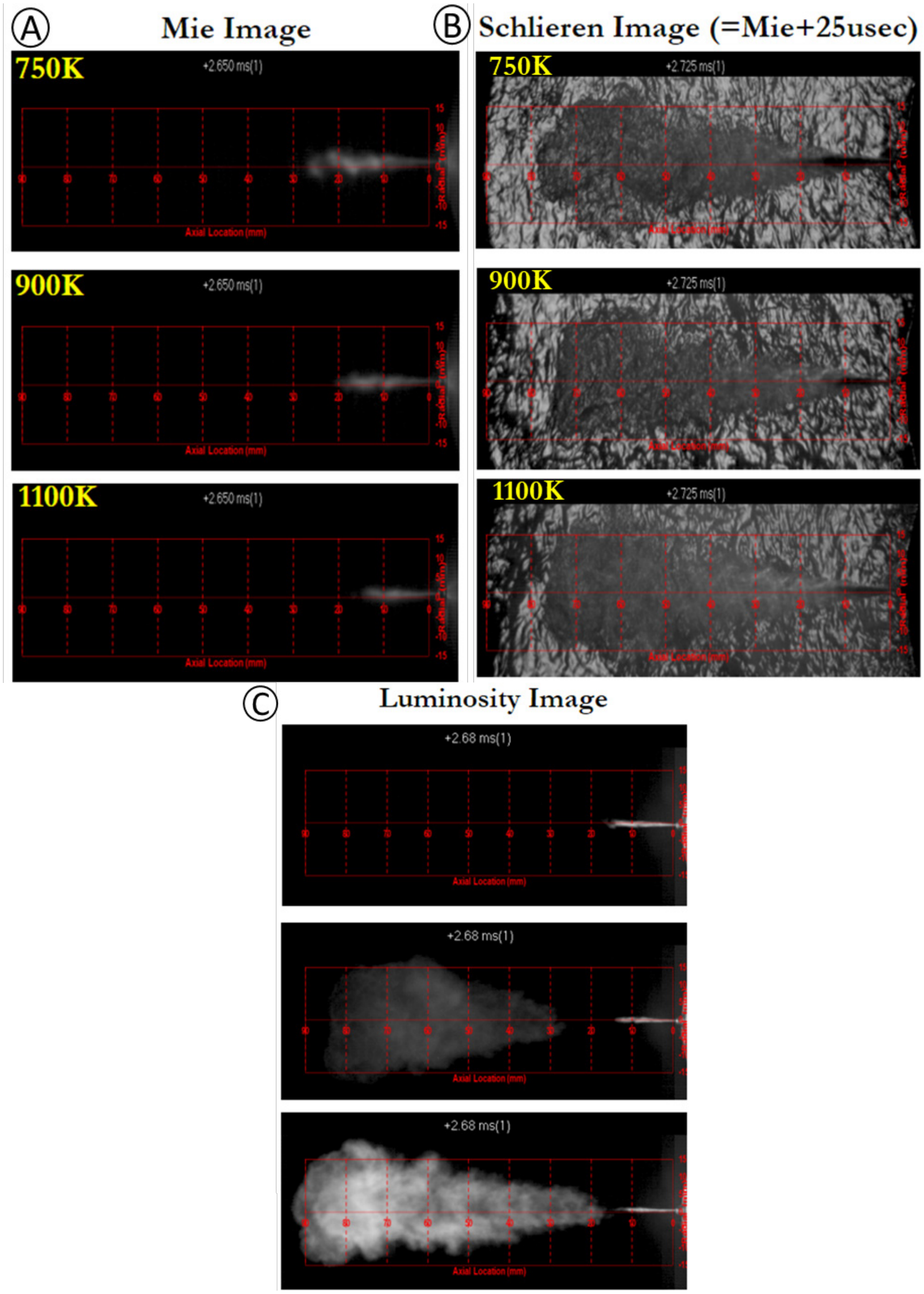

Figure 10-7 The effect of ambient temperature, images at ASOI= 2.68 ms (A)Mie scattering, (B)schlieren, (C) luminosity imaging

The liquid and vapor penetration length profiles are valuable information for the validation of spray simulation. Figure 10-8 is the comparison of liquid (solid line) and vapor (dash line) penetration profile between diesel and DME. Vapor penetration profiles have similar trends at different ambient temperature because the vapor penetration is dominated by the momentum. The higher ambient temperature introduces fast vaporization that leads to earlier air mixing and thicker air mixing zone. This mainly affects the peripheral boundary of the spray; however, the spray tip penetration won't be disrupted. Unlike vapor penetration, liquid penetration length has a negative correlation with ambient temperature, due to the faster evaporation. The ROI is a constant, the evaporation rate is increased due to the high ambient temperature. The quasi-steady location of the liquid tip is pushed toward the nozzle direction. The Figure also shows diesel results. It is found that even at the same ambient temperature, diesel has both longer vapor and liquid penetration length. For DME, there are two other solid lines which are the flame front locations in the reacting condition (known as flame height). Higher ambient temperature (1100 K) benefits the flame propagation.

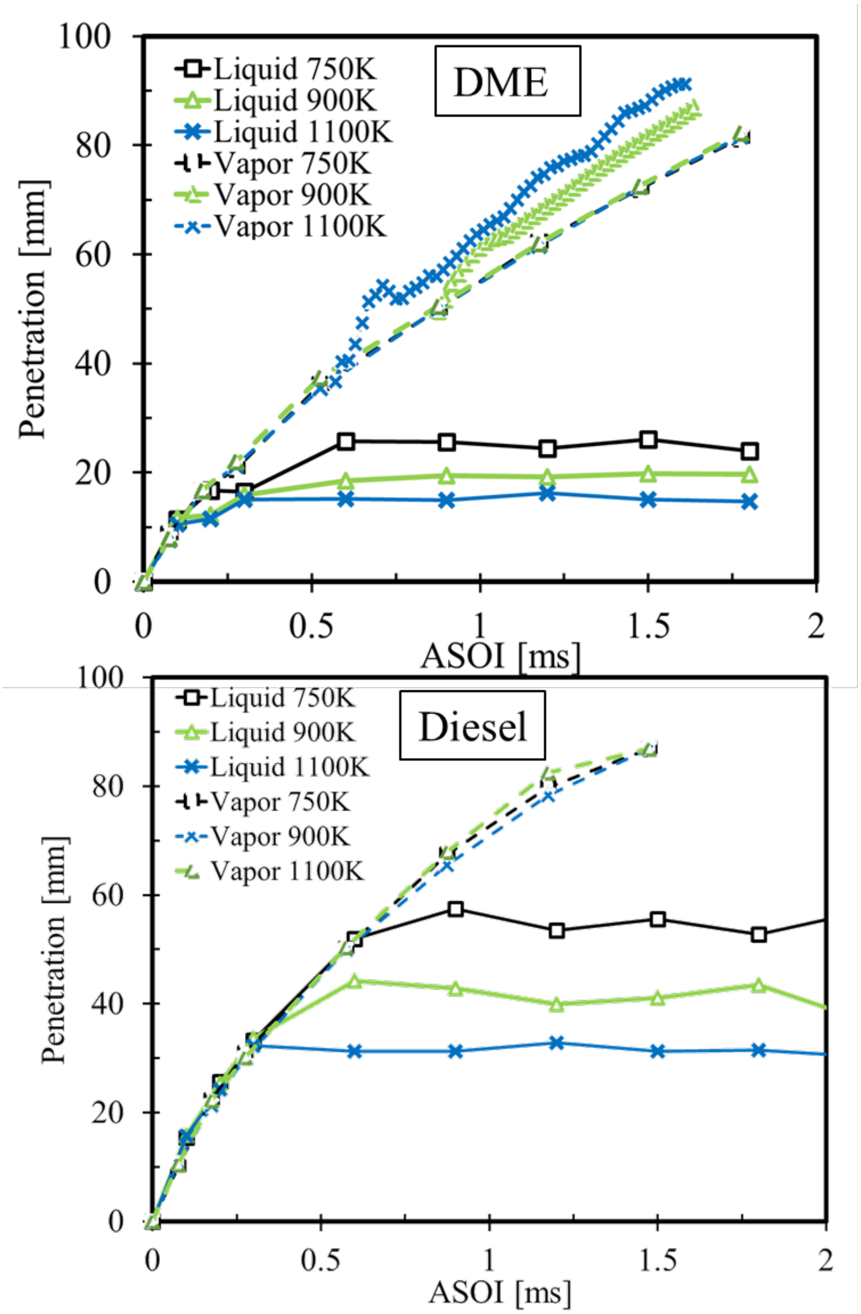

Figure 10-8 Liquid (solid line) and vapor (dash line) penetration profile of diesel and DME

10.2.3 Combustion of DME

Figure 10-9 shows the images of diesel and DME combustion at ambient condition 900 K, 14.8 kg/m^3. For better presentation, a gamma reduction to 0.5 value was applied to all the combustion images. DME combustion images were taken without any filter for camera setup, but diesel combustion images were taken with a neutral density filter (ND 0.8). Ignition delay is described as the time between the SOI and the first ignition. Ignition delay can be measured from several different sources: pressure trace from the pressure transducer inside the CV, photodiode signal, and high-speed flame luminosity image. The method used in the section to determine the ignition delay is to measure from HS flame luminosity image. In Figure 10-9, the images on the left-hand side are at the timing of the ignition. Images on the right-hand side are at the same timing ASOI 1.9 ms. The ignition delay of DME is 0.8 ms which is shorter than 1.5 ms of diesel combustion because DME has faster evaporation. The red circles are indicating the first ignition location. The first ignition location of DME is about 35 mm away from the nozzle, and diesel's location is about 75 mm away from the nozzle. Besides, diesel accumulated near the CV wall, which may further delay the ignition due to the heat loss to the cold wall (383 K). The right-hand side images show the fully develop flame. Even with the signal reduction of ND (OD = 0.8) filter, diesel still has very strong flame luminosity. Because diesel combustion produces soot whose soot luminosity is much stronger than chemiluminescence. The flame luminosity of DME combustion is very low, implying very low soot formation.

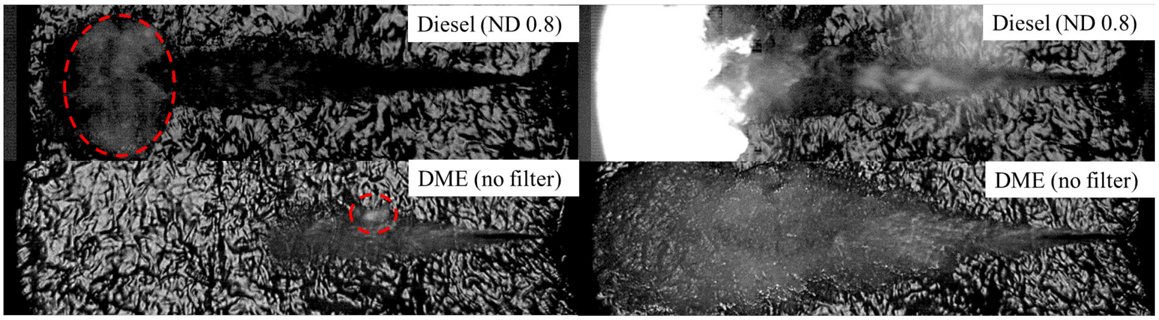

Figure 10-9 Combustion of diesel and DME (Inj P= 1500 bar, Ambient= 900 K, 14.8 kg/m3, 15% O_2, D= 180 μm)

10.3 Apparent heat release rate (AHRR)

The temperature effect, oxygen level effect, and injection pressure effect on HRR is shown in Figure 10-10. First, the start of AHRR rising is clearly different from three different ambient temperatures. 1100K case rises at the earliest timing of 0.25 ms. As ambient temperature decreases, the start of rising further delayed to 0.66 ms (increased by 0.41 ms) and 1.36 ms (increased by 1.11 ms) respectively for 900K and 750K cases. The 1.11 ms is a notable long delay. There is no obvious first stage ignition that can be distinguished from the AHRR curves. The first stage ignition and the second stage ignition are merged together. Second, the peak of the heat release rate for 750K ambient is much higher (217 J/ms at 2.91 ms) than 1100 k (176 J/ms at 2.25 ms) and 900K (163 J/ms at 2.59 ms) ambient cases, since there is more mass of combustible mixture accumulated which undergoes a second stage due to the notable delay. It can be seen that flames for all 750K, 900K, and 1100K shows a combination of the premixed combustion phase and a mixing-controlled combustion phase characteristic. Only 900 K shows the small separation of the premixed combustion phase and the mixing-controlled combustion phase at around 1.9 ms.

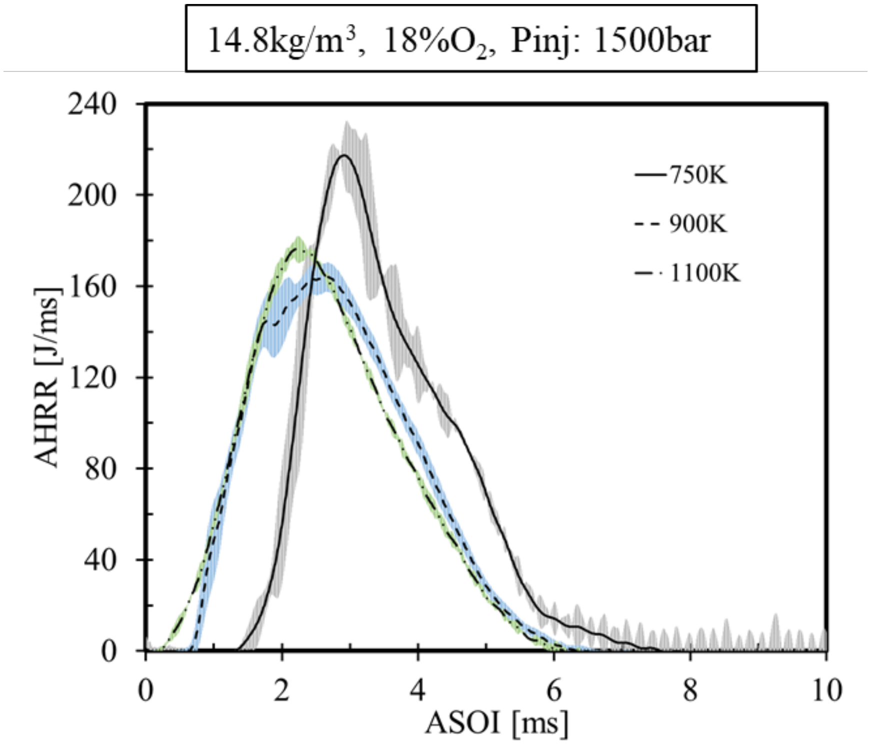

Figure 10-10 The effect of ambient temperature on the HRR of DME combustion

For the 1100 K ambient, there is a change of slope on the falling edge of the AHRR curve, which is a sign of merged weak mixing-controlled combustion phase. In a premixed combustion phase, the conversion of the premixed fuel (fuel+oxidizer) into some product species takes place. The mixing-controlled combustion phase is dependent on the level of oxidizer available to the fuel as a result of air-entrainment induced by the injection event.

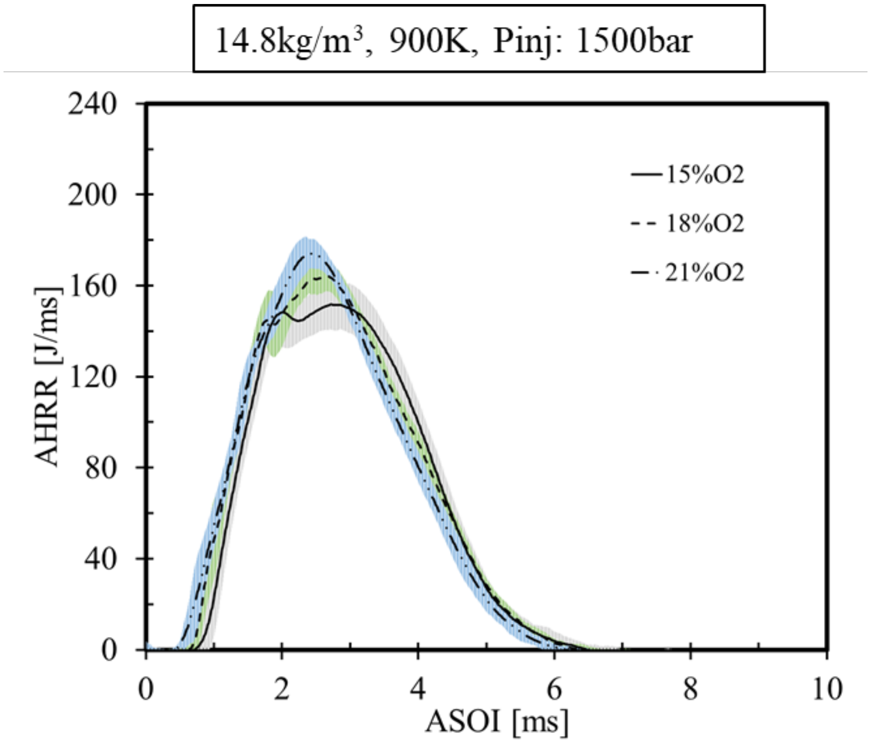

Figure 10-11 The effect of Oxygen level on the HRR of DME combustion

The effect of oxygen level on HRR is shown in Figure 10-11. It can be seen that the decrease in O_2 concentration slightly reduce the maximum HRR. The 21% O_2 case shows a single peak in the AHRR curve (merged premixed and mixing-controlled combustion phase), while the other two oxygen concentrations still have the separation of the premixed phase and the mixing-controlled phase, even though the separation isn't obvious. 21% O_2 case also has an ~0.2 ms reduction in ignition delay compared to 15% and 18% cases. The 15% and 18% cases have almost the same ignition delay, however, the 18% draws a faster AHRR which can be seen from the slop of the AHRR rising edge.

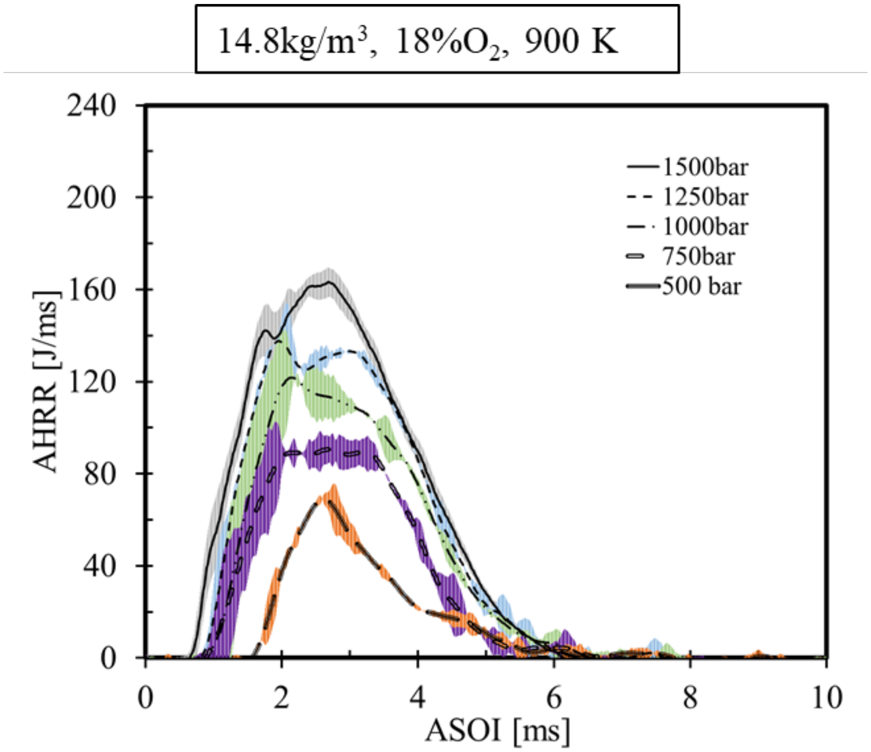

Figure 10-12 The effect of injection pressure on the HRR of DME combustion

The effect of injection pressure effect on HRR is shown in Figure 10-12. An increase in injection pressure (same dwell time) leads to longer actual injection duration of DME and eventually increases AHRR. The ignition delay is also found to decrease as the increase the injection pressure, due to the stronger mixing caused by the higher spray velocity and air drag. The overall combustion of 50 MPa injection pressure is dominated by the premixed burning phase, meanwhile, the mixing-controlled phase is diminished and forms a long-tail shape of AHRR. As the increase of injection pressure, the increase in real injection duration and total injected mass is beneficial to the mixing-controlled combustion phase, because the elongated injection mostly falls into the mixing-controlled phase; In addition, the short ignition delay limits the fuel amount in the premixed mixture. As a result, from 50 MPa to 150 MPa, the peak AHRR magnitude of the mixing-controlled portion keeps increasing until it exceeds the peak AHRR magnitude of the premixed portion at 150 MPa condition.

Cumulative heat release (CHR) is the integration of HRR over time, also known as total heat release. A CHR comparison between diesel and DME is shown in Figure 10-13. The DME's time axis is reversed for a mirror type comparison. It shows that the total heat releases of diesel and DME are comparable, where DME has slightly lower final CHR.

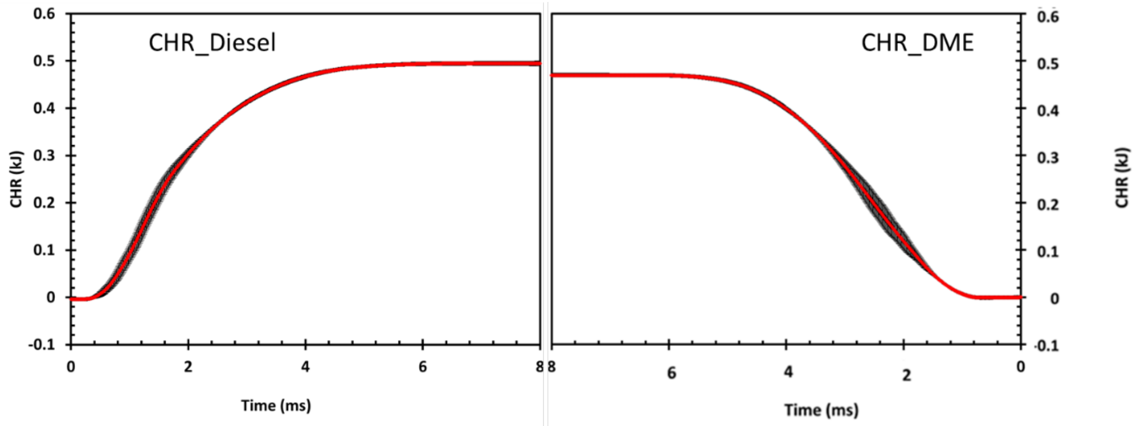

Figure 10-13 Cumulative heat release of diesel and DME combustion at the condition: ambient density is 14.8 kg/m^3; injection pressure is 1500 bar; nozzle size is 180 µm; injection duration is 2.0 ms, ambient temperature is 900 k, 15% O_2

10.4 Ignition delay

Ignition delay is described as the time between the SOI and the first ignition. Ignition delay can be measured from several different sources: pressure trace from the pressure transducer inside the CV (or HRR), photodiode signal, and HS flame luminosity image. The method used in the section to determine the ignition delay is to measure from the HRR curve. A threshold value of 5 J/ms is applied to HRR to find the ignition timing.

The effect of O_2 concentration on ignition delay has been studied for DME, as shown in Figure 10-14. When ambient temperature increases from 750 K to 900K, the ignition delay decrease is about 0.8 ms for both 15% and 18% O_2 concentration. There is another 0.4 ms deduction with the ambient temperature changing from 900 K to 1100 K. The O_2 concentration has an almost linear relation with ignition delay (about 0.1 ms ignition delay reduction per 3% O_2 concentration change). It is reasonable to conclude that ignition delay is reduced significantly when increasing the ambient temperature while O_2 concentration shows less ignition delay reduction.

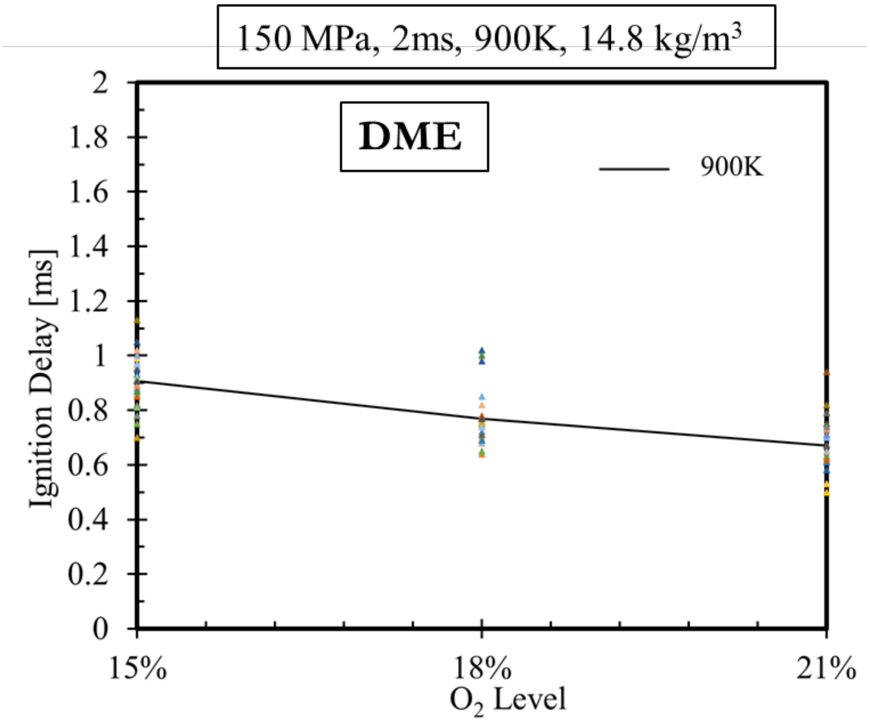

Figure 10-14 Effect of O_2 concentration effect on ignition delay

The effect of O_2 concentration, the ambient temperature on ignition delay has been studied for DME, as shown in Figure 10-15. From 750K to 900K then to 1100K, the averaged ignition delay decreases ~ 0.8 ms and 0.4 ms respectively for both 15% and 18% O_2. Reduction in ignition delays tends to become less sensitive to temperature increase. For the 1100K case, the variations of the repeated test under the same condition in ignition delay are small, while the variations in 900 K and 750 K can be ignored (up to ~ 0.2 ms). 18% O_2 has a 0.1- 0.15 ms ignition reduction throughout the ambient temperature sweeps.

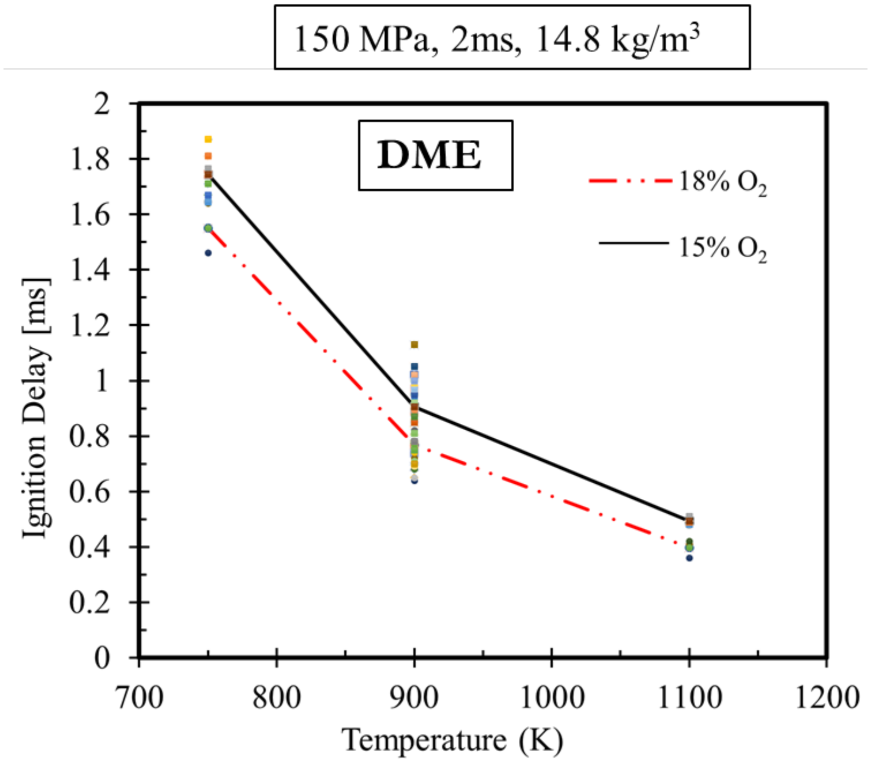

Figure 10-15 Effect of ambient temperature on ignition delay

The effect of injection pressure on ignition delay has been studied for Diesel, as shown in Figure 10-16. For 50 MPa injection pressure, the average ignition delay of DME spray combustion is ~1.565 ms. As the injection pressure increases to 75 MPa, there is a dramatical drop (~0.68 ms, 43% reduction) in the averaged ignition delay. For the injection pressure larger than 75 MPa, the averaged ignition delays are all below 1 ms. Refer to the imaging in Figure 10-3, the high injection pressure 150 MPa showed the flash boiling type of vapor (transparent portion) earlier and with larger area compared to 50 MPa case. The fast atomization and vaporization caused by the high injection pressure contribute to ignition delay reduction. Interestingly, from 75 MPa to 125 MPa, the ignition delay changes slowly and forms a flat portion on the plot. Until the injection pressure reaches 150 MPa, the ignition delay starts to show a further reduction in ignition delay. The short ignition delay of high injection pressure 150 MPa provides a potential for high efficiency and more accurate combustion phase control in the engine.

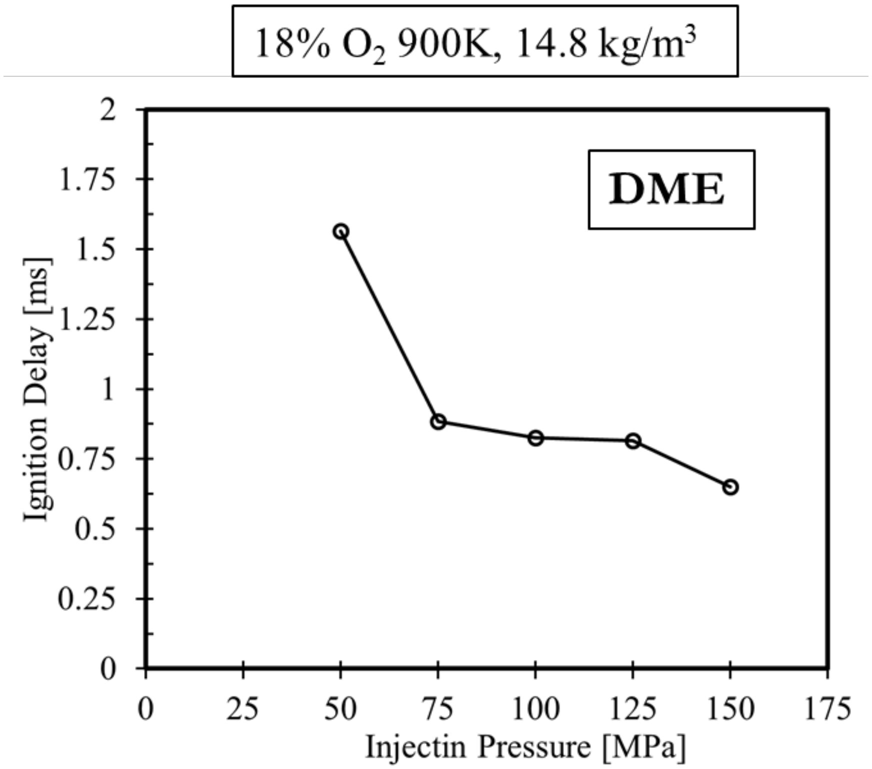

Figure 10-16 The effect of injection pressure on ignition delay of DME combustion

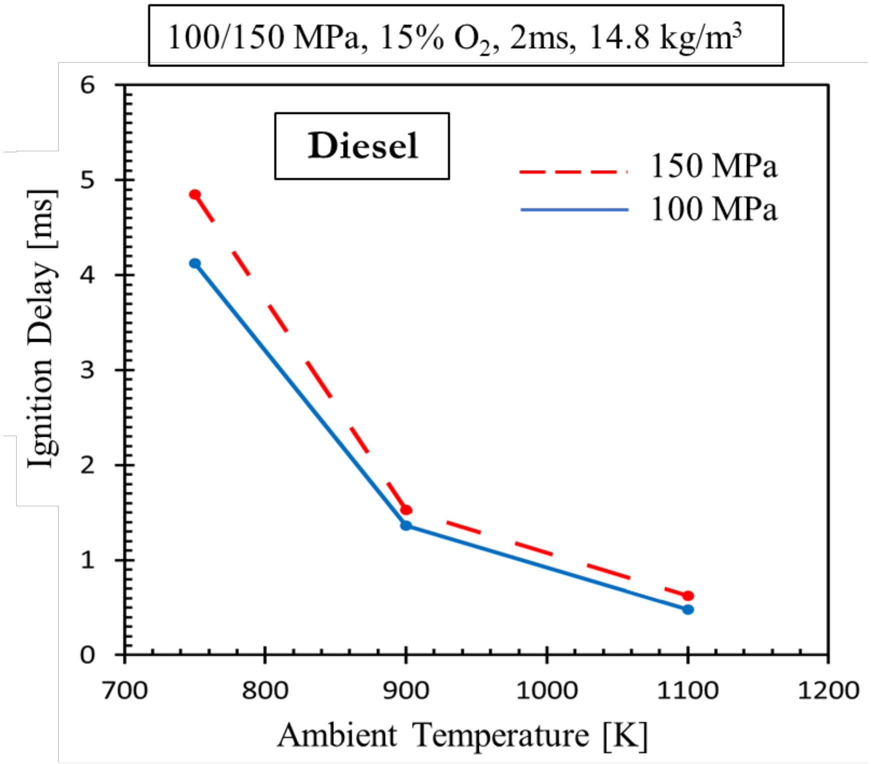

Figure 10-17 Effect of injection pressure on ignition delay

The effect of injection pressure, the ambient temperature on ignition delay have been studied for Diesel, as shown in Figure 10-17. Similarly, the increase in ambient temperature leads to shorter ignition delay at both 100 MPa and 150 MPa injection pressure. The ignition delay at 750 K is about 4~5 ms which is much high than the ignition delay (1.7~1.8 ms) of DME at the same conditions. The improvement (more than 65% reduction) in ignition delay is dramatic by increasing the ambient temperature to 900 K. At an ambient temperature of 1100K, the ignition delay of Diesel combustion first time reaches a comparable level of DME combustion. From the two injection pressure curves, it can conclude that the Diesel has an opposite react of DME in terms of ignition delay. Compared to 100 MPa case, the 150 MPa results in little longer ignition delay (varied from 0.1 ms to 0.8 ms based on ambient temperature) throughout all the ambient temperature. This is because the high injection pressure leads to more liquid fuel passing the nozzle within the same amount of time. Considering the high density of diesel, the increased liquid fuel forms a denser liquid core and poses a charge cooling effect, which results in the later ignition. DME's fuel density is smaller, so it can still gain ignition reduction benefits from the increase injection pressure at the 150 MPa level.

10.5 Intensity axial time (IXT) plot

IXT plots provide a new way to visualize the spray and combustion from high levels by composing spatial and temporal information into a 2-D plot. The focus points of using IXT plots in this study are the start of flame, LOL, and flame recession behavior. Please note the time shown in these IXT is not the ASOI time. The time zero means the start of injection triggering signal.

It was found that for 15%, 18%, and 21% O_2 concentration respectively: ignition delays are 2.2 ms, 1.8 ms, and 1.6 ms; LOLs are 32 mm, 28 mm, and 22 mm, as shown in Figure 10-19. In 15% and 18%, the LOLs are usually very stable from the beginning of flame until the end of the injection. However, the LOL in 21% case initially started at location 16 mm, then got pushed away gradually, and finally stabilized at 22mm at around 2.7 ms. DME IXT flame shows the flame recession. The minimum nozzle tip to flame distance during the flame recession is negatively correlated with the O_2 concentration. In addition, higher O_2 concentration increases flame height and moves the high-intensity region to the left.

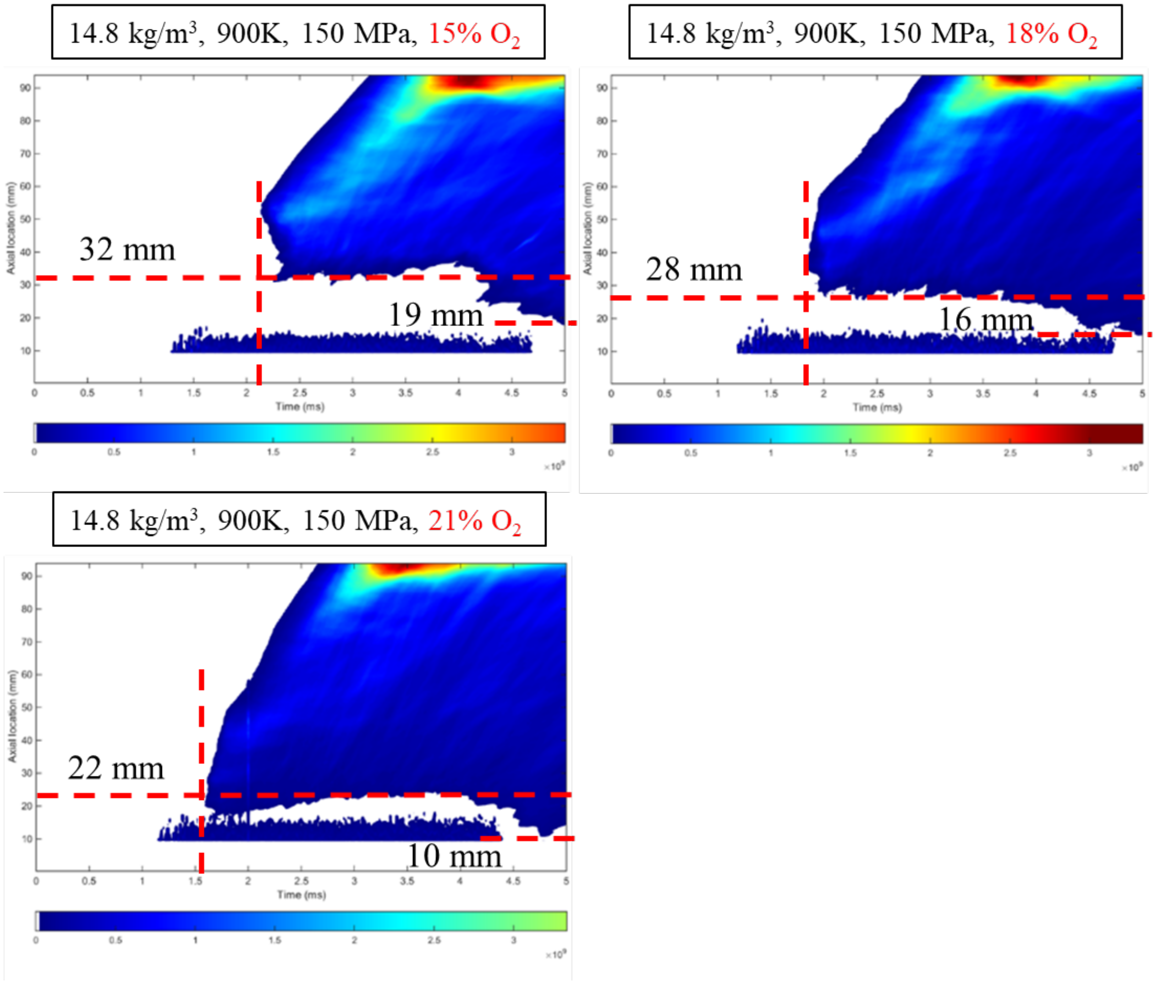

Figure 10-18 IXT plot of DME combustion with different O_2 concentrations (15%, 18%, and 21%)

The results from different injection pressure are shown in Figure 10-20. The LOL increases from 18 mm to 23 mm when the injection pressure increased from 50 MPa to 75 MPa and keeps constant at a value of 26 mm when injection pressure is no less than 1000 MPa. The minimum flame recession distance ranges from 9 mm to 16 mm, as the injection pressure less to high momentum of the end gas.

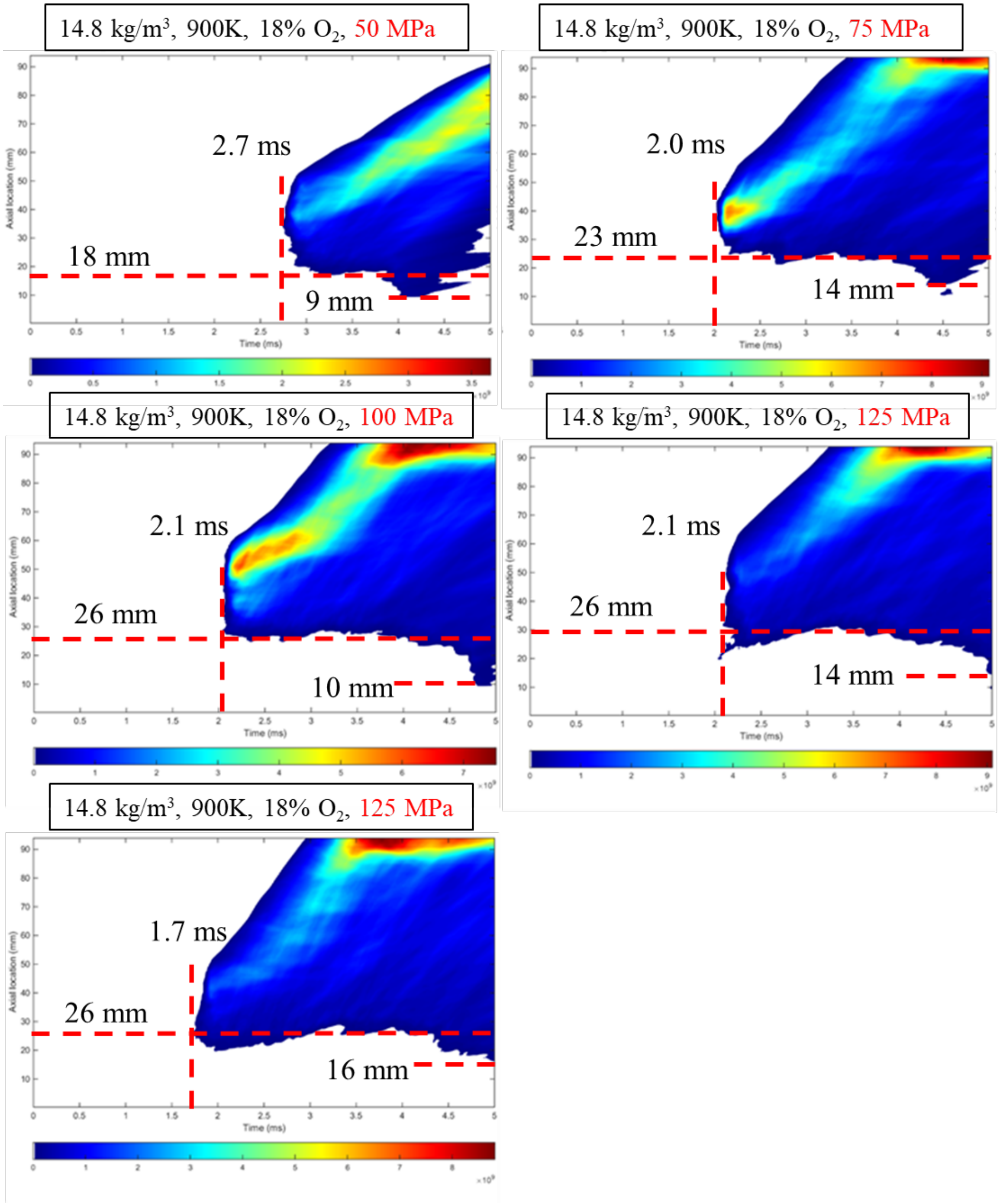

Figure 10-19 IXT plot of DME combustion with varied injection pressure (50/75/100/125/150 MPa)

10.6 PLIF of CH_2O and overlapped schlieren images

Figure 10-19 shows the overlap of schlieren images (blue) and PLIF images (yellow) with time sweeping for a combusting case. CH_2O-PLIF region is processed with false-color. The dashed line indicates the front of the CH_2O region. Formaldehyde is known to be an important radical to recognize the first stage of ignition. The formation and concentration change of formaldehyde can be used to investigate the combustion characteristics, such as ignition delay. Before ignition (t_A), the DME mixes with ambient. During this stage, the CH_2O is formed and accumulated due to the hot ambient temperature. CH_2O-PLIF image occupies the same region of schlieren. After ignition (between t_A and t_B), the penetration length of CH_2O keeps relative constant, due to the stable ROI (the first stage in Figure 9-13). The liquid DME is injected into the combustion chamber at a constant flow rate, mixing with hot ambient gas, forms CH_2O. On the downstream side, the combustion is consuming CH_2O. Therefore, during this stage, the concentration of CH_2O is relatively stable. As seen in Figure 9-13, there is a sudden decrease in ROI at T_B, resulting in the retreat of formaldehyde front. Between t_B and $t_{C,}$ the second stable stage shows up for both CH_2O penetration and ROI profile. Point B is the stage changing point, and the needle starts dropping. At t_C, the injection enters the closing stage. Therefore, CH_2O keeps decreasing after t_C until the end of the injection.

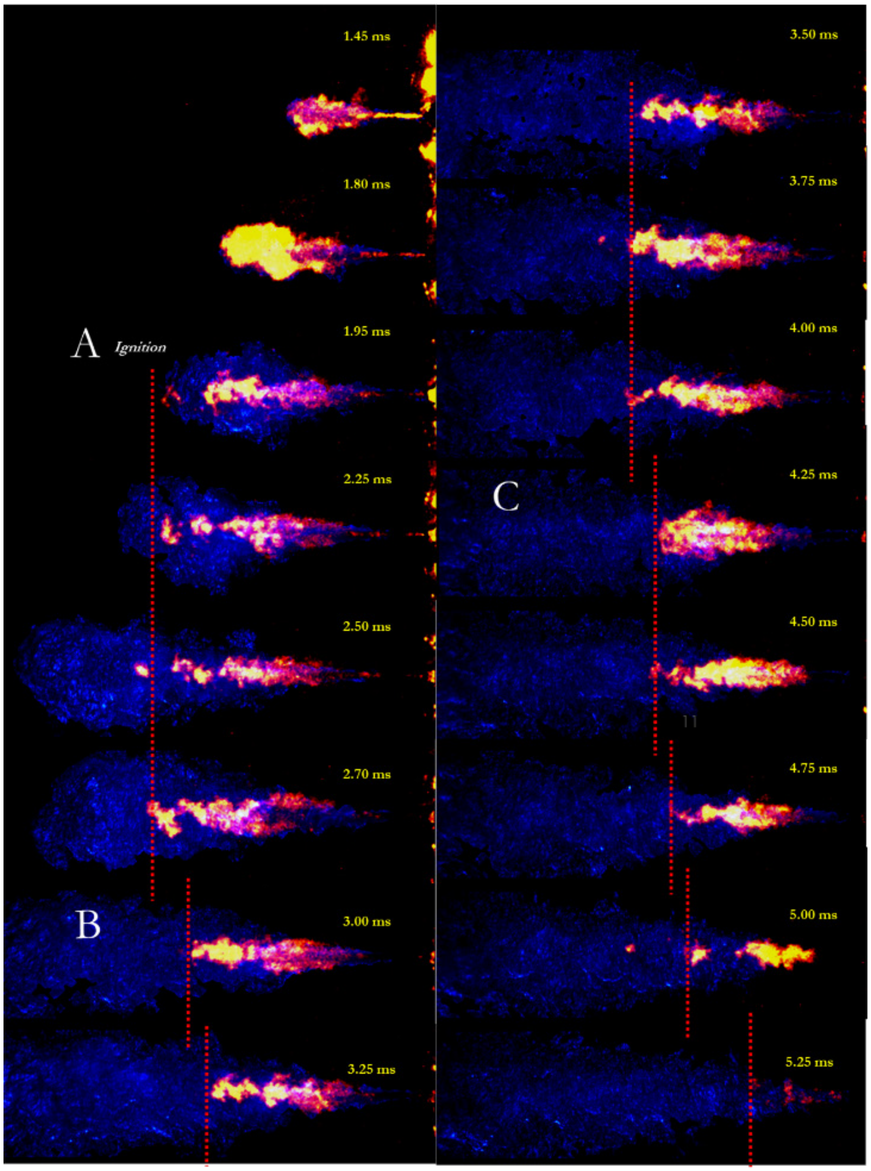

Figure 10-20 Schlieren images (blue) overlap with PLIF images (yellow) under conditions: injection pressure is 1500 bar. Ambient is 900 K, 18% O_2. Injector nozzle size is 180 µm. Injection energizing duration is 2 ms. A, B, and C are corresponding to those in Figure 9-13. The dashed line indicates the front of CH_2O region

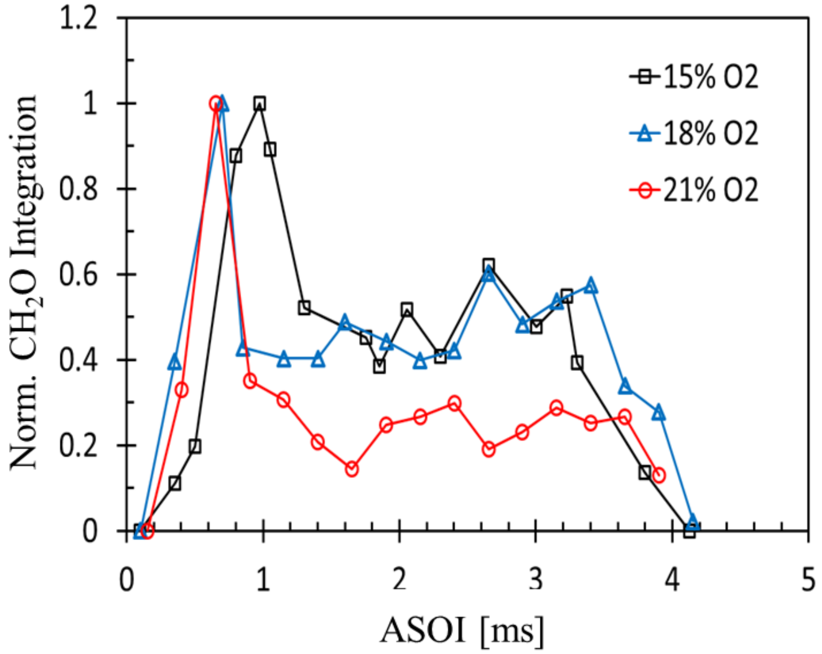

Figure 10-21 Normalized total Integration of CH_2O under conditions: injection pressure is 1500 bar; Ambient is 900 K, 14.8 kg/m^3, 15%/18%/21% O_2; Injector nozzle size is 180 µm; Injection energizing duration is 2 ms

This CH_2O-PLIF image overlap technique is used to understand the CH_2O evolution associated with the ROI profile. Integrate the intensity in CH_2O-PLIF images and normalize it with the highest intensity frame under different O_2 concentrations, as shown in Figure 10-20. It is found that formaldehyde concentration reaches a peak, then stays in a stable stage, and drops after injection ends. 15% O_2 case takes longer time to reach the peak, while 18% O_2 and 21% O_2 cases reach the peak at a similar time. 15% O_2 and 18% O_2 cases have a higher CH_2O concentration level (~0.45) at the stable stage, while 21% O_2 has a lower CH_2O level (~0.25).

11 Experimental and numerical study of diesel vs. DME in a CV: multi-hole results[2]

11.1 Introduction

Many compression engine combustion technologies such as retardation of injection timing, split injections, using Exhaust Gas Recirculation (EGR) and techniques enabling low-temperature combustion are introduced to decrease the emissions [11-1], especially particulate matter (PM) and NO_X emissions from diesel combustion. Although there are significant progress achieved, continuous work in this field is still necessary. The usage of alternative fuels like DME is an effective way to reduce NO_X and PM emissions. DME can be derived from a variety of feedstock such as natural gas, crude oil, residual oil, coal, waste products, and bio-mass [11-2] and DME has the advantages of higher cetane number (> 55) than diesel (40-55) and nearly soot-free combustion. Furthermore, DME considerably reduces combustion noise levels. However, there are also a few challenges by applying DME in the CI engine due to its lower dynamic viscosity and low lower heating value (LHV) compared with diesel which affects the durability of components and the size of fuel tanks.

Much research has been conducted to establish extensive data for fuel properties [11-3], to study the kinetic mechanism and chemical pathways [11-4], and to investigate the DME spray and combustion features [11-5] under engine-like conditions. The previously published work on DME done by the present authors mainly focuses on an experimental

---

[2] Rearranged from 10th U. S. National Combustion Meeting paper "Experimental and Numerical Study of Diesel vs. DME in a Constant Volume Combustion Vessel", 2017. Reference format is shown in 11-X.

and numerical study in a combustion vessel, to provide the fundamental research of DME vs. diesel at different engine-like conditions through various optical techniques [11-6]. To further investigate the combustion characteristics and compare DME with diesel, the current study is performed using both experiments and numerical simulation. Among combustion characteristics, ignition delay and burn duration are investigated. CFD simulations were able to able to sufficiently predict the combustion process of the 8-hole injector. Low-temperature and high species were evaluated against chemical heat release rate and temperature evolution to understand the complex chemical process using a few 'indicator' species.

11.2 Experiment apparatus and conditions

The spray tests were performed in a 1.1-liter constant volume combustion vessel (CV) [11-7]. Two pulsed light-emitting diodes (LEDs), HPLS-36AD3500, are used to shine the liquid region of the injected spray to obtain Mie scattering. The pulsed LEDs are operated as per a 67% duty cycle. The scattered light from the liquid droplets is directed into a high-speed camera facing the injector window. As soon as the ignition is initiated, natural luminosity is captured through the same optical path as of Mie scattering. A high-speed camera of Photron Fastcam SA 1.1 was used to obtain the liquid fuel spray and flame luminosity images at 30000 fps. The camera lens is a Nikon Nikkor 85 mm lens with f-stop 1.4 for diesel and 2 for DME. For diesel imaging (sooty flame), the luminosity was bright enough to saturate the image. A neutral density filter (ND 0.8) was used to reduce the image intensity spectrally along with using a shutter time of 1 µs. DME flames were non-sooty, so no such spectral filtering was employed but exposure time is increased to 32.67 μs to capture more light.

The dual fuel (diesel and DME) delivery system is used in the CV described in Ref. [11-6]. The engine-like thermodynamic conditions were generated in CV for both fuels. The same energy content of 2.12 KJ for both fuels is provided with DME injected mass of 71.56 mg and diesel injected mass of 48.18 mg. DME has an extended injection duration of 1.69 ms to accommodate for its lower LHV compared with diesel fuel injection duration of 1.0 ms (injection pressures were maintained the same for tests with both fuels). An 8-hole diesel injector was tested and the nozzle has 155 μm in diameter, the inclined angle of 145 degrees. The test conditions are the 15 % oxygen by volume, injection pressure of 150 MPa, the ambient density of 14.8 kg/m^3, and temperature of 750, 900, and 1100 K.

11.3 Numerical Approach

The numerical simulation of a 1.1-liter volume vessel with a multi-hole injector was carried out using CONVERGE CFD software [11-8]. Spray model includes the liquid portion of any spray until it vaporizes, and is dealt with Lagrangian particles as the liquid indicators. In the current study, the KH-RT model was used [11-9] and the KH break-up time constant can be tuned to result in an accurate prediction of spray penetration by comparing experimental results. The validated value of the KH break-up time constant for DME is 4 [11-6]. A Re-Normalization Group (RNG) k-ε model was used as a turbulent model [11-10]. SAGE[11-11] model was used as the combustion model which allows using detailed chemical kinetics in combustion simulations with a set of CHEMKIN formatted input files.

For this study, the reaction mechanism of DME consisting of 45 species and 249 reactions was used [11-12]. The rest of the models are implemented in the code in our previous studies [11-13].

All the simulations were performed with a base mesh size of 1.4 mm with a total number of cells of 50,000 in the simulation and with three levels of adaptive mesh refinement (AMR) based on temperature and velocity gradients. Further, two levels of fixed embedding were included near the nozzle and boundaries. Thus, the minimum cell size in the entire domain was 175 μm. It was found in the author's previous work that for these RANS simulations a 175 μm fine grid resolution gave grid-converged results [11-6].

11.4 Results and Discussion

Ignition delay trends with ambient temperature variation using DME and diesel fuels are shown in Figure 11-1. The results are for a 1500 bar injection pressure, the ambient density of 14.8 kg/m^3 and 15% of oxygen with an 8-hole injector. Ignition delay is defined here as the time difference between the start of injection (SOI) time and the time when pressure rises by 0.028 bar. As a general observation, higher ambient temperature decreases the ignition delay of both fuels. In addition, at the ambient temperature of 900 K and 1100 K, ignition delays of DME are 24% and 27% shorter than those of diesel, whereas ignition delay of DME is 43% shorter than that of diesel at an ambient temperature of 750 K. At lower ambient temperature, such as 750 K, DME retains its better reactivity due to its high cetane number (55-60) than diesel (40-45).

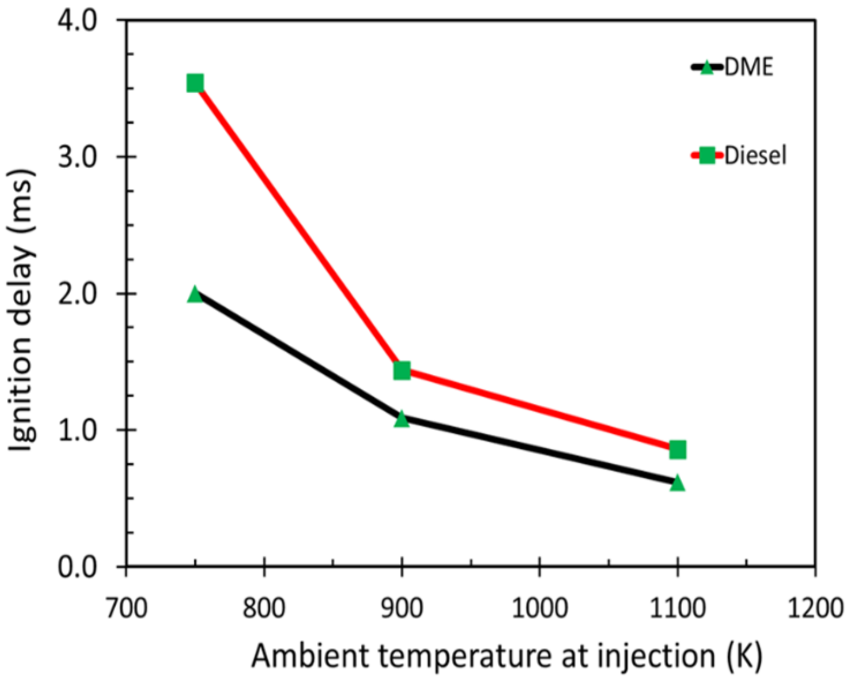

Figure 11-1 Ignition delay comparison between DME and diesel at an injection pressure of 1500 bar.

A series of events in DME and diesel ignition and combustion with the same energy content is provided in Figure 11-2 from left to right images, including (a) start of ignition, (b) stable combustion, (c) combustion recession, (d) the second burn, and (e) end of combustion. The injected mass of DME is 71.56 mg and diesel fuel injected mass is 48.18 mg, and DME has an extended injection duration (1.69 ms) to accommodate for its lesser LHV when compared to diesel fuel (1.0 ms).

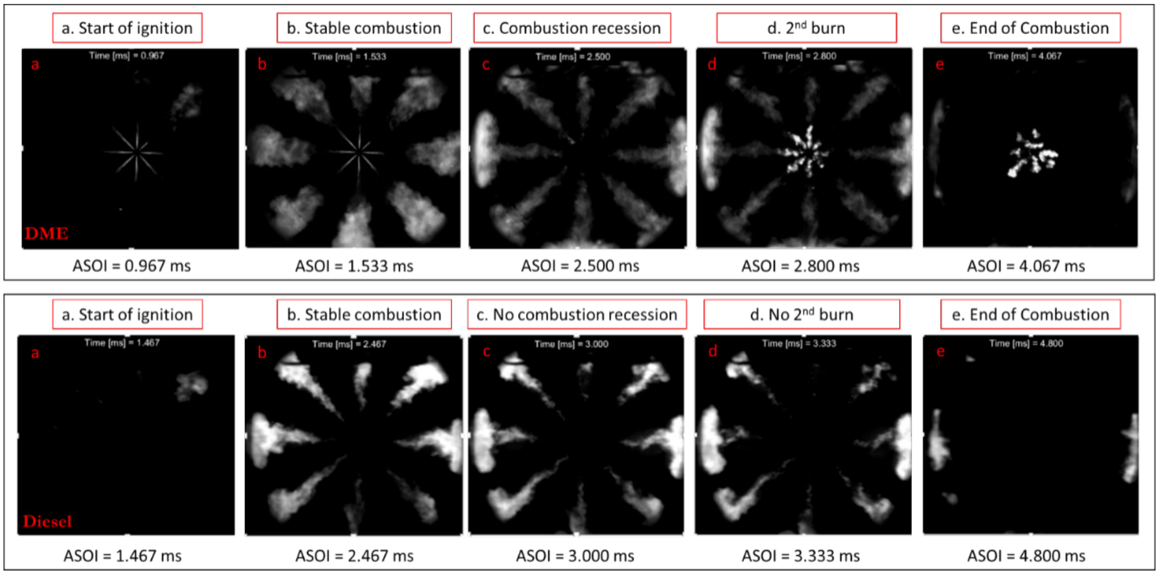

Figure 11-2 Comparison of events in DME (top) and diesel (bottom) ignition and combustion

Figure 11-2 gives a visual understanding of multi-hole DME and diesel spray combustion in quiescent combustion chambers. For diesel imaging (sooty flame), the luminosity was bright enough to saturate the image and the diesel flame luminosity is nearly 53 times higher than DME flame luminosity based on the current combustion images. Therefore, a neutral density (ND 0.8) was used in diesel combustion resulting in a minimum contribution of the scattering light from the liquid injection, while no neutral density filer was adopted in DME sprays since the flame intensities were already very low. This is explained the obvious difference in the visualization of liquid injection in DME which can be seen in Figure 11-2 (top) (a) and (b). Besides, the timestamps shown below each image illustrate significant differences in ignition and combustion behavior of both fuels. The timestamps are based on the start of injection times for both fuels. Diesel ignition might be seen after a longer time than it actually happens (confirmed from the pressure trace) due to neutral density filter used, however, Figure 11-1 shows longer ignition delay for diesel. In

Figure 11-2 (top) (a) and bottom (a), DME fuel has an early ignition time of 0.97 ms whereas diesel ignites later at 1.5 ms; early DME ignition might be due to fast vaporizing time of DME. Note that the ignition time of 0.97 ms for DME and 1.5 ms for diesel fuel are acquired from high-speed images, which is a little shorter compared with the ignition delay from a pressure measurement in Figure 11-1. Figure 11-2 (b) shows the quasi-steady flames where diesel tends to be much brighter even after using ND 0.8 filter since it is much sooty than DME. Combustion recession event which is useful to burn the liquid dribble is shown in Figure 11-2 (top) (c) but diesel case did not have it. The DME fuel starts to the second burn as seen in Figure 11-2 (top) (d), which produces soot (since it is rich combustion), as evident from the brightness near the nozzle. Figure 11-2 (e) shows late combustion times of 4 ms after the start of injection (ASOI) for DME and 4.8 ms for diesel, where DME liquid dribble still burns and downstream combustion continues but upstream combustion is not evident for diesel fuel.

Apparent heat release rate (AHRR) and burn duration comparisons of the combustion events are shown in Figure 11-3. As seen in Figure 11-3, the ignition starts earlier in the DME case than that of diesel which is the same trend as shown in Figure 11-2. Additionally, the peak heat release rate of diesel is higher than that in DME case since DME ignites at ASOI of 0.97 ms and injection duration is 1.69 ms while diesel ignites at ASOI of 1.5 ms and injection duration is 1.0 ms, which means that there is 54% DME fuel energy but 100% diesel fuel energy available at the time of ignition even the total energy content the same. Burn duration in this work is defined as the time from 10% to 90% of fuel mass burned and the effective burn duration is defined as the burn duration divides by injection duration.

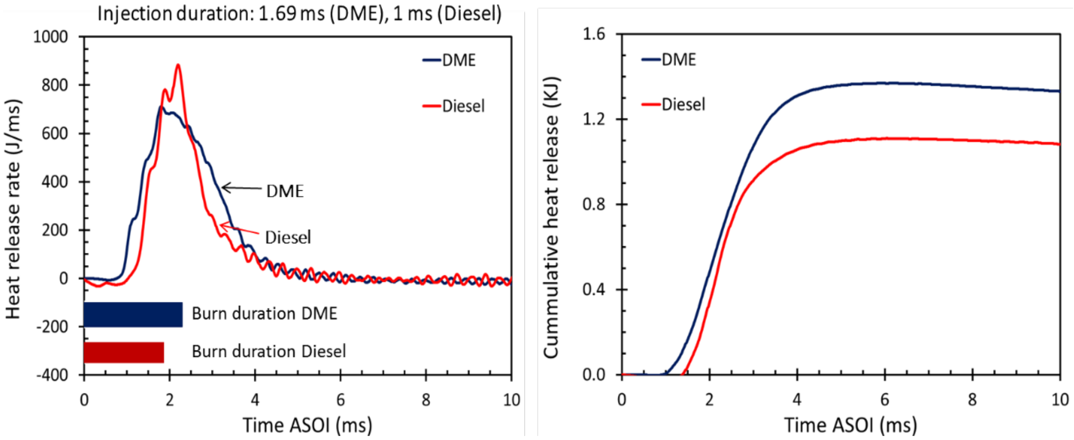

Figure 11-3 Impact of Injection Duration on AHRR (left) and CHR (right) for equivalent DME and diesel energy.

The burn duration of DME (2.1 ms) is longer than that in diesel cases (1.8 ms), however, the DME effective burn duration is 1.2 ms which is smaller than that of diesel (1.8 ms). Figure 11-3 (right) provides the cumulative heat release (CHR) of two fuels. The CHR of diesel fuel is smaller than that in DME, additionally, comparison of the percentage obtained by dividing peak CHR with an injected mass estimated from actual injection durations shows that diesel fuel is 21% smaller than DME, which indicates that the DME combustion efficiency under the CV condition is significantly higher than diesel fuel. Overall, CV tests show DME has faster reactivity than diesel and is efficient in its combustion.

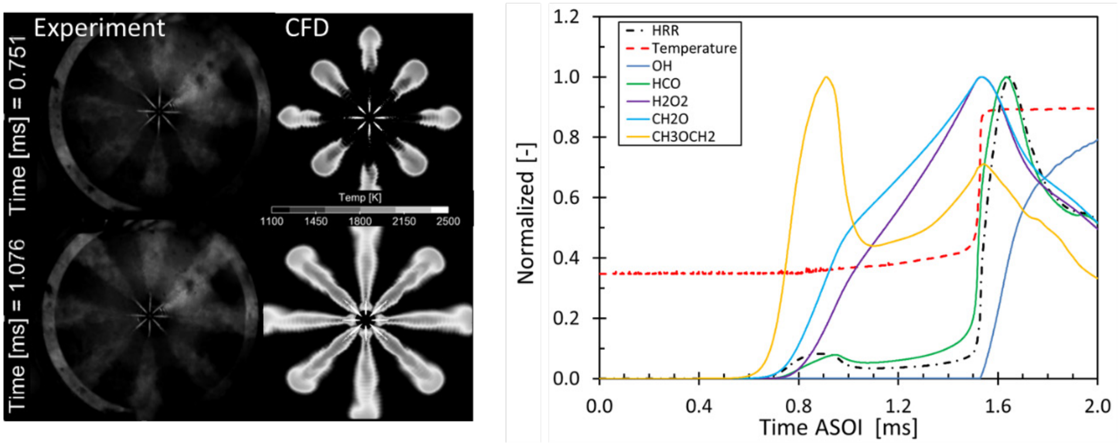

Figure 11-4 Comparison of Experiment vs. CFD (left); Species, HRR and Temperature evolution (right)

A CFD simulation was performed with the 8-hole injector in a constant volume combustion vessel environment with 750 bar injector pressure, 18% oxygen and 14.8 kg/m^3 ambient density. CFD was well-validated with experiments in terms of ignition delay and lift-off length. Figure 11-4 (left) shows two snapshots of the CFD and experimental spray-flames for their resemblance. Species evolution was then studied using the CFD data. Figure 11-4 (right) shows the species evolution along with heat release rate and temperature progress. It can be said the CH_3OCH_2 species is one of the earlier species to form among the rest of the species during hydrogen abstraction from DME. This is followed by low-temperature heat release and the creation of species like CH_2O and H_2O_2 species. These low-temperature species are consumed as high-temperature reactions take place which leads to the formation of species like OH. It can also be seen that HCO species evolution closely mimics the transients of initial heat release rate, so HCO can be said to be as a heat release rate indicator or ignition indicator species.

11.5 Conclusions

In this work, the combustion characteristics comparison between DME and diesel was done through both experiments and numerical study. Experimental work was performed in a combustion vessel examining the spray behavior of DME and diesel. A RANS-type turbulence model with SAGE (well-mixed type) combustion model was applied to achieve a better understanding of the DME spray properties. 8-hole HEUI injector was tested in a combustion vessel for both DME and diesel fuels. The effects of ambient temperature on DME and diesel combustion characteristics for the same fuel energy content were compared. Fuel energy content for both fuels was matched by varying injection duration. Tests show DME has faster reactivity than diesel. CFD simulations were able to accurately capture the combustion process of the 8-hole injector. Low-temperature and high species were evaluated against chemical heat release rate and temperature evolution. HCO species was seen to a good indicator of the initial heat release rate.

12 Ignition and Formaldehyde Formation in Dimethyl Ether (DME) Reacting Spray under Various EGR Levels: CFD Results[3]

12.1 Introduction

Dimethyl Ether (DME) has become a promising diesel engine fuel alternative that produces ultra-low soot due to its lack of C-C bonding in the chemical structure [12-1, 2]. There are numerous research on DME establishing an extensive data for fuel properties [12-3]; studying the kinetic mechanism and chemical pathway [12-4-6]; investigating its spray and combustion feature in direct injection (DI) system [12-7, 8] or experiments in a combustion vessel using optical diagnostics for flame visualization [12-9, 10]. In most of these studies, the fast ignition characteristic of DME was demonstrated due to its higher cetane number compared to diesel [12-11]. Prior to ignition, certain chemical reactions during the mixing of vapor fuel and oxidizers play an important role in determining the flame structure (e.g. lift-off length) and the later emissions of soot and NO_x during the high-temperature combustion process of diffusion flame [12-12, 13].

The use of exhaust-gas recirculation (EGR) has been known in the utilization of low-temperature diesel combustion concepts with the benefit of reducing both NO_x and emissions by burning at lower temperatures and leaner in-cylinder fuel/air mixture [12-14]. Higher EGR levels generally delay the ignition timing by providing more time for the mixing of fuel and air prior to combustion. In this study, we performed an experiment of

---

[3] Rearranged Proceedings of the combustion institute 36, no. 3 (2017): 3605-3612. Reference format is shown in 12-X.

DME reacting spray in a constant-volume combustion chamber at various oxygen concentrations imitating different EGR levels. Planar laser-induced fluorescence (PLIF) technique was used to capture the formation of CH_2O before, at, and after the time of ignition. Ignition delay from photodiode measurement and the visualization of CH_2O from PLIF imaging were used to validate a CFD model using detailed chemistry solver in order to further understand the relationship between formaldehyde and different stages of ignition. In a DME reaction mechanism, CH_2O plays an important role in the chemical pathway of the fuel oxidation process: it is formed from methoxymethyl (CH_2OCH_3) decomposition [12-4] and is consumed later to form carbon dioxide through basic combustion path ($CH_2O+HCO \rightarrow CO+CO_2$) [12-15]. The objective of this study is not only to confirm the commonly known hypothesis that CH_2O is formed mostly prior to ignition delay at upstream region before lift-off length for typical diesel combustion [12-12, 16], but also seek to conceptualize the ignition process of DME flame based on formation of CH_2O mainly with support from simulation efforts.

12.2 Experimental and Numerical Setup

12.2.1 Combustion vessel and fuel injection system

Liquid DME was delivered by a fuel injection system that couples with a single-hole nozzle injector (D_0=180 μm) of a hydraulically activated electronic unit injector (HEUI). The advantage of HEUI injector lays in the minimization of exposing DME fuel to the injector nozzle because its lower viscosity and lubricity of DME can potentially damage the physically moving parts. In other studies, a lubricity additive such as Lubrizol or Infineum R655 is often used to facilitate this downside [12-1]. The injector was driven by two iPod coil power EFS drivers that control the opening and closing coil events, therefore they are responsible, for the start and end of the injection event respectively. In this study, the electrical injection duration was kept to 2.0 ms. The injection pressure was 750 bar.

The single-hole HEUI injector system was integrated into the current combustion vessel research facility [12-17, 18]. The baseline condition of the experiment consists of 18% O_2 ambient composition, the ambient density of 14.8 kg/m^3. The ambient pressure was approximately 38 bar at injection events for all the conditions in this study. The initial ambient temperature of 900 K at injection was obtained by igniting a combustible mixture of C_2H_2, H_2, O_2, N_2 using an electrode. The test condition is summarized in Table 12-1.

Table 12-1 Summary of test condition

	Value
Fuel	DME
Nozzle Diameter (µm)	180
Injection Pressure (MPa)	75
Ambient Composition (%	21, 18, or
Ambient Temperature (K)	900
Ambient Pressure (MPa)	3.8
Ambient Density (kg/m^3)	14.8
Fuel Temperature (K)	383
Energizing Duration (ms)	2.0

12.2.2 Optical diagnostics

Formaldehyde (CH_2O) was excited at the wavelength of 355 nm by Nd:YAG laser (Continuum Surelite III) with a 10 ns laser pulse width. A schematic of the setup is shown in Figure 12-1 with a laser sheet directed toward injector tip through spray centerline. Other similar studies have been performed to visualize CH_2O in spray combustion using the same excitation wavelength [12-12, 16, 19]. The species fluorescence was captured through an intensified CCD camera (DiCam Pro) at several ASOI timings to visualize the formation and consumption of CH_2O. The camera was equipped with a 105 mm UV lens f/4 (250-650 nm transmission) and band-pass filter 400 nm centered, 20 nm FWHW. The filter selection was found to obtain sufficiently formaldehyde signals while avoiding elastically scattered light or reflection from the laser excitation. Camera gate was set at 200 ns covering the time when the laser is activated and the final spatial resolution is 0.091 mm/pixel. A full view of the spray from the tip of the injector to the oppositely impinging wall was visualized.

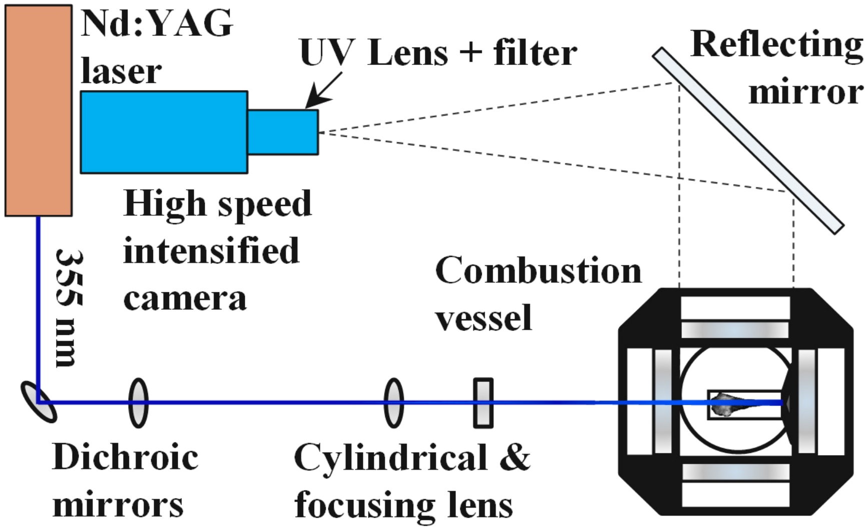

Figure 12-1 A schematic of experiments

A photodiode (Thorlab DET36A) was also used to detect the time of ignition. The photodiode is not sensitive to liquid scattering signal as confirmed from the recorded signal over time. The laser was deactivated to eliminate laser signal to a photodiode for a number of runs in order to determine the time of ignition. The ignition delay is calculated as the time difference between the start of actual injection to photodiode signal rise.

12.2.3 CFD simulation setup

The actual injector nozzle's diameter was measured through scanning electron microscope (SEM) imaging with a value of 174.2 µm. The rate of injection (ROI) was measured experimentally through the Bosch tube technique [12-20]. The total injected mass at 750 bar and 2.36 ms (actual duration) was about 15.16 mg. A simplified version of the ROI was generated using the ROI profile generator developed by Payri et al. [12-21] with given conditions of injection pressure, nozzle size, discharge coefficient, injection duration, and fuel density. This ROI profile, as shown in Figure 12-2 with experimental measurement, was used as input in CFD simulation.

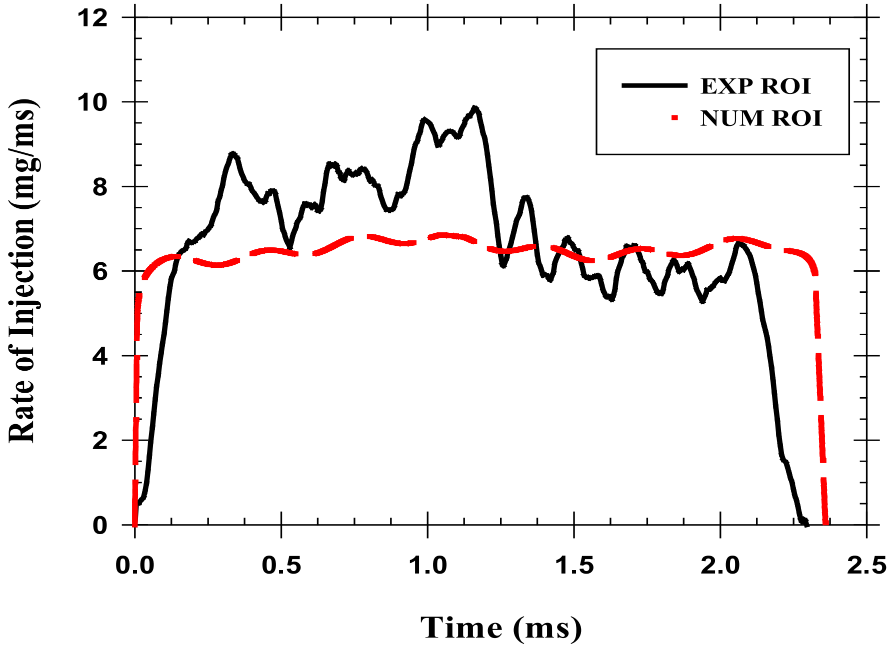

Figure 12-2 Measured and numerical rate of injection

As the selected simulation tool used in this study, CONVERGE CFD [12-22] has the capability of using adaptive mesh refinement (AMR) to generate a grid automatically based on sub-grid gradients of certain parameters, for this case, temperature, and velocity. A base grid size of 2 mm was used for all simulation runs. The finest grid is 0.125 mm with a base grid size of 2 mm. The selected grid size in this study was considered to be appropriate and robust for validating both non-reacting and reacting spray as suggested by Senecal et al. [12-23] for currently selected Reynolds-Average Navier-Stokes (RANS) Re-normalization Group (RNG) k-ε turbulence model. A Lagrangian spray “blob” injection model of Reitz and Diwakar [12-24] with subsequent breakup and atomization of liquid blobs model of Kelvin-Helmholtz and Rayleigh-Taylor (KH-RT) [12-25] with no break-up length were used in the simulation. Additionally, the No Time Counter (NTC) collision method of

Schmidt and Rutland [12-26] is included in the simulation to model droplet collision with a linearly increase in computational cost at a higher number of spray parcels. The SAGE detailed chemistry solver [12-27] which is a well-mixed reactor-based model running on CHEMKIN-format of chemical kinetic inputs was used with consideration of all species and reactions in DME reduced mechanism (45 species, 249 reactions) developed from detailed mechanism by Cung et al. [12-28] with 260 species and 1039 reactions which is well correlated with experimental data by Pfahl [12-29]. The reducing mechanism method is based on a direct relation graph with error propagation (DRGEP) using Reaction Workbench utility [12-30] and compared with original detailed mechanism over a number of parameters (ambient density, temperature, oxygen concentration) with no significant difference in the prediction of ignition delay. Important species and reactions are kept in the final reduced mechanism: (1) CH_3OCH_3 (dimethyl ether), CH_3OCH_2 (methoxymethyl radical), $CH_3OCH_2O_2$ (methoxymethyl-peroxy radical), $CH_2OCH_2O_2H$ (hydroperoxymethoxymethyl radical), $O_2CH_2OCH_2O_2H$ (peroxy-methoxymethyl-hydroperoxide radical) and HO_2CH_2OCHO (hydroperoxy-methylformate) [12-31]; (2) soot precursors including C_2H_2 (acetylene), C_2H_4 (ethylene) [12-1], with similarly selected soot precursor and soot indicator from ref [12-32] of C_6H_6 (benzene), and $C_{16}H_{10}$ (pyrene); and (3) the NO_x formation species including NO, NO_2, N_2. The combination of the detailed chemistry solver (SAGE) for reaction rate calculation, CFD transport equation solver, and a well-validated mechanism provides an efficient tool for modeling combustion including ignition.

12.3 Results and discussion

A comparison of ignition delays from experiments and CFD simulations for three different O_2 levels is shown in Figure 12-3. Note that, prior to performing combusting case in CFD simulation, non-reacting spray simulations were well-validated with liquid/vapor penetrations profiles from a separate experiment (Mie/Schlieren hybrid imaging) of different ambient temperatures (750 K, 900 K, and 1100 K) for non-reacting condition (0% O_2, similar other parameter as described in Table 1). The ignition delay in the simulation was defined as the time when the temperature of any cell is above 2000 K, while experimental ignition is defined by the very initial rise of the photodiode signal. Overall, the time of ignition is shortened by increasing the amount of oxygen content. The difference between the actual and simulated ignition delays is relatively small (0.01 ms in average). This shows that the simulation has good predictions for the ignition event in DME reacting spray at a given condition.

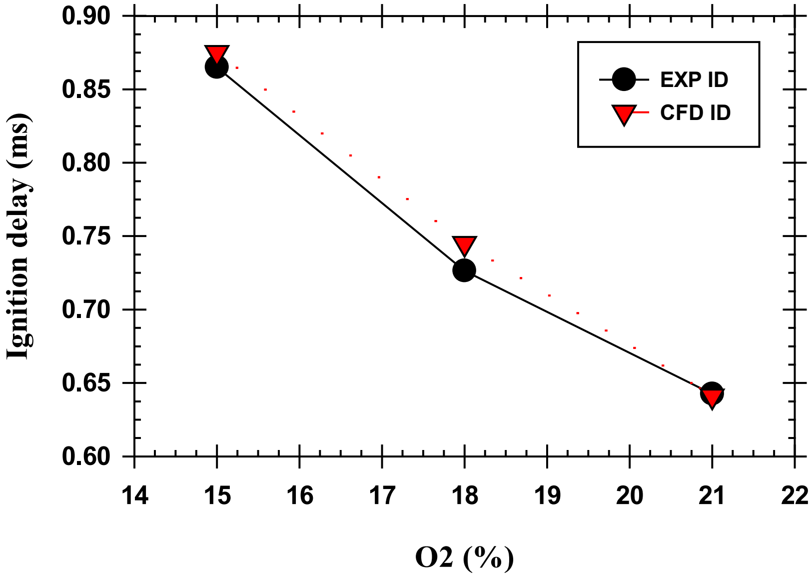

Figure 12-3 Ignition delay from experiment and simulation at various O_2 concentrations

Side-to-side comparison of the PLIF and CFD formaldehyde formation regions over varying ASOI is shown in Figure 12-4 for 18% O_2. Here CFD simulation predicts the trend of CH_2O formation fairly well compared to experimental images (false color with same range level of legend) within the time resolution difference of ± 10 μs. It can be seen that CH_2O is mostly formed upstream near the nozzle region with higher concentrations along the spray centerline. In the simulation, CH_2O is formed initially in the periphery of the spray while this was not illustrated in PLIF images. Since the RANS model simplified the dynamic structure of the spray compared to the LES model [12-33, 34], it seems to underpredict turbulence within the spray centerline where the low-temperature reactions to form CH_2O may take place. However, other experiments showed that CH_2O does form at the radial periphery of the spray initially rather than at core [12-12, 16]. Perhaps, the different conditions of ambient oxygen levels, injection strategies (injection pressure, duration, nozzle diameter, etc.), and even differences in reaction pathway from fuel to fuel would result in the different structures of CH_2O especially at its initial formation. The simulated ignition delay was 0.745 ms (about 6% higher than the experiment).

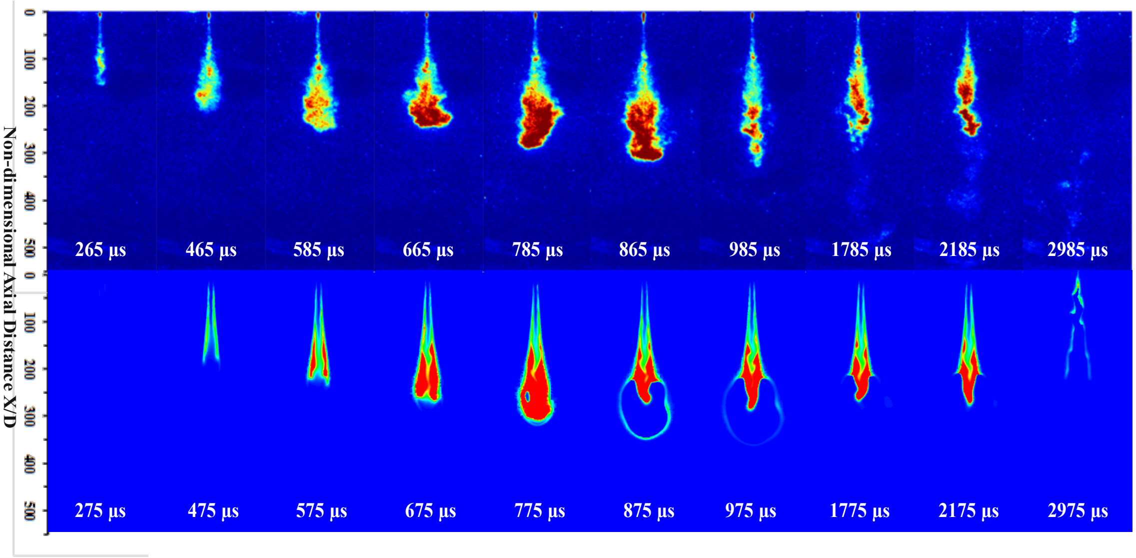

Figure 12-4 Time-elapsed CH_2O from PLIF images (upper) and simulation (lower) at 18% O_2

As shown in both the simulation and experiment, CH_2O appeared to start diminishing after ignition. This vanishing phenomenon of CH_2O has been pointed out in other literature for the diesel combustion [12-13, 35]. In Ref. [12-13], it was mentioned that CH_2O is a common species that appears during the first stage of ignition where the low-temperature reaction takes place. As temperature increases, certain concentrations of OH are released by the decomposition of H_2O_2, and OHs are immediately oxidized with other unburned hydrocarbon (UHC). Specifically, in the DME kinetic mechanism, the reaction of OH and CH_2O is one of the most important reactions via $CH_2O + OH \Leftrightarrow HCO + H_2O$ [12-4, 15]. Wang et al. [12-4] also pointed out that CH_3, H, and HO_2 both contribute to the consumption of CH_2O to form HCO in their chemical pathway analysis of DME reaction with air at lean and rich conditions. This chemical conversion is similar to what Musculus et al. [12-13] described as an indicator of the second stage of ignition. At the time of 875 μs in simulation, a void region appears near the front stream of CH_2O formation and limits the extension of CH_2O prior to X/D = 250. CH_2O is eventually diminished as seen between ~ 2.1 to 2.9 μs. Note that injection in both the experiment and simulation has already finished at 2.36 ms ASOI. It is reasonable that CH_2O is near its complete extinction as no further parent fuel is supplied to initiate chemical reactions as described in Ref. [12-4] through this reaction path: CH_3OCH_3□CH_3OCH_2□CH_2O.

In order to illustrate further the formation and consumption of CH_2O, the global mass formation profiles of various species are shown in Figure 12-5 together with the temperature and heat release rate (HRR).

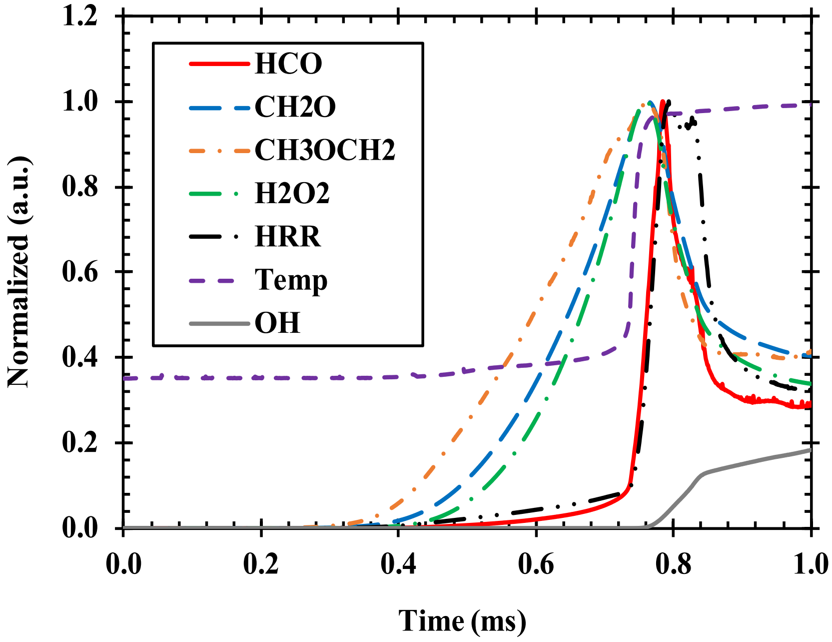

Figure 12-5 Species evolution from CFD simulation at 18% O_2

As temperature gradually increases before 0.745 ms, CH_2O is produced abundantly, and almost simultaneously with CH_3OCH_2 (produced via H-abstraction from DME) which confirms again a well correlation between these two species from the reaction step: $CH_3OCH_2 \Leftrightarrow CH_2O + CH_3$. As temperature rises significantly and maximum HRR occurs at time of ignition, CH_2O production reaches peak value and starts to decrease. At the same time, OH is formed, indicating a transition to high temperature combustion process. OH is known to later consume CH_2O through H-abstraction to form HCO [12-4, 13]. It can also be seen that there are slow and fast reactions for each species to reach its peak value. The fast reaction would probably be related to HCO where a sudden release of the species as a large amount of heat release is present. In summary, the formation of formaldehyde marks the initial stage of ignition where low temperature oxidation of DME takes places. Its production drop may be used as an indicator for the on-set high-temperature combustion process where the release of OH radicals is commonly known for the oxidation of unburned hydrocarbon.

Going beyond the oxygen concentration conditions performed in the experiment, a more diluted ambient was simulated in CFD model for 12 and 9 % O_2. Ignition still occurs even at these conditions but at lower peak temperature and longer ignition time as expected by the effect of more diluents, but results in somewhat different stages of ignition as shown in temperature profile in Figure 12-6. It can be seen that as O_2 level is reduced, the combustion duration lengthens because ignition is delayed due to the slower chemical kinetics resulting from lack of oxygen entrainment. Therefore, for the same amount of fuel injected, it would take longer time to completely consume all the hydrocarbons. Negative temperature coefficient (NTC) regime can also be seen at different oxygen levels with longer NTC period at lower oxygen levels where HRR continues to decrease despite the temperature still increases.

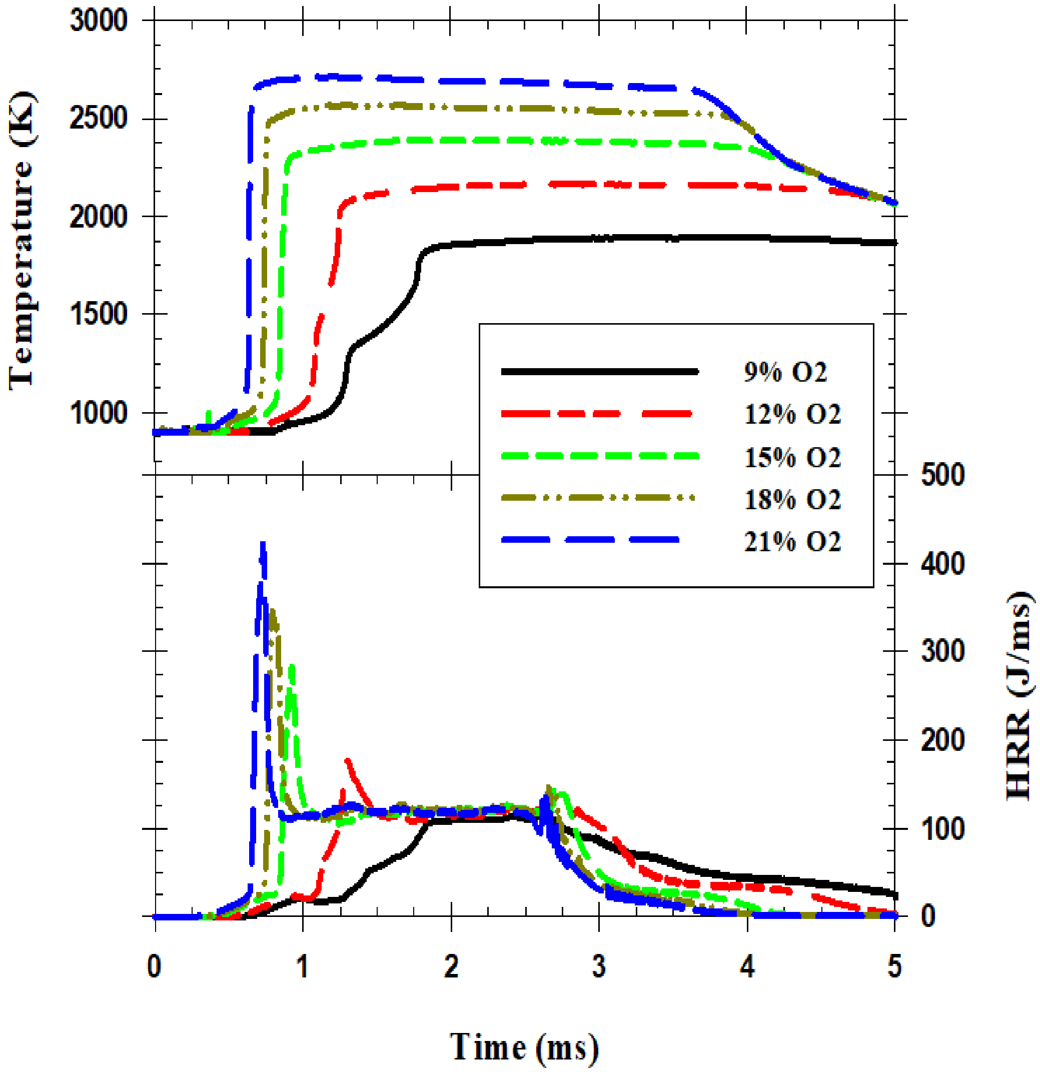

Figure 12-6 Simulated temperature (top) and HRR (bottom) at each O_2 concentration.

The importance of CH_2O and OH as indicators of different ignition stages is considered at different oxygen levels in Figure 12-7. While early stage of ignition process can be defined by the formation of formaldehyde, it is believed that the consumption of formaldehyde should be used as an indicator of hot ignition instead of the release of OH. As shown in Figure 12-7, the time difference between the peak of CH_2O and rise of OH increases as the oxygen level is decreased. The defining ignition delay proposed by temperature ($T_{cell} > 2000$ K), CH_2O peak, and OH rise are shown in Figure 12-8 over various oxygen concentrations to compare with each other.

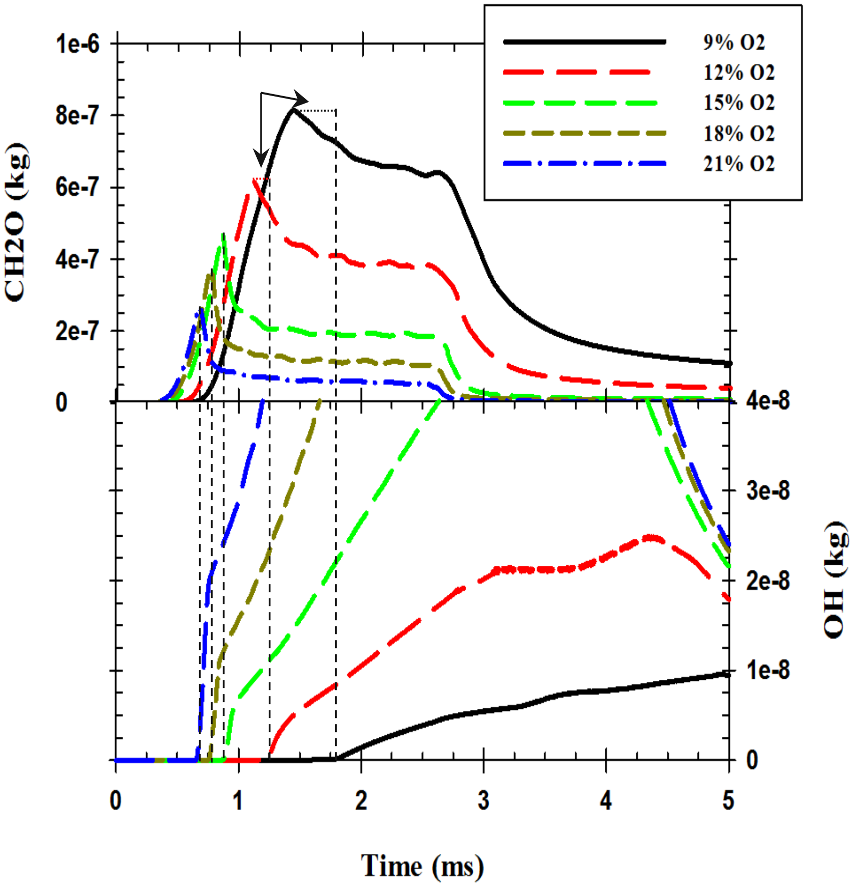

Figure 12-7 CH_2O (top) & OH (bottom) formation over simulation time at each O_2 concentration

At O_2 level of 15% or higher, there is negligible difference in ignition delay defined by these parameters. However, as O_2 level is decreased below 15%, the difference in predicting ignition delay between CH_2O-approach and others becomes larger. The shortest ignition delay is defined by CH_2O peak. Note that for 9% O_2 case, the peak temperature is below 2000 K, therefore the ignition defined by cell temperature of over 2000 K cannot be determined. Note that the temperature at the ignition time defined by peak CH_2O for 9 and 12% O_2 cases is about 1400 K, which is considerably high to indicate the start of ignition.

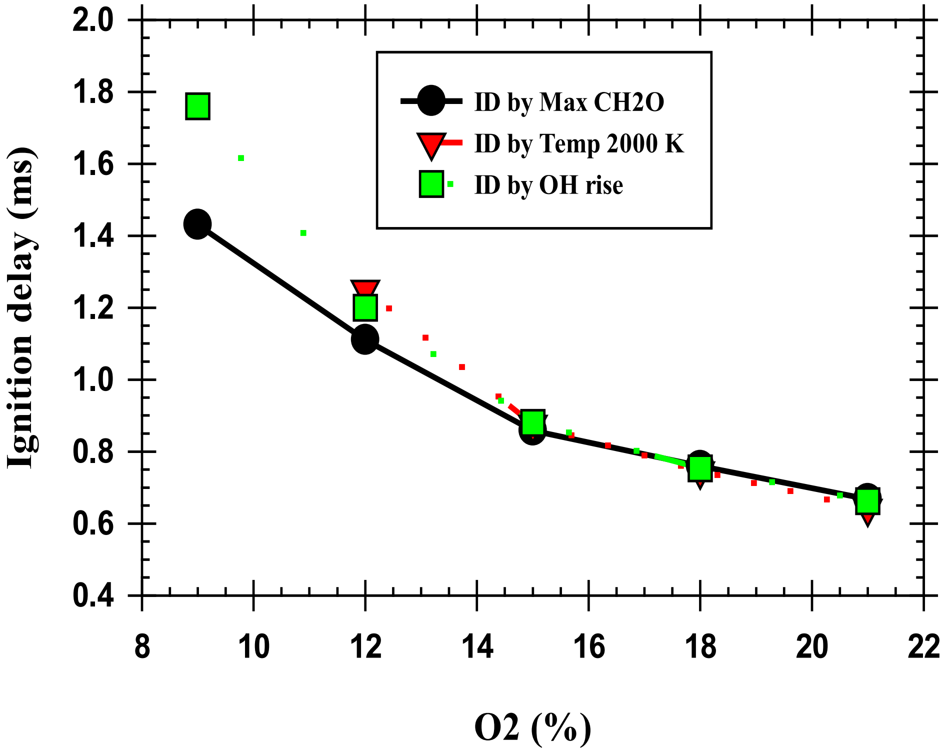

Figure 12-8 Computed ignition delay over O_2 concentration based on temperature, CH_2O, and OH

In order to further confirm the hypothesis of ignition timing by formation of CH_2O spatially, different contour images of CH_2O and OH are shown in Figure 12-9 along with the temperature and equivalence ratio (or "Phi") scatter plots from all simulated cases. Phi-T plot can provide very important tool where ignition can be easily recognized by period of high temperature and locally fuel rich region. The plots in Figure 12-9 are arranged to represent the pre, at and post ignition times for the varying O_2 cases. Each point in the Phi-T scattering plot represents a point in the computational domain. This type of scattering plot gives information about equivalence ratio of the ignited computation cell and the intensity of reactivity based on the temperature rise. It can be seen, based just on the Phi-T scatter plots, that the reactivity of the sprays is reduced when O_2 concentration reduces from 21% to 9% with the peak temperature at the time of ignition reducing from 2600 to 1450 K. However, the equivalence ratio at ignition time is almost similar for all the cases simulated ($Phi_{ignition}$~1.65).

Additional information about the behavior of ignition can be obtained by relating CH_2O and OH species contours together. In the case with higher ambient oxygen levels, the generation of ignition kernels takes place at multiple spots, randomly, but within CH_2O region. Nonetheless, at lower ambient oxygen level case in which the fuel-air mixture is given longer time to react due to less favorable conditions for ignition, it has longer time to reach homogeneity, making it to react as a lump and not as disjointed ignition spots as in a higher oxygen level case. As a general note with respect to Figure 12-9, it can be said that the depletion of formaldehyde prior to an ignition event creates a flame kernel which can be visualized as OH species presence at the void spot in formaldehyde images. Thus depletion of formaldehyde or increase in OH can be generally considered as an estimate to the ignition delay.

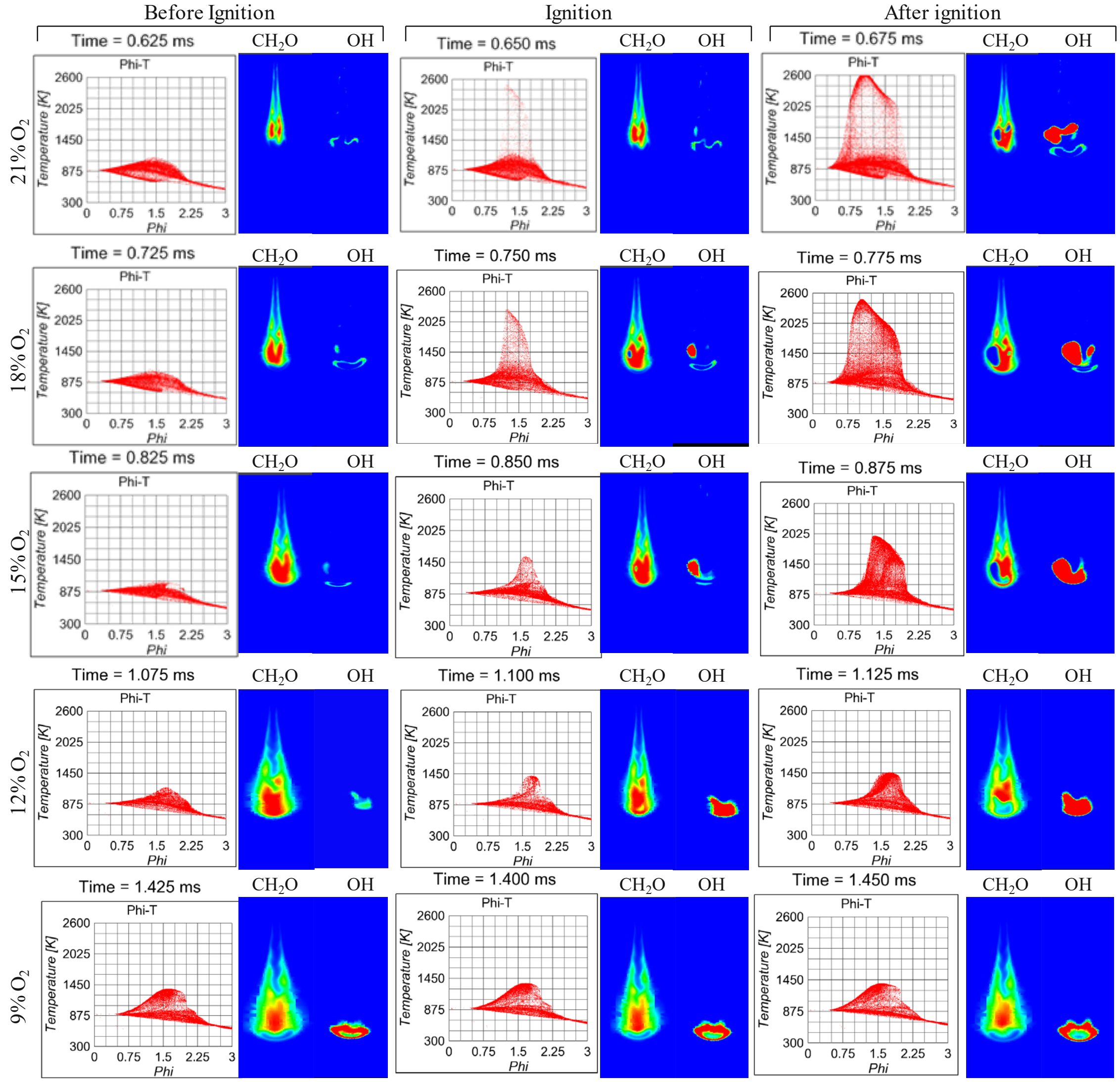

Figure 12-9 Phi-Temperature scatter and contour plots of CH$_2$O and OH from simulation

12.4 Conclusions

Correlation of formaldehyde to ignition process in DME reacting spray was investigated in both the experiment and simulation. Fluorescence of formaldehyde (CH_2O) excited by a 355 nm laser wavelength was captured at different ASOIs over separate runs to provide a temporal and spatial view of its progression and recession. It was confirmed that the general concept of diesel combustion can be applied to DME combustion, meaning that CH_2O appears abundantly in low temperature combustion process. CH_2O starts depleting when temperature increases significantly, usually known as time of ignition, or ignition delay. Validated CFD simulation predicted this phenomenon very well. Different stages of ignition were described by the profiles of: CH_2O (low temperature combustion or 1st stage of ignition), and OH (2nd stage of ignition characterized by high temperature diffusion flame). CH_2O is seen upstream near nozzle and is extended up to the flame lift-off location where OH is present. By studying the effect of oxygen levels in the ambient on DME combustion, ignition process was reviewed by temperature profile, CH_2O, and OH. Regardless of which criteria is being considered, it was shown that ignition delay increases as the oxygen concentration reduces. However, at the lower oxygen concentrations, indication of ignition was shown to be more reliable by the formation of CH_2O. It was seen that CH_2O was formed firstly during 1st stage ignition, and its depletion marks an important stage where high temperature combustion is initiated as shown in the reactivity of fuel/air mixture in Phi-T scatter or overall temperature profile. OH* is formed around the time of CH_2O depletion indicating the start of 2nd stage ignition where high temperature reactions are present. However, this is not clearly observed in the cases of lower oxygen concentration as the initial formation of OH appears at longer time after CH_2O is consumed. The temperature at the time of CH_2O depletion was already high (~ 1400 K) suggesting that CH_2O profile can be a reliable source for understanding the ignition process. Overall, the results of this study provide information on single or two stage behavior of ignition in DME reacting spray with general suggestion on the use of CH_2O (its depletion) as the marker for ignition from low-to-high oxygen ambient conditions. With the growing research in combustion using laser diagnostic on CH_2O, it is prominence that the ignition process can be defined more accurately by the profile of CH_2O.

13 Mechanism of Ignition and Flame Stabilization of High Injection Pressure Dimethyl Ether (DME) Sprays

13.1 Introduction

With nearly smokeless combustion, Dimethyl Ether (DME) can be pressurized and used as a liquid fuel for compression-ignition (CI) combustion. However, due to its inferior lower heating value and lower liquid density compared to diesel fuel, DME has a smaller energy content per unit volume. To obtain an equivalent energy content of diesel, approximately 1.86 times more quantity of DME is required. For the same injection duration, this can be addressed by a larger nozzle size or higher injection pressure. However, high injection pressure characteristics have not yet been well understood for DME. To fill this gap, spray and combustion processes of DME were studied extensively via a series of experiments in a constant-volume and optically accessible combustion vessel. A hydraulic electric unit injector (HEUI) with a 180 μm single-hole nozzle was used to achieve an injection pressure of 1500 bar. In the current study, the liquid and vapor regions of DME jet were visualized using a hybrid Schlieren/Mie scattering at non-reacting conditions. At reacting conditions, the high-speed flame luminosity was used to capture the flame intensity, and planar laser-induced fluorescence (PLIF) imaging was used to characterize formaldehyde (CH_2O) evolution. Spray and combustion characteristics of DME were compared with diesel in terms of penetrations and ignition delay (ID). High-speed imaging of flame lift-off length (LOL), flame structure, and CH_2O formation of DME were also studied. Further insight on the DME ignition mechanism including cool-flame was also given through a validated large-eddy simulation (LES) model. The results showed that, compared to diesel, DME has shorter liquid and vapor penetrations due to its low fuel density and fast evaporation. DME evaporates rapidly after exiting nozzle even before the secondary breakup. CH_2O consumption indicates the transition from low-temperature combustion to high-temperature combustion and is affected by ROI and chemical pathway.

13.2 Background

Dimethyl ether (DME), as a promising alternative fuel for diesel, has been proven to have soot-free combustion, due to its high Cetane number (> 55), low auto-ignition temperature and no carbon-carbon (C-C) bond linkage [13-1,2]. DME is the simplest ether with a low C/H ratio (0.337), and it evaporates rapidly due to high vapor pressure (530 kPa at 293K, where diesel only has <<10 kPa). Conventional diesel combustion usually produces a large amount of particulate matter (PM). With nearly smokeless combustion, DME/air mixture can still ignite even at a very high level of exhaust gas recirculation (EGR). Higher EGR can further reduce NO_X emission below US 2010 regulated levels without the use of Selective Catalyst Reduction or NO_X storage catalysts [13-3]. Eliminating both the PM filter and NO_X catalysts lowers engine pumping work (lowered backpressure) and improves engine brake specific fuel consumption. However, DME generates more carbon monoxide and hydrocarbon emissions because of much higher volatility [13-4], especially when air and fuel are poorly mixed at low ignition temperature. There are numerous studies on DME spray and combustion characteristics in both direct injection systems [13-5,6] and the combustion vessels [13-7-9].

Due to the inferior lower heating value (28.43 MJ/kg) and liquid density of DME, additional DME should be injected during one injection event compared to diesel (42.5

MJ/kg), in order to deliver comparable energy. One of the solutions is to use high injection pressure. However, the effect of the high injection pressure on DME spray combustion characteristics has not been well understood. In this study, we explored experimentally ignition and combustion processes of DME reacting spray in a constant volume combustion vessel (CV). The pressure and temperature of the CV experiment were at engine-like conditions. DME is introduced into the spray chamber using a hydraulic electric unit injector (HEUI) [13-10]. A wide range of injection pressure from 50 to 150 MPa were tested. The liquid and vapor regions of DME jet were visualized using a hybrid Schlieren/Mie scattering at non-reacting conditions. Cung et al. [13-11] studied the formation of formaldehyde (CH_2O) in DME combustion and suggested that the start of the depletion of CH_2O can be used as an ignition indicator. In this study, high-speed natural flame luminosity of DME combustion was used to capture the flame intensity. PLIF imaging was used to characterize CH_2O evolution to study the low-temperature reaction prior to ignition. Spray and combustion characteristics of DME were compared with diesel including liquid/vapor penetration, ignition delay (ID), flame lift-off length (LOL), flame structure, and CH_2O formation of DME through visualization techniques. The detailed DME spray and flame structure were also investigated numerically through Large-Eddy Simulations (LES). Therefore, the main objectives of this study are to firstly, characterize high injection pressure (150 MPa) DME spray combustion using optical diagnostics and compare with diesel; and secondly, investigate the CH_2O formation, ignition process and subsequent cool flame formation mechanism under condition of high injection pressure using experiments and high-fidelity LES modeling.

13.3 Results and discussions

13.3.1 Non-vaporizing and Vaporizing Spray Characteristics

Non-vaporizing condition in this work refers to a 383 K N_2 ambient with 14.8 kg/m^3 ambient density. Non-vaporizing condition is defined based on diesel because 383 K is much lower than diesel's boiling point (>453 K). However, at 383 K, DME shows quick evaporation due to the larger vapor pressure (3.95 MPa [13-18]).

To investigate the fast evaporation characteristics of DME under different injection pressures (50 MPa and 150 MPa), microscopic images at the near nozzle region (0 ~ 6.5 mm from nozzle tip) are shown in Figure 13-1. These images are taken with a frame rate of 40,000 fps and high resolution. There are some transparent sections at the interface of fuel and air. For example, they are seen at 0.05 and 0.075 ms after the start of injection (ASOI) in 50 MPa injection pressure cases and 0.075 ms ASOI in 150 MPa cases. The transparent region is DME vapor partially due to the flash boiling effect. The edge of the spray showed wavy disturbance but not multiple droplets. Since DME has very high vapor pressure and low surface tension (only 44% of diesel surface tension at 297 K [13-19]), we assume the evaporation occurs rapidly and there is no sufficient time for secondary breakup occurrence. A Levich liquid breakup length correlation is [13-20]:

$$L_{brk} = C_l d_{noz} \left(\frac{\rho_l}{\rho_a}\right)^{1/2} \qquad (13-1)$$

where ρ_l is liquid density, ρ_a is air density, d_{noz} is the effective diameter of the injector nozzle, and C_l is Levich constant. Levich constant C_l= 11.0 is found to be the full breakup length in Schneider 's experiments [13-21]. Reitz et al. also reported a similar number C_l

= 10 [13-22]. A smaller value $C_l = 5.5$ was used by F. X. Tanner [13-23] to determine the initial drop deformation velocity. For DME, L_{brk} is $6.65\,mm\ (C_l = 5.5)\ to\ 13.29\,mm\ (C_l = 11)$. As seen in Figure 13-1, the DME vapor is present within the 6.5 mm distance from the injector tip, which is even shorter than the minimum possible breakup length of 6.65 mm. This confirms the hypothesis that the evaporation of DME happens before the secondary breakup. Noted that the liquid DME will not evaporate completely before the secondary breakup, most of the evaporation process still occur in a downstream location. However, the evaporation of diesel is only from the secondary break-up and atomization and not from the primary break-up. Besides, high injection pressure leads to high exiting velocity from the nozzle and further enhances fuel-air mixing, which shortens the evaporation process. As it is shown in Figure 13-1, the vapor region is seen earlier time in 150 MPa case compared to 50 MPa case. Note that DME is not strictly following a typical fuel atomization process including 4 sub-processes: primary break-up, secondary break-up, coalescence of droplets, and the evaporation. The sub-processes of DME may not have a very clear boundary and overlap in temporal and special manner.

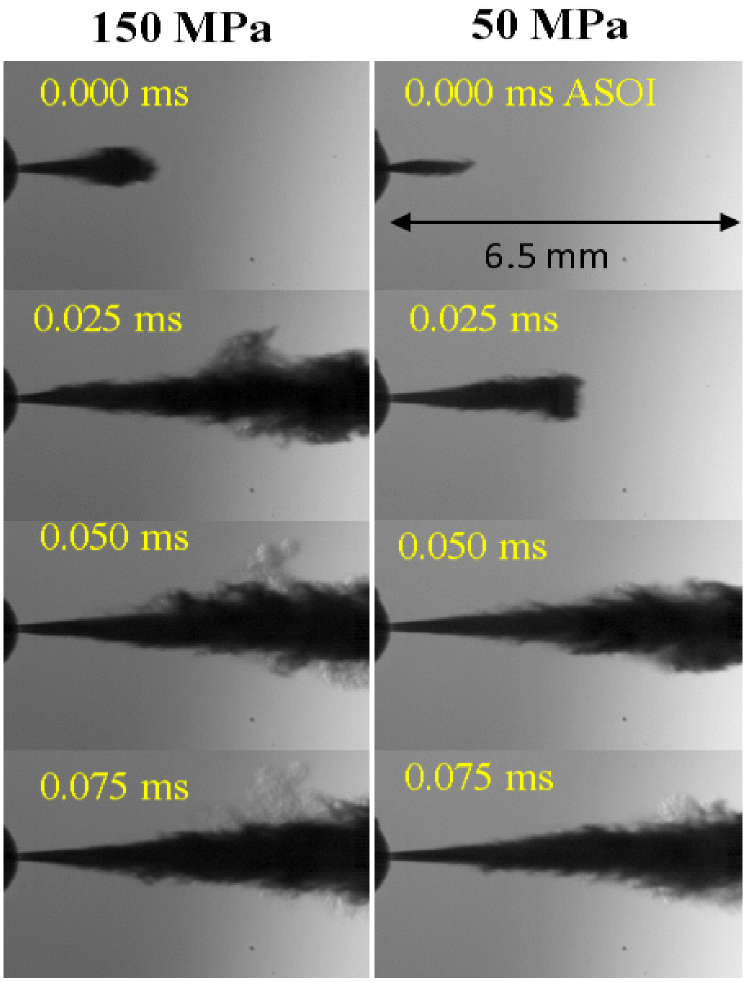

Figure 13-1 Microscopic imaging of DME spray at the initial stage of injection (non-vaporing condition)

The penetration is defined as the distance in the axial direction from the injector tip to the leading edge of the spray. For both diesel and DME fuels, liquid penetrations in non-vaporing spray, and liquid/vapor penetrations in vaporizing spray are shown in Figure 13-2. Overall, the penetrations of DME and diesel follow a similar trend, but penetrations of DME are always shorter than diesel cases at any given time ASOI at all conditions. The penetrations under non-vaporizing condition increase until the fuel spray reaches the wall of the vessel (89 mm to the nozzle). The vapor penetration follows a similar trend of non-vaporing liquid penetration that increases with decreasing velocity, but with slightly lower penetration distance due to more aerodynamic drag caused by high air entrainment at vaporizing condition. The initial velocity of DME at the nozzle exit is higher than diesel because of DME's low liquid density as expressed by the following equation, $U_f = C_l\,(2\frac{p_f - p_a}{\rho_f})^{1/2}$. However, the fast evaporation of DME leads to strong air entrainment which dissipates the kinetic energy quickly and slows down the spray. Liquid length of diesel was about 40 mm during the steady state of injection while it was about 18 mm for DME. The shorter liquid length of DME will reduce the possibility of impingement on the piston and/or cylinder wall which can cause pool fire and an increase in soot emission.

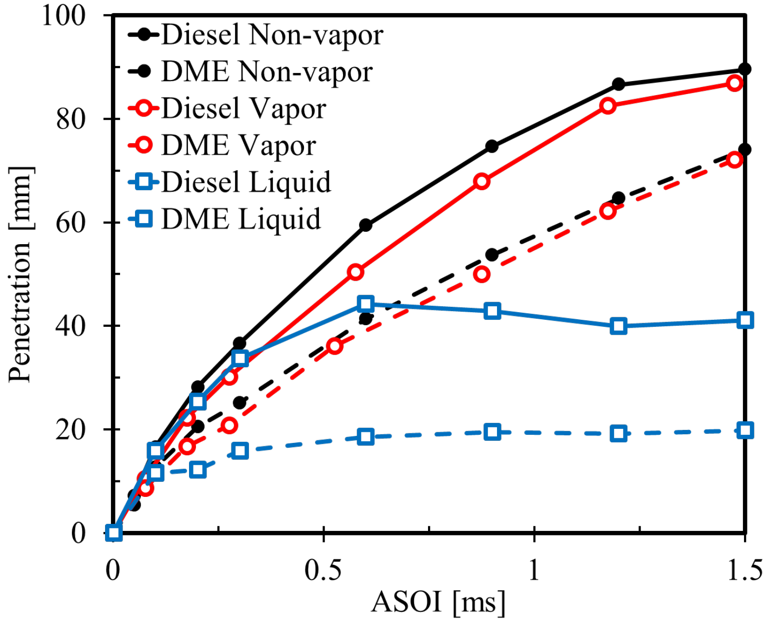

Figure 13-2 The spray penetrations of diesel (solid line) and DME (dashed line) (non-vaporing and vaporing conditions)

13.3.2 Combustion Characteristics

The combustion tests were conducted at the ambient conditions of 900 K and 14.8 kg/m^3. The ID is described as the time between the start of injection and the start of combustion. The method used in the study to determine the ID is to measure from high-speed flame luminosity image. The ID of DME is 0.8 ms which is shorter than that in diesel combustion (1.5 ms) because DME has a higher Cetane number. The ignition location of DME is about 35 mm away from the nozzle while diesel's ignition location is about 75 mm away from the nozzle. The ignition location in this study defined as the first visual bright spot in the high imaging. The bright spot is detected through a threshold method during image processing. If at the lower ambient temperature that below 900 K, the ignition location of diesel will be closer to the CV wall (89 mm away from the nozzle). This will raise the chance of heat loss from the diesel vapor to the cold wall (383 K), which may further delay the ignition. In that situation, the ignition of diesel happens at the wall location. DME has very low flame luminosity implying low soot production. Diesel tests used the same optical setup as DME but with a neutral density filter (OD 0.8). Even with the signal reduction, diesel still has very strong flame luminosity caused by higher soot formation. A comparison of AHRR between diesel and DME is shown in Figure 13-3. Each case shows an averaged value of 3 test repeats. The AHRR curve can be divided into two parts by the first "abrupt peak". It is the premixed combustion regime before the peak and the diffusion combustion regime after the peak. Firstly, because a higher Cetane number (55-60) of DME leads to faster ignition and less time for DME to be premixed with the oxidizer. DME shows around 0.4 ms shorter ID than that in diesel case seen in Figure 13-3. In addition, the mixing rate of diesel with air is higher than that of DME [13-25]. Therefore, DME has both less time for mixing before ignition and less mixing rate compared to diesel. This may explain why the peak AHRR of DME is lower than that of diesel, indicating weaker premixed combustion. Secondly, DME has a large diffusion combustion portion (under the second peak at 2.4 ms). The ratios of the first peak and the rounded peak are 1.93 and 1.05 for diesel and DME, respectively, which gives the idea of heat release distribution between the premixed combustion and diffusion combustion. The strong diffusion combustion of DME is because its fast evaporation property keeps a high evaporation rate after the ignition happens.

A cumulative heat release (CHR) comparison between diesel and DME is also shown in Figure 13-3. DME produces only half of the CHR of diesel with similar high injection pressure (150 MPa) since DME has lower fuel density and inferior lower heating value than diesel at the same temperature. Therefore, more DME should be delivered to reach comparable energy output of diesel (to maintain similar fuel energy content). Several rates of injection results have been reported in the authors' previous work [13-26]. The overall injection duration of DME is more sensitive to the injection pressure change than diesel's. At low injection pressure, DME has a shorter actual injection duration. Only at high injection pressure (>100 MPa), DME has a similar injection duration with diesel. Overall, the total injected mass in diesel case is larger than that in DME within the injection pressure range of 70 MPa to 150 MPa. Both fuels show a monotonically increasing trend but with a different increasing rate when injection pressure increases. The high injection pressure effect on increasing the total injection mass is more favored in DME injection. This trend implied the high injection pressure can mitigate the differences in energy content for DME and diesel mainly introduced by the low heating value of DME. In addition, DME has long hydraulic injection delay using HEUI at low injection pressure due to higher compressibility (e.g. inverse of the modulus of elasticity) than diesel (2x) and thus its pressure release process through injector tip takes longer time. The high injection pressure can dramatically reduce DME's injection delay and let it reach a similar level of diesel when injection pressure is above 150 MPa.

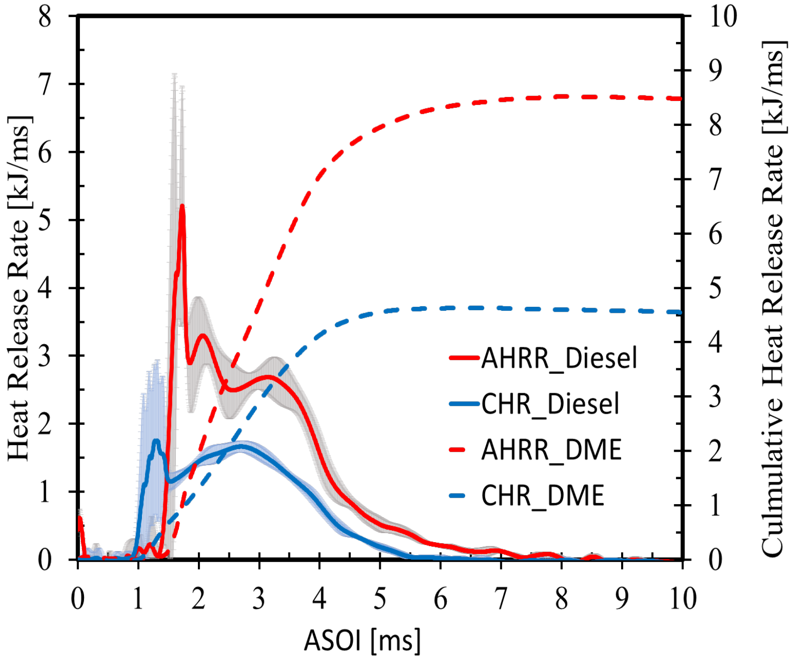

Figure 13-3 AHRR and CHR comparison between diesel and DME, (combusting condition, 15% O_2)

Figure 13-4 shows the overlap of schlieren images (blue color highlighted with red boundary) and PLIF images (highlighted with yellow boundary) with time sweeping for a combusting case. Test conditions are ambient of 14.8 kg/m3, 18% O2, 900 K. Laser were shot at a different time during the spray to obtain the temporal CH_2O formation information. CH_2O-PLIF region is processed with false-color. The outer boundary indicates the schlieren image contains the density gradient information from the liquid spray, vapor spray, and the flame. The flame luminosity (the higher intensity region) was superimposed on the image too. The dashed line indicates the front of the CH_2O region. CH_2O is known to be an important radical during the first stage (cool flame) of ignition. Its formation and concentration change can be used to identify ID [13-11]. Before ignition, DME mixes with hot ambient. During this low-temperature reaction stage, CH_2O is formed. CH_2O-PLIF image occupies the same region of schlieren. At the timing of ignition, the temperature rises significantly and AHRR reaches its peak. CH_2O concentration reaches a peak. CH_2O seems to start diminishing upon ignition (0.85 ms). It starts at the radial periphery region. As shown in Figure 13-4, the schlieren signal first time uncovered from the CH_2O-PLIF at the radial periphery region. According to the combusting test results, the ignition can happen at any location outside the CH_2O region, which may not necessary on the leading edge. After ignition (from 0.85 ms to 1.6 ms ASOI), CH_2O only extended to a certain length (~57 mm) from the nozzle tip. The rate of injection (ROI) profile shown in Figure 13-5 also shows steady value during this period, and the liquid length is 18 mm. Liquid DME is injected into the combustion chamber at a constant flow rate, mixing with hot ambient gas, forms CH_2O. On the downstream side, the combustion is consuming CH_2O through H-abstract reaction with OH to form HCO [13-27, 14]. Therefore, during this stage, the concentration of CH_2O is relatively stable. At the ASOI 1.9 ms, the injector starts closing, and there is a sudden decrease in ROI, resulting in the shorter CH_2O penetration. From 2.9 to 4.15 ms, CH_2O was gradually decreasing. Please note that the injection has already ended at 3.3 ms. The diminishing CH_2O is reasonable because the parent species of CH_2O is finished while there is no more incoming spray.

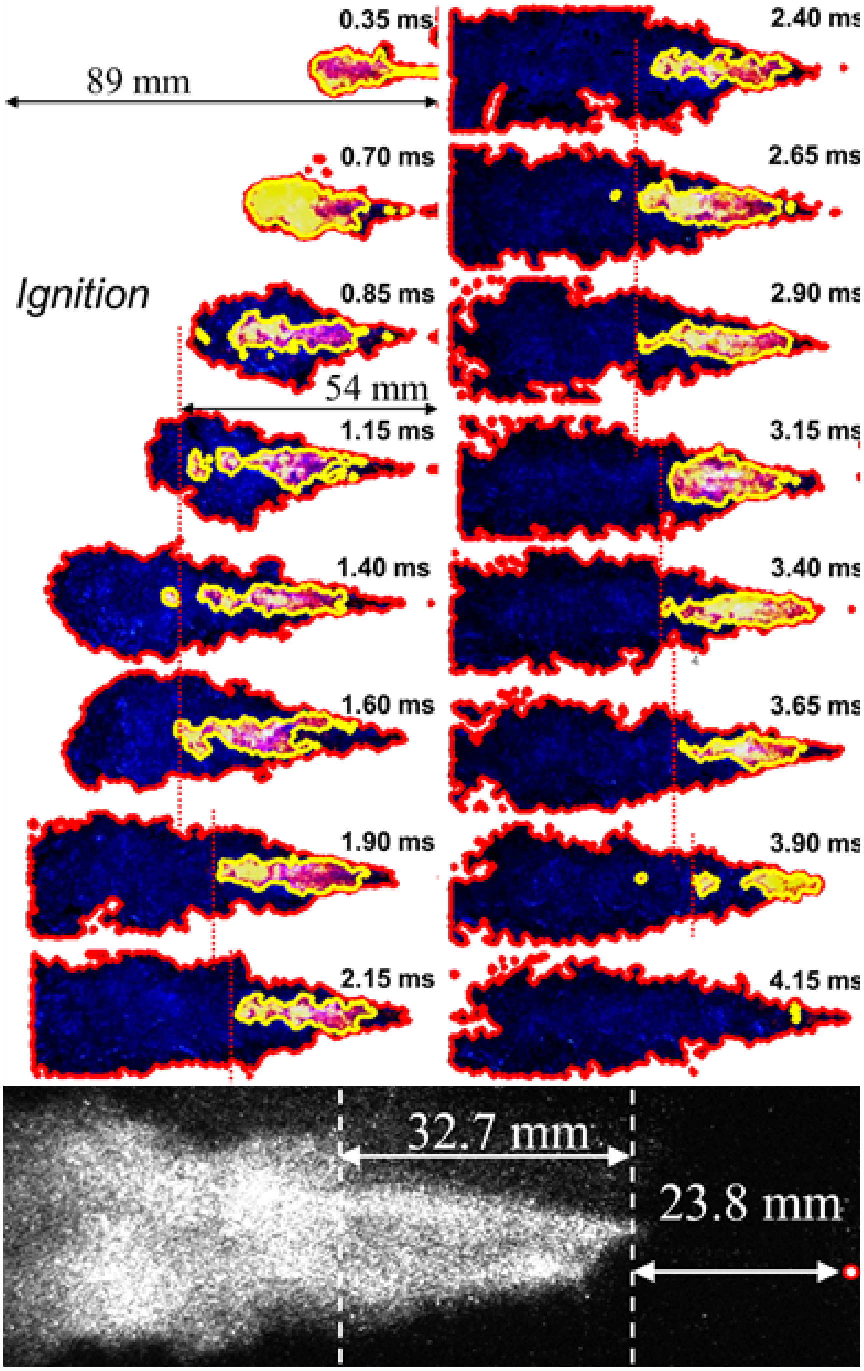

Figure 13-4 Schlieren (outer) overlap with PLIF (inner) images (top) and OH* chemiluminescence (bottom), (combusting condition, 18% O_2)

The OH* image shows the LOL is 23. 8 mm which is higher than the liquid length. There is a low intensity region after the LOL spans 32.7 mm. This region is at the spray core location corresponding to the CH_2O. The leading edge of the CH_2O-PLIF during the steady-state after ignition located 54 mm away from the nozzle. It agrees with the low-intensity region leading-edge location 32.7+23.8= 56.5 mm. This implies the transition from the cool flame to high-temperature combustion.

The overlapping CH_2O-PLIF images were used to understand the CH_2O evolution associated with the ROI profile. The integration of the intensity in CH_2O-PLIF images was performed and normalization of the total integration at each frame with the highest intensity frame, as shown in Figure 13-5. The normalization method is applicable because the laser was kept running at least 20 mins to warm up and to guarantee a stable energy output (145±5 mJ/pulse). It was found that CH_2O concentration reached a peak, then stayed a quasi-steady state during injection, and eventually dropped until injection ends. The peak in CH_2O is corresponding to the ignition timing.

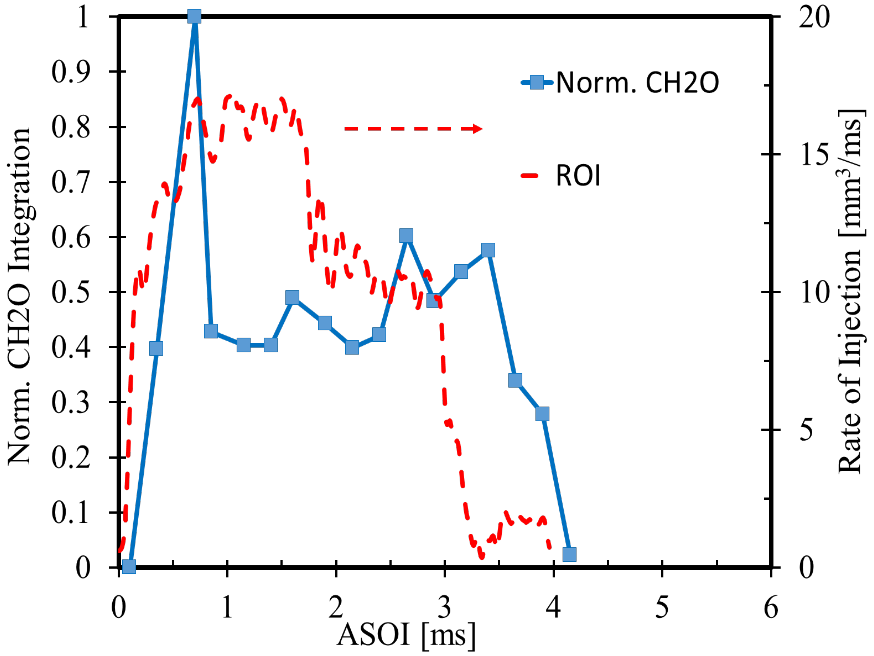

Figure 13-5 Normalized total Integration of CH_2O under combusting condition (18% O_2)

13.4 CFD simulation results

Based on DME spray and combustion experimentation, CFD simulations have been performed using the Converge CFD code [13-28]. CFD work was done for non-reacting sprays first to ensure proper spray mixing (not shown here), later analyzing the DME ignition process using the LES turbulence model with a 62.5 µm fine grid and total of 25 million cells. Validation with experimental data pertaining to cool-flame species formation (CH_2O) and spray-flame generation (ignition and stabilization) was performed. The injection duration of liquid DME was 2.3 ms at 75 MPa rail pressure, and ambient temperature/density was 900K/14.8 kg/m^3 in an 18% O_2 ambient. Simulations were performed at a lower injection pressure of 75 MPa, unlike a higher-pressure of 150 MPa, since there was more validation data available for the lower injection pressures to aid LES model setup development.

For both experiments and CFD, ID is calculated based on AHRR (pressure derived), where 10% of the rise in AHRR corresponds to high-temperature ignition. For CFD, LOL follows the traditional definition of diesel spray flames corresponding to an axial extent of 2% of mass fraction of hydroxyl species in the upstream region. LES calculations were performed using three realizations. The ID was 0.915 ms, 0.95 ms, and 0.93 ms (averaged value is 0.93±0.017 ms), for three realizations respectively, and the LOL is 25.96 mm, 30.59 mm, and 27.92 mm (averaged value is 28.16±2.32 mm). Experimental ID and LOL are 1.03±0.015 ms and 20.87±2.20 mm. The LOLs predicted are ~4 mm higher than experiments considering the deviations, which can be due to the LOL definition employed by CFD and also considering the fact that OH was used as measurement species and not OH* as in experiments.

Stabilization of the flame is related to the formation of cool flame since fuel-air gets mixed and heat is released at the upstream zone prior to LOL. CH_2O species are the commonly considered species signifying cool flame. Figure 13-6 shows experimental CH_2O profiles compared with LES. The overall extent and temporal CH_2O formation are captured well by the simulations. Experiments show some CH_2O signals in the far-upstream regions near the injector, which is mostly due to liquid scattering of the incident laser. The upstream formation of CH_2O near the end of the liquid length (~10 mm) is an indicator of low-temperature chemistry initiation in those zones. This paves the way for the generation of high-temperature ignition kernels upstream, which would in-turn stabilize the flame.

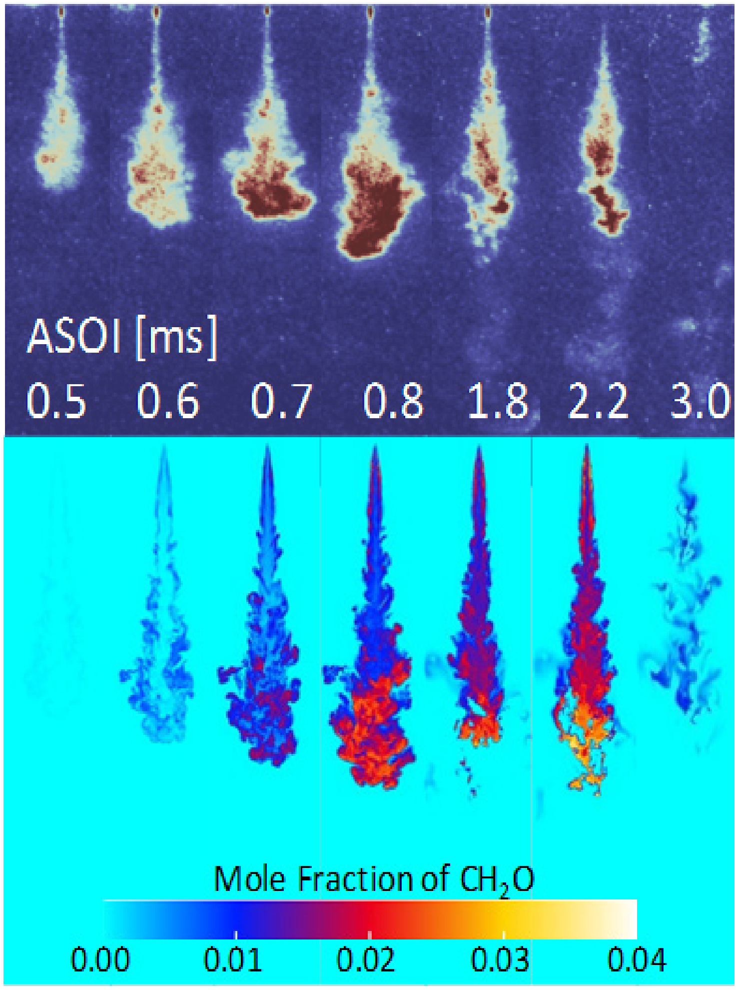

Figure 13-6 CH_2O profile comparison between experiment and LES

Some key features of DME spray combustion from both experimental and simulation results are shown in Figure 13-7. For the top and middle CFD snapshots, there are high-temperature ignition kernels generated out of an auto-ignition event in the boundary of low-temperature species (CH_2O) and high-temperature species (OH). These auto-ignition kernels keep the flame stabilized causing a quasi-steady LOL and maybe quenched and re-ignited depending on the surrounding spray induced turbulence field. The presence of auto-ignition kernels was also found in diesel simulations performed with LES and was validated with experiments [13-29]. In the last CFD snapshot, an event termed as a combustion recession is seen to take place (as also found in the accompanying experimental image). This recession event is generated when all the low-temperature species (CH_2O) are consumed by OH species indicating a high-temperature reaction.

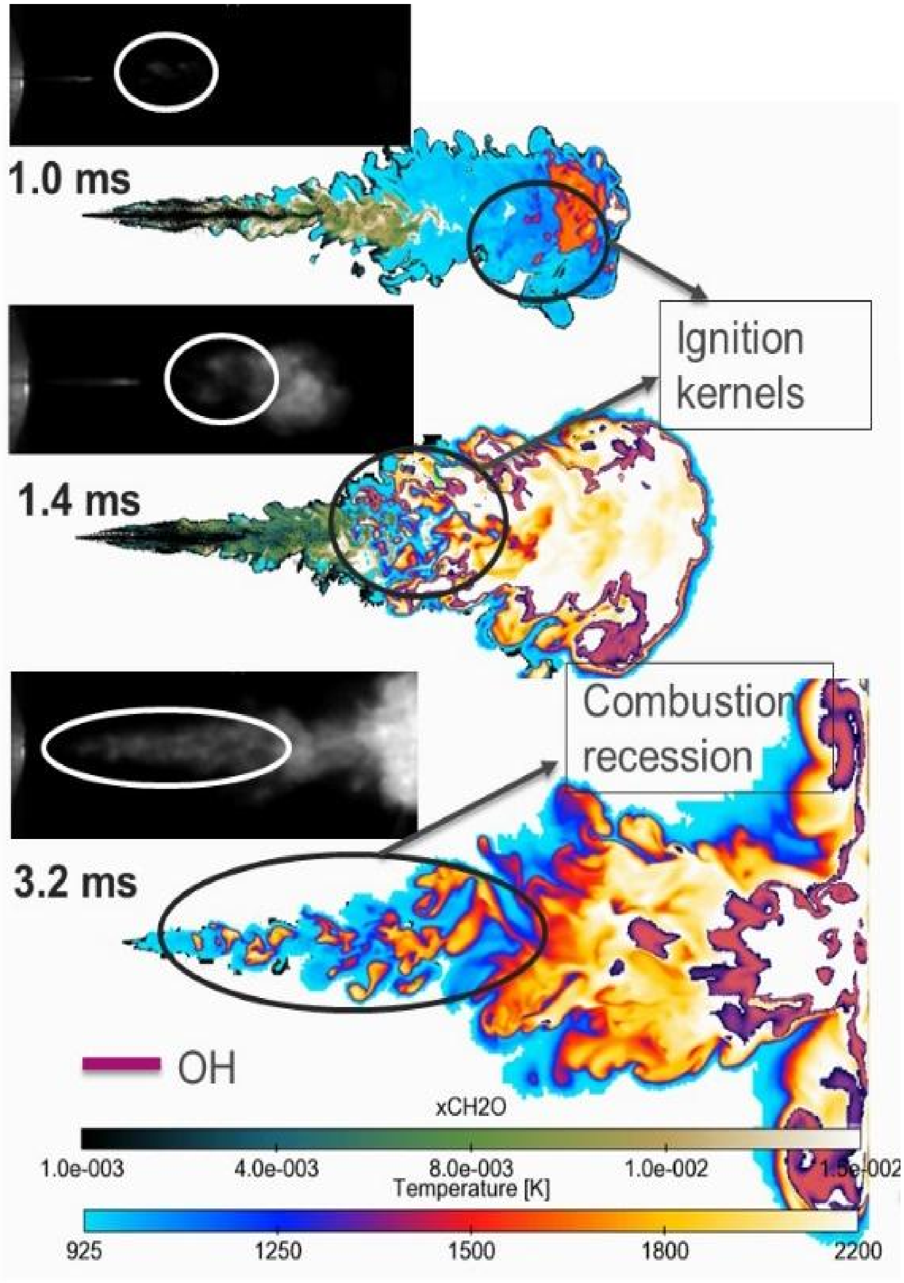

Figure 13-7 Key transient DME flame development features.

13.5 Summary and discussions

In this study, ROI and spray tests have been done with a high injection pressure dual-fuel delivery system. The spray test consists of non-vaporizing, vaporizing, and combusting tests in a constant volume combustion vessel under engine-like conditions. High injection pressure DME and diesel spray and combustion characteristics have been observed and compared carefully through experiments. A summary of the results is as follows:

- Compared to diesel, DME has shorter liquid and vapor penetrations due to its low fuel density and fast evaporation. The microscopic imaging also shows DME evaporates quickly before the secondary breakup. The fast evaporation leads to shorter liquid length.
- DME shows shorter ignition delay at high injection pressure. The flame luminosity also appears with low intensity implying near-zero soot production.
- From the AHRR and CHR results, DME has faster ignition, weak premixed combustion, and high ratio of distribution on the diffusion combustion due to the fast evaporation property.
- CH_2O concentration reaches its peak at the same time of ignition and maximum AHRR but starts to decrease after the ignition. CH_2O consumption indicates the transition from low-temperature combustion to high-temperature combustion and is affected by ROI and chemical pathway.

14 DME Combustion Instability Investigation

14.1 Brief overview

While the development of the LTC combustion concept, the operation conditions are pushed to limit. In addition, some undesired operation scenarios like cold start or high altitude increased the possibility of unstable combustion events. The unstable combustion usually deviates from the desired equivalence ratio, leads to low efficiency as well as engine damage (e.g. piston erosion). This study is trying to identify the occurrence conditions of instability and attempts to quantify the instability and understand its mechanism. With a well-validated instability quantification tool, we will be able to predict and evaluate the instability, moved the operating map away from the instability region in the engineering design process. Otherwise, identify all the instability regions through numerous tests is a very costly process.

14.2 Experimental observation:

14.2.1 Evidence of occurrence: ringing pressure

During the tests at conditions of injection pressure of 150 MPa (2ms duration), ambient temperature of 750K, the ambient density of 14.8Kg/m^3, and Oxygen level of 18%, some unusual pressure traces with a large level of pressure oscillations were recorded.

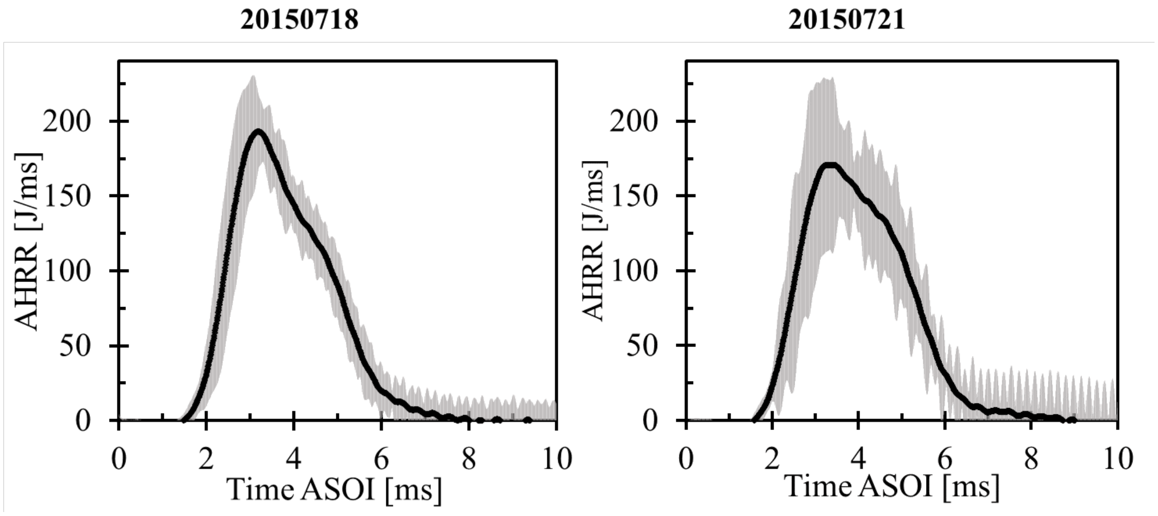

Figure 14-1 Two averaged AHRR results of the combustion at the conditions of injection pressure of 1500 bar (2ms duration), the ambient temperature of 750K, the ambient density of 14.8Kg/m3, and Oxygen level of 18%

As shown in Figure 14-1, The averaged AHRR traces (out of five repeats) from two different test dates both show large standard deviations, which means the large variations from case to case. This implies the unstable combustion which needs to be further investigated. Two single AHRR results are selected out, one has ringing pressure, another has a normal smooth trace. As shown in Figure 14-2, compared to the less ringing case, the ringing case has a slightly higher peak AHRR and ringing oscillation throughout the combustion event. The magnitude of the ringing is about 30 to 40 J/ms, which is about 12% of the peak AHRR. The oscillation tends to occur with a relative stable frequency.

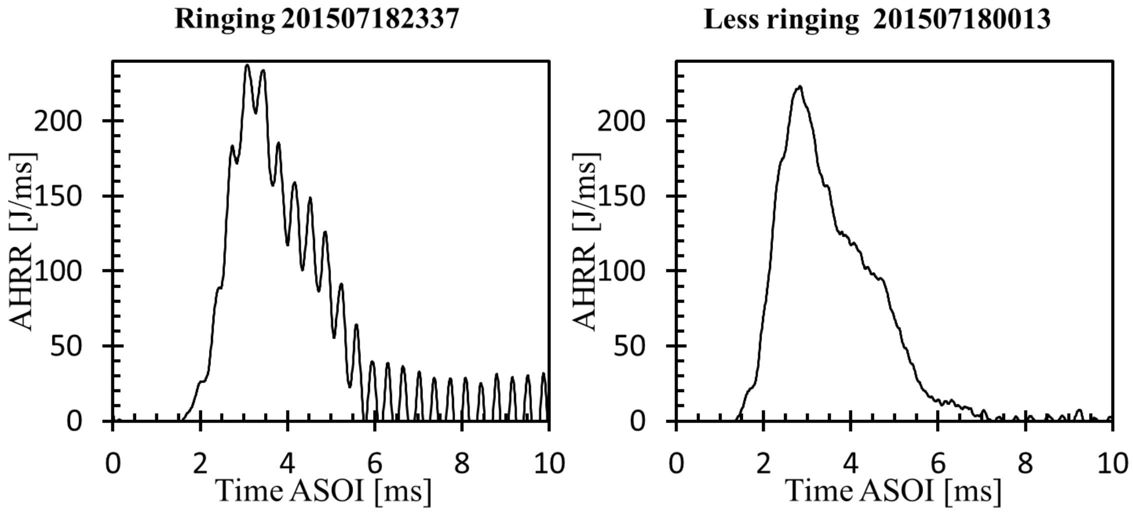

Figure 14-2 Single AHRR result from a ring case and less ringing case at the conditions of injection pressure of 150 MPa (2ms duration), the ambient temperature of 750K, the ambient density of 14.8Kg/m3, and Oxygen level of 18%

Figure 14-3 shows the photo of flame luminosity imaging in a temporal sequence. The three images are selected at ASOI 3.15 ms, 5.00 ms, and 6.26 ms which correspond to before ignition, after ignition, and ending phase of the combustion. With an LED light shining at the injector tip, the liquid portion of the spray is also visual through Mie scattering signals. The less ringing case already showed an early flame kernel at ASOI 3.15 ms, while the ignition of ringing was still not happening until 0.2 ms later. The delay ignition of the ringing case contributes to an elongated premixed combustion phase. A larger amount of fuel penetrates towards the wall and was mixed with ambient air and accumulated near the wall. After the onset of the ignition, the luminosity imaging of the ringing case exhibits higher intensity compared to the less ringing cases. In the raw imaging (intensity ranges from 0 to 255), the peak intensity in the image of ASOI 5.00 ms is 61 and 20 for the ringing cases and less ringing cases respectively (three-fold difference).

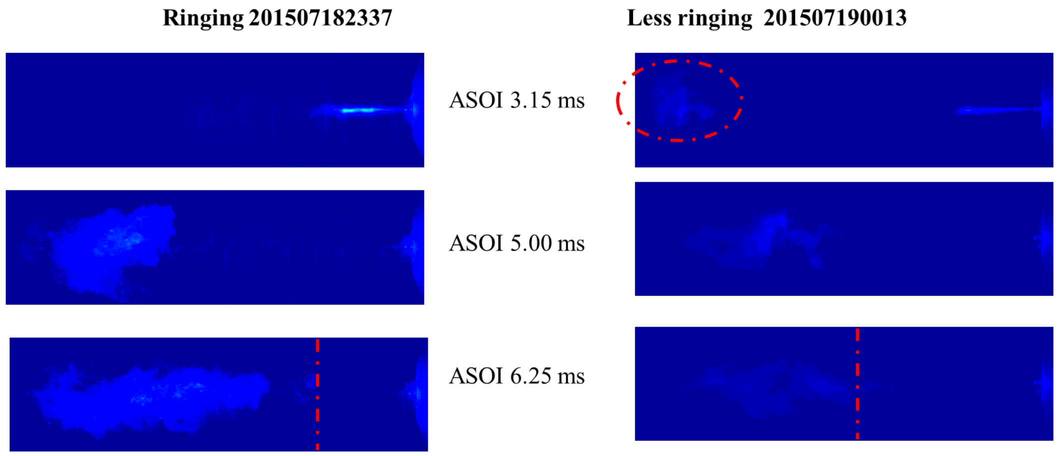

Figure 14-3 Natural luminosity from a ring case and less ringing case at the conditions of injection pressure of 1500 bar (2ms duration), the ambient temperature of 750K, the ambient density of 14.8Kg/m3, and Oxygen level of 18%

The difference of the cumulative intensity of the whole flame excluding the injector parts are even bigger, 621335 vs 116520, holding a 5.33 times difference. The high intensity of the flame can be related to the rate of rising from the rising edge of the AHRR curve. The ringing case has a 156 J/ms^2 which is 10 percent faster than the less ringing case (143 J/ms^2). The high intensity was kept in the ringing case untill the end of the combustion. A flame recession towards the injector tip side was found both in ringing and less ringing cases. However, the flame recession of ringing cases approached closer to the injector tip. A typical flame recession term in diesel spray combustion usually happens at high-temperature conditions, whereby a lifted flame retreats toward the injector tip at the end of injection. The flame recession is beneficial to clear out the unburned hydrocarbons, thus, to reduce the emissions. The recession of the DME flame is in a different scenario. First, the ambient temperature is low compared to a conventional diesel flame recession case.

Second, the elongated flame recession in the ringing cases can be partially related to the pressure wave generated from the onset of the ignition. The pressure wave tends to push the combusting mixture to the injector tip direction.

14.2.2 Data processing methodology

In order to further analyze the data from both experimental and simulation. A MATLAB script has been developed to process the data. For experimental data, the analysis is based on the AHRR data (as shown in Figure 14-4). A moving average filter with a mesh size of 50 data points was used to get the averaged value. The oscillation part was extracted out by subtracting the averaged value from the original AHRR value, shown in Figure 14-4 as the orange line on the bottom. The reference baseline is 0 for the oscillation portion.

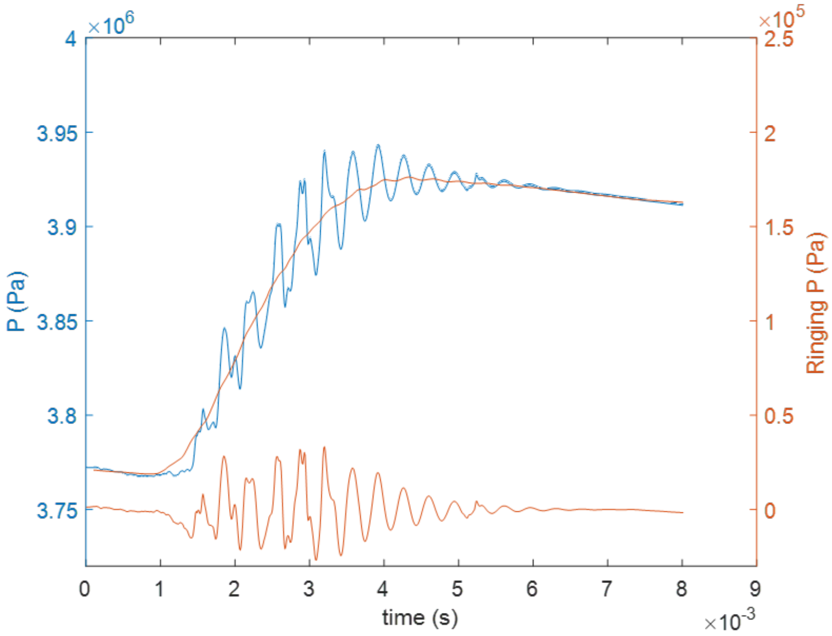

Figure 14-4 Data processing illustration of the oscillation AHRR portion extraction

The positive, negative peak value, the P2P (peak to peak) value of the extracted oscillation AHRR portion have been calculated. A ringing index (RI) was defined to evaluate the severity of the ringing oscillation by doing the integration of the extracted oscillation AHRR portion over time. An FFT analysis was performed on the AHRR traces to unveil the frequency pattern that may relate to the oscillation. A similar analysis was also performed on the pressure data from the CFD results.

14.2.3 Statistic summary of all the ringing cases: qualitatively summarize occurrence conditions

This part summarizes all the ringing cases (total 11) from the specific condition of injection pressure of 1500 bar (2ms duration), the ambient temperature of 750K, the ambient density of 14.8Kg/m3, and Oxygen level of 18%, and tries to understand more about the occurrence of oscillations. First, AHRR profiles of all the repeated tests are shown in Figure 14-5. Most of the cases except for case 0013 shows some level of the oscillation in AHRR. Through visual checking, it can be easily found that cases such as 1710 and 2323 experienced massive oscillation and cases 1724 and 2325 only show very mild signs of ringing. The next step to use the results from the MATLAB processing to quantitatively analyze these cases.

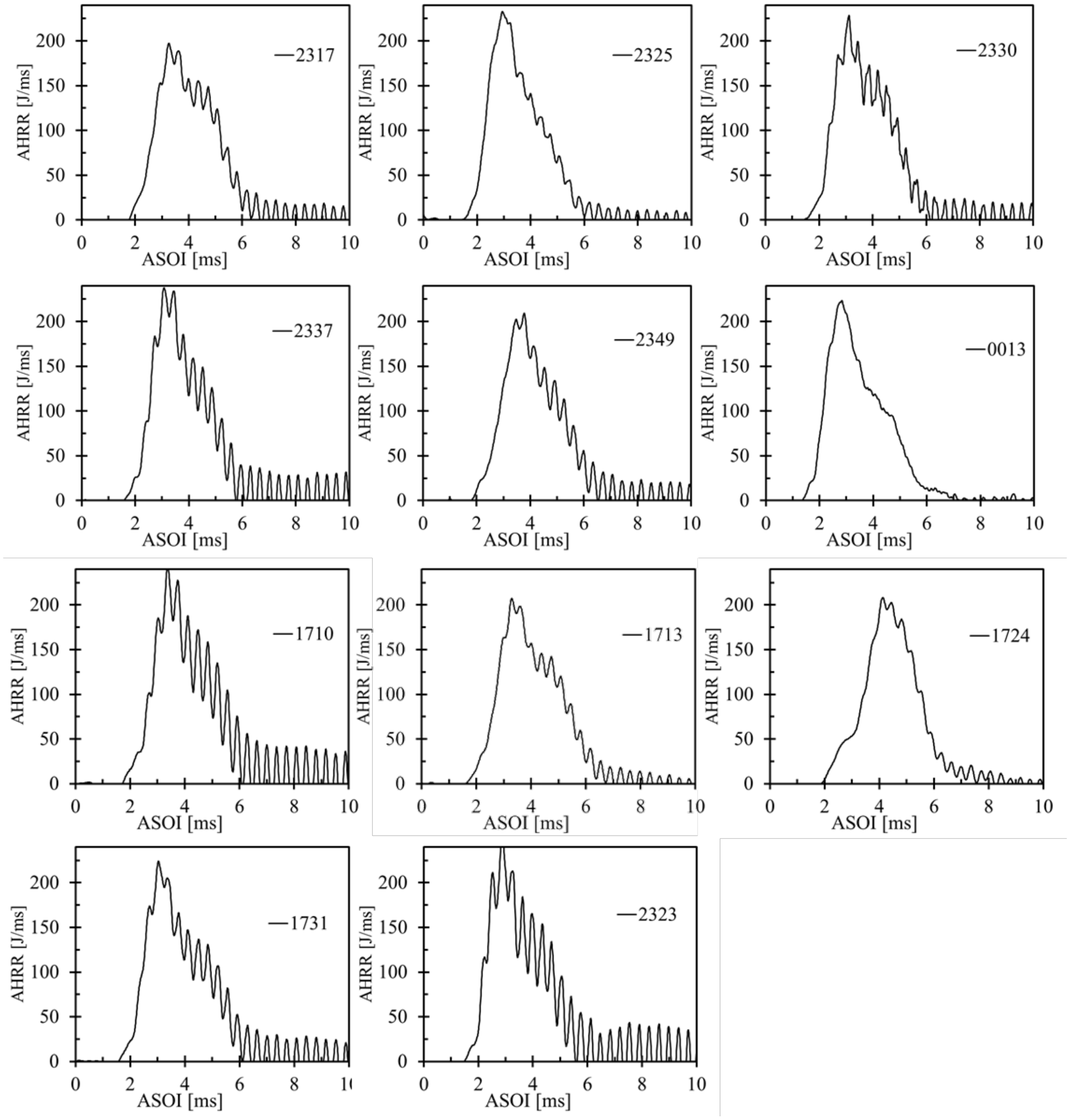

Figure 14-5 AHRR of all the repeated tests (total 11) from the condition of injection pressure of 150 MPa (2ms duration), ambient temperature of 750K, ambient density of 14.8Kg/m3, and Oxygen level of 18%

Table 14-1 Statistic summary of all the ringing cases

20170718	**2317**	**2325**	**2330**	**2337**	**2349**	**0013**
Peak AHRR [J/ms]	197.14	232.86	228.55	237.57	209.35	223.36
Peak timing [ms]	3.26	2.94	3.12	3.08	3.77	2.84
Peak positive [J/ms]	23.49	17.18	30.29	41.16	25.71	12.64
Peak negtive [J/ms]	23.13	17.87	35.91	40.72	25.95	11.08
P2P [J/ms]	46.63	35.05	66.19	81.88	51.66	23.73
Rate of rise [J/ms]	2.02	1.96	1.84	2.01	1.99	2.14
Ringing index	0.12	0.08	0.15	0.21	0.13	0.04
Ringing or not [0/0.5/1]	1	0.5	1	1	1	0
20150721	**1710**	**1713**	**1724**	**1731**	**2323**	
Peak AHRR [J/ms]	242.93	207.20	208.26	223.94	254.36	
Peak timing [ms]	3.37	3.29	4.13	3.03	2.87	
Peak positive [J/ms]	48.69	18.63	14.88	32.32	52.98	
Peak negtive [J/ms]	48.87	16.53	11.94	32.65	51.03	
P2P [J/ms]	97.56	35.16	26.82	64.97	104.00	
Rate of rise [J/ms]	2.00	2.13	2.25	1.99	2.04	
Ringing index	0.27	0.08	0.05	0.17	0.29	
Ringing or not [0/0.5/1]	1	0.5	0.5	1	1	

As listed in table 14-1, there is one line called rate of rising of the AHRR which is calculated from the start of raising to the peak of the AHRR. The “ringing or not” judgment includes three levels (0, 0.5, and 1) which is only determined using the ringing index from this condition and not a rigorous standard. The criteria used here is level 0 means no ringing case (RI < 0.04), level 0.5 is transient stage with only small ringing (0.04 < RI < 0.1), and level 1 means the ringing case (RI > 0.1). The purpose of developing this RI criterion is to extend the analysis to detect and compare other oscillation cases from different test conditions. The criteria used here can be tuned for better accuracy with more data point training. To verify the functionality of the RI method. P2P of the AHRR extraction is plotted against the RI value, as shown in Figure 14-6. It shows the clear linear correlation, which means the RI is honestly reflecting the oscillation severity. This conclusion still remains true when replacing the P2P with Peak_positive and Peak_negative data.

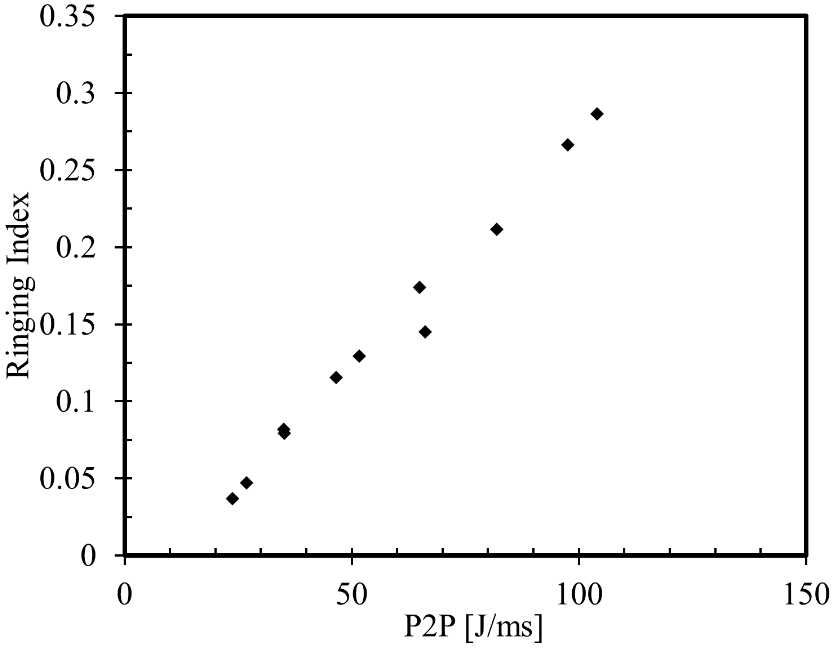

Figure 14-6 P2P of the AHRR extraction vs ringing index

To explore the causes of the ringing cases, the RI was evaluated in terms of the peak AHRR value and the rate of rise of the AHRR respectively, as shown in Figure 14-7. The RI has a gross positive correlation with the peak AHRR. Under the same test condition, the peak AHRR is affected by the premixed combustion which is influenced by the ignition delay. 700 K is a relatively low ambient temperature in the ICE applications, the combustion becomes unstable and the ignition time varies in a wide range. As shown in Figure 14-7, the peak AHRR has a week negative correlation with the ignition delay. Interestingly, even the high RI is related to a high AHRR peak, however, the rate of rise of AHRR doesn’t have a clear effect on the RI. All the ringing cases discussed so far are from the ambient conditions of 700 K. The next section will explore other ringing conditions at a lifted ambient temperature of 800 K.

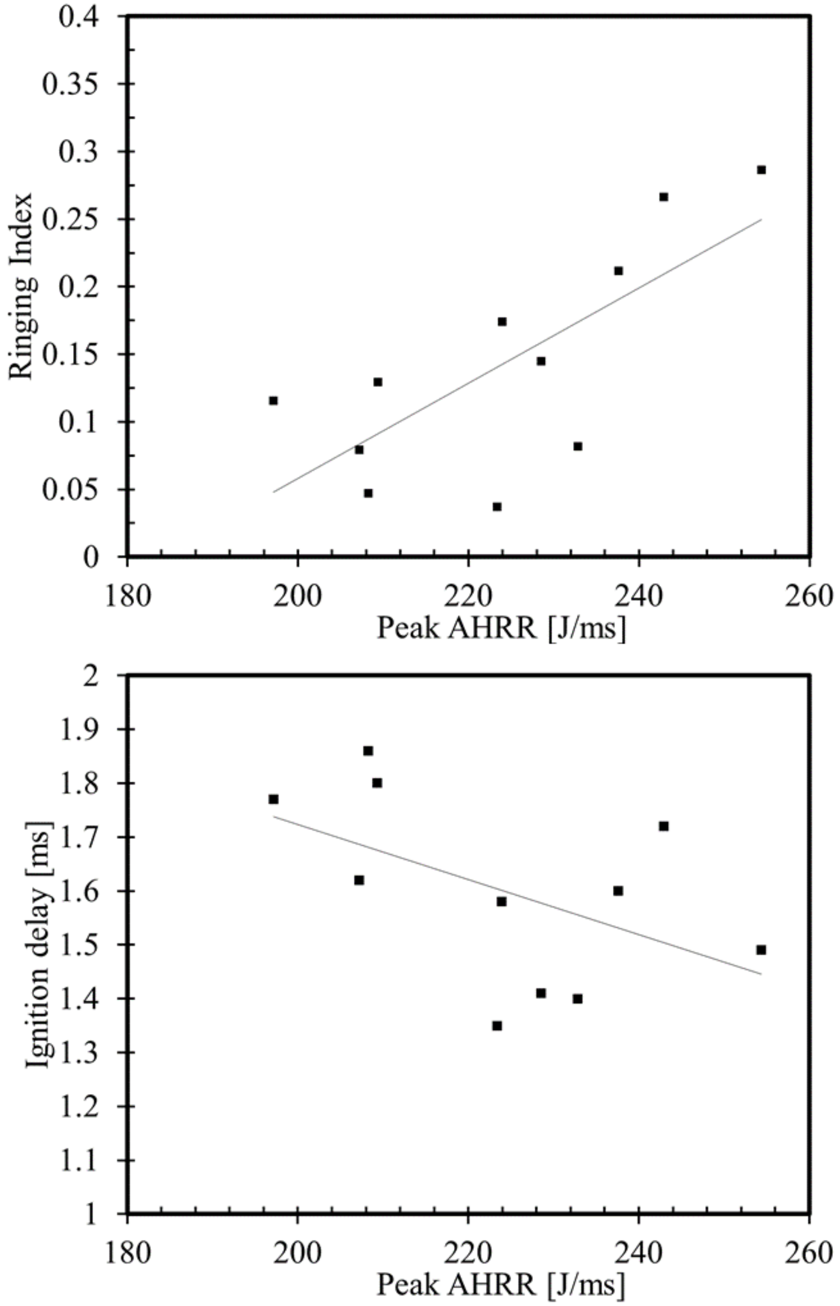

Figure 14-7 Ringing index evaluation against peak AHRR

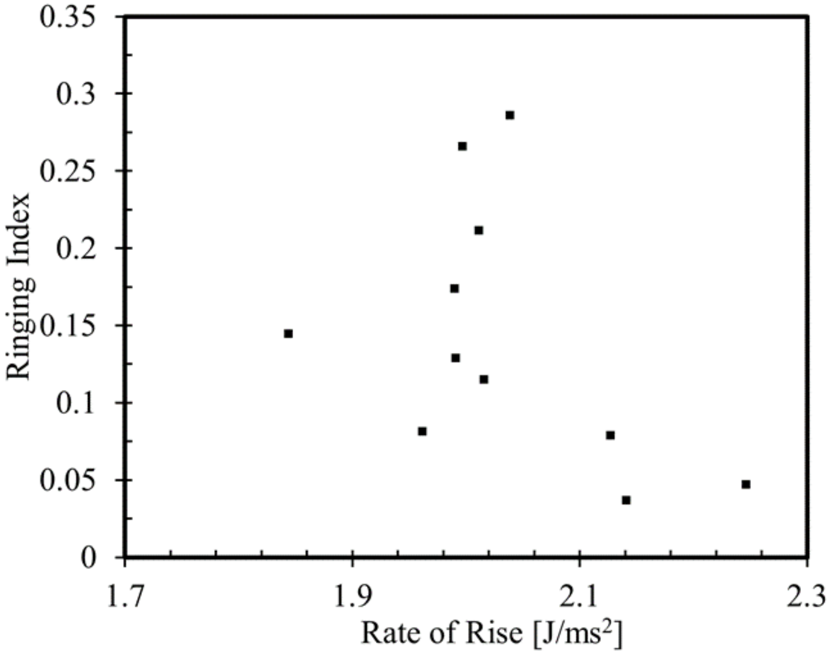

Figure 14-8 Ringing index evaluation against the rate of rise of AHRR

14.2.4 Other ringing cases

From the 700 K experiments, we found that the elongated premixed combustion starts off near the wall will produce a ringing case when the peak AHRR is high. In this section, the combination of injection pressure and injection duration were varied to explore the possibility of reproducing similar ringing scenarios. With the fixed injection pressure equals to 50 MPa, it extends the injector energizing time from 2ms to 3.3 ms. As shown in Figure 14-9, the injection duration of 2 ms case has a small AHRR peak (less than 50% of the 3.3 ms case), and almost no oscillations. The injection duration of 3.3 ms case delivers more fuel with higher sustainability, the injection persists until the fuel reaches the wall. The circled portion shows a flat but oscillating AHRR. It correlates to the timing of spray wall impingement from the high-speed natural luminosity imaging. According to the RI criteria, the 2ms and 3.3 ms cases are no-ringing (RI = 0.035) and ringing (RI = 0.102) respectively.

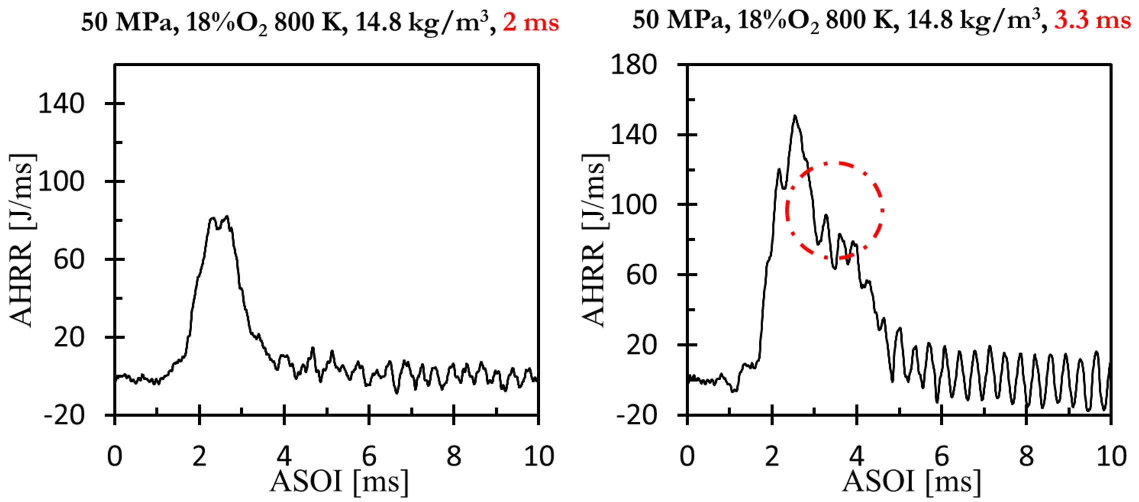
50 MPa, 18%O$_2$ 800 K, 14.8 kg/m^3, 2 ms

50 MPa, 18%O$_2$ 800 K, 14.8 kg/m^3, 3.3 ms

Figure 14-9 AHRR at 50 MPa injection pressure but with two different injection durations: 2ms and 3.3ms

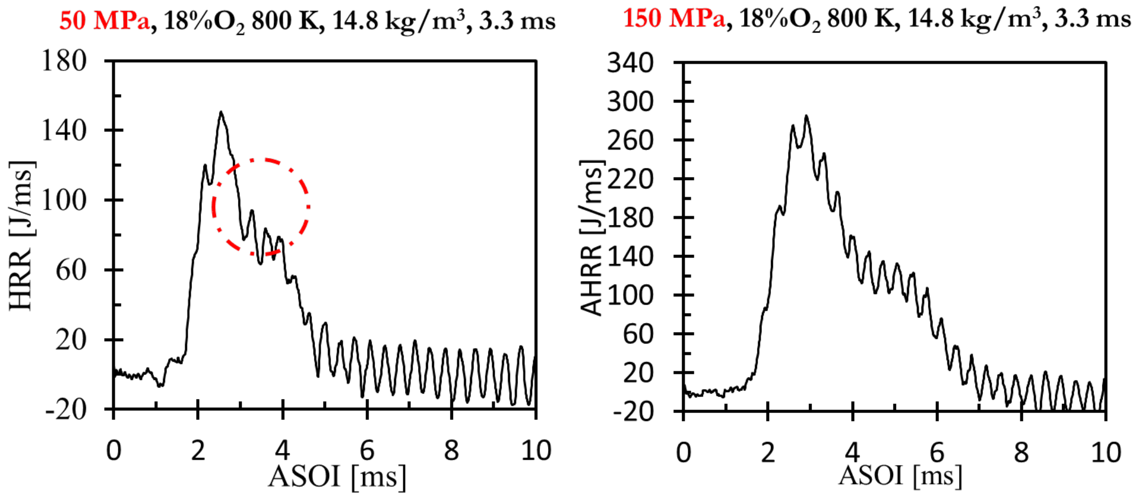
50 MPa, 18%O$_2$ 800 K, 14.8 kg/m^3, 3.3 ms

150 MPa, 18%O$_2$ 800 K, 14.8 kg/m^3, 3.3 ms

Figure 14-10 AHRR at 3.3ms injection duration but with two different injection pressures: 50 MPa and 150 MPa

With the fixed injection duration equals to 3.3ms, the spray wall impingement is guaranteed. A higher injection pressure of 150 MPa was tested, expecting to generate higher ringing with more spray wall interaction. As shown in Figure 14-10, the peak of AHRR from 150 MPa is almost twice of the 50 MPa case. With more injected fuel, stronger impingement, the 150 MPa did generate a higher ringing index of 0.142 which has a 40% increase.

14.2.5 FFT analysis

The FFT analysis was performed on one representative case 2337. The time domain was divided into three: A is from beginning to the peak of the AHRR, B is falling edge, and C is the flat oscillating portion. The FFT analysis was done independently in three regions. The y-axis shown in Figure 14-11 is the normalized power density spectral density (PSD) to emphasize the key frequency spikes. All three regions have a common spike at around 3000 Hz. Considering the geometry of the CV (0.1 m cube), 3000 Hz corresponds to a 600 m/s acoustic wave bouncing inside the CV.

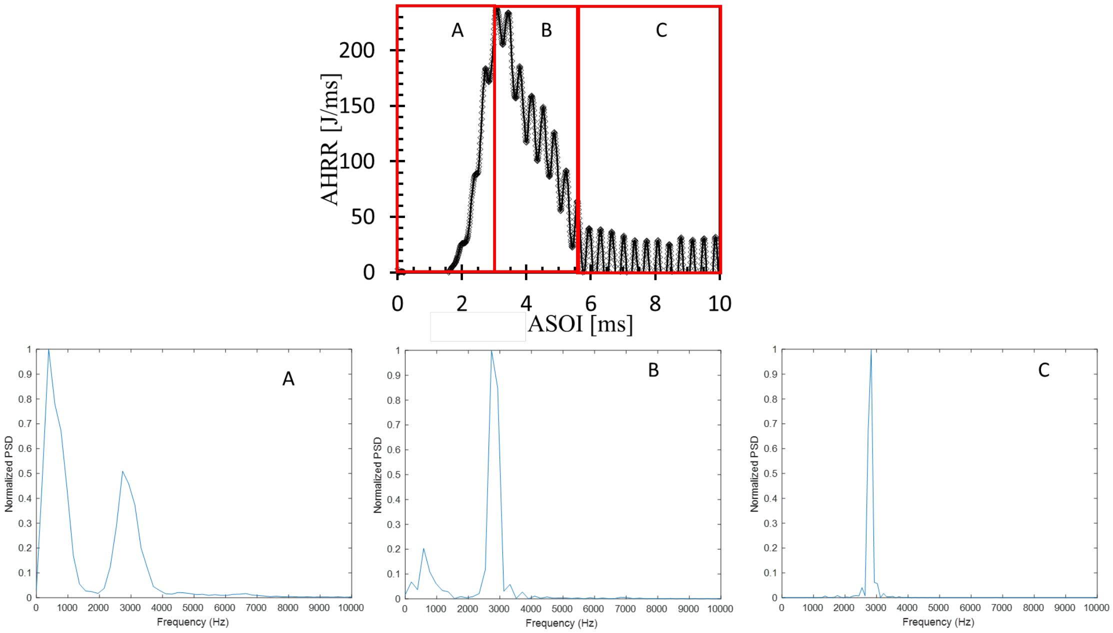

Figure 14-11 FFT analysis for three consecutive time domains of the AHRR curve

14.3 Results of CFD simulations

14.3.1 CFD setup

CFD simulations were performed to reproduce and explore the ringing case using the CV geometry (10 x 10 x 10 cm cube). Several attempts with the ambient temperature of 750 K failed to get successful combustion. Therefore, a new approach was adopted to reproduce a ringing case. The ambient temperature was increased to 900 K to guarantee the successful combustion, then the injector nozzle tip was moved closer to the wall. Two different nozzle-to-wall distances were tested, as shown in Figure 14-12. The intentional enhanced spray wall interaction was expected to produce ringing. In order to diagnose the high-frequency pressure oscillation, the simulation time step was set between 2.5 x 10^{-5} to 1.0 x 10^{-8} s, and the time interval for text output was set as 1e-06 to 1e-08 s. The typical CFD outputs use the region averaged pressure. However, the local pressure was measured at 125 selected virtual sensor locations. As shown in Figure 14-12, the CV was evenly divided into 64 small cubes. A virtual sensor was placed at each vertex (total 125) and numbered using (x,y,z) Cartesian coordinate system. The origin (0,0,0) which represents the pressure location in the experiment in the coordinate is the bottom left corner of the CV. The impinging point (2,2,0) is the center of the bottom wall.

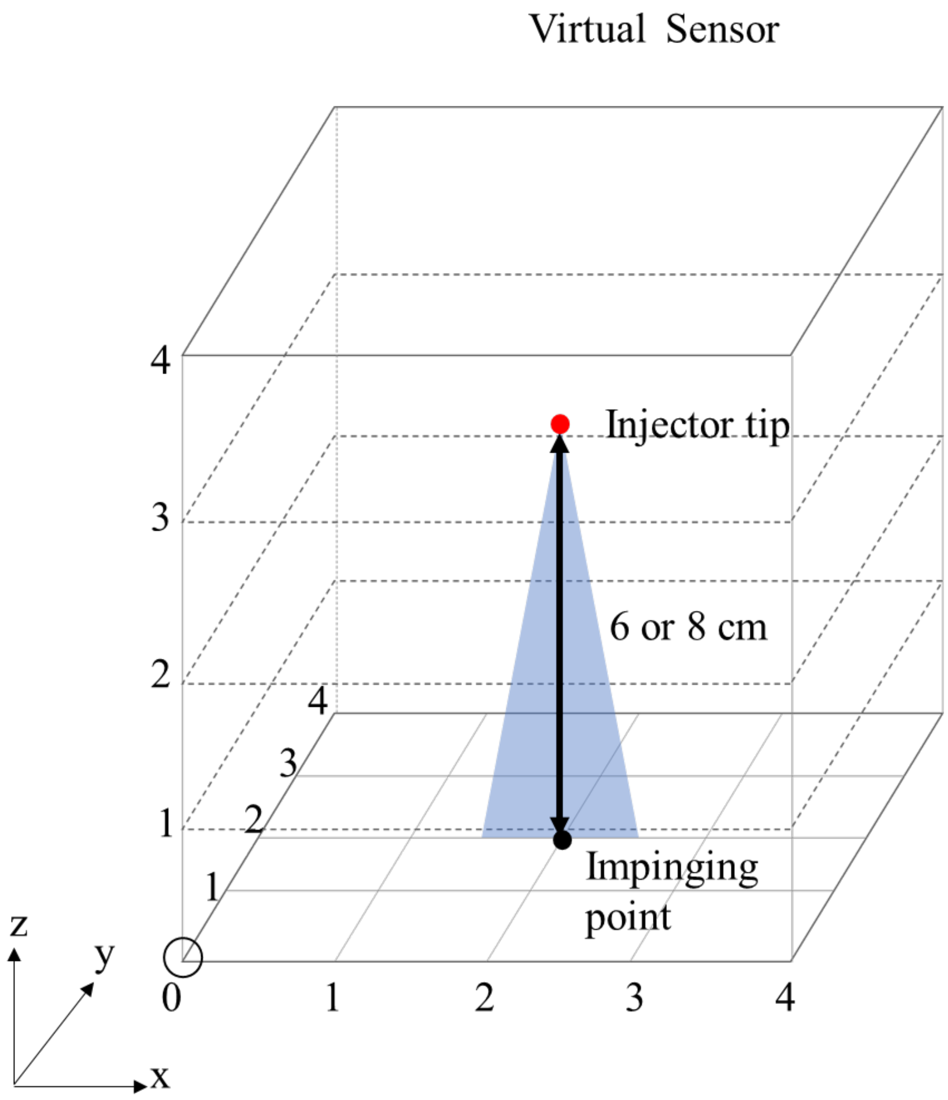

Figure 14-12 Schematic of the CFD simulation setup

14.3.2 Local pressure

With the adaptive meshing, the cell size and total cell counts in Converge simulation vary overtime based on the predefined criterion. It is hard to track the pressure in a specific cell, since the cell location and size may change during the simulation. The virtual sensor is developed with the Eulerian method. With an input of a specific location, the MATLAB code can find the closest cell and read its data. As shown in Figure 14-13, the local pressure at the location (0,0,0) is extracted using the virtual sensor is overlapping on the CV average pressure. The averaged pressure curve is smooth, and oscillation is smeared during the averaging process. The local pressure at the (0,0,0) did pick up the pressure oscillation successfully. Compared to the 80 mm nozzle-to-wall distance case, the 60 mm case showed similar oscillation frequency but less oscillation magnitude. The chemical HRR within the CV is also shown in Figure 14-13 as the second Y-axis. The HRR curve of the 60 mm case shows a shape of double peaks, while the 80 mm case has a higher single peak. The correlation between the high HRR peak and the high oscillation is verified through CFD. The double-peaks shape caused by the HRR interruption of the spray wall interaction. The heat loss through the wall holds temperature rise. The combustion is wobbling between the first-stage ignition sand the second stage ignition. The 60 mm case is also found to have longer second ignition delay (1.35 ms) compared to 1.20 ms of the 80 mm case.

Figure 14-14 and 14-15 show the time elapsed temperature field from the CFD simulation of 60 mm case and 80 mm case respectively. The color scale was adjusted per frame to maximize the contract. The first image is corresponding to the start of the impingement. The AOSI 2.4 ms is the start of the second HRR peak in the 60 mm case and the AOSI 3.0

ms is the end of it. The same time instances were also selected for the 80 mm for comparison. From Figure 14-14, at ASOI 2.4 ms, the flame only exists at the front location of the impinged spray (left and right most); at ASOI 3.0 ms, there was a clear flame recession from the impinged spray front location toward the impinging point, and even turned up pointing to the nozzle direction. The flame recession is corresponding to the second HRR peak, most of the recession flame is touching the wall. In Figure 14-15, after the start ignition near the imping point, the flame propagated toward outside away from the impinging point. It was also found a flame recession at ASOI 3.0 ms, however, this flame recession location is above impinging point and not touching the wall.

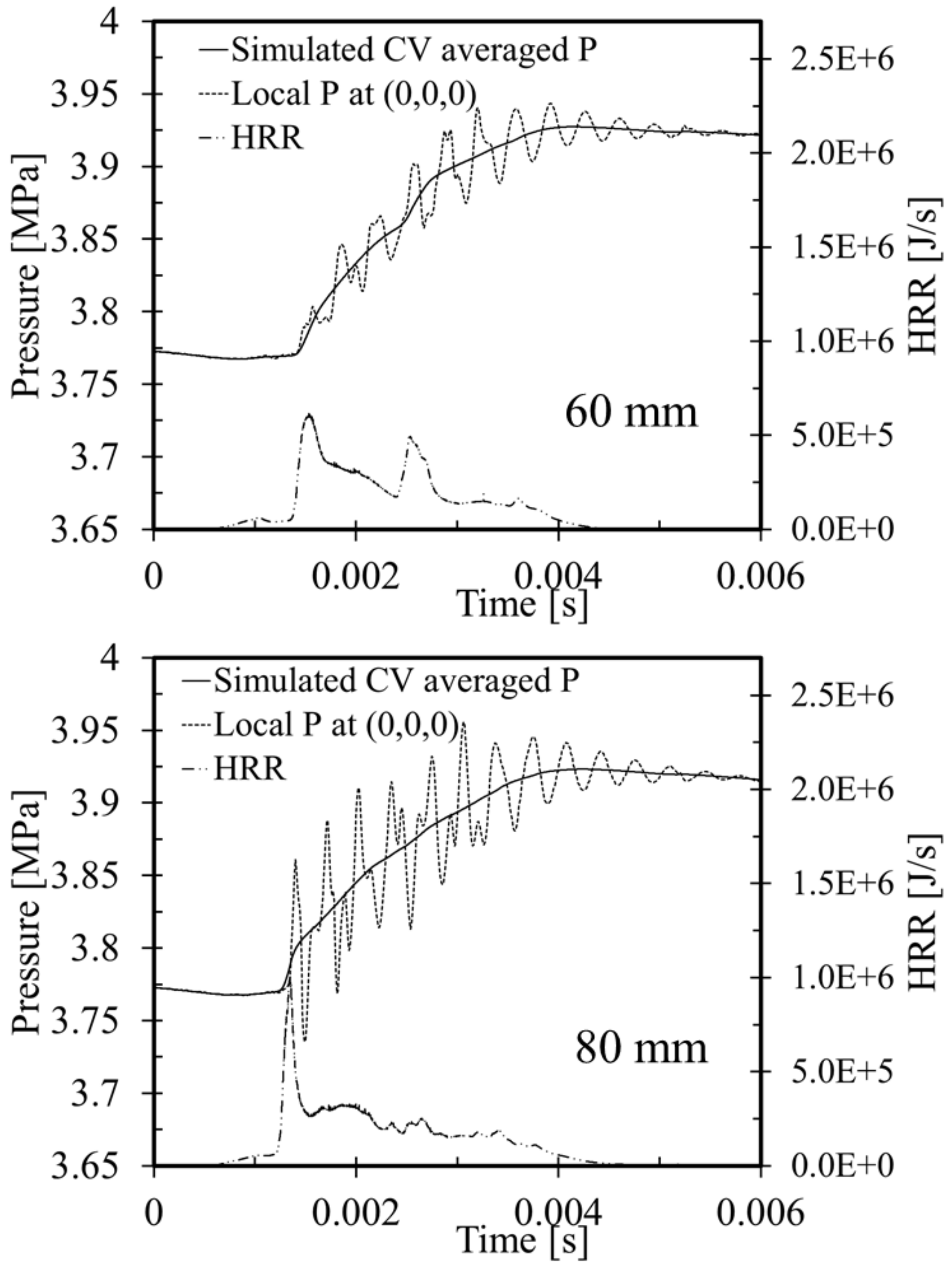

Figure 14-13 CFD results of CV averaged pressure and local pressure at the sensor location (0,0,0)

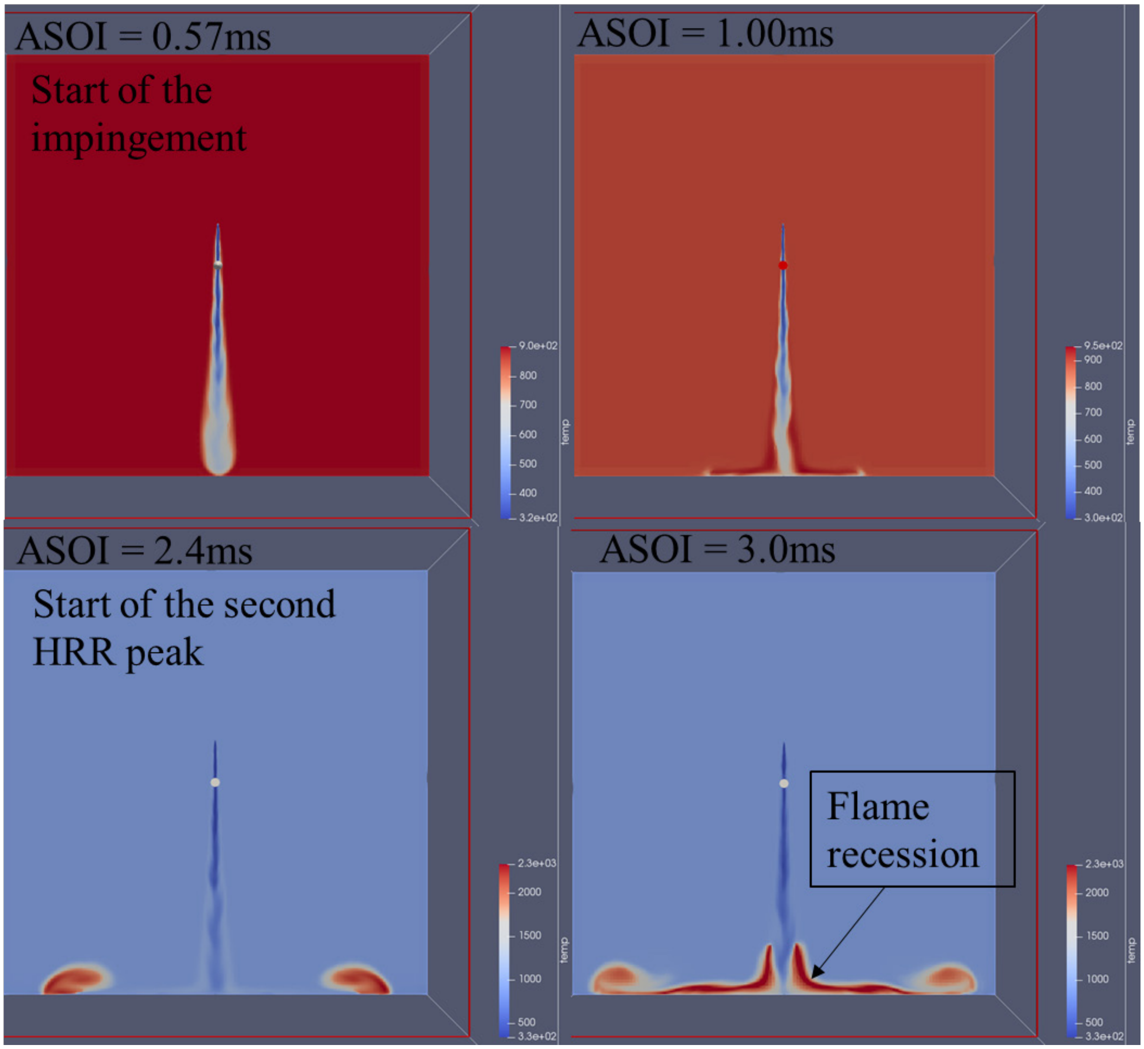

Figure 14-14 Time elapsed temperature field from the CFD simulation: ambient of 900K and 18% O_2, and nozzle to plate distance is 60 mm

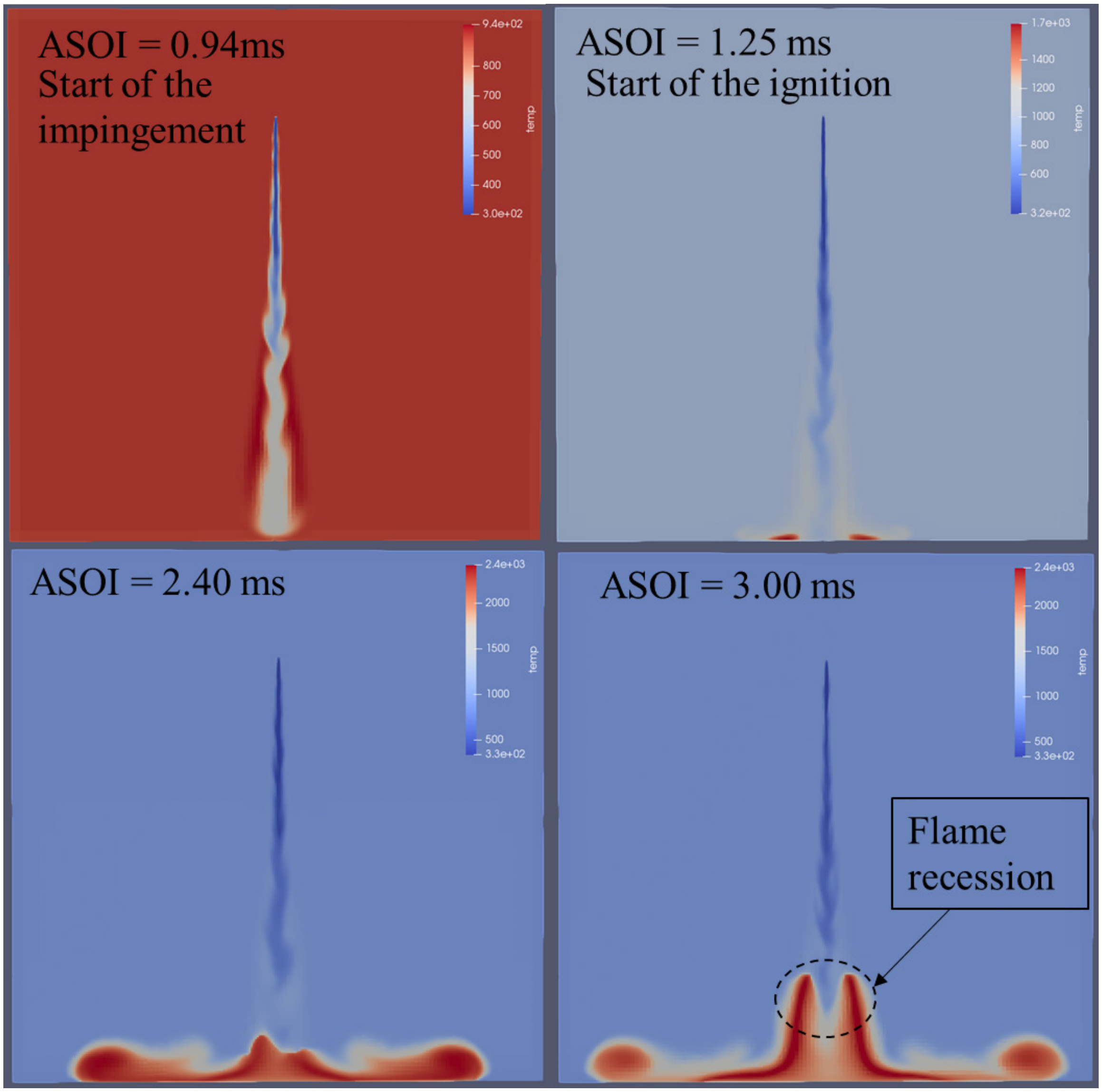

Figure 14-15 Time elapsed temperature field from the CFD simulation: ambient of 900K and 18% O2, and nozzle to plate distance is 80 mm

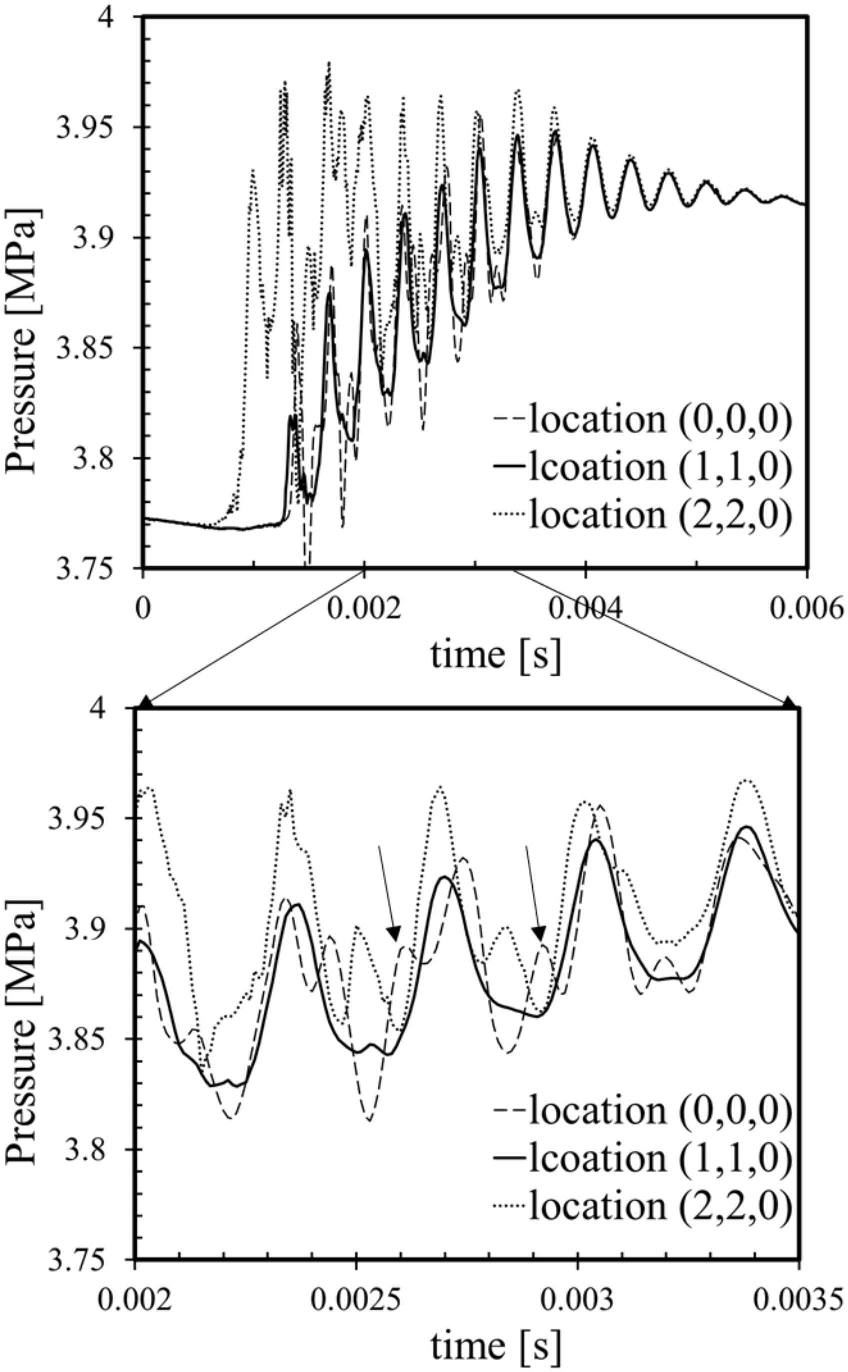

Figure 14-16 Local pressure from three different locations

To investigate the pressure oscillation cause and phasing, local pressure from three different locations are selected: corner location (0,0,0), impinging point (2,2,0), and the middle point location of them (1,1,0). As shown in Figure 14-16, overall the oscillation from different locations follows the same pattern and overlaps on top of each other in terms of the peaks and valleys. As time increases (t > 0.003 s), the synchronization becomes better. Regarding the magnitude of the pressure, the pressure read from the impinging point (2,2,0) is the largest because it is the source of the volumetric pressure wave (spray combustion), the corner location (0,0,0) is the second-largest because of the wall reflects the pressure wave and builds up the oscillations, and the pressure from the middle point (1,1,0) is the smallest one. The bottom plot in Figure 14-16 shows a zoomed-in view of the pressure. It is found that the pressure peaks from the middle point and the corner always have a temporal delay with respect to the pressure from the impinging point. The middle point pressure has a relatively constant temporal delay. However, the temporal delay of the pressure wave from the corner varies, because there seems to be another embedded wave pattern (marked out with arrows in Figure 14-16) which could be from the vertical direction.

14.3.3 FFT from CFD

The same FFT method used in the experimental data analysis was applied to the CFD pressure output at four different locations. The four locations were selected on the bottom wall. Figure 14-17 shows the FFT result of the 6 cm distance case, indicating that all the pressure has the same 3000 Hz characteristic peak on the frequency domain, which agrees with the experimental FFT results. Since the CFD simulations and the experiments were performed under different test conditions, the same frequency peak implies that it may be related to the CV geometry which is the same for both CFD simulations and experiments.

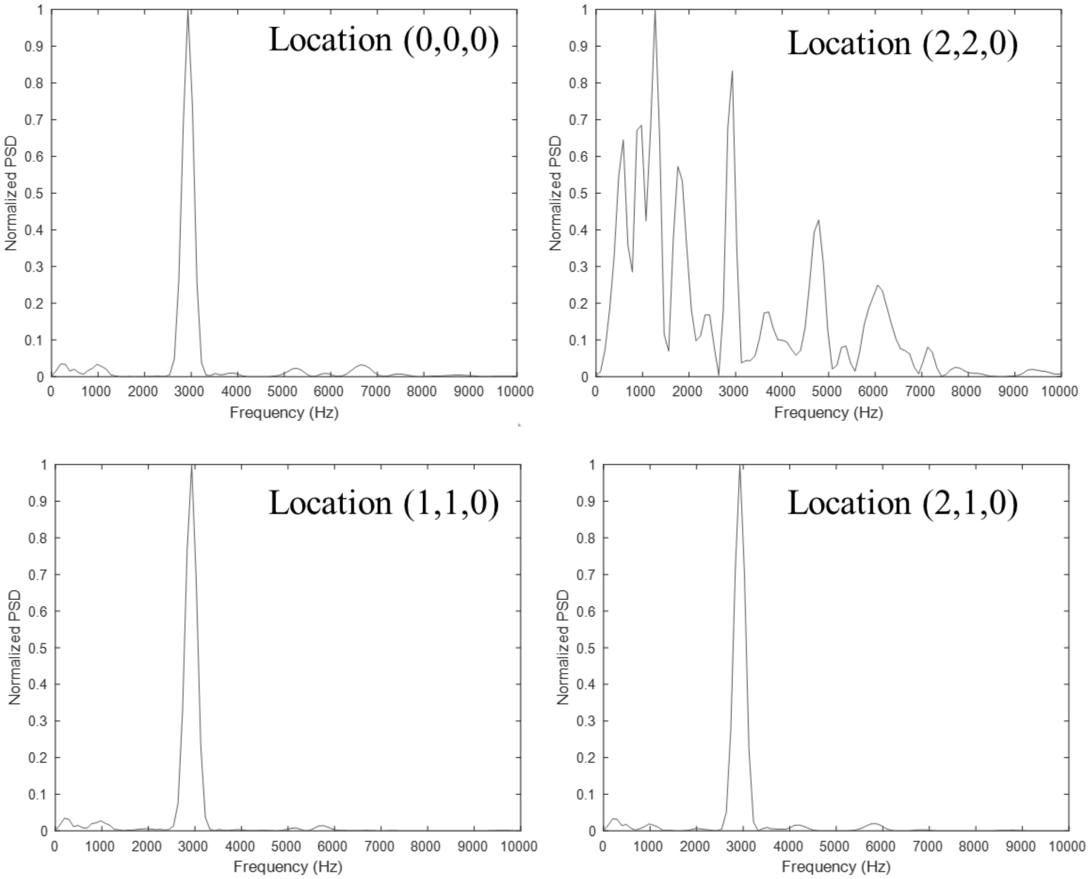

Figure 14-17 FFT results of pressure output from CFD

14.3.4 Pressure and heat release coupling

In order to evaluate the coupling between pressure oscillation and heat release within the CV chamber, the "Rayleigh criterion" was used to analyze this combustion process,

$$RCI = \int p'(t)q'(t)\, dt \qquad [14\text{-}1]$$

where RCI is the Rayleigh criterion index, p′ is the pressure fluctuation, and q′ is the heat release rate. If RCI > 0, the coupling is proved to be strong, meaning the pressure oscillations are in phase with the heat release oscillations and the magnitude of the thermoacoustic instability is maximized. Figure 14-18 shows the pressure, HRR, and the RCI at the location (2,2,0) of the 60 mm case. The HRR here is calculated using the ideal gas law. The pressure, volume, temperature, Cp, Cv were read from the cell value. The RCI was always positive during the whole process and in phase with the HRR of the cell. The coupling between pressure oscillation and the heat release was validated.

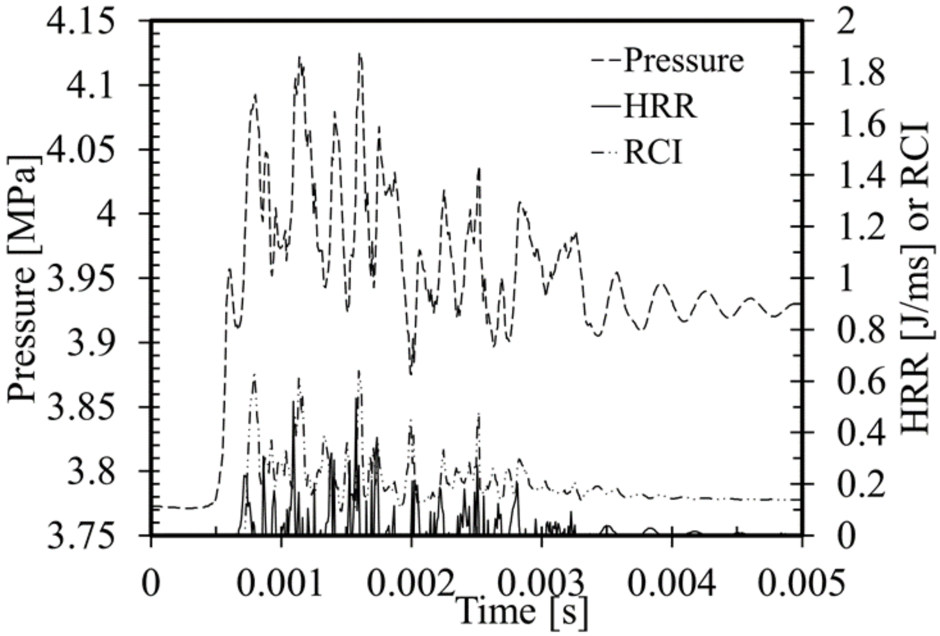

Figure 14-18 Pressure, HRR, and the Rayleigh criterion index at the location (2,2,0) of 60 mm case

14.3.5 Ringing index results

Applied the ring index calculation to the CFD results, and organized the results of 125 virtual sensors into 5 groups based on the plane height Z. As shown in Figure 14-19, the RI shows a bowl shape from Z =0 to Z=5 plane, which means the RI value is larger when the location is close to the top and bottom wall. There are several standing points with high RI value, which comes from the spray location. Those points were excluded from the analysis. At each plane height, the 80 mm case showed higher RI value compared to 60 cases. In addition, the 80 mm showed an overall large RI range (from 16 to 80), where 60 case only has the range of 16 to 45.

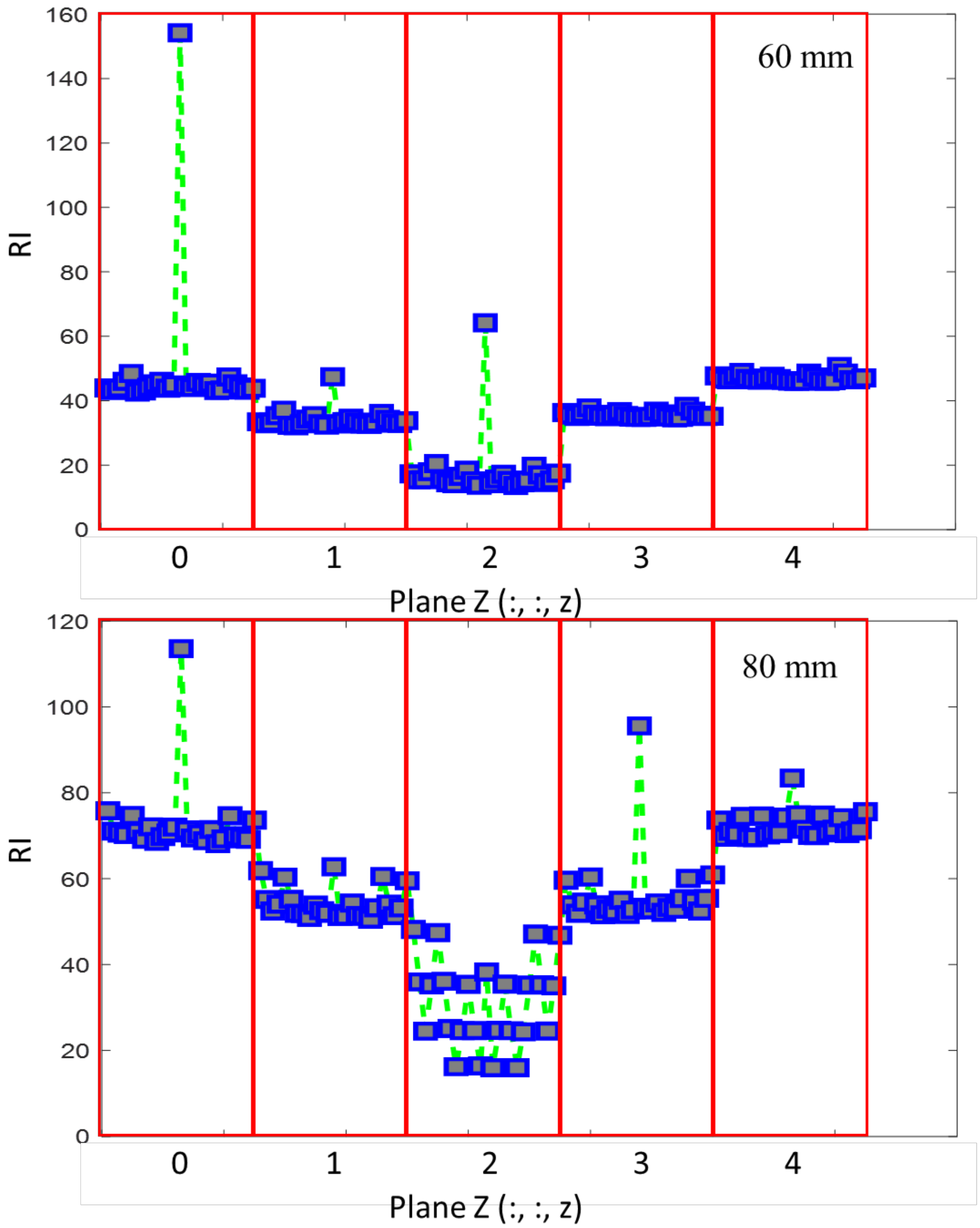

Figure 14-19 RI results of the CFD simulation

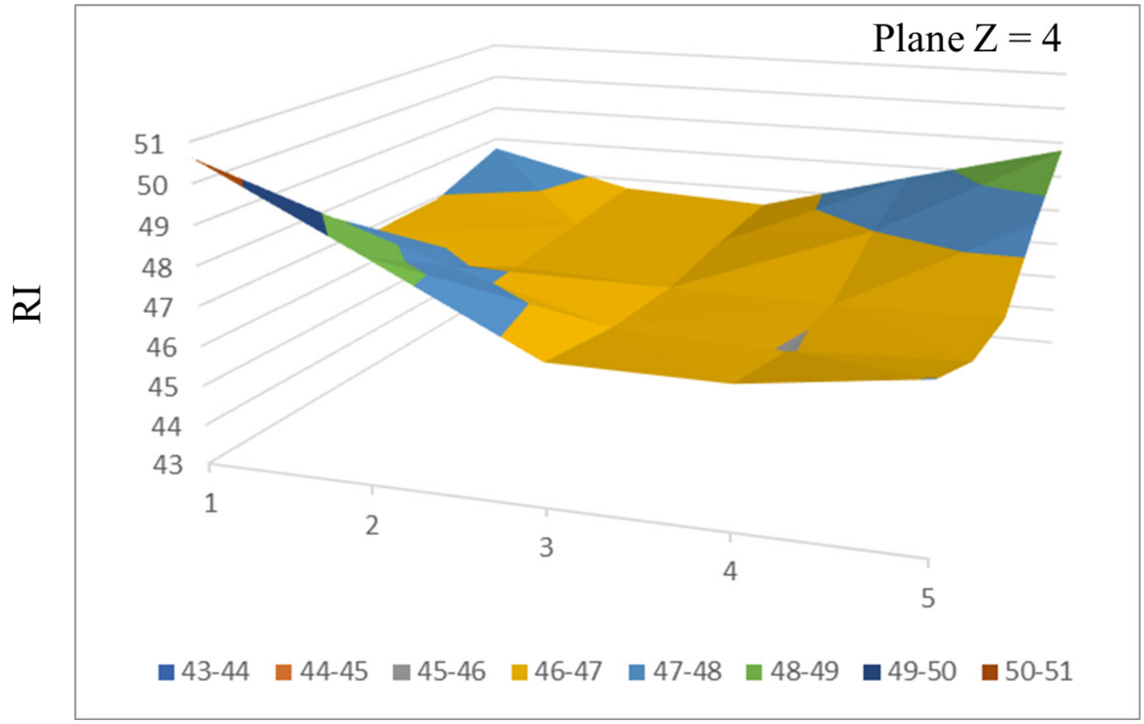

Figure 14-20 Visualization of RI results of the CFD simulation at plane Z = 4 of case 60 mm

Now, the RI results were visualized with one plane Z = 4 of the case 60 mm.

From Figure 14-20, it can be seen that the RI is not uniformly distributed within the same plane. The corner locations always have a higher RI value which has about 10% differences.

14.4 Summary and discussions

The analysis of the ringing cases from both experimental and numerical perspectives proved the pressure oscillation is in phase with the heat release rate. It is mainly caused by the elongated premixed combustion phase and the high premixed HRR peak. The pressure oscillations propagate from the impinging point to the bottom corner then from the bottom to the top of the CV. The distance from the nozzle to wall determines the impinging timing, ignition delay, and the premixed combustion phase distribution. The distance 80 mm showed higher RI and a larger level of pressure oscillations compared to the 60 mm case.

The RI method was developed to evaluate the severity of the ringing combustion event. The results of the RI showed the locations close to the bottom and top wall and the locations of corners usually have large RI.

15 Conclusions and Future Work

With the objectives of investigating the effect of high injection pressure on DME spray combustion characteristics spray and combustion processes of DME were studied extensively via a series of experiments in a constant-volume and optically accessible combustion vessel. In the current study, an HEUI with a 180 µm single-hole nozzle was driven by an oil-pressurized fuel injection system to achieve injection pressure up to 150 MPa. The liquid and vapor regions of DME jet were visualized using a hybrid Schlieren/Mie scattering at non-reacting conditions. At reacting conditions, high-speed natural flame luminosity of DME combustion was used to capture the flame intensity, and PLIF imaging was used to characterize CH2O evolution. Spray and combustion characteristics of DME were compared with diesel in terms of ROI, liquid/vapor penetration and, ignition delay. Flame LOL, flame structure, and formaldehyde formation of DME were also studied through high-speed imaging. The RANS Converge CFD simulation was validated against the experimental and used as a powerful tool to explore the DME spray characteristics under various conditions. Further insights into DME spray and flame structure were obtained through experimentally validated LES simulations.

Firstly, A 1-D MATLAB/Simulink single-hole/multi-hole injector model has been built and validated against experimental data. The validated model is used to predict the ROI profile of SH 180 µm injector at 150 MPa injection pressure. It is found from both experimental and simulation results that higher injection pressure leads to longer injection and shorter injection delay. For SH injector used for dedicated combustion studies and a constant volume chamber, the ROI profiles show a two-stages shape, with the 1st stage ending at the same time. In the 2^{nd} stage, ROIs for different injection pressures all hold the same magnitude. Comparing DME and diesel ROI for the same condition, it is shown that the injection of DME responds slowly and sustains longer than diesel, due to high compressibility. The MH injector results show that the compressibility effect dominates at low pressure (below 1000 bar injection pressure), but flow resistance has more impact on the high injection pressure side. Therefore, at low injection pressure, diesel has more injected volume than DME, but it is opposite on high injection pressure. The large flow rate in the MH injector shortens the needle closing process dramatically, and the 2^{nd} stage of the SH injector does not occur. DME results in higher injected total volume (approximately 12 %) at same pressure and duration when tested and simulated with the same nozzle as diesel; however, due to lesser energy content in the DME (approximately 33 %), nozzle size needs to be increased to get injection duration equivalent at the same pressure.

Secondly, the combustion characteristics comparison between DME and diesel was done through both experiments and numerical study. Experimental work was performed in a combustion vessel examining the spray behavior of DME and diesel. A RANS-type turbulence model with SAGE (well-mixed type) combustion model was applied to achieve a better understanding of the DME spray properties. 8-hole HEUI injector was tested in a combustion vessel for both DME and diesel fuels. The effects of ambient temperature on DME and diesel combustion characteristics for the same fuel energy content were compared. Fuel energy content for both fuels was matched by varying injection duration. Tests show DME has faster reactivity than diesel. CFD simulations were able to accurately capture the combustion process of the 8-hole injector. Low-temperature and high species were evaluated against chemical heat release rate and temperature evolution. HCO species was seen to a good indicator of the initial heat release rate.

Then, the correlation of formaldehyde to the ignition process in DME reacting spray was investigated in both the experiment and simulation. Fluorescence of formaldehyde (CH_2O) excited by a 355 nm laser wavelength was captured at different ASOIs over separate runs to provide a temporal and spatial view of its progression and recession. It was confirmed that the general concept of diesel combustion can be applied to DME combustion, meaning that CH_2O appears abundantly in low-temperature combustion process. CH_2O starts depleting when the temperature increases significantly, usually known as the time of ignition, or ignition delay. Validated CFD simulation predicted this phenomenon very well. Different stages of ignition were described by the profiles of CH_2O (low-temperature combustion or 1st stage of ignition), and OH (2nd stage of ignition characterized by high-temperature diffusion flame). CH_2O is seen upstream near the nozzle and is extended up to the flame lift-off location where OH is present. By studying the effect of oxygen levels in the ambient on DME combustion, the ignition process was reviewed by temperature profile, CH_2O, and OH. Regardless of which criteria are being considered, it was shown that ignition delay increases as the oxygen concentration reduce. However, at the lower oxygen concentrations, the indication of ignition was shown to be more reliable by the formation of CH_2O. It was seen that CH_2O was formed firstly during 1st stage ignition, and its depletion marks an important stage where high-temperature combustion is initiated as shown in the reactivity of fuel/air mixture in Phi-T scatter or overall temperature profile.

OH* is formed around the time of CH_2O depletion indicating the start of 2nd stage ignition where high-temperature reactions are present. However, this is not clearly observed in the cases of lower oxygen concentration as the initial formation of OH appears at a longer time after CH_2O is consumed. The temperature at the time of CH_2O depletion was already high (~ 1400 K) suggesting that the CH_2O profile can be a reliable source for understanding the ignition process. Overall, the results of this study provide information on single or two-stage behavior of ignition in DME reacting spray with the general suggestion on the use of CH_2O (its depletion) as the marker for ignition from low-to-high oxygen ambient conditions. With the growing research in combustion using laser diagnostic on CH_2O, it is prominence that the ignition process can be defined more accurately by the profile of CH_2O.

Thirdly, high injection pressure DME and diesel spray and combustion characteristics have been observed and compared carefully through experiments. Compared to diesel, DME has shorter liquid and vapor penetrations due to its low fuel density and fast evaporation. The microscopic imaging also shows DME evaporates quickly before the secondary breakup. The fast evaporation leads to shorter liquid length. DME shows shorter ignition delay at high injection pressure. The flame luminosity also appears with low intensity implying near-zero soot production. From the AHRR and CHR results, DME has faster ignition, weak premixed combustion, and high ratio of distribution on the diffusion combustion due to the fast evaporation property. CH_2O concentration reaches its peak at the same time of ignition and maximum AHRR but starts to decrease after the ignition. CH_2O consumption indicates the transition from low-temperature combustion to high-temperature combustion and is affected by ROI and chemical pathway.

Finally, the ringing case with large level pressure oscillation during DME spray combustion at low ambient temperature was observed and investigated. The ringing occurrence is highly related to the elongated premixed combustion phase. The low ambient temperature and the spray wall impingement both contribute to it. An evaluation method using the ringing index was established. It was found that the high ringing is related to the peak AHRR. The CFD simulations were also performed to simulate the ringing cases. The coupling between heat release rate and the pressure oscillations was proved using the Rayleigh criterion.

Future work will extend the study to a different injection system and explore the performance of the diesel and DME blending approach which has the huge benefits of no needs of adding fuel lubrications for DME. Regarding the ringing combustion issue at the low ambient temperature conditions, an improved spray wall interaction model and a wall heat transfer model will be added to the CFD simulation for a better prediction.

16 Reference List

Numbering method: chapter 1-8 is numbering 1 to 78. Starts from chapter 9, the references are numbers independently starting from 1 again.

[1] Energy Information Administration, Monthly Energy Review, March 2016, http://www.eia.gov/totalenergy/data/monthly/pdf/sec1_3.pdf .

[2] US Department of Transportation (US DOT), 2011. Federal Register 76, 48758-48769.

[3] An, F., Earley, R., and Green-Weiskel, L., “Global Overview on Fuel Efficiency and Motor Vehicle Emission Standards: Policy Options and Perspectives for International Cooperation,” United Nations Background Paper, (3), 2011.

[4] Takeishi, Kaoru. "Dimethyl ether (DME): a clean fuel of the 21st century and catalysts for it." synthesis 2 (2010): 3.

[5] Arcoumanis, Constantine, Choongsik Bae, Roy Crookes, and Eiji Kinoshita. "The potential of di-methyl ether (DME) as an alternative fuel for compression-ignition engines: A review." Fuel 87, no. 7 (2008): 1014-1030.

[6] Olah, G., Goeppert, A., and Prakash, G., Beyound Oil and Gas: The Methanol Economy, John Wiley & Sons, 2009.

[7] Schnepf, R., Yacobucci, B., Renewable fuel standard (RFS): Overview and Issues, January 23, 2012.

[8] Hara, T., Shimazaki, N., Yanagisawa, N., Seto, T. et al., “Study of DME Diesel Engine for Low Nox and CO2 Emission and Development of DME Trucks for Commercial Use,” SAE Int. J. Fuels Lubr. 5(1):233-242, 2012 doi:10.4271/2011-01-1961.

[9] Kapus PE, Cartellieri WP. ULEV potential of a DI/TCI diesel passenger car engine operated on di-methyl ether. SAE Paper 952754;1995.

[10] Hansen, J., Voss, B., Joensen, F., and Siguroardóttir, I., “Large ScaleManufacture of Dimethyl Ether - a New Alternative Diesel Fuel fromNatural Gas,” SAE Technical Paper 950063, 1995, doi:10.4271/950063.

[11] Sorenson, S. and Mikkelsen, S., “Performance and Emissions of a 0.273 Liter Direct Injection Diesel Engine Fuelled with Neat Dimethyl Ether,”SAE Technical Paper 950064, 1995, doi:10.4271/950064.

[12] Kajitani, S., Chen, Z., Konno, M., and Rhee, K., “Engine Performanceand Exhaust Characteristics of Direct-injection Diesel Engine Operatedwith DME,” SAE Technical Paper 972973, 1997, doi:10.4271/972973.

[13] Gill, D., Ofner, H., Schwarz, D., Sturman, E. et al., “The Performance of a Heavy Duty Diesel Engine with a Production Feasible DME Injection System,” SAE Technical Paper 2001-01-3629, 2001, doi:10.4271/2001-01-3629.

[14] An, B., Sato, Y., Lee, S., and Takayanagi, T., "Effects of Injection Pressure on Combustion of a Heavy Duty Diesel Engine With Common Rail DME Injection Equipment," SAE Technical Paper 2004-01-1864, 2004, doi:10.4271/2004-01-1864.

[15] Kim, M. Y., Yoon, S. H., Ryu, B. W., & Lee, C. S. (2008). Combustion and emission characteristics of DME as an alternative fuel for compression ignition engines with a high pressure injection system. Fuel, 87(12), 2779-2786.

[16] Mitsugi, Y., Wakabayashi, D., Tanaka, K., and Konno, M., "High-Speed Observation and Modeling of Dimethyl Ether Spray Combustion at Engine-Like Conditions," SAE Int. J. Engines 9(1):2016, doi:10.4271/2015-01-1927.

[17] Tow, T., Pierpont, D. and Reitz, R. D. (1994). Reducing particulate and NOx emissions by using multiple injections in a heavy duty DI diesel engine, SAE Technical Paper.

[18] Han, Z., Uludogan, A., Hampson, G. J. and Reitz, R. D. (1996). Mechanism of soot and NOx emission reduction using multiple-injection in a diesel engine, SAE Technical Paper.

[19] Pickett, L. M., Kook, S. and Williams, T. C. (2009). "Visualization of Diesel Spray Penetration, Cool-Flame, Ignition, High-Temperature Combustion, and Soot Formation Using High-Speed Imaging." SAE Int. J. Engines 2(1): 439-459.

[20] Pickett, L. M., Genzale, C. L., Bruneaux, G., Malbec, L.-M., Hermant, L., Christiansen, C. A. and Schramm, J. (2010). "Comparison of diesel spray combustion in different high-temperature, high-pressure facilities." SAE International Journal of Engines 3(2): 156-181.

[21] Pickett, L. M. (2011). "Relationship Between Diesel Fuel Spray Vapor PenetrationDispersion and Local Fuel Mixture Fraction."

[22] Lillo, P. M., Pickett, L. M., Persson, H., Andersson, O. and Kook, S. (2012). "Diesel Spray Ignition Detection and Spatial/Temporal Correction." SAE Int. J. Engines 5(3): 1330-1346.

[23] Cung, K., Moiz, A., Johnson, J., Lee, S.-Y., Kweon, C.-B. and Montanaro, A. (2014). "Spray–combustion interaction mechanism of multiple-injection under diesel engine conditions."

[24] Skeen, S. A., Manin, J. and Pickett, L. M. (2015). "Simultaneous formaldehyde PLIF and high-speed schlieren imaging for ignition visualization in high-pressure spray flames." Proceedings of the Combustion Institute 35(3): 3167-3174.

[25] Lin, S. P., and R. D. Reitz. "Drop and spray formation from a liquid jet." Annual Review of Fluid Mechanics 30, no. 1 (1998): 85-105.

[26] Baumgarten, C. (2006). Mixture formation in internal combustion engines, Springer Science & Business Media.

[27] Soid, S. and Zainal, Z. (2011). "Spray and combustion characterization for internal combustion engines using optical measuring techniques–a review." Energy 36(2): 724-741.

[28] Suh, H. and Lee, C. (2008). "Experimental and analytical study on the spray characteristics of dimethyl ether (DME) and diesel fuels within a common-rail injection system in a diesel engine." Fuel 87(6): 925-932.

[29] Dent, J. (1971). A basis for the comparison of various experimental methods for studying spray penetration, SAE Technical Paper.

[30] Pastor, J. V., Arrègle, J., García, J. M. and Zapata, L. D. (2007). "Segmentation of diesel spray images with log-likelihood ratio test algorithm for non-Gaussian distributions." Applied optics 46(6): 888-899.

[31] Heywood, J. B. (1988). Internal combustion engine fundamentals, Mcgraw-hill New York.

[32] Park, S., Kim, H. and Lee, C. (2010). "Macroscopic spray characteristics and breakup performance of dimethyl ether (DME) fuel at high fuel temperatures and ambient conditions." Fuel 89(10): 3001-3011.

[33] Hiroyasu, H., Arai, M. and Tabata, M. (1989). Empirical equations for the Sauter mean diameter of a Diesel spray, SAE Technical Paper.

[34] Dec, John E. 1997. A conceptual model of di diesel combustion based on laser-sheet

imaging*. SAE technical paper.

[35] Higgins, B. and Siebers, D. L. (2001). Measurement of the Flame Lift-Off Location on DI Diesel Sprays Using OH Chemiluminescence, SAE International.

[36] Dec, J. E. and Espey, C. (1998). Chemiluminescence Imaging of Autoignition in a DI Diesel Engine, SAE International.

[37] Pickett, L. M., Siebers, D. L. and Idicheria, C. A. (2005). Relationship between ignition processes and the lift-off length of diesel fuel jets, SAE technical paper.

[38] Lee, S.-Y., Turns, S. R. and Santoro, R. J. (2009). "Measurements of soot, OH, and PAH concentrations in turbulent ethylene/air jet flames." Combustion and Flame 156(12): 2264-2275.

[39] Semelsberger, T., Borup, R. and Greene, H. (2006). "Dimethyl ether (DME) as an alternative fuel." Journal of Power Sources 156(2): 497-511.

[40] Park, S. and Lee, C. (2014). "Applicability of dimethyl ether (DME) in a compression ignition engine as an alternative fuel." Energy Conversion and Management 86: 848-863.

[41] Cung, Khanh, Jaclyn Johnson, and Seong-Young Lee. Development of Chemical Kinetic Mechanism for Dimethyl Ether (DME) with Comprehensive Polycyclic Aromatic Hydrocarbon (PAH) and NOx Chemistry. No. 2015-01-0807. SAE Technical Paper, 2015.

[42] Jung, D. and Iida, N. (2015). "Closed-loop control of HCCI combustion for DME using external EGR and rebreathed EGR to reduce pressure-rise rate with combustion-phasing retard." Applied Energy 138: 315-330.

[43] Kim, H. J., Park, S. H., Suh, H. K. and Lee, C. S. (2009). "Atomization and evaporation characteristics of biodiesel and dimethyl ether compared to diesel fuel in a high-pressure injection system." Energy & Fuels 23(3): 1734-1742.

[44] Suh, H. K., Yoon, S. H. and Lee, C. S. (2010). "Effect of multiple injection strategies on the spray atomization and reduction of exhaust emissions in a compression ignition engine fueled with dimethyl ether (DME)." Energy & Fuels 24(2): 1323-1332.

[45] Kim, M. Y., Yoon, S. H., Ryu, B. W. and Lee, C. S. (2008). "Combustion and emission characteristics of DME as an alternative fuel for compression ignition engines with a high pressure injection system." Fuel 87(12): 2779-2786.

[46] Kim, M. Y., Bang, S. H. and Lee, C. S. (2007). "Experimental investigation of spray and combustion characteristics of dimethyl ether in a common-rail diesel engine." Energy & fuels 21(2): 793-800.

[47] Ying, Wang, Li Genbao, Zhu Wei, and Zhou Longbao. "Study on the application of DME/diesel blends in a diesel engine." Fuel Processing Technology 89, no. 12 (2008): 1272-1280.

[48] Kaiser, W., Wallington, T., Hurley, M., Platz, J., Curran, H., Pitz, W., and Westbrook, C., “Experimental and Modeling Study of Premixed Atmospheric-Pressure Dimethyl Ether-Air Flames,” Journal of Physical Chemistry A 104, No. 35, 8194-8206 (2000), Lawrence Livermore National Laboratory, Livermore, CA, UCRL-JC-136123.

[49] Fischer, L., Dryer, F., and Curran, H., "The Reaction Kinetics of Dimethyl Ether. I: High-Temperature Pyrolysis and Oxidation in Flow Reactors," Int. J. Chem. Kinet. 32:

713–740, 2000. Lawrence Livermore National Laboratory, Livermore, CA, UCRL-JC-239461.

[50] Curran, H., Fischer, S., and Dryer, F., "The Reaction Kinetics of Dimethyl Ether. II: Low-Temperature Pyrolysis and Oxidation in Flow Reactors,"Int. J. Chem. Kinet. 32: 741–759, 2000. Lawrence Livermore National Laboratory, Livermore, CA, UCRL-JC-239496.

[51] Pfahl, U., Fieweger, K., and Adomeit, G., Self-ignition of diesel-relevant hydrocarbon-air mixtures under engine conditions, Symposium (International) on Combustion, Volume 26, Issue 1, 1996, Pages 781-789, ISSN 0082-0784, 10.1016/S0082-0784(96)80287-6.

[52] Rosado-Reyes, C.M., Francisco, J.S., Szente, J.J., Maricq, M.M., and Oostergaard, L.F., "Dimethyl Ether Oxidation at Elevated Temperatures (295-600 K)," J. Physical Chemistry A 109(48):10940-10953, 2005.

[53] Mittal, G., Chaos, M., Sung, C.-J. and Dryer, F. L. (2008). "Dimethyl ether autoignition in a rapid compression machine: Experiments and chemical kinetic modeling." Fuel Processing Technology 89(12): 1244-1254.

[54] Cung, K., Bhagat, M., Zhang, A. and Lee, S.-Y. (2013). "Numerical Study on Emission Characteristics of High-Pressure Dimethyl Ether (DME) under Different Engine Ambient Conditions." SAE Technical Paper.

[55] Dagaut, P., Daly, C., Simmie, J., and Cathonnet, M., Twenty-Seventh Symposium (International) on Combustion., The Combustion Institute, Pittsburgh, 1998, pp. 361-369.

[56] Liu, F., Ju, Y., Qin, X., and Smallwood, G., "An updated detailed mechanism for dimethyl ether combustion.", NRC National Publications Archive, 2006, 1-6.

[57] Anderson, John David, and J. Wendt. Computational fluid dynamics. Vol. 206. New York: McGraw-Hill, 1995.

[58] Wendt, John, ed. Computational fluid dynamics: an introduction. Springer Science & Business Media, 2008.

[59] Richards, K. J., Senecal, P. K., and Pomraning, E., CONVERGE (v2.2.0), Convergent Science, Inc., Middleton, WI (2014).

[60] Halstead, M. P., L. J. Kirsch, and C. P. Quinn. "The autoignition of hydrocarbon fuels at high temperatures and pressures—fitting of a mathematical model."Combustion and flame 30 (1977): 45-60.

[61] Amsden, Anthony A., P. J. O'rourke, and T. D. Butler. KIVA-II: A computer program for chemically reactive flows with sprays. No. LA-11560-MS. Los Alamos National Lab., NM (USA), 1989.

[62] Colin, O., A. Benkenida, and C. Angelberger. "3D modeling of mixing, ignition and combustion phenomena in highly stratified gasoline engines." Oil & gas science and technology 58, no. 1 (2003): 47-62.

[63] Chen, Q. "Comparison of different k-ε models for indoor air flow computations."Numerical Heat Transfer, Part B Fundamentals 28, no. 3 (1995): 353-369.

[64] Han, Zhiyu, and Rolf D. Reitz. "Turbulence modeling of internal combustion engines using RNG κ-ε models." Combustion science and technology 106, no. 4-6 (1995): 267-295.

[65] Neely, Gary D, Shizuo Sasaki, Yiqun Huang, Jeffrey A Leet, and Daniel W Stewart. 2005. New diesel emission control strategy to meet US Tier 2 emissions regulations. SAE Technical Paper.

[66] Musculus, Mark PB, Paul C Miles, and Lyle M Pickett. 2013. "Conceptual models for partially premixed low-temperature diesel combustion." Progress in Energy and Combustion Science 39 (2):246-283.

[67] Internet source, https://en.wikipedia.org/wiki/Combustion_instability

[68] Lieuwen, T. C. and Yang, V. (2005). Combustion instabilities in gas turbine engines. AIAA.

[69] Rayleigh, J. W. S. (1896). The Theory of Sound Volume 2. Dover Publications.

[70] Zhu, Xiucheng, Sanjeet Limbu, Khanh Cung, William De Ojeda, and Seong-Young Lee. HEUI Injector Modeling and ROI Experiments for High Injection Pressure of Diesel and Dimethyl Ether (DME). No. 2016-01-0855. SAE Technical Paper, 2016.

[71] Bhagat, Meghraj, Khanh Cung, Jaclyn Johnson, Seong-Young Lee, Jeffrey Naber, and Sam Barros. “Experimental and Numerical Study of Water Spray Injection at Engine-Relevant Conditions.” No. 2013-01-0250. SAE Technical Paper, 2013.

[72] Zhang, A., Montanaro, A., Allocca, L., Naber, J. et al., "Measurement of Diesel Spray Formation and Combustion upon Different Nozzle Geometry using Hybrid Imaging Technique," SAE Int. J. Engines 7(2):1034-1043, 2014, DOI: 10.4271/2014-01-1410.

[73] J. E. Nesbitt, J. D. Naber, S.-Y. Lee, E. Kurtz, H.-W. Ge, and N. Robarge, “Investigation of Vaporizing Diesel Liquid Spray Plume to Plume Penetration Variations,” in Proceedings of 23rd ILASS Americas Conference, Paper, 2011, no. 132.

[74] Mie, Gustav (1908). "Beiträge zur Optik trüber Medien, speziell kolloidaler Metallösungen". Annalen der Physik 330(3): 377–445.

[75] Settles, Gary S. Schlieren and shadowgraph techniques, 2001.

[76] Otsu, N., "A Threshold Selection Method from Gray-Level Histograms," Automatica 11(285-296):23-27, 1975,

[77] Cung, Khanh, Abdul Moiz, Jaclyn Johnson, Seong-Young Lee, Chol-Bum Kweon, and Alessandro Montanaro. "Spray–combustion interaction mechanism of multiple-injection under diesel engine conditions." Proceedings of the Combustion Institute 35, no. 3 (2015): 3061-3068.

[78] Ahmed Abdul Moiz, "LOW TEMPERATURE SPLIT INJECTION SPRAY COMBUSTION: IGNITION, FLAME STABILIZATION AND SOOT FORMATION CHARACTERISTICS IN DIESEL ENGINE CONDITIONS", Open Access Dissertation, Michigan Technological University, 2016. http://digitalcommons.mtu.edu/etdr/253

CHAPTER 9

[9-1] EPA, 2014. Regulatory Impact Analysis, U.S. Environmental Protection Agency, Office of Transportation and Air Quality. EPA-420-R-14-005, February 2014. Available at http://www.epa.gov/otaq/models/nmim/420r05024.pdf.

[9-2] US Department of Transportation (US DOT), 2011. Federal Register 76, 48758-48769.

[9-3] Takeishi, Kaoru. "Dimethyl ether (DME): a clean fuel of the 21st century and catalysts for it." synthesis 2 (2010): 3.

[9-4] Arcoumanis, Constantine, Choongsik Bae, Roy Crookes, and Eiji Kinoshita. "The potential of di-methyl ether (DME) as an alternative fuel for compression-ignition engines: A review." Fuel 87, no. 7 (2008): 1014-1030.

[9-5] Fleisch, Theo H., and Peter C. Meurer. "DME: the Diesel fuel for the 21st Century?." In AVL Conference on Engine and Environment. 1995.

[9-6] Park, Su Han, and Chang Sik Lee. "Applicability of dimethyl ether (DME) in a compression ignition engine as an alternative fuel." Energy Conversion and Management 86 (2014): 848-863.

[9-7] Cung, Khanh, Jaclyn Johnson, and Seong-Young Lee. Development of Chemical Kinetic Mechanism for Dimethyl Ether (DME) with Comprehensive Polycyclic Aromatic Hydrocarbon (PAH) and NO x Chemistry. No. 2015-01-0807. SAE Technical Paper, 2015.

[9-8] Phan, Anthony. "Development of a rate of injection bench and constant volume combustion chamber for diesel spray diagnostics." (2009).

[9-9] Bosch, Wilhelm. The fuel rate indicator: a new measuring instrument for display of the characteristics of individual injection. No. 660749. SAE Technical Paper, 1966.

[9-10] Takamura, Akio, Susumu Fukushima, Yukimitsu Omori, and Takeyuki Kamimoto. Development of a new measurement tool for fuel injection rate in diesel engines. No. 890317. SAE Technical Paper, 1989.

[9-11] Bower, Glenn R., and David E. Foster. A Comparison of the Bosch and Zuech rate of injection meters. No. 910724. SAE Technical Paper, 1991.

[9-12] Hansen, John Bogild, and Svend-Erik Mikkelsen. "DME as a Transportation Fuel." Prepared for the Danish Road Safety and Transport Agency and the Danish Environmental Protection Agency, Lyngby, Denmark (2001).

[9-13] Tsuchiya, Takayuki, and Yoshio Sato. Development of DME engine for heavy-duty truck. No. 2006-01-0052. SAE Technical Paper, 2006.

[9-14] Szybist, James P., Samuel McLaughlin, and Suresh Iyer. "Emissions and Performance Benchmarking of a Prototype Dimethyl Ether Fueled Heavy-Duty Truck." In ABSTRACTS OF PAPERS OF THE AMERICAN CHEMICAL SOCIETY, vol. 248. 1155 16TH ST, NW, WASHINGTON, DC 20036 USA: AMER CHEMICAL SOC, 2014.

[9-15] Bennett, Sean. Medium/Heavy Duty Truck Engines, Fuel & Computerized Management Systems. Cengage Learning, 2012.

CHAPTER 10

[10-1] Mitsugi, Y., Wakabayashi, D., Tanaka, K., and Konno, M., "High-Speed Observation and Modeling of Dimethyl Ether Spray Combustion at Engine-Like Conditions," SAE Int. J. Engines 9(1):2016, doi:10.4271/2015-01-1927.

[10-2] Levich, V.G., “Physicochemical Hydrodynamics,” Prentice-Hall, New Jersey, ISB-10: 0136744400, 1962.

[10-3] Kapus P, Ofner H. Development of fuel injection equipment and combustion system for DI diesels operated on di-methyl ether. SAE Paper 950062, SAE Trans J Fuel Lubr 1995;104(4):54–9.

[10-4] Ikeda T, Ohmori Y, Takamura A, Sato Y, Jun L, Kamimoto T. Measurement of the rate of multiple fuel injection with diesel fuel and DME. SAE Paper 2001-01-0527, SAE Trans J Engine 2001;110(3): 372–80.

CHAPTER 11

[11-1] H. Wang, M. Frenklach, A detailed kinetic modeling study of aromatics formation in laminar premixed acetylene and ethylene flames, Combustion and Flame 110 (1997) 173-221.

[11-2] C. Arcoumanis, C. Bae, R. Crookes, E. Kinoshita, The potential of di-methyl ether (DME) as an alternative fuel for compression-ignition engines: A review, Fuel 87 (2008) 1014-1030.

[11-3] H. Teng, J.C. McCandless, J.B. Schneyer, Thermodynamic properties of dimethyl ether-An alternative fuel for compression-ignition engines, Report No. 0148-7191, SAE Technical Paper, 2004.

[11-4] G. Mittal, M. Chaos, C.-J. Sung, F.L. Dryer, Dimethyl ether autoignition in a rapid compression machine: Experiments and chemical kinetic modeling, Fuel Processing Technology 89 (2008) 1244-1254.

[11-5] H. Teng, J.C. McCandless, J.B. Schneyer, Compression ignition delay (physical+ chemical) of dimethyl ether-An alternative fuel for compression-ignition engines, Report No. 0148-7191, SAE Technical Paper, 2003.

[11-6] K.D. Cung, Spray and combustion characteristics of dimethyl ether under various ambient conditions: An experimental and modeling study, MICHIGAN TECHNOLOGICAL UNIVERSITY, 2015.

[11-7] L. Zhao, A.A. Moiz, S.-Y. Lee, J. Naber, S. Barros, W. Atkinson, Investigation of Multi-Hole Impinging Jet High Pressure Spray Characteristics under Gasoline Engine-Like Conditions, Report No. 0148-7191, SAE Technical Paper, 2016.

[11-8] K.J. Richards, Senecal, P. K., and Pomraning, E., CONVERGE Manual (Version 2.3), in: C.S. Inc. (Ed.), 2016.

[11-9] R. Reitz, F. Bracco, Mechanisms of breakup of round liquid jets, Encyclopedia of fluid mechanics 3 (1986) 233-249.

[11-10] Z. Han, R.D. Reitz, Turbulence Modeling of Internal Combustion Engines Using RNG κ-ε Models, Combustion Science and Technology 106 (1995) 267-295.

[11-11] P.K. Senecal, E. Pomraning, K.J. Richards, S. Som, An Investigation of Grid Convergence for Spray Simulations using an LES Turbulence Model, SAE International, 2013.

[11-12] H. Wang, Y. Ra, M. Jia, R.D. Reitz, Development of a reduced n-dodecane-PAH mechanism and its application for n-dodecane soot predictions, Fuel 136 (2014) 25-36.

[11-13] K. Cung, A. Moiz, J. Johnson, S.-Y. Lee, C.-B. Kweon, A. Montanaro, Spray–combustion interaction mechanism of multiple-injection under diesel engine conditions, Proceedings of the Combustion Institute 35 (2015) 3061-3068.

CHAPTER 12

[12-1] S. Park, and C. Lee, Energy. Convers. Manage. 101 (86) (2014) 848-863.

[12-2] C. Arcoumanis, C. Bae, R. Crookes, E. Kinoshita, Fuel. 87 (7) (2008) 1014-1030.

[12-3] H. Teng, J.C. McCandless, J.B. Schneyer, SAE Technical Paper 2001-01-0154, (2001).

[12-4] J. Wang, M. Chaos, B. Y, T.A. Cool, F.L. Dryer, T. Kasper, N. Hansen, P. Oßwald, K. Kohse-Höinghausd, P. Westmorelande, Phys. Chem. Chem. Phys. 11 (2009) (9) 1328-1339.

[12-5] G. Mittal, M. Chaos, C.-J. Sung, F.L. Dryer, Fuel Process. Technol., 89 (2008) (12) 1244-1254.

[12-6] Curran, H., W.J. Pitz1, C.K. Westbrook, P. Dagaut, J.-C. Boettner, M. Cathonnet, Int. J. Chem. Kinet., 30 (1998) (3) 229-241.

[12-7] C. Spencer, M.G. Sorenson, A.L. Duane, SAE Technical Paper 981159, (1998).

[12-8] H. Teng, J.C. McCandless, J.B. Schneyer, SAE Technical Paper 2003-01-0759, (2003).

[12-9] H.J. Kim, S.H. Park, C.S. Lee, Fuel Process. Technol. 91 (2010) (3) 354-363.

[12-10] Y. Kim, J. Lim, K. Min, Int. J. Engine Res. 8 (2007) (4) 337-346.

[12-11] G. Thomas, B. Feng, A. Veeraragavan, M.J. Cleary, N. Drinnan, Fuel Process. Technol. 119 (2014) 286-304.

[12-12] C.A. Idicheria, L.M. Pickett, SAE Technical Paper 206-01-3434, (2006).

[12-13] M.P.B. Musculus, P.C. Miles, L.M. Pickett, Prog. Energy Combust. Sci. 39 (2013) (2-3) 246-283.

[12-14] C.A. Idicheria, L.M. Pickett, Proc. Combust. Inst. 31 (2007) (2) 2931-2938.

[12-15] V. Dias, C. Duynslaegher, F. Contino, J. Vandooren, H. Jeanmart, Combust. Flame, 159 (2012) (5) 1814-1820.

[12-16] S.A. Skeen, J. Manin, L.M. Pickett, Proc. Combust. Inst. 35 (2015) (3) 3167-3174.

[12-17] S.F. Glassey, A.R. Stockner, M.A. Flinn, SAE Technical Paper 930270, (1993).

[12-18] K. Cung, A. Moiz, J. Johnson, S.Y. Lee, C.B. Kweon, A. Montanaro, Proc. Combust. Inst. 35 (2015) (3) 3061-3068.

[12-19] Engine Combustion Network Experimental Data Archive, available at <http:// http://www.sandia.gov/ecn/>.

[12-20] G. Bruneaux, M. Auge, C. Lemenand, Int. Symp. Diagn. Model. Combust. Internal Combust. Engines. (2004) (6) 551-559.

[12-21] W. Bosch, SAE Technical Paper 660749, (1966).

[12-22] R. Payri, F.J. Salvador, J. Gimeno, G. Bracho, Exp. Tech., 32 (2008) (1) 46-49.

[12-23] K. Richards, P. Senecal, E. Pomraning, CONVERGE 2.1. 0 Theory Manual, Convergent Science. Inc., Middleton, WI, 2013.

[12-24] P.K. Senecal, E. Pomraning, K.J. Richards, S. Som, SAE Technical Paper 2013-01-1083, (2013).

[12-25] R.D. Reitz, R. Diwakar, SAE Technical Paper 1987-02-01, (1987).

[12-26] P.K. Senecal, K.J. Richards, E. Pomraning, T. Yang, M.Z. Dai, R.M. McDavid, M.A. Patterson, S. Hou, T. Shethaji, SAE Technical Paper 2007-04-16, (2007).

[12-27] D. P. Schmidt, C.J. Rutland, J. Comput. Phys. 164 (2000) (1) 62-80.

[12-28] P.K. Senecal, E. Pomraning, K.J. Richards, T.E. Briggs, C.Y. Choi, R.M. McDavid, M. A. Patterson, SAE Technical Paper 2003-01-1043, (2003).

[12-29] K. Cung, Spray and combustion characteristics of dimethyl ether under various ambient conditions: An experimental and modeling study, PhD thesis, Michigan Technological University, Houghton, Michigan, USA, 2015.

[12-30] U. Pfahl, K. Fieweger, G. Adomeit, Int. Symp. Combust. 26 (1996) (1) 781-789.

[12-31] Reaction Design, ReactionWorkbench Manual, Reaction Design: San Diego, 2013.

[12-32] J. Beeckmann, L. Cai, O. Röhl, H. Pitsch, N. Peters, SAE Technical Paper 2010-01-2108, (2010).

[12-33] K. Cung, M. Bhagat, A. Zhang, S.Y. Lee, SAE Technical Paper 2013-01-0319, (2013).

[12-34] P.K. Senecal, E. Pomraning, K.J. Richards, S. Som, ASME ICEF2012-92043 (2012) 697-710.

[12-35] P.K. Senecal, S. Mitra, E. Pomraning, Q. Xue, S. Som, S. Banerjee, B. Hu, K. Liu, D. Rajamohan, J.M. Deur, ASME ICEF2014-5488 (2014) (2) V002T06A002.

[12-36] H. Kosaka, T. Aizawa, T. Kamimoto, Int. J. Engine Res. 6 (2005) (1) 21-42.

Chapter 13

[13-1] T. Kaoru, Synthesis 2 (2010): 3.

[13-2] C. Arcoumanis, C. Bae, R. Crookes, E. Kinoshita, Fuel 87 (7) (2008) 1014-1030.

[13-3] R. Song, K. Li, Y. Feng, S. Liu, Energy Fuels 23 (11) (2009) 5460-5466.

[13-4] D. Jung, N. Iida, Applied Energy 138 (2015) 315-330.

[13-5] C. Spencer, M.G. Sorenson, A.L. Duane, SAE Technical Paper 981159, (1998).

[13-6] H. Teng, J.C. McCandless, J.B. Schneyer, SAE Technical Paper 2003-01-0759, (2003).

[13-7] H.J. Kim, S.H. Park, C.S. Lee, Fuel Process. Technol. 91 (3) (2010) 354-363.

[13-8] Y. Kim, J. Lim, K. Min, Int. J. Engine Res. 8 (4) (2007) 337-346.

[13-9] Y. Mitsugi, D. Wakabayashi, K. Tanaka, M. Konno, SAE Int. J. Engines 9 (1) (2016) 210-221.

[13-10] S.F. Glassey, A.R. Stockner, M.A. Flinn, SAE Technical Paper 930270, (1993).

[13-11] K Cung, AA Moiz, X Zhu, SY Lee, Proc. Combust. Inst. 36 (3) (2017) 3605-3612.

[13-12] K. Cung, A. Moiz, J. Johnson, S.Y. Lee, C.B. Kweon, A. Montanaro, Proc. Combust. Inst. 35 (2015) (3) 3061-3068.

[13-13] B. Higgins, D. L. Siebers, SAE Technical Paper, 2001-01-0918, (2001).

[13-14] M.P.B. Musculus, P.C. Miles, L.M. Pickett, Prog. Energy Combust. Sci. 39 (2-3) (2013) 246-283.

[13-15] C.A. Idicheria, L.M. Pickett, SAE Technical Paper 2006-01-3434, (2006).

[13-16] S.A. Skeen, J. Manin, L.M. Pickett, Proc. Combust. Inst. 35 (3) (2015) 3167-3174.

[13-17] K.N. Gabet, J.A. Sutton, Exp. Fluids (2014) 55: 1774.

[13-18] J. Wu, J. Yin, J. Chem. Eng. Data 53 (9) (2008): 2247-2249.

[13-19] B. An, Y. Sato, S. Lee, T. Takayanagi, SAE Technical Paper 2004-01-1864, (2004).

[13-20] V.G. Levich, Physicochemical Hydrodynamics, Prentice-Hall, New Jersey, ISB-10: 0136744400, 1962.

[13-21] B. Schneider, CRFD and Laser Diagnostic Workshop, 21st CIMAC Congress, (1995).

[13-22] R. D. Reitz and R. Diwakar, SAE Technical Paper 870598, (1987).

[13-23] F. X. Tanner, SAE Technical Paper, 970050, (1997).

[13-24] J.B. Heywood, Internal combustion engine fundamentals, Vol. 930, New York, McGraw-Hill Education, 1988.

[13-25] M.Y. Kim, S.H. Bang, C.S. Lee, Energy Fuels 21 (2) (2007) 793-800.

[13-26] X. Zhu, S. Limbu, K. Cung, W.D. Ojeda, S.-Y. Lee, SAE Technical Paper 2016-01-0855, (2016).

[13-27] J. Wang, M. Chaos, B. Y, T.A. Cool, F.L. Dryer, T. Kasper, N. Hansen, P. Oßwald, K. Kohse-Höinghausd, P. Westmorelande, Phys. Chem. Chem. Phys. 11 (2009) (9) 1328-1339.

[13-28] K. Richards, P. Senecal, and E. Pomraning, "Converge theory manual," Convergent Sciences Inc., Madison, WI, http://www. convergecfd. com, 2014.

[13-29] A.A. Moiz, M.M. Ameen, S.-Y. Lee, S. Som, Combust. Flame, 173 (2016), pp. 123-131.

A Copyright documentation

Figures in chapter 9 are from: Zhu, Xiucheng, Sanjeet Limbu, Khanh Cung, William De Ojeda, and Seong-Young Lee. HEUI Injector Modeling and ROI Experiments for High Injection Pressure of Diesel and Dimethyl Ether (DME). No. 2016-01-0855. SAE Technical Paper, 2016.

Copyright Clearance Center | Marketplace™

SAE International - License Terms and Conditions

This is a License Agreement between Xiucheng Zhu ("You") and SAE International ("Publisher") provided by Copyright Clearance Center ("CCC"). The license consists of your order details, the terms and conditions provided by SAE International, and the CCC terms and conditions.

All payments must be made in full to CCC.

Order Date	05-Dec-2019	Type of Use	Republish in a thesis/dissertation
Order license ID	1007427-1	Publisher	SAE International
System ID	2016-01-0855	Portion	Chapter/article

LICENSED CONTENT

Publication Title	HEUI Injector Modeling and ROI Experiments for High Injection Pressure of Diesel and Dimethyl Ether (DME)	Country	United States of America
		Rightsholder	SAE International
		Publication Type	Report
Author/Editor	Zhu, Xiucheng		
Date	12/31/2015		

REQUEST DETAILS

Portion Type	Chapter/article	Rights Requested	Main product
Page range(s)	1-9	Distribution	Worldwide
Total number of pages	9	Translation	Original language of publication
Format (select all that apply)	Print, Electronic	Copies for the disabled?	No
Who will republish the content?	Academic institution	Minor editing privileges?	No
Duration of Use	Life of current edition	Incidental promotional use?	No
Lifetime Unit Quantity	Up to 99,999	Currency	USD

NEW WORK DETAILS

Title	HIGH INJECTION PRESSURE DME IGNITION AND COMBUSTION PROCESSES: EXPERIMENT AND SIMULATION	Institution name	Michigan Technological University
		Expected presentation date	2019-12-15
Instructor name	Seong-Young Lee		

ADDITIONAL DETAILS

Order reference number	N/A	The requesting person / organization to appear on the license	Xiucheng Zhu

REUSE CONTENT DETAILS

Title, description or numeric reference of the portion(s)	The whole article	Title of the article/chapter the portion is from	N/A
Editor of portion(s)	N/A	Author of portion(s)	Zhu, Xiucheng
Volume of serial or monograph	N/A	Issue, if republishing an article from a serial	N/A
Page or page range of portion	1-9		
		Publication date of portion	2015-12-31

Figures in chapter 11 are from: Le Zhao, Ahmed Abdul Moiz, Xiucheng Zhu, Seong-Young Lee, Experimental and Numerical Study of Diesel vs. DME in a Constant Volume Combustion Vessel, 10th U. S. National Combustion Meeting Organized by the Eastern States Section of the Combustion Institute, April 23-26, 2017 College Park, Maryland

The combustion institute do not hold a copyright on the papers that were presented at the 10th USNCM. In addition, this work was not published elsewhere.

Figures in chapter 12 are from: Cung, Khanh, Ahmed Abdul Moiz, Xiucheng Zhu, and Seong-Young Lee. "Ignition and formaldehyde formation in dimethyl ether (DME) reacting spray under various EGR levels." Proceedings of the combustion institute 36, no. 3 (2017): 3605-3612.